Computer modelling for the prediction and analysis of spectroscopic data: Application to lyotropic aggregates and transition metal centres

Christopher C. Prior

Thesis for the degree of Doctor of Philosophy

University of East Anglia

School of Chemistry

Norwich

September 2017

Abstract

In this thesis Density Functional Theory (DFT) and Molecular Dynamics (MD) simulations are used to predict, interpret and analyse a range of Electron Paramagnetic Resonance (EPR) and Nuclear Inelastic Scattering (NIS) spectra of different molecular systems. By relating theory and experiment, the models are rigorously tested as well as enabling a clearer interpretation of complex spectra.

Firstly, slow motion EPR spectra of microaggregate, micellar, hexagonal and lamellar lyotropic liquid crystal aggregations are investigated for two different surfactant/water systems. Geometric parameters predicted from MD simulations, such as aggregate radii and eccentricity, are compared with experimental data and the dynamics investigated through the use of the Model-Free (MF) approach, allowing for prediction of EPR spectra using the Stochastic Liouville Equation (SLE) in order to relate dynamics and geometry. For the complex hexagonal and lamellar lineshapes, the MF-SLE predicted spectra are compared with those predicted directly and completely from MD. These techniques and simulation approaches are then expanded to the investigation of the structure and dynamics of spin labelled DNA. A scheme for rotation about triple bonds in MD is found to produce good agreement with the spectra observed for acetylene tethered spin labelled DNA using the new parmbsc1 forcefield.

The geometry and magnetic parameters of two molybdenum complexes are calculated using DFT. The fast motion EPR spectra are then simulated using these parameters, thereby confirming the proposed rearrangement of core geometry in the catalytic cycle.

Finally, the NIS spectra of a range of iron-sulphur clusters are predicted using DFT for a series of model compounds and hypothetical structures and compared with available experimental spectra. This tests both the accuracy of DFT and the ability of NIS to discriminate between iron sulphur clusters, whilst additionally confirming spectral assignments.

Acknowledgements

Firstly I would like to thank my supervisor Dr Vasily Oganesyan for his guidance, support, and knowledge throughout my undergraduate and postgraduate degrees at the University of East Anglia and for introducing me to different aspects of molecular modelling and EPR and NIS spectroscopies. I would also like to extend my appreciation to my secondary supervisor Prof. Andy Cammidge for his helpful, down to earth advice. This thesis would not have been possible without them.

My special thanks go all the members of Dr Oganesyan's group; in particular Dr Fatima Chami for her introduction to AMBER and assistance with forcefields and to Dr Andrea Catte and Pauline Walton for many helpful discussions. I would also like to express my appreciation to Dr Gaye White from the School of Biology for assistance with sample preparation.

I gratefully acknowledge the University of East Anglia for funding my PhD studentship. My gratitude also goes to both the university's high performance cluster Grace, with whom I have had almost daily exchanges since the end of my undergraduate degree, and her dedicated supporting team at UEA HPC.

I would also like to acknowledge Prof. Andrew Thomson and Prof. Nick Le Brun for insightful discussions on iron-sulphur proteins and their role in biology.

Thanks to the occupants of Prof. Cammidge's lab, the Energy and Materials laboratory and all the other people who have lent me equipment and workspace over the years. In particular in this regard I would like to thank Simon who almost always managed to fulfil my need for increasingly tiny spatulas and pots, as well as for the welcome tea breaks, walks and other adventures. Also thanks to my good friends Dave, Peter, Louis, Lisa and my brother Tim, as well as the occupants of the desk room for providing distractions of the best possible kind!

Finally, I would like to thank both my parents without whose encouragement and support I would not be where I am today.

Publications arising from this work

- C. Prior and V. S. Oganesyan; Prediction of Lyotropic Liquid Crystal EPR Spectra using Molecular Dynamics and the Model-Free Approach; *Chemistry - A European Journal*, 2017; **23**; 13192-13204 [1]

- C. Prior, L. R. Webster, S. K. Ibrahim, J. A. Wright, A. F. Alghamdi, V. S. Oganesyan and C. J. Pickett; EPR detection and characterisation of a paramagnetic Mo(III) dihydride intermediate involved in electrocatalytic hydrogen evolution; *Dalton Trans.*; 2016 ; **45**; 2399-2403 [2]

- P. N. Serrano, H. Wang, J. C. Crack, C. Prior, M. I. Hutchings, A. J. Thomson, S. Kamali, Y. Yoda, J. Zhao, M. Y. Yu, E. E. Alp, V. S. Oganesyan, N. E. Le Brun and S. P. Cramer; Nitrosylation of Nitric-Oxide-Sensing Regulatory Proteins Containing [4Fe-4S] Clusters Gives Rise to Multiple Iron-Nitrosyl Complexes; *Angew. Chem. Int. Ed.*; 2016; **55**; 14575-14579 [3]

- C. Prior, L. Danilane and V. S. Oganesyan; Direct Prediction of Spin Labelled DNA EPR Spectra from Molecular Dynamics - *In Preparation*

Abbreviations

Full Name	Abbreviation
5-DOXYL Stearic Acid	5DSA
Assisted Model Building with Energy Refinement	AMBER
CHarges from ELectrostatic Potentials using a Grid based method	CHELPG
Critical Micelle Concentration	CMC
Density Functional Theory	DFT
Dinitrosyl Iron Complex	DNIC
Dodecyltrimethylammonium Chloride	DTAC
Effective Core Potential	ECP
Electron Paramagnetic Resonance	EPR
Electron-Nuclear Dipole Interaction	ENDI
Fokker-Planck	FP
Gaussian Type Orbital	GTO
General Amber Force Field	GAFF
Hartree-Fock	HF
Infrared	IR
Microscopic Order Macroscopic Disorder	MOMD
Model-Free	MF
Molecular Dynamics	MD
Normalised Root-Mean-Square Deviation	NRMSD
Nuclear Inelastic Scattering	NIS
Nuclear Magnetic Resonance	NMR
Partial Vibrational Density of States	PVDOS
Polarizable Continuum Model	PCM
Potential Energy Surface	PES
Quantum Mechanics	QM

Full Name	Abbreviation
Restrained ElectroStatic Potential	RESP
Root-Mean-Square Deviation	RMSD
Roussin's Black Salt	RBS
Roussin's Black Ester	RBE
Roussin's Red Ester	RRE
Roussin's Red Salt	RRS
Self-Consistent Field	SCF
Singly Occupied Molecular Orbital	SOMO
Slater Type Orbital	STO
Slowly Relaxing Local Structure	SRLS
Sodium Dodecyl Sulphate	SDS
Stochastic Liouville Equations	SLE

Contents

List of Figures

List of Tables

Chapter 1

Introduction

Since the publication of "*Opticks: Or, A Treatise of the Reflexions, Refractions, Inflexions and Colours of Light*" by Isaac Newton in 1704, spectroscopy has become fundamental to the scientific method to a degree where it would be hard to imagine modern science without it. Today, advanced spectroscopic techniques such as electron paramagnetic resonance (EPR), nuclear magnetic resonance (NMR), nuclear inelastic scattering (NIS), Raman, infrared, fluoresence and X-ray spectroscopies allow for the measurement of a wide range of processes, systems and properties. However, as spectroscopic techniques have advanced, so has the complexity of the data they produce, making interpreting data often more challenging than obtaining it. For example in the case of magnetic resonance spectroscopies such as EPR and NMR, spectra are sensitive to the magnetic and dynamic properties of both the target molecule and surrounding environment, resulting in a large number of parameters being required to describe the observed experimental output.

Fortunately, advances in computing power and computational methods have made *ab initio* prediction viable for an increasing range of spectral phenomena. In modern computational chemistry this typically involves the use of density functional theory (DFT) to determine the properties of individual molecules through the application of quantum mechanics and molecular dynamics (MD) using classical

mechanics for the study of bulk properties and dynamics.

Here these computational techniques are applied in a complementary manner to the prediction and analysis of EPR and NIS spectra. Both EPR and NIS are highly selective and sensitive, and as such have seen substantial use in the study of complex systems in which many other techniques may result in highly convoluted spectra [14][17][18]. In chapters 2 and 3 the slow motion EPR spectra of spin doped lyotropic aggregates and spin labelled DNA are predicted and interpreted using a combination of MD and spectral modelling. The link between simulation and experiment is provided by direct prediction and parameterisation of the autocorrelation function using the model-free (MF) approach to separate motional contributions. The fast motion EPR spectra of molybdenum complexes are investigated in chapter 4 through the use of DFT and spectral fitting in order to confirm the geometry of an unstable intermediate. In chapter 5 the potential of NIS to discriminate between biologically relevant iron-sulphur clusters is examined using DFT to predict spectra of a range of known and hypothetical structures.

1.1 Electron Paramagnetic Resonance

Electron paramagnetic resonance (EPR) spectroscopy (sometimes called electron spin resonance - ESR) can offer substantial insights into structural, chemical and magnetic environments of unpaired spins as well as the dynamic processes they are involved in over a broad timescale. The sister technique of nuclear magnetic resonance (NMR) has seen wider use as a result of early technical developments allowing the technique to be applied in a more versatile manner [19]. However, due to the difference in mass, the magnetic moment of an electron is substantially higher than that of a nucleus, affording EPR a greater resolution. Additionally, as the majority of molecules are diamagnetic, by introducing paramagnetic species into targeted parts of systems via a specific label (covalently attached to

sample) or probe (unattached), EPR can be used in a highly selective manner in complex samples. This selectivity is particularly important for biochemical systems where EPR has been used to study lipids [20][21][22], DNA [23][24][25][26] and proteins (metalloproteins [27][28][29] and spin labelled mutants [30][31][32]) where conventional NMR spectra can be overwhelmed by signals from the host. The technique has also been applied in the areas of liquid crystals [8][14][33][34] with EPR being able to resolve critical sub-nanosecond dynamics inaccessible to NMR which typically operates on the millisecond timescale. EPR has also been applied extensively to transition metal complexes where the magnetic properties of many oxidation states permit a convenient way to study the redox chemistry metal centre [35].

Additionally, as well as being used for studies of dynamics [36] and electron distributions [37], EPR experiments have also been developed to measure oxygen concentration [38], redox chemistry [39], distance measurements [40], imaging [41] and viscosity [42], making modern EPR a highly flexible technique.

1.1.1 Principles of EPR

Magnetic Resonance

The EPR phenomenon results from spin angular momentum, S, which in turn arises from the behaviour of unpaired electrons described by (1.1):

$$S = \frac{h}{2\pi}\sqrt{s(s+1)} \tag{1.1}$$

where s is the spin quantum number ($\frac{1}{2}$ for a single electron) and h is the Planck constant. This leads to a magnetic moment, μ, described by (1.2):

$$\mu = -g\beta S \tag{1.2}$$

where β is the Bohr magneton and g is the Zeeman splitting factor. For a free electron, $g_e = 2.002319$. In real systems, a truly free electron g value is not usually observed due to spin-orbit coupling resulting in mixing with excited states,

as well as in response to local magnetic fields such as those produced by other paramagnetic species, quadrupoles or ligand fields. As a result although nitroxides and organic radicals, particularly those with highly delocalised electrons, tend to exhibit g values near that of the free electron, transition metals often demonstrate greater deviations. As S and magnetic field, B_0, both have an orientational dependence, g assumes a general 3×3 tensor form (1.3):

$$g = \begin{pmatrix} g_{xx} & g_{xy} & g_{xz} \\ g_{yx} & g_{yy} & g_{yz} \\ g_{zx} & g_{zy} & g_{zz} \end{pmatrix} \tag{1.3}$$

However, by choosing an appropriate coordinate system, this can be diagonalized leaving only three principal values: g_{xx}, g_{yy} and g_{zz}.

The Bohr magneton, β, relates the magnetic moment to spin angular momentum via (1.4):

$$\beta = \frac{eh}{4\pi M_e} \tag{1.4}$$

where e and M_e are the electron charge and mass respectively. Under normal conditions, electron magnetic moments are randomly aligned and therefore all spin state energy levels, E, are degenerate. Applying an external magnetic field, B_0, results in magnetic moments orienting either parallel (low energy) or anti-parallel (high energy) with the magnetic field lifting the degeneracy as described by (1.5):

$$E = m_s g \beta B_0 \tag{1.5}$$

where m_s is the spin quantum number ($\pm\frac{1}{2}$). This allows for radiation of energy ΔE to be absorbed for transitions of $\Delta m_s = \pm 1$ (1.6):

$$\Delta E = E(m_s = +\frac{1}{2}) - E(m_s = -\frac{1}{2}) = hv = g\beta B_0 \tag{1.6}$$

where v is microwave frequency.

Continuous Wave EPR

Continuous Wave EPR is by far the most common EPR experimental procedure and uses a microwave of a fixed wavelength whilst scanning the magnetic field as shown in Figure 1.1. Starting from $B_0 = 0$ where the energy levels are degenerate, B_0 is increased until the separation of energy levels matches the microwave energy as in equation (1.6) and absorption occurs. This experimental set-up has mainly been used as a result of it being much harder to engineer a stable microwave

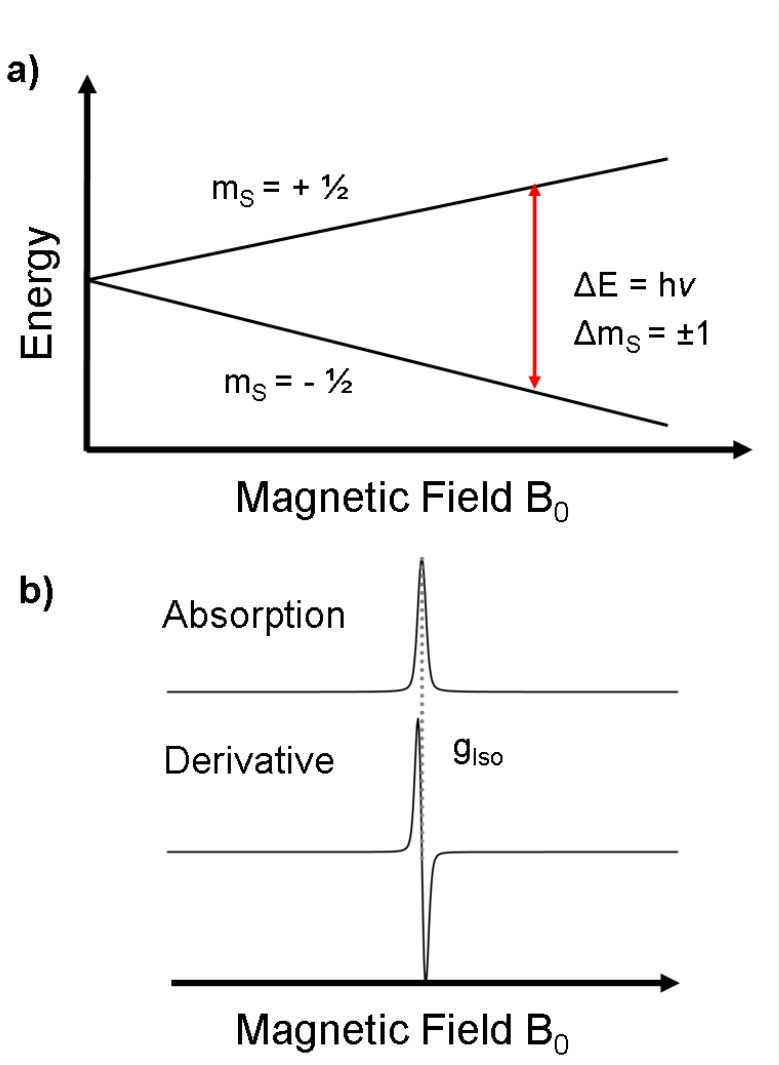

Figure 1.1: a) Effect of varying magnetic field, B_0 on energy levels of the spin states. b) Resulting absorption and derivative continuous wave EPR spectra.

source that can be scanned than it is to vary the magnetic field. Also, in order to improve the signal to noise ratio, the magnetic field is modulated sinusoidally which results in the spectra being recorded as the first derivative instead of the direct absorption as in standard NMR experiments.

Nuclear Hyperfine Splitting

The unpaired electron is also highly sensitive to nearby nuclear spins resulting in nuclear hyperfine splitting of the energy levels as described by (1.7):

$$E = hv = g\beta B_0 + Am_I \tag{1.7}$$

where A is the hyperfine coupling constant and m_I is the nuclear spin quantum number. The spin Hamiltonian, $\hat{H}$, for this can be written as (1.8):

$$\hat{H} = \beta SgB_0 + SAm_I \tag{1.8}$$

As long as the hyperfine splitting is greater than the linewidth, this results in additional lines being visible with the transitions bound by the selection rule, $\Delta m_I = 0$. The intensity of the lines are described by Pascal's triangles with three lines of equal intensity for the single ($n = 1$) ^{14}N nucleus (m_I=1) in a nitroxide:

$n = 0$:				1			
$n = 1$:			1	1	1		
$n = 2$:		1	2	3	2	1	
$n = 3$:	1	3	6	7	6	3	1

As a result, the single line spectra shown in Figure 1.1b splits into three lines of equal intensity as shown in Figure 1.2b. As with the g tensor, hyperfine coupling is usually anisotropic with a strong dependence on the direction of the magnetic field.

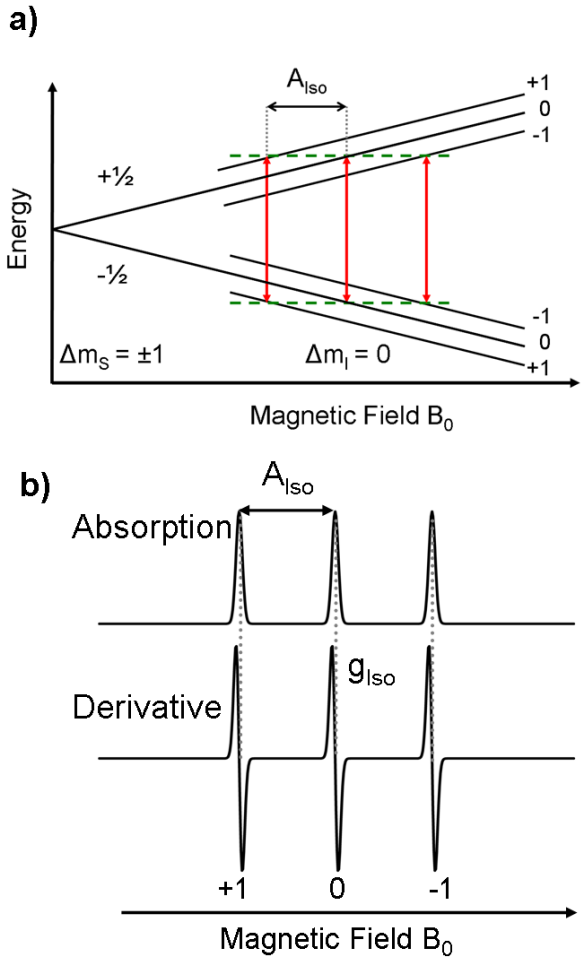

Figure 1.2: a) Splitting by ^{14}N nuclear spin. b) Resulting absorption and derivative nitroxide continuous wave EPR spectra.

Effect of motion

Another factor which has significant effect on the line shape is the dynamic behaviour of the spin system. EPR is highly sensitive to rotational diffusion, D, through its ability to average out the anisotropy of g and A as shown in Figure 1.3). Rotational diffusion is a random process and the timescale can be characterised by a rotational correlation time, τ_c, describing the time taken for molecules with identical orientations to lose alignment with each other. For isotropic rota-

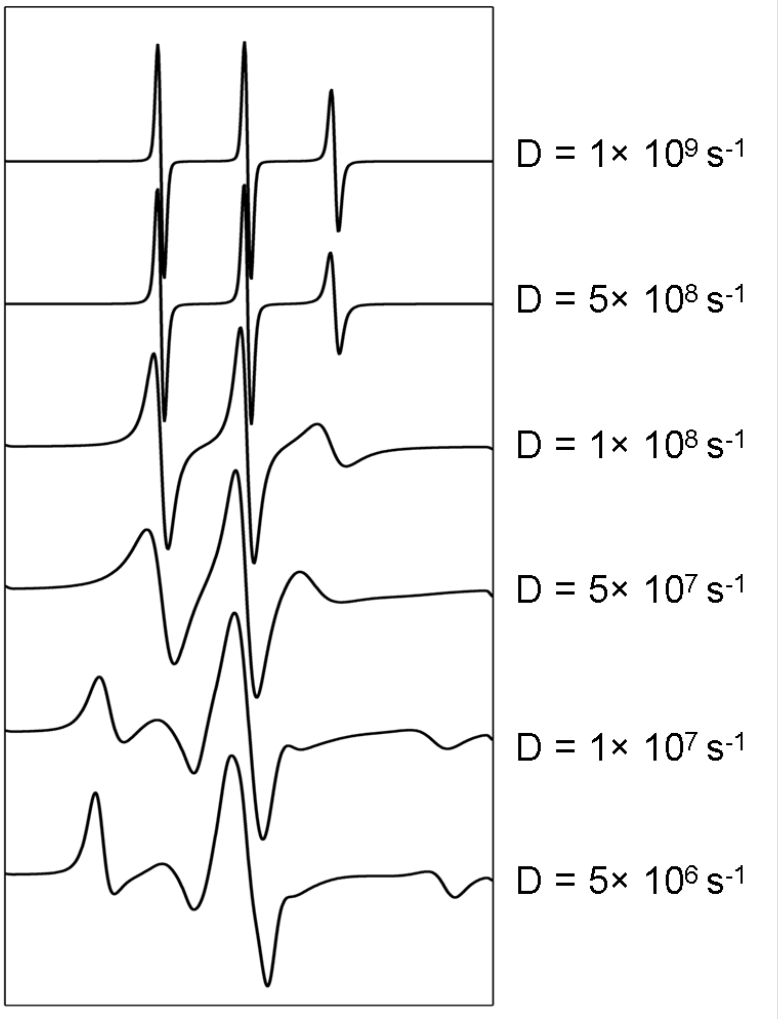

Figure 1.3: Effect of isotropic diffusion on simulated nitroxide X-band EPR spectra

tion, τ_c, can be related to the diffusion tensor, D_{Iso}, via:

$$\tau_c = \frac{1}{6D_{Iso}} \tag{1.9}$$

At low rotational rates, an anisotropic "powder-like spectrum" is observed with significant line broadening. By increasing the rotational rate these features are averaged out until the three line form is visible. The motional regime detected by EPR depends on the irradiation frequency used, with higher frequencies resolving faster rotational behaviour.

However in liquid crystals and macromolecules, the dynamic behaviour can

frequently be more complicated than simple isotropic rotation, with multiple or restrained motional components giving rise to an even wider range of line shapes. Restrained motions can be characterised by the use of an order parameter, S_{Order}, given by equation 1.10:

$$S_{Order} = \frac{1}{2}\langle(3cos^2\theta - 1)\rangle \tag{1.10}$$

where the angular brackets denote the average taken over the orientation distribution, time and the number of available molecules and θ is the angle between the molecular z axis and the magnetic field.

For soft matter systems it is common for the dynamic behaviour to include the effect of multiple motional components which may have their own order parameters.

1.1.2 Simulation of EPR Spectra

As a result of the sensitivity to a wide range of parameters, interpretation and quantitative analysis of EPR spectra can often be complex. Although some data can be extracted via mathematical relationships, such as order parameters from powder-like spectra, spectra are usually fitted or simulated using one of several different models depending on the motional regime experienced. For dynamics at the isotropic limit, where anisotropy is fully averaged, line shapes can be defined using the Breit-Rabi formula [43] where the main parameters are A_{Iso} and g_{Iso}. For spectra near the isotropic limit, Redfield theory [44][45] expands on this by introducing line broadening from simple dynamic contributions. For systems at the rigid limit such as powders, glasses and frozen solutions, spectra are normally treated as a superposition of spectra arising from a uniform random orientational distribution of a large number of paramagnetic centres [4][46]. The intermediate slow motion regime however often demonstrates the most complex line shapes with partially averaged features, and are modelled with the Stochastic Liouville Equation and shall form the majority of spectra analysed in this thesis. An approach which calculates spectra directly from trajectories (molecular or

Brownian dynamics) will also be discussed [47][48].

Stochastic Liouville Equations

The Stochastic Liouville equation (1.11) describes the magnetic probability density in terms of the spin Hamiltonian from equation (1.8) and the spin density matrix, ρ [49]:

$$\frac{\partial \rho}{\partial t} = -\frac{i}{\hbar}\left[\hat{H}(\Omega), \rho\right] = -i\hat{\hat{L}}(\Omega)\rho \tag{1.11}$$

where the square brackets represent the commutator, $\hbar$ is the reduced Planck constant, Ω indicates the rotational coordinates and $\hat{\hat{L}}$ is the Liouvillian superoperator which describes the interaction between the spin system and the environment. Diffusion is a stochastic Markov process - it is inherently random and depends only on the current state of the system, and thus can only be treated statistically [50]. The Stochastic Fokker-Planck operator, $\hat{\Gamma}$, is one way in which this can be achieved via:

$$\frac{\partial P(\Omega, t)}{\partial t} = -\hat{\Gamma} P(\Omega, t) \tag{1.12}$$

where $P(\Omega, t)$ is the probability density. The stochastic generalized diffusive operator , $\hat{\Gamma}$, can be written as 1.13 [51]:

$$\hat{\Gamma} = -\left(\frac{\partial}{\partial \Omega}\right)^T \boldsymbol{D} P_{eq}(\Omega) \left(\frac{\partial}{\partial \Omega}\right) P_{eq}^{-1}(\Omega) \tag{1.13}$$

where $\boldsymbol{D}$ is the diffusion tensor and $P_{eq}(\Omega)$ is the equilibrium Boltzmann distribution defined with respect to the total energy of the system and is predetermined by the orienting potentials [51]. The order parameter, S, given in equation 1.10, can be related to the orienting potential, λ, through the orientational distribution function, $P(\theta)$, using equations 1.14 and 1.15 [46]. S and λ describe the extent of microscopic ordering with the relationship between these parameters shown by Figure 1.4, indicating that as λ increases the order parameter,S, slowly approaches unity [52].

$$S = \frac{1}{2}\langle(3\cos^2\theta - 1)\rangle = \int P(\theta)\left[\frac{1}{2}(3\cos^2\theta - 1)\right]\sin\theta d\theta \tag{1.14}$$

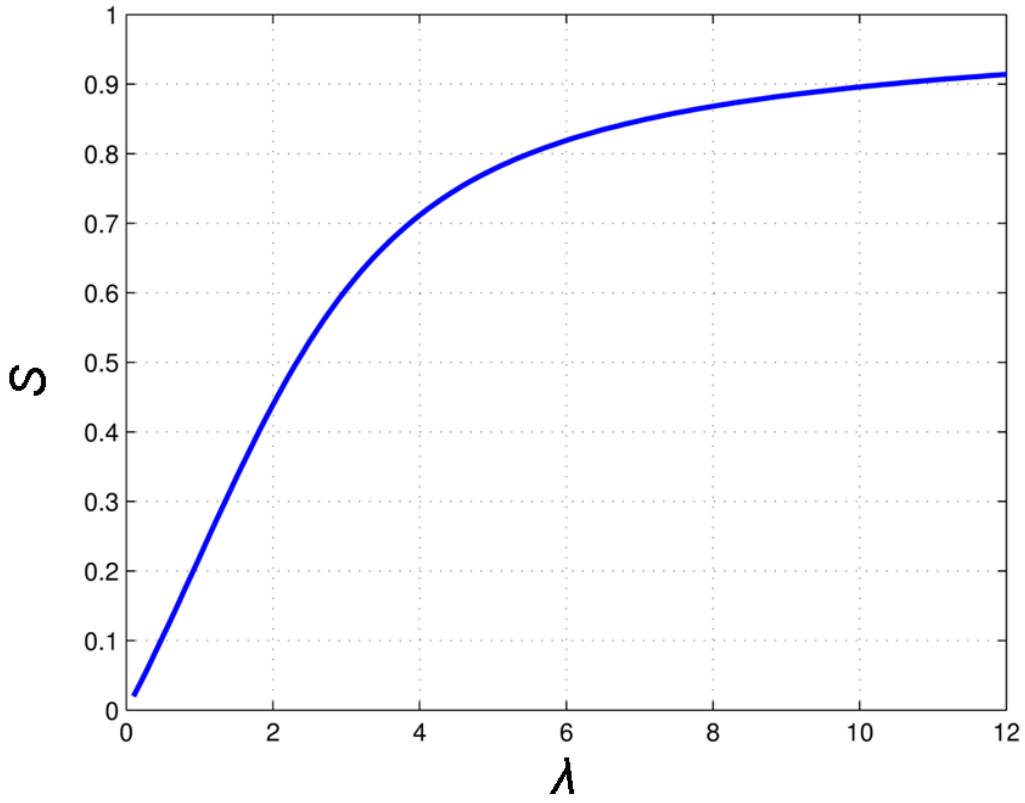

Figure 1.4: Plot of the relationship between order parameter, S, as a function of orienting potential, λ. Generated using the Order script from Easyspin [4].

$$P(\theta) = \exp\left[\frac{1}{2}\lambda(3\cos^2\theta - 1)\right] \int \exp\left[\frac{1}{2}\lambda(3\cos^2\theta - 1)\right] \sin\theta d\theta \tag{1.15}$$

For a single rotational motion, and in the absence of restricted potentials, $\hat{\Gamma}$ reduces to equation 1.16.

$$\hat{\Gamma} = D_{xx}\hat{J}_x^2 + D_{yy}\hat{J}_y^2 + D_{zz}\hat{J}_z^2 \tag{1.16}$$

where D_{ii} are the principle values of the rotational diffusion tensor describing this motion and $\hat{J}_i$ are the components of the angular momentum operator.

By introducing $\hat{\Gamma}$ to equation 1.11 the time evolution of the density matrix can be described, resulting in the stochastic Liouville equation (SLE) (1.17) [53].

$$\frac{\partial\rho(\Omega,t)}{\partial t} = -i\left[\hat{\hat{L}}(\Omega + i\hat{\Gamma}(\Omega)\right]\rho(\Omega,t) \tag{1.17}$$

By using the Fokker-Planck form of this operator part of the calculation is still able to be performed in a time independent manner [54].

The real (**Re**) component of the continuous wave EPR line shape function, $I(\omega - \omega_0)$, can then be calculated by solving the SLE in the frequency domain using a Fourier-Laplace transform via (1.18):

$$I(\omega - \omega_0) = \frac{1}{\pi} \mathbf{Re}\langle\langle \Lambda | i(\omega - \omega_0) + i\hat{\hat{L}} + \hat{\Gamma})^{-1} | \Lambda P_{eq} \rangle\rangle \tag{1.18}$$

where ω is the sweep frequency, ω_0 is the Larmor frequency, P_{Eq} is the probability density at equilibrium and the double angular brackets indicate integration over Ω and internal torsional angle θ. The basis functions, $|\Lambda\rangle$, for the stochastic part of the equation, are constructed using Wigner rotation matrices (D^L_{MK}) [49]:

$$|\Lambda\rangle = |L, M, K, n\rangle = \sqrt{\frac{2L+1}{8\pi^2}} D^L_{MK}(\Omega) \otimes \frac{1}{\sqrt{2\pi}} e^{-in\theta} \tag{1.19}$$

Development of efficient iterative computational methods to solve equation 1.18 for EPR simulations using the Lanzcos algorithm were primarily carried out by Freed and co-workers [33][36][55][56][57][58], with the majority of modern EPR simulation software for the slow-motional regime building upon this [4][52][59].

Composite Dynamics

Many soft matter systems such as liquid crystals, DNA, proteins and polymers exhibit dynamic behaviour arising from multiple motional components at the timescales probed by X-band EPR and thus require augmented SLE methods for modelling and fitting. The slowly relaxing local structure (SRLS) model of Freed and co-workers [60] uses a more general form of $\hat{\Gamma}$ which can describe local and global motion and order explicitly, as well as the coupling between them allowing reorientation processes to be modelled. The closely related two-dynamic/disordered hexagonal models of Westlund and co-workers, used in the study of lyotropic aggregates [61][14], is a simplified version of the SRLS model and does not consider coupling between motions thus preventing independent motion or slippage of the probe relative to the global frame [60].

An alternative approach is to account for the fast local motions by scaling the magnetic parameters g and A in response to the local order parameter [62][63] and has previously been used to interpret the spectra of spin probe doped lyotropic aggregates [8], membranes [62] and spin labelled DNA [26]. This assumes that the local motions are within the motional narrowing limit ($\tau_L < 1$ns for X-band [24]), and that the residual anisotropy of the magnetic parameters is axial. Global diffusion rates of an appropriate symmetry are then used to further average spectra. Although this method has been widely used it is not always appropriate [17].

Whilst these methods offer a better approximation to the complex dynamics of soft matter systems, fitting of spectra becomes significantly more complicated due to the greater computational expense, introduction of multiple parameters and non-unique line shapes [14][64]. As a result, these models require additional experimental data in order to be able to reach unambiguous conclusions. In the case of the aligned SDS hexagonal phase for example it is possible to exploit the anisotropy of the system to remove the effect of lateral diffusion through multi-orientation measurements; however the effects of residual disorder still need to be accounted for [14]. More generally applicable is the multi-frequency approach developed by Liang and Freed for use with the SRLS model [64] which uses simultaneous fitting of EPR spectra recorded at different frequencies that are sensitive to different motional regimes. In the case of macromolecules, such as DNA and globular proteins, well established hydrodynamic models exist to estimate global tumbling and are often used as the basis for fitting of experimental data [65][66][67][25].

When the global motion reaches the static limit for a particularly frequency, powder-like spectra (Figure 1.5) are observed and these models all become equivalent to the microscopic order macroscopic disorder (MOMD) model [46]. As the global motion is effectively frozen, no further averaging occurs and the resulting line shape is reliant only on the local order and dynamics.

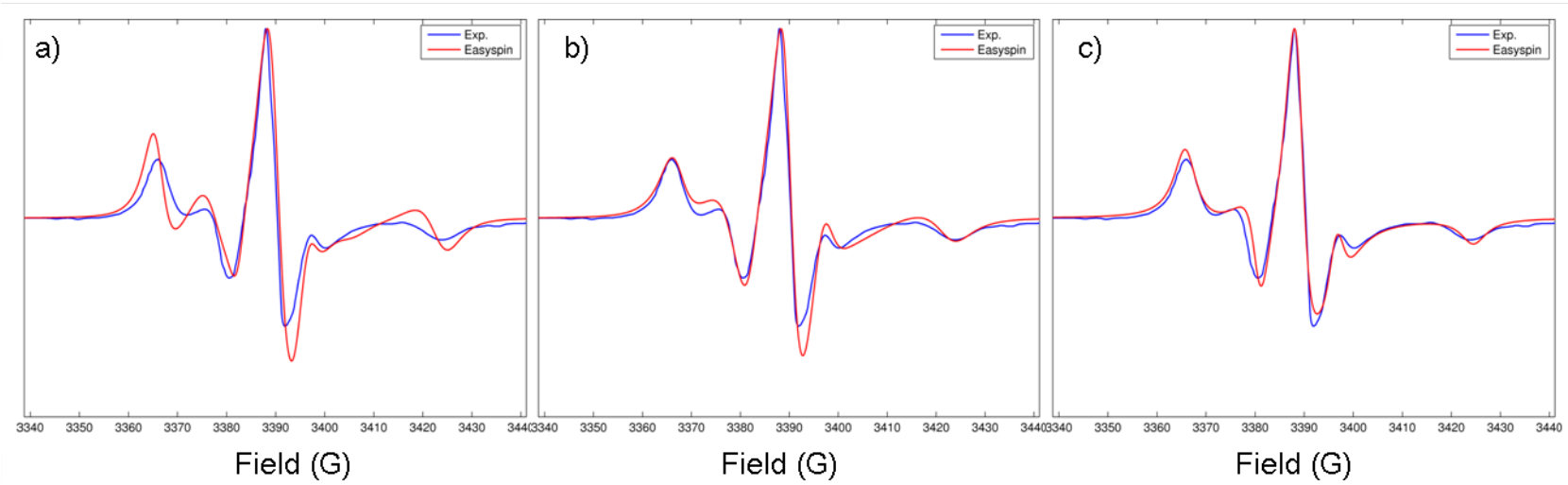

Figure 1.5: EPR spectra of 5-PC doped POPC lipid membrane with 10 mol% $[(LA)_{12}]$ peptide(Reproduced from [5] with permission from the American Chemical Society) fitted with a) $\tau = 14.07$ ns, $lw = 0.71$ G, $S = 0.35$, b) $\tau = 7.7$ ns, $lw = 0.74$ G, $S = 0.35$ and c) $\tau = 2.4$ ns, $lw = 2.2$ G, $S = 0.65$ using the MOMD model.

Although these models have yielded highly useful data, they also have several limitations. Firstly they are all, to differing degrees, simplifications that treat molecular motions in a mesoscopic manner [68]. DNA, for example, exhibits a wide range of different local motions over the 1 ps to 100 ns timescale [69] which can only be approximated using these simulation models [69]. Secondly many line shapes are non-unique, even at the rigid limit (Figure 1.5). Thirdly it is not uncommon for complex systems to show significant variations in the correlation times depending on the model used to extract them [14][61][64].

Direct Prediction Method

A recent alternative method is that of direct prediction from molecular or Brownian dynamics trajectories without the use of stochastic models, allowing for more complicated dynamic regimes to be treated with a fully atomistic representation and scale [34][49][70][71][72]. Here the approach developed by Oganesyan [47][48] is used which utilises the Von Neumann form of the Stochastic Liouville equation with the Liouville superoperator expressed in the time dependent form (1.20).

$$\frac{d\rho(t)}{dt} = \hat{\hat{L}}(t) \cdot \rho(t) \tag{1.20}$$

As time dependence is already explicitly included in this form and, as the density matrix only depends on spin variables, fewer coupled differential equations are required to describe the system [49]. Due to this though, it is necessary to explicitly define the time evolution of the system using supplementary computer modelling. The formal solution for the propagation of ρ in equation 1.20 is given by (1.21):

$$\rho(t) = \left\langle \exp\left(-i \int_0^t \hat{\hat{L}}(\tau) d(\tau) \right) \right\rangle \rho(0) \tag{1.21}$$

where $\rho(0)$ is the density matrix at equilibrium and the angular brackets represent ensemble averaging. As the transverse magnetisation is directly proportional to the density matrix (1.22), equation 1.21 can be rewritten as equation 1.23.

$$\langle M_+(t) \rangle \propto \mathbf{Tr}\left(\hat{\hat{S}}_+ \rho(t) \right) \tag{1.22}$$

$$\langle M_{+}^{m_I}(t)\rangle = \langle M_{+}^{m_I}(0)\rangle \left\langle \exp\left(-\left[i\bar{\omega}t \int_0^t \omega^{m_I}(\tau)d\tau\right]\right)\right\rangle \tag{1.23}$$

where $\hat{\hat{S}}_{+}$ is the transverse component of electron spin and **Tr** implies the trace of the matrix. The resonance frequencies for the three hyperfine coupling lines of the nitroxide spectrum can be calculated using the principal g and A values via (1.24):

$$\omega^{m}(t) = \left(g_{zz}(\Omega(t))\beta B + m\sqrt{A_{xz}(\Omega(t))^2 + A_{yz}(\Omega(t))^2 + A_{zz}(\Omega(t))^2}\right)/\hbar - \omega_0 \tag{1.24}$$

This approach offers a significant advantage over traditional approaches as the lack of parameters, approximations and fitting makes the resulting spectra unambiguous and absolute. The quality of predicted spectra with this method depends only on ensuring a suitable number conformations of the probe have been sampled in order to sufficiently represent the general behaviour [34][73]. All EPR spectra simulations using the propagation approach were performed using the the EPRSSP_DYN code [47][74].

1.2 Computational Chemistry

Many of the basic techniques of computational chemistry predate computers, with the Copenhagen interpretation of quantum mechanics, the Hartree-Fock method[75] and early forms of density functional theory all approaching 100 years old. However, as a sub-field, it has only risen to prominence relatively recently as modern computing methods and hardware have become powerful enough for larger and more relevant chemical systems to be investigated. The increasing array of *ab-initio* (calculated from first principles) and semi-empirical (using approximations derived from empirical data) computational techniques can now be applied to predict molecular and bulk structures, charge distributions, dynamic behaviour and a wide range of spectroscopic data. In particular this has benefited molecular dynamics which has seen system sizes grow from 32 particles in the original work of Adler and Wainwright in 1957 [76] to hundreds of thousands of atoms which can be treated today. Here *ab initio* quantum chemical calculations, in the form of density functional theorem, will be used to underpin a range of MD simulations and spectroscopic modelling.

1.2.1 Quantum Chemistry

The Schroedinger Equation

Central to quantum chemical calculations is the wave function, Ψ, describing the quantum state of a system, which can be related to energy through the Schroedinger equation (1.25):

$$\hat{H}(\boldsymbol{r})\Psi(\boldsymbol{r}) = E(\boldsymbol{r})\Psi(\boldsymbol{r}) \tag{1.25}$$

where $\hat{H}$ is a Hamiltonian operator, Ψ is a multi-electron wave function and E is the energy for position vector $\boldsymbol{r}$. As this can only be solved for certain eigenvalues of energy, quantization occurs and all observable properties arise as solutions from valid operators. As in classical mechanics where the Hamiltonian,

H, can be represented as the sum of the kinetic, T, and potential, V, energies, the quantum mechanical $\hat{H}$ is described by (1.26):

$$\hat{H} = \hat{T}_{Tot} + \hat{V}_{Tot} \tag{1.26}$$

where $\hat{T}_{Tot}$ and $\hat{V}_{Tot}$ are the operators for total kinetic and potential energy respectively. For a system of N electrons and M nuclei, the kinetic operator can be described by (1.27):

$$\hat{T}_{Tot} = \hat{T}_e + \hat{T}_n = -\frac{1}{2}\sum_{i=1}^{N}\nabla_i^2 - \sum_{A=1}^{M}\frac{1}{2m_A}\nabla_A^2 \tag{1.27}$$

where $\hat{T}_e$ and $\hat{T}_n$ are the kinetic energy operators for electrons and nuclei respectively, m_A is the ratio of the mass of the nucleus to the that of the electron. ∇ is the Laplace operator representing partial differentiation in x,y,z (1.28):

$$\nabla_i^2 = \left(\frac{\partial^2}{\partial x_i^2} + \frac{\partial^2}{\partial y_i^2} + \frac{\partial^2}{\partial z_i^2}\right) \tag{1.28}$$

The total potential energy is described by (1.29):

$$\hat{V}_{Tot} = \hat{V}_{ee} + \hat{V}_{ne} + \hat{V}_{nn} = \sum_{i=1}^{N}\sum_{i\neq j}^{N}\frac{1}{r_{ij}} - \sum_{i=1}^{N}\sum_{A=1}^{M}\frac{Z_A}{r_{iA}} + \sum_{A=1}^{M}\sum_{A\neq B}^{M}\frac{Z_A Z_B}{r_{AB}} \tag{1.29}$$

where $\hat{V}_{ee}$, $\hat{V}_{ne}$ and $\hat{V}_{nn}$ are the operators for electron-electron, nuclear-electron and nuclear-nuclear Coulomb interactions respectively. Z_A and Z_B are the atomic numbers of nuclei A and B separated by r_{AB}. r_{ij} is the separation of two electrons i and j, and r_{iA} is the separation of electron i and nuclei A.

The Born Oppenheimer Approximation

As nuclei are considerably heavier than electrons and thus move much more slowly, the Born-Oppenheimer approximation can be invoked to simplify the Hamiltonian produced from combining equations 1.28 and 1.29 by splitting the wave function down into electronic and nuclear components (1.30):

$$\Psi = \psi_{Electronic}\psi_{Nuclear} \tag{1.30}$$

This means the electronic wave function depends parametrically on the coordinates of frozen nuclei in a particular arrangement. As a result, $\hat{T}_n$ can be considered to be zero and the Coulombic term for nuclear interactions, $\hat{V}_{nn}$, constant. As such, the electronic Hamiltonian becomes (1.31):

$$\hat{H}_e = -\frac{1}{2}\sum_{i=1}^{N}\nabla_i^2 + \sum_{i=1}^{N}\sum_{i\neq j}^{N}\frac{1}{r_{ij}} - \sum_{i=1}^{N}\sum_{A=1}^{M}\frac{Z_A}{r_{iA}} \tag{1.31}$$

The solution to the time-independent Schroedinger equation (1.25) with the electronic Hamiltonian therefore becomes:

$$\hat{H}_e\Psi_e(X_1, X_2, ..., X_M|R_1, R_2, ..., R_M) = E_e\Psi_e(X_1, X_2, ..., X_M|R_1, R_2, ..., R_M) \tag{1.32}$$

where X_i and R_i are the space-spin coordinates for the ith electron and nucleus respectively. This provides a way to construct a potential energy surface (PES) on which nuclei can move, with electrons responding instantaneously to any change. In the case of single electron systems such as the hydrogen atom this can be solved analytically, however for systems with more that two particles it is no longer possible to find a set of coordinates that allows for a separation of degrees of freedom. For a non-linear molecule the PES has 3N-6 degrees of freedom to describe all the possible atomic arrangements, with the number of points to define the surface being to the power of this number. Therefore although the Schroedinger equation can be solved for small molecules using computational methods, it rapidly becomes too complex and an approximation of the wave function is required.

The Hartree-Fock Method

The Hartree-Fock (HF) or self-consistent field (SCF) method was the first *ab-initio* method to attempt this through the use of a pseudo one particle model where each electron interacts with an average potential resulting from the other electrons in the system [75]. In order to approximate single electron wave functions, spin orbitals, $\psi(\vec{x})$, are constructed by combining spatial orbitals, ϕ, with a

spin function, σ via (1.33):

$$\psi(\vec{x}) = \phi(\vec{r})\sigma \tag{1.33}$$

The spin function represents one of two spin states, α or β, with a spin quantum number of $\pm\frac{1}{2}$ depending on the direction of the angular momentum in the presence of a magnetic field. These spin orbitals must fulfil the orthonormality conditions (1.34):

$$\begin{aligned} \langle\alpha|\alpha\rangle &= \langle\beta|\beta\rangle = 1 \\ \langle\alpha|\beta\rangle &= \langle\beta|\alpha\rangle = 0 \end{aligned} \tag{1.34}$$

Furthermore wave functions describing fermions, such as electrons, have to be antisymmetric; i.e. change sign if electron coordinates are interchanged. This leads to the Pauli exclusion principle which states that two electrons cannot have all quantum numbers the same and thus two electrons cannot occupy the same spin orbital [77]. Therefore in order to approximate the ground state multi-electron wave function, N one-electron wave functions or spin orbitals are combined as an antisymmetrised product known as a Slater determinant (1.35):

$$\Psi(1,...,N) = \frac{1}{\sqrt{N!}} \begin{vmatrix} \phi_1(\vec{x}_1) & \dots & \phi_N(\vec{x}_1) \\ \vdots & \ddots & \vdots \\ \phi_1(\vec{x}_N) & \dots & \phi_N(\vec{x}_N) \end{vmatrix} \tag{1.35}$$

where $\frac{1}{\sqrt{N!}}$ is a normalisation factor with the columns denoting the orbitals and the rows are the electron coordinates. The variational principle provides the framework by which to determine the lowest energy Slater determinant [78](1.36):

$$E_0 = \mathbf{Min}_{\Psi} \frac{\langle\Psi|\hat{H}_e|\Psi\rangle}{\langle\Psi|\Psi\rangle} \tag{1.36}$$

where E_0 is the ground state energy (the lowest eigenvalue of $\hat{H}$). This means that the energy of a wave function can be calculated for a normalised Hamiltonian, and that an approximated wave function will always be an upper limit for the ground state energy. Therefore by constructing a series of trial wave functions with varying parameters and minimising the energy, the best approximation of

the ground state can be found. At this point $E_{Approximate} = E_0$ and the energy is self-consistent.

In order to compute this numerically the Fock operator, $\hat{F}$, is used which can be more easily manipulated mathematically. This has a similar pseudo-eigenvalue form (1.37) to the Schroedinger equation (1.25) and acts on the one-electron orbitals to give the variation in total energy:

$$\hat{F}\phi_i = \varepsilon_i \phi_i \tag{1.37}$$

where the $\hat{F}$ is described by (1.38):

$$\hat{F}_i = \hat{h}_i + \sum_{j}^{N} (\hat{J}_j - \hat{K}_j) \tag{1.38}$$

$\hat{J}_j$ and $\hat{K}_j$ are the Coulomb and exchange interaction operators respectively. $\hat{h}$ describes the motion of a single electron via (1.39):

$$\hat{h}_i = -\frac{1}{2}\nabla_i^2 - \sum_{A=1}^{M} \frac{Z_A}{r_A} \tag{1.39}$$

By diagonalising the Fock matrix for a set of approximated one-electron orbitals, an improved set of orbitals will be determined. This process can then be repeated in a cyclic manner to determine better approximations of the orbitals until a threshold value is reached at which the orbitals are considered to be close enough to the ground state for the properties to be calculated reliably.

Basis Sets

As one-electron atomic orbitals are complex functions with unknown exact analytical forms, they are generally approximated using a linear combination of basis functions known as a basis set. Slater type orbitals (STOs) accurately represent orbitals at all distances from the nucleus and have the form (1.40) [79]:

$$\Psi_{STO}(r) = r^L e^{-\zeta r} \tag{1.40}$$

where L and ζ are the angular momentum quantum number and the spatial extent of the orbital respectively. However, STOs are difficult to integrate and

computationally expensive, so in most cases they are approximated using a linear combination (1.41) of Gaussian type orbitals (GTOs) (1.42) [80]:

$$\Psi_{STO}(r) = \sum_i C_i \Psi_{GTO}(r) \tag{1.41}$$

$$\Psi_{GTO}(r) = x^{l_x} y^{l_y} z^{l_z} e^{\alpha r^2} \tag{1.42}$$

where l_x, l_y and l_z are the angular momentum quantum numbers for the x,y and z Cartesian coordinates. The sum of these values defines the orbital type with $l = 0$, $l = 1$ and $l = 2$ corresponding to s, p and d orbitals respectively. α is the spatial extent of the GTO. Although GTOs do not have a cusp at the nucleus and do not fall off at long range unlike STOs, they still offer multiple advantages; they are both computationally cheap and easy to integrate as well as being easier to manipulate mathematically.

As the molecular structure is mainly determined by the valence electrons, split basis sets are now used for the majority of applications. These use multiple basis functions to describe valence orbitals more accurately and provide good balance between accuracy and computational demand. Pople basis set notation is commonly used to describe such basis sets which can be either double, triple or quadruple zeta depending on the number of functions describing the valence orbitals [81]. In the case of the triple zeta 6-311G basis set, the core atomic orbitals are each described by 6 GTOs and the inner and outer valence orbitals by two basis functions consisting of 3, 1 and 1 GTOs respectively.

Additional functions can also be added where required for certain systems. In the case of anions or excited states, diffuse functions (denoted by +) are often added. These are shallow GTOs which allow the tail portion of the wave function to be more accurately reflected, which is important for loosely bound electrons that are far from the nuclei. Polarisation functions (usually denoted by asterisks) are used to improve the description of bonding through making the molecular orbitals less symmetric. This introduces some character from orbitals with higher angular momentum such as adding d orbital character to p orbitals

allowing them to distort.

Another modification to the basis sets used here is the use of an Effective Core Potential (ECP) which is typically applied to transition metals and higher mass elements as in the LANL2DZ basis set [82][83]. As these elements have a large number of chemically unimportant core electrons, using a standard Pople basis set would be computationally expensive. Furthermore, for elements in the lower half of the periodic table, relativistic effects become prominent which cause the s and p orbitals to contract and the d and f orbitals to expand as well as significant spin-orbit coupling. The use of an ECP solves both of these problems by replacing the core electrons with a function fitted to replicate this behaviour.

Ultimately though, as basis sets consist of a finite number of functions, a limiting accuracy is reached known as the basis set limit. Other types of basis set have been developed such as the atomic natural orbital [84] and correlation consistent basis sets [85] which converge to this limit using empirical extrapolation techniques, however the additional computational cost and complexity has meant that Pople type basis sets are still frequently used.

Correlation Energy

Although the Hartree-Fock method accounts for the majority of the energy, the simplified interactions between electrons results in a further discrepancy, even with an infinite basis set, known as the Hartree-Fock Limit. As the strong electron-electron interactions are described using a mean-field approach, the instantaneous rearrangements which electrons undergo are not fully accounted for. This is known as the correlation energy (1.43) [86] and can be highly significant:

$$E_{Schroedinger} = E_{HF} + E_{Corr} \tag{1.43}$$

where $E_{Schroedinger}$ is the exact energy, E_{HF} is the energy at the Hartree-Fock limit and E_{Corr} is the correlation energy. This is usually accounted for through the use of density functional theory.

Density Functional Theory

Density functional theory (DFT) uses the one-to-one relationship between electron density, ρ, and the energy of a system proven by Hohenberg and Kohn [87] in order to define the properties of the system as shown by equations 1.44 and 1.45.

$$N = \int \rho(r)\,\mathrm{d}r \tag{1.44}$$

$$\rho(r) = \sum_m n_m |\phi_m(r)|^2 \tag{1.45}$$

where N is the number of electrons and n_m is the number of electrons in a molecular orbital with wave function ϕ_m. Functionals act on the functions of electron density allowing an energy to ultimately be extracted from a set of coordinates. This affords a significant advantage as although the complexity of a wave function increases exponentially with system size, the number of parameters defining electron density does not change, making the computational cost similar to the HF method. However although the existence of a universal functional linking electron density and energy has been proven [87], it has not yet been identified so a number of task specific functionals have been developed. Early attempts at using electron density employed an orbital free approach via the functional (1.46)

$$E_{DFT}[\rho] = T[\rho] + E_{ne}[\rho] + E_{ee}[\rho] \tag{1.46}$$

where $T[\rho]$ is the kinetic energy, E_{ne} and E_{ee} are the nuclear-electron attraction and electron-electron repulsion energies respectively. The electron-electron repulsion can be further divided into Coulomb, $J[\rho]$, and exchange $K[\rho]$ terms via (1.47):

$$E_{ee}[\rho] = J[\rho] + K[\rho] \tag{1.47}$$

Although these terms include correlation between electrons, this approach was limited by the lack of good approximations for the kinetic energy functional and lead to high errors. By re-introducing orbitals for non-interacting electrons and then calculating the electron density from this, Kohn and Sham [88] were able to

split the kinetic energy functional into two parts. One of these terms can be calculated exactly from HF, leaving only a small correction term to be approximated, greatly reducing the errors (1.48 and 1.49).

$$E_{DFT,KS}[\rho] = T[\rho] + E_{ne} + J[\rho] + E_{XC}[\rho] \tag{1.48}$$

$$E_{XC}[\rho] = (T[\rho] - T_{KS}[\rho]) + (E_{ee}[\rho] - J[\rho]) \tag{1.49}$$

where E_{XC} is the exchange-correlation energy and T_{KS} is the kinetic energy of the non-interacting Kohn-Sham electrons. This allows DFT to predict energies and vibrational frequencies with a much greater accuracy than HF for a similar computational cost.

Solvation

Solvation can have a pronounced effect on magnetic properties through polarisation and the molecular conformation [89]. Typically when using DFT these effects are modelled through the use of an implicit solvent scheme which treats molecules in response to a self-consistent reaction field (SCRF) rather than using individual solvent molecules. The solvation free energy, $\Delta G_{Solvation}$, is described by three different components (1.50):

$$\Delta G_{Solvation} = \Delta G_{Cavity} + \Delta G_{Dispersion} + \Delta G_{Electronic} \tag{1.50}$$

where ΔG_{Cavity} is the energy for the creation of the cavity around the molecule, $\Delta G_{Dispersion}$ results from the stabilising electrostatic contributions between solute and solvent and $\Delta G_{Electronic}$ is the stabilisation of charge over the solute molecule. This indicates the solvation free energy is dependent on both contributions from the solute and solvent, and thus must be determined using a self-consistent iterative method. The polarizable continuum model (PCM) [90][91] has become the most common of these approaches which treats the cavity created by the presence of solute as a series of atom-centred interlocking spheres of empirically determined radii to create a Van der Waals cavity. Individual solvent molecules may still be included explicitly when significant to a mechanism or function.

1.2.2 Molecular Dynamics

Newton's Second Law of Motion

As molecules are large enough that their quantum effects are small, they can generally be described well using classical mechanics based around Newton's second law of motion (Equation 1.51):

$$F_i = m_i a_i = m_i \frac{d\boldsymbol{v_i}}{dt} = m_i \frac{d^2\boldsymbol{r_i}}{dt^2} = -\nabla_i V \tag{1.51}$$

where F is the force acting on particle i of mass m with acceleration a, velocity of v and position r. ∇ indicates the gradient of potential energy V. This allows the atomic coordinates to be propagated through integration. Although there is no analytical solution to this set of simultaneous equations due the large number of coordinates involved, this can be performed numerically through use of integration algorithms such as the Leapfrog Verlet [92]. This enables step-by-step solutions for these equations over small time steps and makes calculations much computationally cheaper than quantum chemical methods, allowing MD access to bulk properties.

Forcefields

MD calculations are generally performed with parameterised "ball and spring" type models known as forcefields. These describe the potential energy of a system in terms of the atomic coordinates and have the general form (1.52):

$$V_{Total} = V_{Stretch} + V_{Bend} + V_{Torsional} + V_{VDW} + V_{Coulomb} + V_{Special} \tag{1.52}$$

where $V_{Stretch}$, V_{Bend} and $V_{Torsional}$ describe the bonded interactions, V_{VDW} and $V_{Coulomb}$ describe the non-bonded interactions and $V_{Special}$ describes other contributions. Stretching and bending motions are typically described using the form of a simple harmonic oscillator (1.53):

$$V_{Harmonic} = k(v - v_{Eq})^2 \tag{1.53}$$

where k is a force constant, v is the variable (bond length or angle) and v_{eq} is the equilibrium point. The bending term can also be used to describe improper dihedrals which are used to maintain planarity and prevent inversion. Although harmonic potentials display incorrect behaviour at long or short range they provide a reliable description near the equilibrium geometry as shown in Figure 1.6. This is adequate for the majority of behaviour of chemical systems but means the dissociation region where Morse/Lennard-Jones potentials level off are inaccurately described, and therefore hybrid QM/MD methods are required. The advantage of the harmonic form though is a far lesser computational cost.

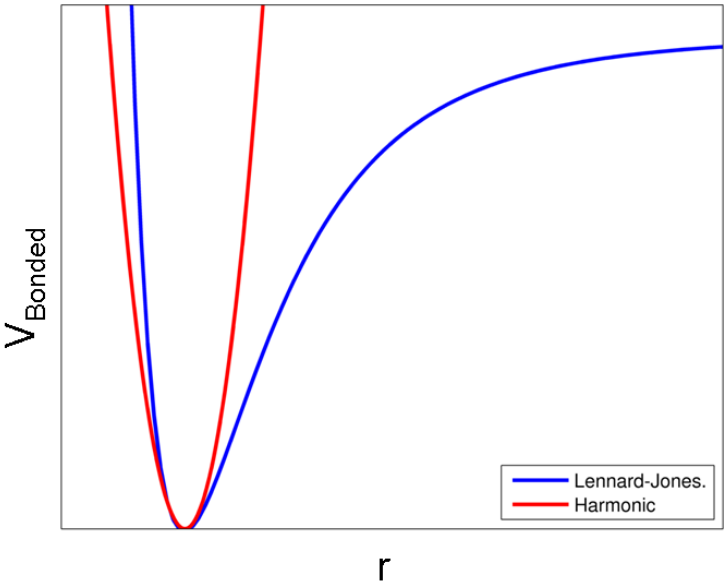

Figure 1.6: Comparison of harmonic (red) and Lennard-Jones (blue) type potentials

Torsional angles display periodic behaviour and are modelled using a potential of the form (1.54):

$$V_{Trigonometric} = k[1 + \cos(n\varphi - \gamma)] \tag{1.54}$$

where n is the periodicity, φ is the torsional angle and γ is the phase angle. Torsional energies result from both bonded and non-bonded interactions with contributions from sterics, optimal electron cloud configurations, Van-der Waals

and electrostatics, which can lead to asymmetric energy profiles. In order to replicate this a Fourier series of these terms with multiple force constants and phase angles is sometimes used.

The Van der Waals interaction can only be modelled with an anharmonic form due to the close range repulsion but diminishing interaction at longer range. Usually this is achieved with a Lennard-Jones type potential (1.55) due to the lower computational cost.

$$V_{VDW} = \left(\frac{A}{R^{12}} - \frac{B}{R^6} \right) \tag{1.55}$$

where A and B are repulsive and attractive coefficients for an atomic separation of R.

The Coulombic term describes the interactions of partial atomic charges and can be expressed generally as:

$$V_{Coulomb} = \frac{q_i q_j}{4\pi\varepsilon_0 \varepsilon R} \tag{1.56}$$

where qi and qj are partial charges and ε is the dielectric constant.

Additionally, $V_{Special}$ terms can be introduced to describe extra effects, the most common of which are bond restraints. Typically these restraints are used to maintain hydrogen bond lengths in order to improve the stability or performance of the simulation. Alternatively this term can be used to temporarily increase the rigidity of the bonds of solute to maintain structure in macromolecules or aggregates during minimisation and equilibration procedures.

Here, forcefields of the AMBER (Assisted Model Building with Energy Refinement) [93] type are used for MD simulations (1.57):

$$\begin{aligned} V_{Potential} = & \sum_{Bonds} k_r (r - r_{eq})^2 + \sum_{Angles} k_\theta (\theta - \theta_{eq})^2 + \\ & + \sum_{Dihedrals} \frac{v_n}{2} [1 + \cos(n\varphi - \gamma)] + \sum_{i \neq j} \left[\frac{A_{ij}}{R_{ij}^{12}} - \frac{B_{ij}}{R_{ij}^6} + \frac{q_i q_j}{\varepsilon R_{ij}} \right] \end{aligned} \tag{1.57}$$

These forcefields were originally designed for proteins [94] but have been further refined for DNA [95], lipids [96] and small organic molecules [93], principally to aid drug development but have since seen much wider use.

Periodic Boundary Conditions

Although MD can perform calculations with large numbers of atoms compared with QM calculation schemes, system sizes are still far smaller than would be encountered experimentally. Furthermore, if molecules are treated as in a box, those at the surface will experience a different environment to those in the centre. This would lead to discrepancies for both bulk properties, particularly density, and dynamics. Therefore periodic boundary conditions are typically used for production runs in which molecules can leave one side of the box and enter on the opposite side (Figure 1.7), effectively producing an infinite lattice. Through the use of Ewald summation [97], electrostatics can also be treated in a periodic manner, however this introduces minimum system sizes to prevent molecules interacting with themselves causing artefacts.

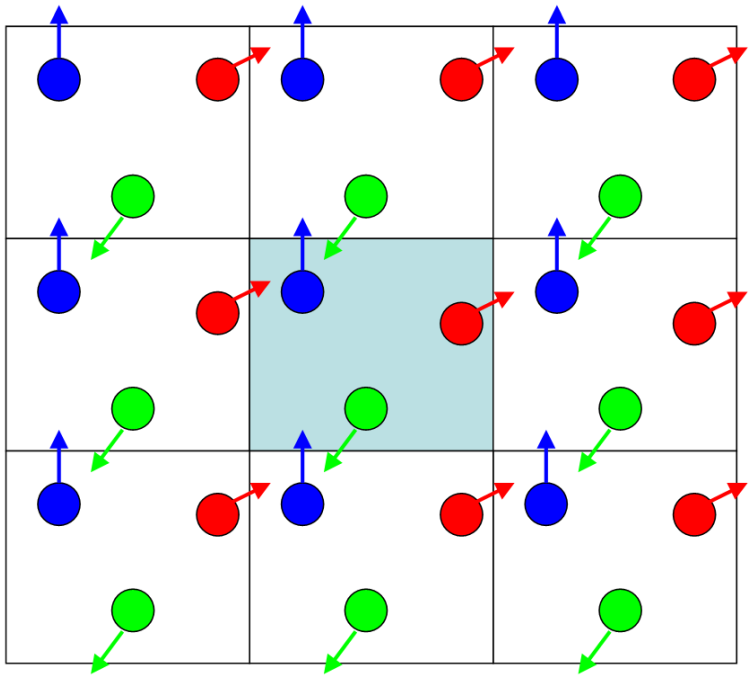

Figure 1.7: Particles crossing periodic boundaries where the pale blue box represents the real system, and white boxes the effective periodic images

Water Models

Solvation in MD uses explicit solvent molecules, i.e. each molecule is individually defined. For the systems modelled here the solvent used is water which has been extensively parameterised for different applications. These can generally be divided into different classes, depending on the number of particles used to construct them, for fully atomistic MD. Three point water models such as TIP3P and SPC use only the three real atoms to define the structure and charges. Four and five point models TIP4P and TIP5P use one and two additional dummy atoms respectively to model the lone pairs on the oxygen in order to better replicate the distribution of partial charges. The properties of these models have also been adjusted in order to better replicate the behaviour for long range interactions in periodic simulations with Ewald summation, typically denoted with "/E" after the model name. Generally, four and five point water molecules have been found to demonstrate more accurate dynamics [98][99], however with the solvent molecules usually being the most numerous in the system the extra atoms can lead to significantly greater computational effort being required. Although the TIP3P water model is known to produce significantly accelerated dynamics, the reparameterised SPC/E water model used here has been shown to replicate dynamics in reasonable agreement with experiment and four point water models [99].

The Ergodic Hypothesis

Results in molecular dynamics are based around the ergodic hypothesis; that the average value of an observable, X, over a simulation of length T and the average over a number of points, M, is the same (1.58):

$$\langle X \rangle_{MD} = \lim_{T\to\infty} \frac{1}{T} \int_0^T X(t)dt = \lim_{M\to\infty} \frac{1}{M} \sum_{i=1}^{M} X_i \tag{1.58}$$

Therefore, average values for an observable obtained from a large number of molecules over a short time should be equivalent to that of a single molecule for a much longer time as long as all significant conformations are sampled. This is

particularly significant for the dynamic parameters considered here as it indicates that more reliable data can be obtained through either longer trajectories or the use of multiple spin probes.

Chapter 2

Prediction of Lyotropic Liquid Crystal Motional EPR Spectra

The contents of this chapter have been published in *Chemistry - A European Journal*, 2017, **23**; Christopher Prior, Vasily S. Oganesyan; [1].

2.1 Introduction

Surfactant-water systems have been utilised by both nature (cell membranes) and humankind (e.g. detergents, lubricants, colloidal agents, drug delivery vectors) in a vast range of processes, and have been the subject of intense study for many years. Sodium dodecyl sulphate (SDS) and dodecyltrimethylammonium chloride (DTAC) (Figure 2.1), representing classical examples of anionic and cationic surfactants, respectively, in particular have been the target of a wide range of experimental techniques including nuclear magnetic resonance (NMR) [100][101], electron paramagnetic resonance (EPR) [8][14][42][102], fluorescence [103], X-ray [104][105], neutron [106] and light scattering [107] as well as theoretical studies [108][109][110][111][112] in order to shed light on their structure and dynamics. Both systems are industrially ubiquitous, have well defined experimental phase diagrams exhibiting multiple lyotropic phases including micellar, rod/hexagonal

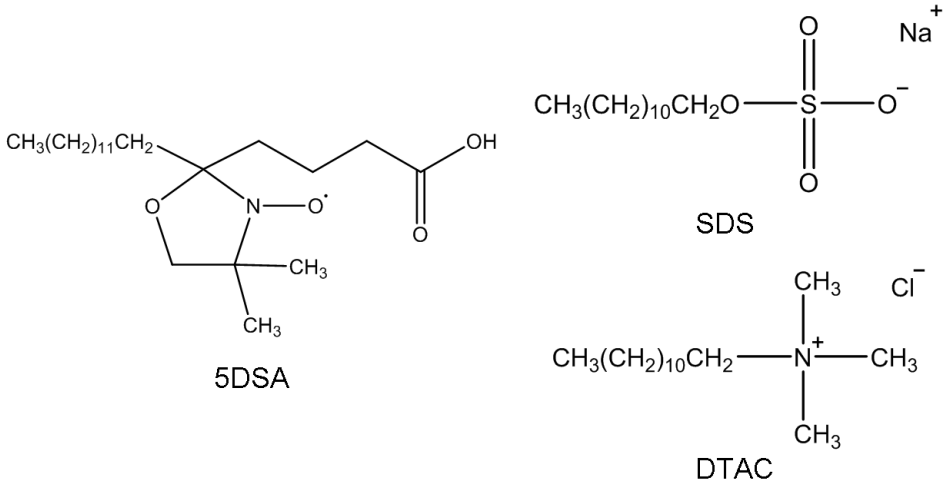

Figure 2.1: Chemical structures of the 5-DOXYL-stearic acid (5DSA) spin probe and sodium dodecyl sulphate (SDS) and dodecyltrimethylammonium chloride (DTAC) surfactant molecules.

and lamellar phases, as well as intermediate mixed structures [8][105][106].

X-band EPR with nitroxide spin probes has proven to be a particularly effective technique in the study of lyotropic liquid crystals due to the overlap with the timescales involved in the molecular reorientational dynamics of these systems [8][14][63][42]. Additionally, as a result of its high sensitivity only a very low concentration of the probe is required, so the host system is effectively unperturbed with the majority of aggregates [42][102].

Motional Continuous Wave (CW) EPR spectra provide two important pieces of information about lyotropic phases; firstly, the local motions and order of molecules averaged over small volumes and, secondly, global (long-range) dynamics and order of the system that reflects on the geometry of the aggregate leading to distinctive spectra [14]. Spectral analysis has previously been performed by fitting with several of the models mentioned in section 1.1.2. For instance, using the two-dynamic and disordered hexagonal models for fitting EPR spectra, Westlund and co-workers found that the local order parameter for the 5-DOXYL stearic

acid (5DSA) doped in SDS/water systems was similar between micellar and aligned hexagonal samples at a given temperature, but that the hexagonal phase had slower dynamics [14]. Bahri et al. found that both 5DSA and 16DSA spin probes result in similar EPR spectra when doped in SDS micelles and through the use of different buffer solutions found EPR to be highly sensitive to micelle formation [42]. Lindblom and co-workers reported a detailed analysis of the phase diagram of the DTAC/water system using EPR [8].

As in the majority of surfactant water systems the two motional contributions, namely the internal restricted dynamics of the probe and the global dynamics of the environment, are well separated on the motional timescale, a useful simplification can be employed [8]. Provided that the local motions of the probe are within the so-called motional narrowing limit ($\tau^L <$ 1 ns) [24] , the magnetic tensors associated with the nitroxide head group can be partially averaged prior to the application of the Stochastic-Liouville Fokker-Planck (SLE-FP) procedure [8][63]. Global diffusion of an appropriate symmetry and restriction then leads to further averaging of the spectrum.

An alternative framework used to interpret the diffusion of macromolecules is the Model-Free (MF) approach which aims to parameterise the time autocorrelation functions of molecular rotations without specific assumptions of the models mentioned above [113]. In particular the MF approach implies that the local and global motions are independent and has been used widely in the interpretation of NMR relaxation data [114][115][116][117][118]. More recently, it has been used to link the results of Molecular Dynamics (MD) simulations of proteins [119] and lipids [120] with the NMR measurements. Although not as rigorous as the models mentioned in section 1.1.2, such as the SRLS approach from which it can be derived [121], the MF approach is popular due to the ease of use and clarity of parameters estimated and interpreted.

The majority of previous MD simulation studies on lyotropic systems have been directed towards the geometry and thermodynamics of their aggregates

[108][110][111][112], with the predominant focus on micellar aggregations. Tang et al compared SDS micelles of different aggregation numbers and found certain versions of OPLS and GROMOS forcefields resulted in unrealistic crystal-like patches for larger aggregates which was exacerbated by the use of TIP3P and SPC water [109]. Kocherbitov investigated the micellar, cubic, hexagonal and lamellar phases of DTAC and found that by careful construction of the starting structure, equilibration times could be reduced to the order of nanoseconds and that the lateral diffusion coefficients primarily depended on the aggregate geometry [111]. The General AMBER Force Field (GAFF) has previously been shown to accurately reproduce structural properties of SDS micelles such as aggregate radii, eccentricity and counterion binding as well as the diffusion of carbon atoms of the alkyl chains [112][110].

In this chapter, a combined MD-EPR methodology is applied for the first time to various lyotropic aggregates. By employing GAFF, extensive MD modelling of the main aggregates formed by SDS and DTAC doped with the 5DSA spin probe is performed. EPR spectral predictions for pre-micellar aggregates, micellar, rod and lamellar phases show good agreement with experiment. The application of the combined MD-EPR approach outlined in section 1.1.2 allows two important questions to be addressed at the same time. Firstly, by providing a direct link with experiment, it serves as a test bed for the forcefields currently employed in the MD modelling of such systems. Secondly, the autocorrelation functions of molecular rotations can be readily generated from the resulting MD trajectories and subsequently fitted using the MF approach. The adjusted parameters, namely correlation times and order parameters, are then used to predict the motional EPR spectra and compare them to the experimental ones, thus testing the validity of the widely used MF approach. Furthermore, by performing the MD analysis on the host liquid crystal molecules, the relationship between the motions of the host and the probe is explored.

2.2 Computational Methods

2.2.1 Parameterisation of 5DSA Nitroxide Probe

The GAFF parameters for the 5DSA spin probe were generated in analogy with previously developed spin probes [34][73]. Quantum chemical calculations of 5DSA were performed with the Gaussian 09 [122] software package at the B3LYP/6-311++g(d,p) level of theory and the CHELPG [123] charge scheme to obtain partial charges. Forcefield parameters for the new atom types of the nitroxide moiety in 5DSA (the unsaturated carbon atoms of the nitroxide ring, saturated carbon atoms of the nitroxide ring, nitrogen and oxygen) were taken from a combination of geometry optimization calculations in the gas phase and previous calculations [34]. Equilibrium bond lengths and angles were taken directly from minimized energy structures. Force constants were interpolated using the reference values in the AMBER99 forcefield [124] and the quantum mechanical calculations of Barone and co-workers [89].

2.2.2 Magnetic Parameter Calculations

Magnetic parameter calculations were performed using the B3LYP functional and N07D basis set which has been tailored for organic radicals using the calculation scheme outlined by Barone et al [125]. Structures were first optimised in vacuo before being reoptimised using the PCM for solvation effects with very tight convergence criteria before calculation of the magnetic parameters in the relevant state [126].

2.2.3 Details of Molecular Dynamics Modelling

Starting configurations for molecular dynamics were generated with the appropriate spherical, cylindrical or planar geometries using the DFT optimised molecular structures and Packmol software [127]. Multiple probes were dispersed in the lar-

ger aggregates in order to enhance the statistical accuracy and to improve the quality of the correlation functions (Table 2.1). MD simulations were performed with version 1.4 of the fully atomistic GAFF [93] supplemented with the additional parameters derived for 5DSA spin probe. Hydrogen bond lengths were constrained using the SHAKE algorithm [128]. The SPC/E water model [129] was used with the associated ion parameters developed by Cheatham and coworkers [130]. All calculations were performed with the AMBER 12 [131] MD package using an NPT ensemble with Ewald summation [97] used to represent the long range Coulomb potential and periodic boundary conditions in all directions. A time step of 1 fs was used with output written to trajectory files every 20 ps. Temperature was maintained using a Langevin thermostat with a friction coefficient of 1 ps. A pressure of 1 atm with relaxation time of 2 ps was used and scaled appropriately for different phases. Simulations of microaggregate and micelle states doped with 5DSA were performed with isotropic pressure coupling. Hexagonal and lamellar phase simulations were performed with fully anisotropic pressure coupling. Microaggregate, micelle and hexagonal phase simulations were equilibrated for up to 30 ns. In the case of the lamellar phases, the structure was initially equilibrated with an applied surface tension (20 dyne/cm) for 15 ns, before a further 15 ns of equilibration without surface tension. Calculations employed a time step of 1 fs, with production runs ranging from 100 to 900 ns (Table 2.1).

2.2.4 Autocorrelation Functions and Model-Free Analysis

The autocorrelation function of each vector, $\vec{l}$, associated with either the nitroxide head group of 5DSA or the host molecules as defined in Figure 2.1, can be calculated from an MD trajectory according to the following expression:

$$C(t) = \left\langle \int_0^\infty P_2(\vec{l}(\tau)) \cdot \vec{l}((t+\tau))d\tau \right\rangle \tag{2.1}$$

Table 2.1: System compositions and trajectory lengths for lyotropic phases. [a]Equilibration times given in brackets.

Phase	**Number of Water Molecules**	**Number of Surfactant Molecules**	**Number of Probe Molecules**	**Trajectory Length[a] (ns)**
SDS Microaggregates	6700	2-5	1	(10) 100
SDS Micelle	6300	58	2	(10) 300
DTAC Micelle	6100	40	2	(10) 300
SDS Hexagonal	2500	160	5	(20) 300
DTAC Hexagonal	1100	180	5	(20) 300
SDS Lamellar	2900	400	6	(30) 600
DTAC Lamellar	640	380	6	(30) 900

where $P_2(x)$ is the second order Legendre polynomial:

$$P_2(x) = \frac{1}{2}\left(3x^2 - 1\right) \tag{2.2}$$

The bracket in equation 2.1 denotes the average taken over the orientation distribution, time and the number of available molecules. A sliding time window approach was used for time averaging [48]. In accordance with the MF approach, assuming that the global molecular motion (Figure 2.2) is slower than the internal dynamics of the probe, $C(t)$ can be decomposed into the product of the correlation functions for the overall tumbling, $C^G(t)$ and the internal motion, $C^L(t)$ (Equation 2.3).

$$C(t) = C^G(t)C^L(t) \tag{2.3}$$

Following the formalism introduced by Lipari and Szabo [113] the MF based expressions of the autocorrelation functions specific for the following states: mi-

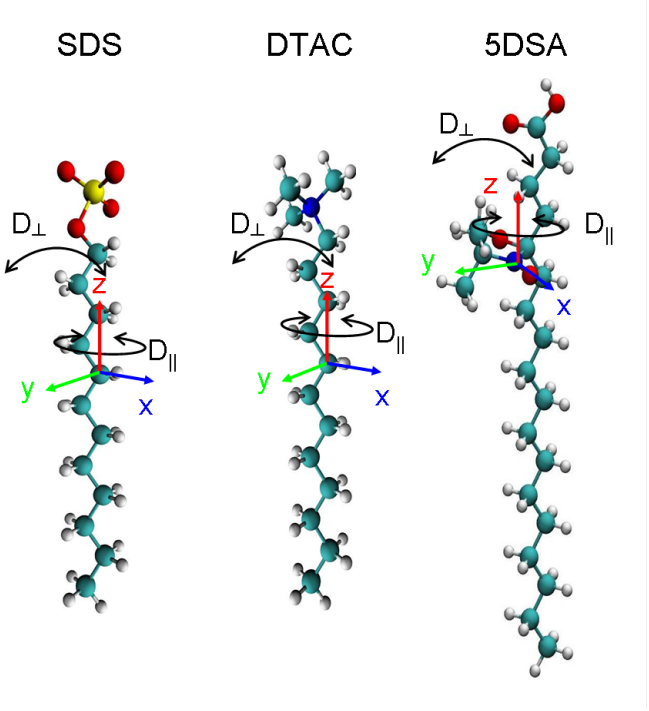

Figure 2.2: Structures of SDS, DTAC and 5DSA molecules with the molecular axes of surfactants SDS and DTAC and magnetic axes of 5DSA spin probe indicated.

croaggregate (Equation 2.4), spherical (micelle) (Equation 2.5), cylindrical (rod/ hexagonal) (Equation 2.6) and bilayer (lamellae) (Equation 2.7) were used to fit the autocorrelation functions, with the relationship between correlation times and the rotational diffusion tensor components indicated in Figure 2.2 given by Equation 2.9.

Microaggregate:

$$\begin{aligned} C_z(t) &= e^{-6D_\perp t} \\ C_{xy}(t) &= \frac{1}{4}e^{-6D_\perp t} + \frac{3}{4}e^{-2D_\perp t - 2D_\parallel t} \end{aligned} \tag{2.4}$$

Spherical:

$$\begin{aligned} C_z(t) &= e^{-6D^G_{Iso}t} \cdot (C_0(t)) \\ C_{xy}(t) &= e^{-6D^G_{Iso}t} \cdot \left(\frac{1}{4}(C_0(t)) + \frac{3}{4}(C_2(t))\right) \end{aligned} \tag{2.5}$$

Cylindrical:

$$\begin{aligned} C_z(t) &= \left(\frac{1}{4}e^{-6D_\perp^G t} + \frac{3}{4}e^{-2D_\perp^G t - 2D_\parallel^G t}\right)\cdot C_0(t) \\ C_{xy}(t) &= \left(\frac{1}{16}e^{-6D_\perp^G t} + \frac{3}{16}e^{-2D_\perp^G t - 2D_\parallel^G t}\right)\cdot C_0(t) + \\ &+ \left(\frac{9}{32}e^{-6D_\perp t} + \frac{3}{8}e^{-D_\perp t - 5D_\parallel t} + \frac{3}{32}e^{-2D_\perp^G t - 2D_\parallel^G t}\right)\cdot C_2(t) \end{aligned} \tag{2.6}$$

where

$$\begin{aligned} C_0(t) &= S_L^2 + (1-S_L^2)\cdot e^{-\frac{t}{\tau_\perp^L}} \\ C_2(t) &= e^{-\frac{2}{3}\frac{t}{\tau_\parallel^L}}(S_L^2 + (1-S_L^2))\cdot e^{-\frac{1}{3}\frac{t}{\tau_\perp^L}} \end{aligned}$$

Bilayer:

$$\begin{aligned} C_z(t) &= \left(S_L^2 + (1-S_L^2)\cdot e^{-\frac{t}{\tau_\perp^L}}\right)\cdot\left(S_G^2 + (1-S_G^2)\cdot e^{-\frac{t}{\tau_\perp^G}}\right) \\ C_{xy}(t) &= \frac{1}{4}\left(S_L^2 + (1-S_L^2)\cdot e^{-\frac{t}{\tau_\perp^L}}\right)\cdot\left(S_G^2 + (1-S_G^2)\cdot e^{-\frac{t}{\tau_\perp^G}}\right) + \\ &+ \frac{3}{4}\left(S_L^2 + (1-S_L^2)\cdot e^{-\frac{t}{3\tau_\perp^L}}\right)\cdot\left(S_G^2 + (1-S_G^2)\cdot e^{-\frac{t}{3\tau_\perp^G}}\right)\cdot e^{\frac{2}{3}t(\frac{1}{\tau_\parallel^{Eff}}} \end{aligned} \tag{2.7}$$

where

$$\frac{1}{\tau_\parallel^{Eff}} = \frac{1}{\tau_\parallel^G} + \frac{1}{\tau_\parallel^L} \tag{2.8}$$

and

$$\begin{aligned} \tau_\parallel &= \frac{1}{6D_\parallel} \\ \tau_\perp &= \frac{(1-S^2)}{6D_\perp} \end{aligned} \tag{2.9}$$

These MF expressions were used to fit the autocorrelation curves to extract the order parameters and rotational correlation times for both local and global motions in all aggregate states. In each case the correlation function for the Z axis was fitted first. The resulting parameters were then fixed and the rest were obtained by fitting the X/Y correlation function.

2.2.5 Simulation of EPR Spectra

The simulation of motional EPR line shapes can be simplified by taking into account the fact that for many surfactant/water systems the internal reorientational dynamics of the probe is usually very fast ($D^L > 10^8$ s^{-1}) on the EPR

timescale at X-Band ($\approx$ 9.5 GHz) [8][14]. In such cases the effects of fast local motions can be accounted for prior to solving the SLE by partial averaging of the magnetic parameters in response to the local axial order, S^L , in accordance with the equations (2.10) derived by Gaffney and McConnell [132]:

$$\begin{aligned}
\bar{g}_\perp &= g_0 - \frac{1}{3}S^L\left(g_{zz} - \frac{1}{2}\left(g_{xx} + g_{yy}\right)\right) \\
\bar{g}_\parallel &= g_0 + \frac{2}{3}S^L\left(g_{zz} - \frac{1}{2}\left(g_{xx} + g_{yy}\right)\right) \\
\bar{A}_\perp &= A_0 - \frac{1}{3}S^L\left(A_{zz} - \frac{1}{2}\left(A_{xx} + A_{yy}\right)\right) \\
\bar{A}_\parallel &= A_0 + \frac{2}{3}S^L\left(A_{zz} - \frac{1}{2}\left(A_{xx} + A_{yy}\right)\right)
\end{aligned} \tag{2.10}$$

where $\bar{g}_\perp$, $\bar{g}_\parallel$, $\bar{A}_\perp$ and $\bar{A}_\parallel$ are the partially averaged principle components of g and A tensors and $g_0 = (g_{xx} + g_{yy} + g_{zz})/3$ and $A_0 = (A_{xx} + A_{yy} + A_{zz})/3$.

The averaged values are then employed in the SLE simulation algorithm with the $\hat{\Gamma}$ operator now dependent only on global diffusion parameters. The principle values of the g and A tensors used in this study were: $g_{xx} = 2.0088$; $g_{yy} = 2.0061$; $g_{zz} = 2.0027$ and $A_{xx} = 6.26$ G; $A_{yy} = 5.85$ G; $A_{zz} = 33.46$ G [62]. EPR spectra were simulated using the Easyspin package [4]. The values of homogeneous line broadening used in EPR simulations are detailed in Table 2.2.

Global diffusion which depends on the geometry of the aggregate further avera-

Table 2.2: Peak to peak linewidths used in simulation of lyotropic EPR spectra. [a] value taken from [14] ; [b] value taken from [8].

Phase	**Lorentzian peak-to-peak line broadening (G)**	
	SDS [a]	**DTAC**
Microaggregates	0.70	n/a
Micelle	0.70	0.45 [b]
Hexagonal	0.70	1.00
Lamellae	0.70	1.20

ges the spectra, as illustrated with the selected model simulations in Figure 2.3. For instance, in spheroidal micelles, global motions due to surface diffusion of the probe and aggregate tumbling totally average out the anisotropy of the local motions, resulting in significant narrowing of the line shapes (Figure 2.3) [14]. On the other hand, in the highly anisotropic cylindrical aggregations of the hexagonal phase, there is only one-dimensional rotational diffusion which is far less effective at averaging out the anisotropy of the local motion, leading to an intermediate powder spectrum (Figure 2.3b) [8][63]. In the lamellar phase, surface diffusion in both directions is assumed to be mainly translational with no effect on the line shape, resulting in significantly broader line shapes that depend sensitively on the S^L value of the internal motion of the probe (Figure 2.3c). A slow restrained motion as a result of ripples on the surface of the lamellae or other tilting motions may exist and affect the dynamics of the probe [133]. As with the other models discussed in section 1.1.2, when the global motion is very slow ($D^G < 10^6$) this model becomes equivalent to the MOMD model.

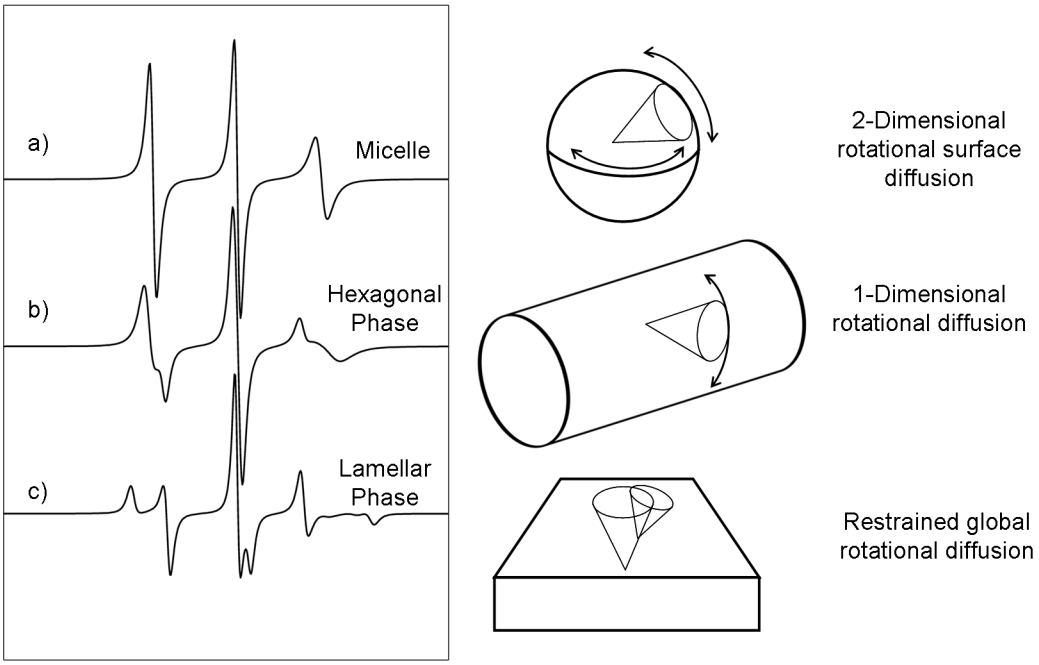

Figure 2.3: Left: Illustrative examples of X-band EPR line shapes simulated using partial averaging of magnetic parameters of a spin probe with restricted local motion ($S_L = 0.4$) and combined with: a) two-dimensional rotational surface diffusion (micelle) ($D_{\perp}^{G} = 5 \times 10^{7}\ s^{-1}$); b) one-dimensional rotational diffusion (rod/-hexagonal phase - unaligned) ($D_{\perp}^{G} = 5 \times 10^{7}\ s^{-1}$); c) restrained global rotational diffusion ($S_G = 0.2$) at the rigid limit (lamellar phase) ($D_{\perp}^{G}\ 1 \times 10^{6}\ s^{-1}$). Right: Diagram showing ordered local motions (cones) and rotational global motions in different aggregates.

2.3 Experimental Methods

2.3.1 Sample Preparation

Spin probe 5-DOXYL-stearic acid (5DSA) and surfactants sodium dodecyl sulphate (SDS) and dodecyltrimethylammonium chloride (DTAC) were purchased from the Sigma-Aldrich Chemical Company (UK) and used without further purification. Water was deionized and distilled. 5DSA was solubilized in minimal ethanol and made up with water to a 4 mM stock solution. A quantity of this was then added to a microcentrifuge tube containing an appropriate amount of surfactant and additional water resulting in a ratio of $\sim$ 1:100 spin probe to host molecules. For thick, gel-like systems, such as hexagonal and lamellar phases, samples were centrifuged and inverted for several days at elevated temperatures to ensure proper mixing. These were then transferred to 1.0 mm (internal diameter) capillary tubes and sealed with wax.

2.3.2 EPR Measurements

EPR spectra were measured using an X-band (9.5 GHz) Bruker EMX spectrometer equipped with the digital temperature control system (ER4131VT) for high temperature measurements using a heated flow of nitrogen gas. For each temperature, samples were equilibrated for 5 minutes before taking the measurement. Variable temperature measurements were performed with the tolerance < 0.1 K. The following conditions were used: microwave frequency of 9.55 GHz; microwave power of 2 mW; modulation frequency of 100 kHz; modulation amplitude of 1.0 G.

2.4 Results and Discussion

2.4.1 Density Functional Theory

The magnetic properties of the 5DSA spin probe were first investigated with DFT using the method outlined by Barone for the accurate determination of these parameters for nitroxide radicals [125][126][134][135] (the calculation of magnetic parameters will be discussed in more detail in section 4.1.1). The isosurfaces of the singly occupied molecular orbital (SOMO) and spin density (Figure 2.4) qualitatively confirm that the radical electron is primarily delocalised in the NO bond π orbital with only slight interaction with the alkyl groups, as is typical for a nitroxide spin label [134][136].

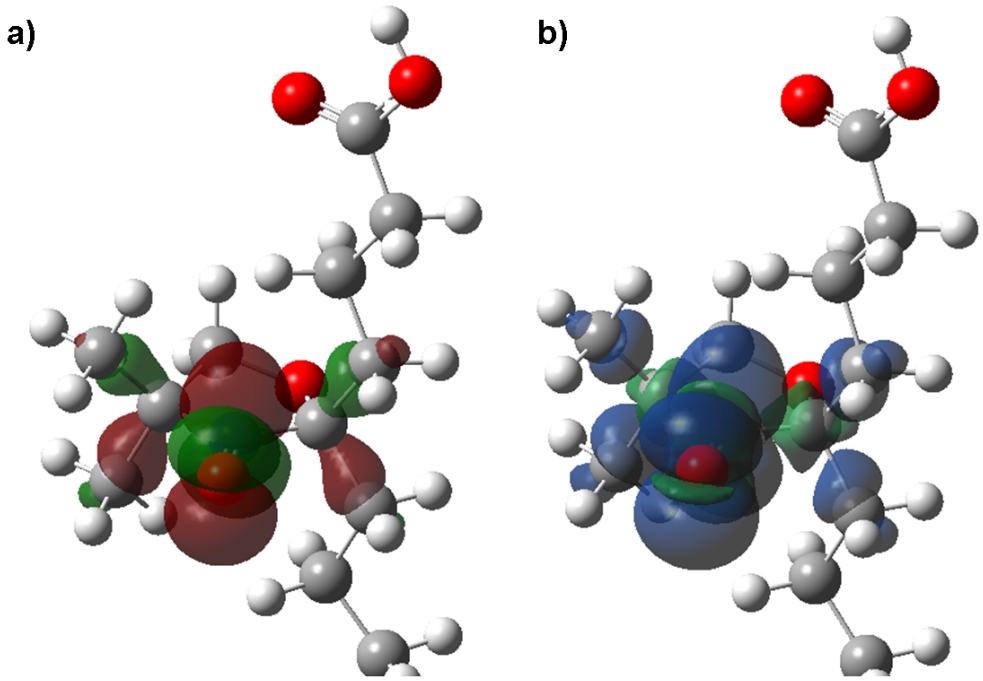

Figure 2.4: Isosurfaces of a) the SOMO and b) the spin density for the 5DSA spin probe where lobe colours indicates relative phase.

Solvation of spin probes can influence the magnetic environment via two mechanisms; directly through polarising electron density and indirectly by modifying

Table 2.3: g and A values for 5DSA in different solvents calculated with B3LYP/N07D. Solvent dielectric constants, ε, are included to indicate solvent polarity.

State	$\mathbf{g}_{xx}$	$\mathbf{g}_{yy}$	$\mathbf{g}_{zz}$	$\mathbf{A}_{xx}$ (G)	$\mathbf{A}_{yy}$ (G)	$\mathbf{A}_{zz}$ (G)
Vacuum ($\varepsilon = 1.0$)	2.0091	2.0058	2.0022	5.14	5.35	30.60
Water ($\varepsilon = 78.4$)	2.0088	2.0057	2.0022	5.76	5.89	32.60
Acetonitrile ($\varepsilon = 35.4$)	2.0087	2.0057	2.0022	5.74	5.87	32.54
Dodecane ($\varepsilon = 2.0$)	2.0090	2.0058	2.0022	5.36	5.54	31.32
Literature(Water)[62]	2.0088	2.0061	2.0027	6.26	5.85	33.46

the structure, and thus is crucial to accurately model the magnetic parameters [134][137]. The g tensor is confirmed to be rhombic with $g_{xx} > g_{yy} > g_{zz}$ (Table 2.3) and in good agreement with the experimentally reported values for 5DSA in water [62]. The hyperfine coupling tensor is approximately axially symmetric ($A_{xx} \approx A_{yy} < A_{zz}$) and also in good agreement with that reported experimentally [62].

The NO bond length is found to show little solvent dependence, however the more polar solvents stabilise the negative charge on the oxygen atom (Table 2.4). This results in a slightly greater solvent shift in the polar solvents (water and acetonitrile) compared with the apolar solvent (dodecane), as noted in previous

Table 2.4: Mulliken charges,δ, and bond length for the 5DSA nitroxide group in different solvents calculated with B3LYP/N07D.

State	$\boldsymbol{\delta_N}$	$\boldsymbol{\delta_O}$	N-O Bond Length (Å)
Vacuum	0.137	-0.598	1.258
Water	0.104	-0.635	1.260
Acetonitrile	0.105	-0.634	1.260
Dodecane	0.127	-0.612	1.259

studies of nitroxides [138]. Despite this however, the shift of g and A between the hydrophobic apolar dodecane and water, representing the interior and surface regions of lyotropic aggregates respectively, is likely to be relatively small (< 2 G) compared with averaging of these parameters by dynamic effects.

2.4.2 EPR Modelling

Figure 2.5 shows the effect of D^G_{Iso} and S^L on model spectra with isotropic global diffusion using partial averaging of magnetic g and A tensors with equations 2.10 and clearly demonstrates the non-unique nature of these line shapes. For example $D^G_{Iso} = 5 \times 10^7$ s^{-1} and $S^L = 0.6$ or $D^G_{Iso} = 1 \times 10^8$ s^{-1} and $S^L = 0.8$ are shown to be virtually indistinguishable. Also notable is that line shapes are potentially indistinguishable from those using the single component isotropic motion with no order parameter, as shown in Figure 1.3, however with significantly different rotational diffusion rates. At the slow motion limit, $D^G_{Iso} = 1 \times 10^6$ s^{-1}, the line shape depends only on the order parameter and is in agreement with the MOMD line shape for local motion at the fast motion limit. When $S^L = 0$ the spectra show the narrow lines of equal intensity indicative of the fast motion limit and are insensitive to the global motion.

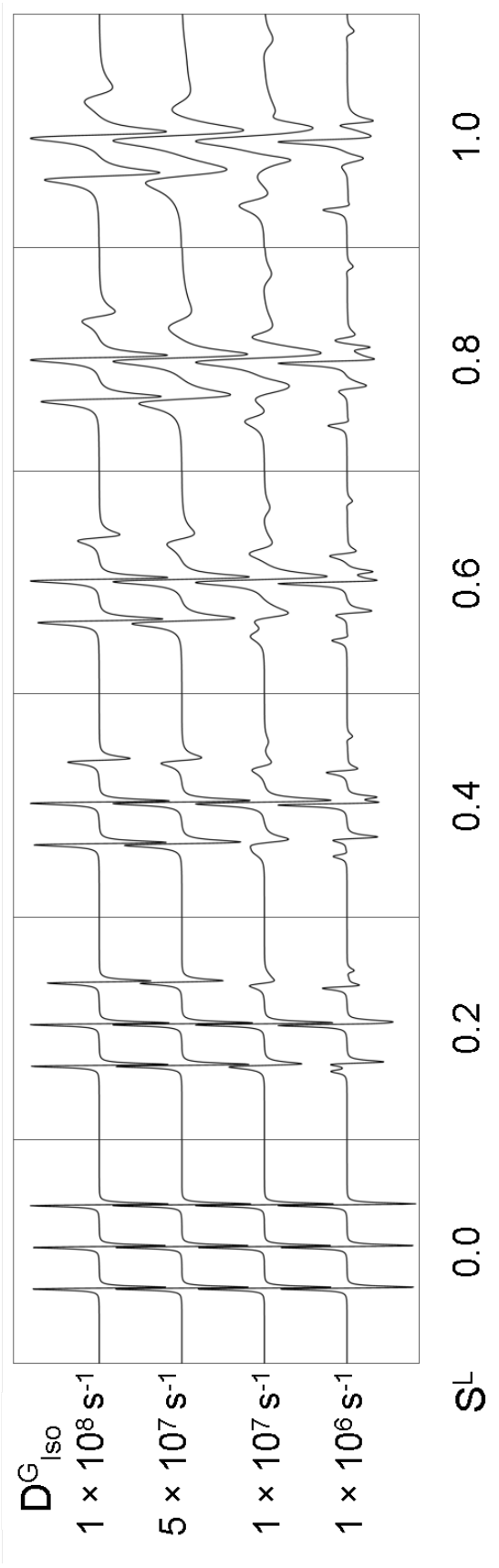

Figure 2.5: Effect of isotropic global rotational diffusion defined by the isotropic diffusional rate D^G_{Iso} and local order parameter S^L on X-band EPR line shape assuming fast local motion with Lorentzian peak-to-peak broadening of 0.7 Gauss.

The unaligned hexagonal phase spectra predicted by this model (Figure 2.6) demonstrate the same slow global motion and low order limiting line shapes as in the isotropic case. However, the spectra in the intermediate region, where the effect of local order is partially averaged by azimuthal diffusion are highly distinctive in the majority of simulations. When $D_{\|}^{G} \approx 1 \times 10^{7}$ and S^{L} is high, spectra may be indistinguishable from those of the lamellar phase.

Figures 2.7, 2.8 and 2.9 show the effects of global diffusion, local and global order on lamellar type spectra which could arise as a result of curvature of the surface [133] or other motional processes. Most notably the effect of the global order parameter, which results in line broadening, increases with the global diffusional rate. As a higher global diffusional rate causes line narrowing the interplay between these effects results in many motional regimes having similar spectra for this aggregate geometry. These line shapes could also be reproduced using a single motional component MOMD model using an effective order parameter, although the validity of the application of these models would not be apparent from experiment alone.

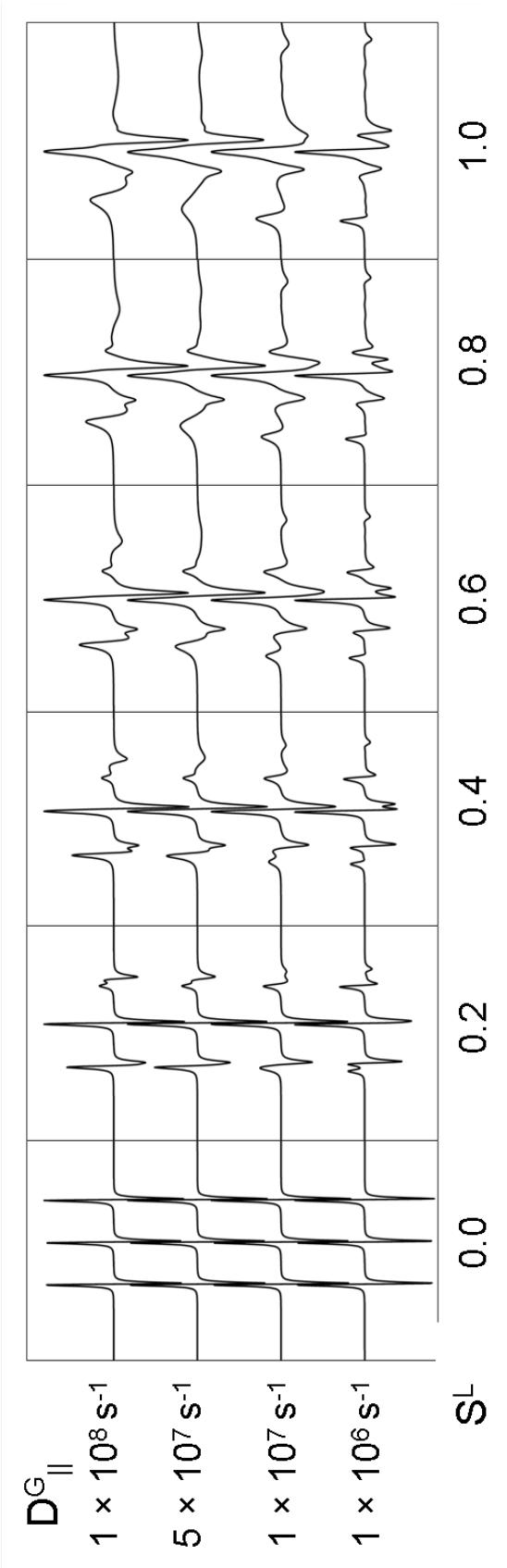

Figure 2.6: Effect of azimuthal global rotational diffusion defined by the azimuthal diffusional rate $D^G_{||}$ and local order parameter S^L on X-band EPR line shape assuming fast local motion and transverse global tumbling defined by $D^G_{\perp}$ is fixed at $1 \times 10^6\ s^{-1}$ with Lorentzian peak-to-peak broadening of 0.7 Gauss.

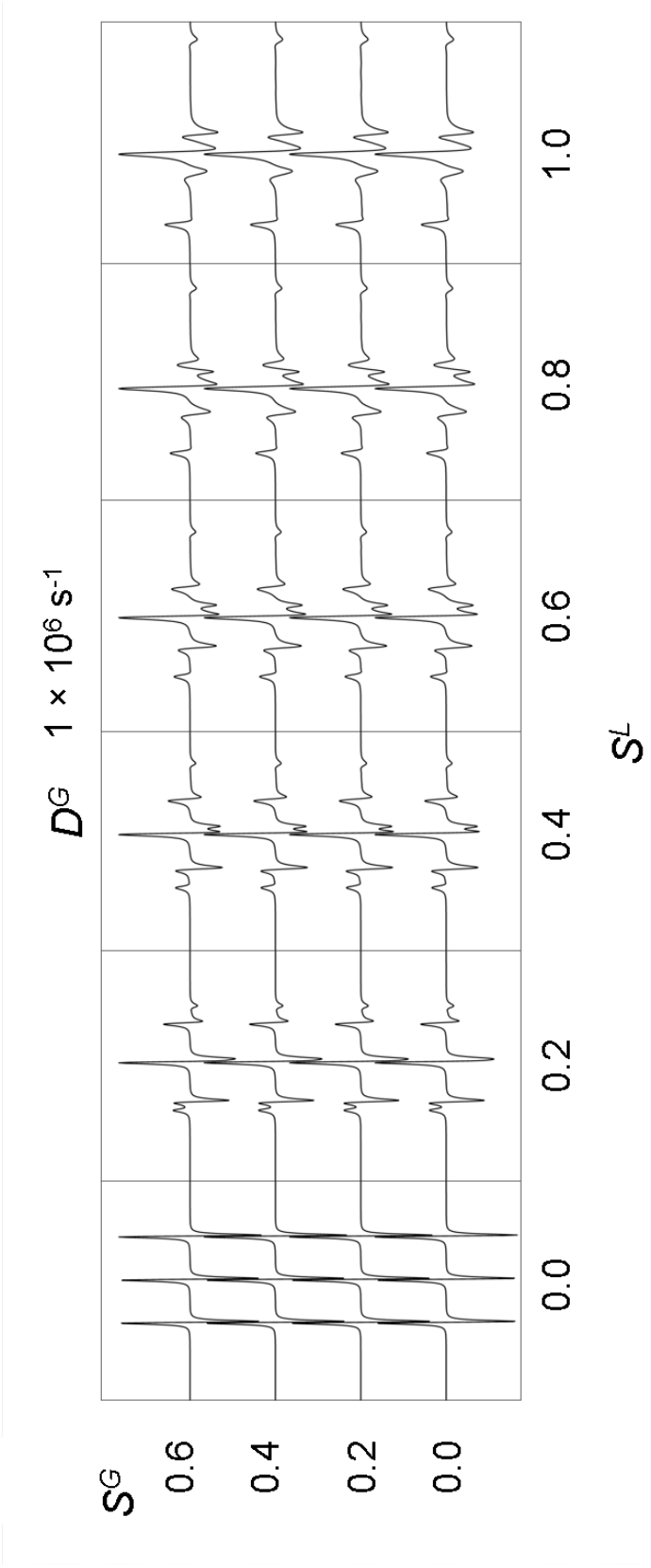

Figure 2.7: Effect of global, S^G, and local, S^L, order parameters on X-band EPR line shape assuming fast local motion with the global diffusion rate, D^G, fixed at 1×10^6 s^{-1} with Lorentzian peak-to-peak broadening of 0.7 Gauss.

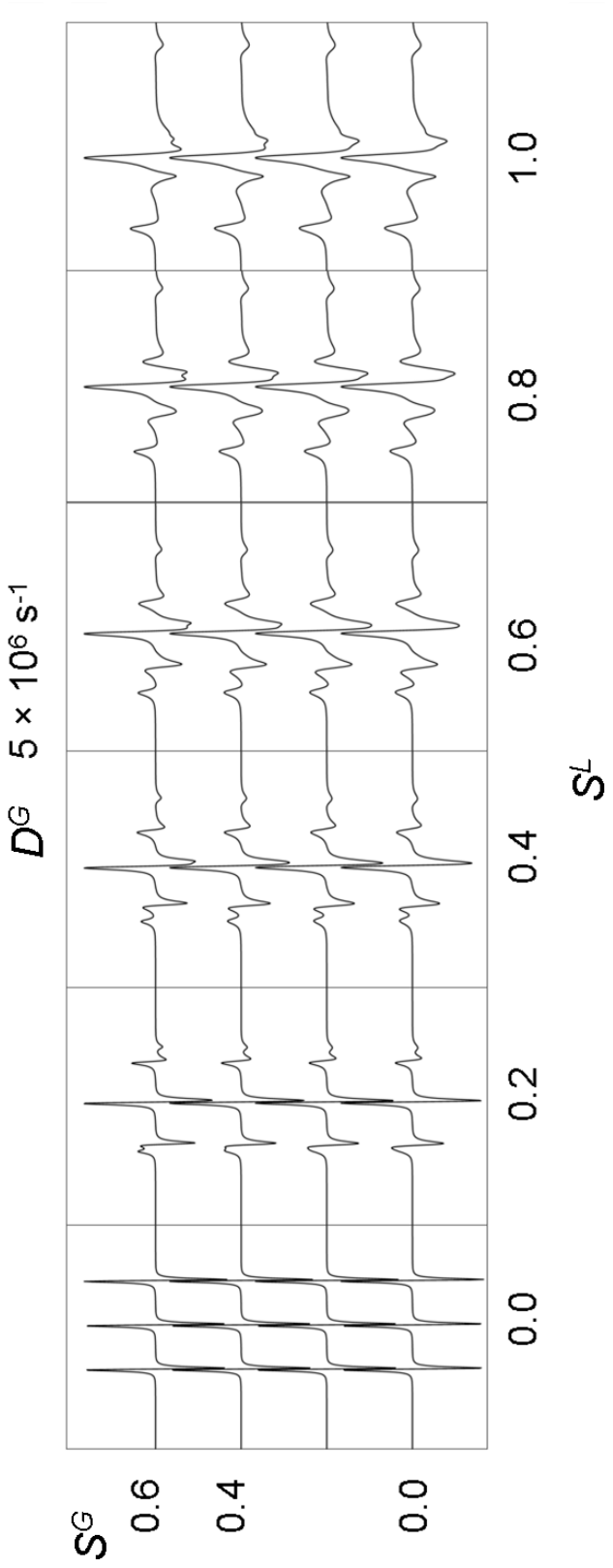

Figure 2.8: Effect of global, S^G, and local, S^L, order parameters on X-band EPR line shape assuming fast local motion with the global diffusion rate, D^G, fixed at 5×10^6 s^{-1} with Lorentzian peak-to-peak broadening of 0.7 Gauss.

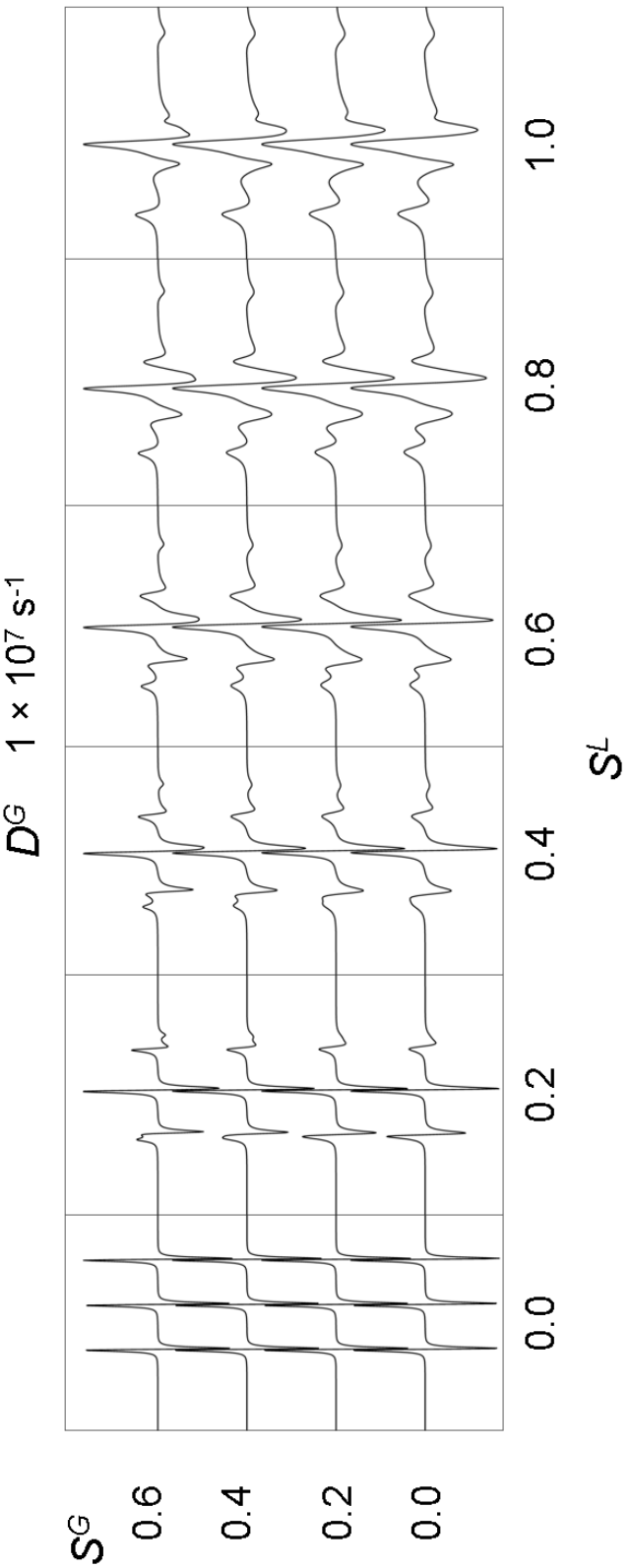

Figure 2.9: Effect of global, S^G, and local, S^L, order parameters on X-band EPR line shape assuming fast local motion with the global diffusion rate, D^G, fixed at 1×10^7 s^{-1} with Lorentzian peak-to-peak broadening of 0.7 Gauss.

2.4.3 SDS Microaggregates

Previous experimental studies have suggested that due to the hydrophobic nature of the 5DSA spin probe, limited aggregation centred around the probe can occur below the critical micelle concentration [102]. In order to test this, microaggregate states of lyotropics have been modelled using SDS molecules. By starting MD simulations with a random dispersion of up to five SDS molecules and one probe in a simulation box filled with water molecules, the formation of flexible microaggregates around the spin probe was observed in < 10 ns (Figure 2.10). In fact, SDS molecules did not form stable microaggregates except in the presence of 5DSA. It was also observed that the larger microaggregates (with either 4 or 5 SDS molecules) were more stable, however infrequent reversible dissociation of SDS molecules still took place.

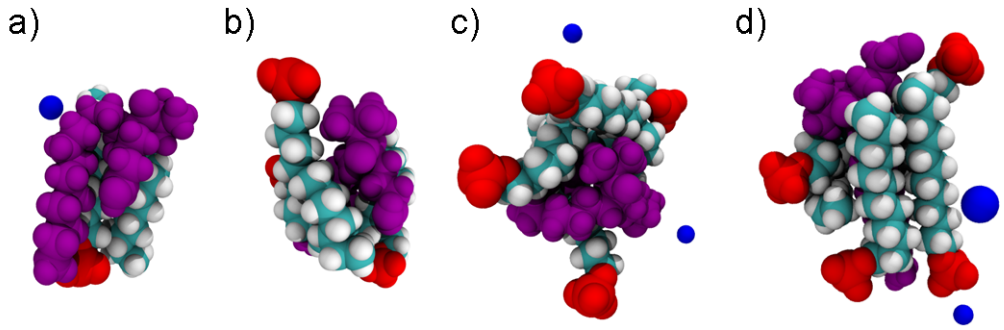

Figure 2.10: Snapshots of equilibrated structures of 5DSA (purple) in SDS microaggregates consisting of 2 (a), 3 (b), 4 (c) and 5 (d) surfactant molecules. In all images water molecules are excluded for clarity. Sodium counterions indicated in blue.

Autocorrelation functions calculated from the MD trajectory for different molecule fixed axes in both probe and host molecules, corresponding to a microaggregate with 3 SDS molecules, are shown in Figure 2.11b. They were fitted using the relevant expression 2.4, along with other microaggregates, and the results are presented in Table 2.5 (For all systems reported in this chapter the fitted curves

are presented in section A.2 of the appendices). The dynamics in all microaggregates were found to have slight axial rotational character, reflecting the rod-like molecular geometry of both the individual molecules and their aggregates. This was particularly noticeable for SDS molecules with the clearly distinguishable correlation decays for the Z and X/Y axes (Figure 2.11a, right panel). Larger aggregates exhibited slower dynamics (Table 2.5) as a result of the greater size and less frequent dissociation of surfactant molecules. In all cases, the rotational dynamics of the nitroxide group on the probe were slower than that of the host SDS backbone. The EPR spectrum of microaggregates with 3 SDS molecules predicted using the MF approach is shown in Figure 2.11b as the green line and is in very good agreement with the experimental one (blue line) measured at 3 mM SDS concentration. A distribution of aggregate sizes would be expected in an experimental sample. The spectrum averaged among the simulated aggregate contributions, assuming a narrow discrete Gaussian distribution (Equation 2.11) around the N = 3 SDS microaggregate with the variance $\sigma^2 = 0.25$, is shown as the red line and is barely distinguishable from the one corresponding to the N = 3 SDS microaggregate.

$$P_N = \frac{1}{\sqrt{2\pi\sigma^2}} e^{-\frac{(N_{centre}-N)^2}{2\sigma^2}} \tag{2.11}$$

Table 2.5: Motional parameters of 5DSA and SDS in different microaggregate states at 300K obtained from the fitting of the relevant autocorrelation functions. $D_\perp$ and $D_{||}$ represent the two components of a single axial rotational diffusion (shown in Figure 2.2) employed in the model for all microaggregates. 95% confidence bounds for the adjusted parameters are provided in Table A.4 of appendices.

Molecule	$\boldsymbol{D}_\perp$ (s^{-1})	$\boldsymbol{D}_{||}$ (s^{-1})
	2 SDS Molecules	
5DSA	12.67×10^8	2.73×10^9
SDS	17.60×10^8	2.01×10^{10}
	3 SDS Molecules	
5DSA	10.75×10^8	2.11×10^9
SDS	15.26×10^8	1.84×10^{10}
	4 SDS Molecules	
5DSA	7.45×10^8	1.79×10^9
SDS	9.73×10^8	1.80×10^{10}
	5 SDS Molecules	
5DSA	6.39×10^8	1.57×10^9
SDS	9.27×10^8	1.75×10^{10}

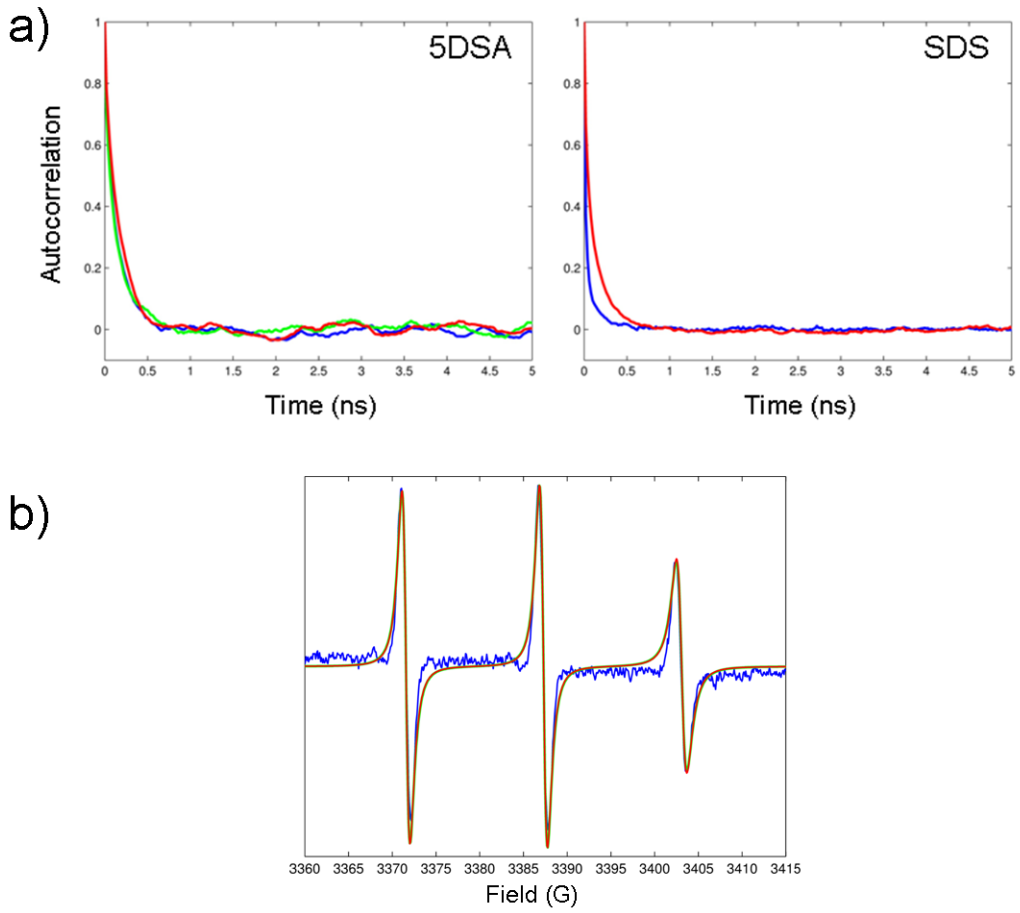

Figure 2.11: a) Rotational autocorrelation functions of 5DSA magnetic axes (left) and SDS geometric axes (right) in $N = 3$ microaggregate at 300K. X, Y and Z are indicated by blue, green and red respectively (in SDS $X = Y$). b) Comparison between experimental (blue) and simulated (red) EPR spectra of 5DSA assuming discrete Gaussian distribution among microaggregates at 300K. The green line represents the EPR spectrum of a single 3 SDS microaggregate at 300K.

2.4.4 Micelles

Figure 2.12 shows the equilibrated structures of 5DSA (purple) doped in SDS (left) and DTAC (right) micelles composed of 60 (N60) [108][109][110][139] and 40 (N40) [8][111] molecules respectively at 320K. The structures clearly highlight the differences in packing between the two surfactant systems. Due to the larger size, many of the alkyl chains in the SDS micelle are solvent exposed. This results in significantly greater geometric disorder compared to the DTAC micelle as the tails fold to minimise contact with water in the former.

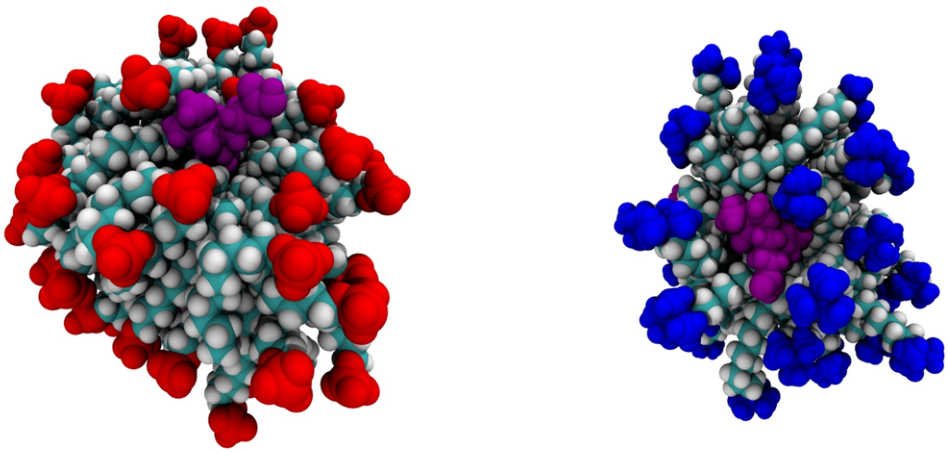

Figure 2.12: Snapshots of equilibrated structures of 5DSA (purple) doped N60 SDS (left) and N40 DTAC (right) micelles at 320 K.

This behaviour has been observed in previous MD studies of SDS micelles [108], as well as inferred by experimental studies that found that changing from the 5DSA probe to 16DSA had little effect on their EPR spectra, indicating that the tail and head of the molecule experienced similar environments [42]. In contrast, in the slightly smaller DTAC micelle, even though a similar bent conformation is observed, the tails tend to remain directed towards the micelle centre. The SDS micelle was found to be stable over the entire MD trajectory at three selected temperatures, in agreement with the previous MD study by Jang

and co-workers which reported that external energy of ≈13 kcal/mol was required for the dissociation of the SDS molecules [108]. Conversely, these results show that in the DTAC micelle individual molecules temporarily dissociate spontaneously, albeit infrequently.

This process contributes to the greater fluctuations in the micelle radii and eccentricity for the DTAC micelle compared to SDS whose time evolutions are presented in Figure 2.13a. The radii, defined as micelle centre of mass (COM)

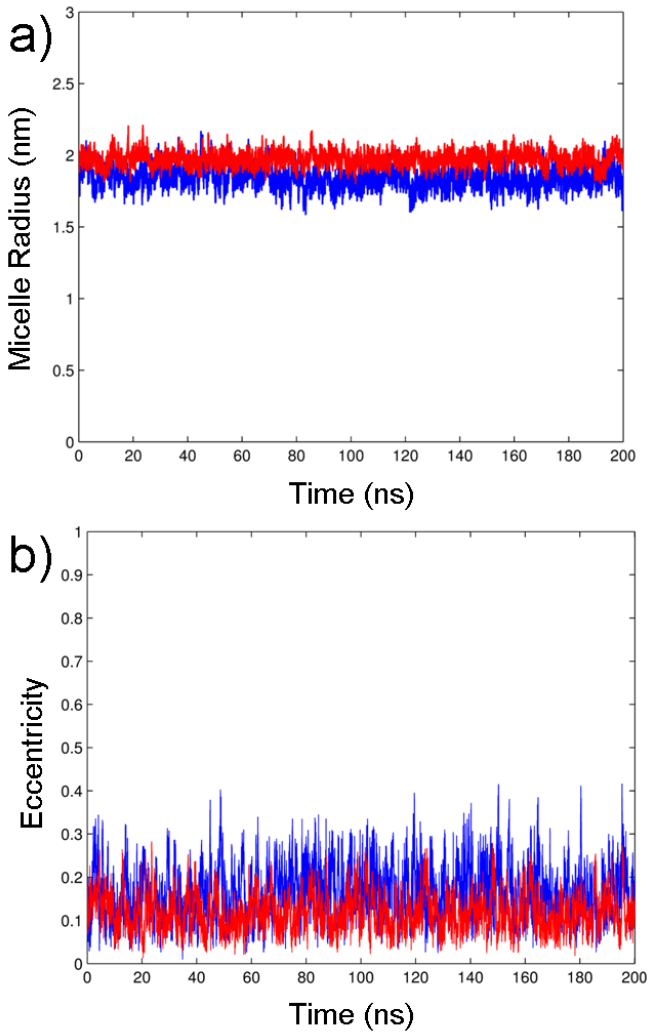

Figure 2.13: a) Micelle radius (centre of mass to sulphur/nitrogen) and b) eccentricity of SDS (red) and DTAC (blue) micelles over the first 200 ns of trajectory at 320 K.

to Sulphur, of the N60 SDS micelle is calculated to be 1.97 ± 0.04 nm which is in very good agreement with the previous MD studies (1.94 ± 0.04 nm [109]) and only slightly lower than the hydrodynamic radius of 2.2 nm measured by quasi-elastic light scattering spectroscopy [107]. The COM to Nitrogen radius of the DTAC micelle was found to be 1.84 ± 0.06 nm, only slightly higher than the one of ≈1.78 nm estimated from NMR measurements [101] and time resolved fluorescence quenching [103], but within the error boundaries.

In order to evaluate the shape of the micelles, eccentricity parameter, e, defined as:

$$e = 1 - \frac{I_{Min}}{I_{Avg}} \tag{2.12}$$

was calculated from the MD trajectories (Figure 2.13b). In equation 2.12 I_{Min} and I_{Avg} are the smallest and averaged moments of inertia along the principal axes [140]. An eccentricity of 0 indicates a perfect sphere, whereas an eccentricity of 1 indicates an ellipsoid. The SDS micelle has an average eccentricity of 0.118 ± 0.035, which falls within the range of previously reported values obtained from MD simulations (0.057 [108] - 0.154 [112]), indicating a slightly prolate spheroidal geometry. Experimentally, the shape of the SDS micelle is still a topic of debate, with scattering data consistent with both slightly prolate and oblate spheroids [141]. The average eccentricity of the DTAC micelle was found to be slightly higher at 0.163 ± 0.050, with greater fluctuations due to the temporary dissociation and smaller aggregation number (blue line in Figure 2.13b).

Cross-correlation functions for the Z axes of host molecules, calculated via:

$$C(t) = \left\langle \frac{1}{2N} \sum_{i=j}^{N} P_2(\vec{Z}_i(t+\tau)) \cdot (\vec{Z}_j(t)) d\tau \right\rangle \tag{2.13}$$

where $\vec{Z}_i$ and $\vec{Z}_j$ represent the Z vectors of pairs i and j of the hosts, for both SDS and DTAC systems are shown in Figure 2.14a. They indicate that relatively fast molecular surface diffusion occurs, leading to the loss of coordinated motions among them on the scale of a few nanoseconds. This is also evident in the snapshots shown in Figure 2.14b where the selected molecules become completely

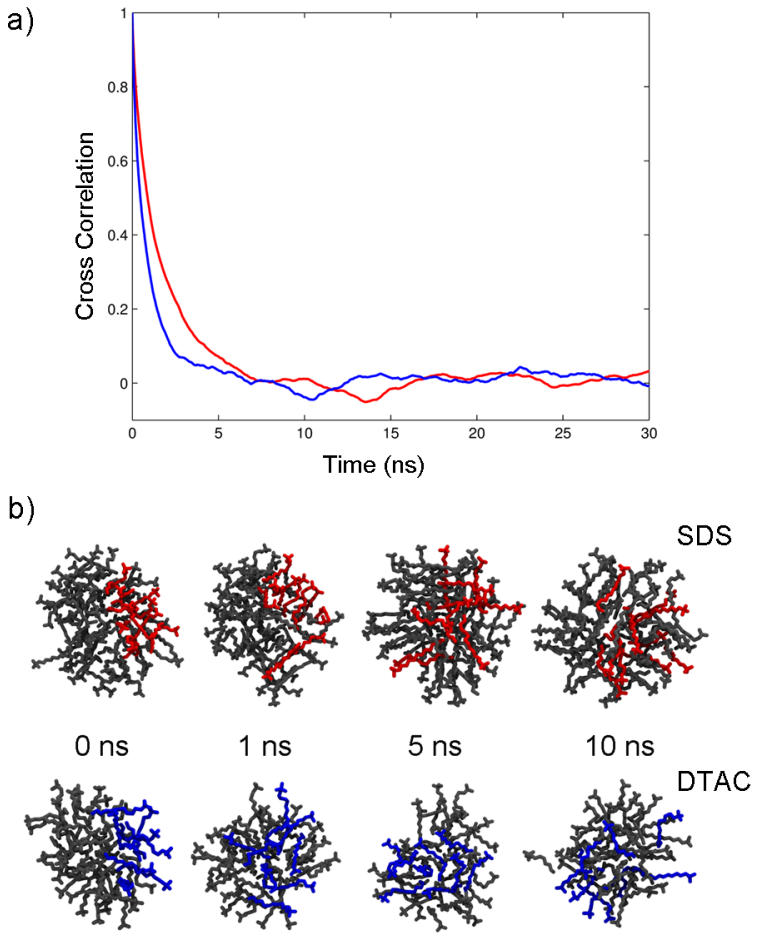

Figure 2.14: a) Cross correlation of SDS (red) and DTAC (blue) molecular z axes in micelles at 320K. b) Snapshots of SDS and DTAC micelles showing effect of random isotropic surface diffusion on a selection of molecules over time.

dispersed throughout the micelle after ∼10ns. These observations have several implications for the dynamics that would not be evident from EPR spectra alone. Firstly, as the micelle radii and eccentricity are in good agreement with those observed in previous studies with micelles free of spin probes, the effect of the probe on the geometry is minimal, even though the formation of microaggregates indicates that it acts as a nucleation site. Secondly, because of fluctuating eccentricity of micelles, global tumbling of the micelle is poorly defined [61][100]. Furthermore, since surface diffusion of the host molecules is comparatively fast

and stochastic, collective motions rapidly fade away as evident in Figure 2.14.

As a result, the effect of aggregate tumbling on the global motion will be very small for these systems. This suggests that the additional contributions of slippage of the probe in the SRLS model are probably not required to describe the motion of the probe in these particular systems, and therefore a simpler model such as the MF approach can be applied adequately. Additionally, in both systems the nitroxide head group of 5DSA is located at the fully solvent exposed surface, thus the spectra are indicative of only one environment.

The autocorrelation plots of the magnetic and molecular axes of the probe and host molecules in the micellar aggregations are presented in Figure 2.15 and were fitted using MF expression 2.5. In each case, the decay curves are consistent with the overall axial dynamics which are of biexponential character, representing the superposition of fast restricted internal and unrestricted global motions. Table 2.6 presents the principle rotational diffusion rates and the local order parameters extracted from the fitting of the autocorrelation functions. These parameters indicate the differences between the SDS and DTAC micelles motions that are consistent with their structural features. The larger but more structurally disordered SDS micelle shows lower local order for both 5DSA and SDS molecules with slower global motions, whereas in contrast the smaller DTAC micelle shows higher local order for both molecules but with much faster global motional contribution. As smaller micelles have greater curvature of the surface, the effect of surface diffusion on the rotational global motion is higher in the case of DTAC. This result is also consistent with the relative rates observed in the cross-correlations (Figure 2.15).

The EPR spectra, shown in Figure 2.16 in red, were simulated using the parameters given in Table 2.6 and are in excellent agreement with the experimental ones shown in blue. It is worth noting that even using multiple probes, relatively long trajectories compared with the microaggregates were required to adequately resolve the slower global dynamics for the micellar phase. The order

Table 2.6: Motional and order parameters of 5DSA ,SDS and DTAC in N60 SDS (top) and N40 DTAC (bottom) micelles obtained from the fitting of the relevant autocorrelation functions. D^G, $D^L_\perp$, $D^L_\parallel$ and S^L represent isotropic global diffusion, the two components of local diffusion and the local order parameter respectively. 95% confidence bounds for the adjusted parameters are provided in Tables A.5 and A.6 of the appendices.

T (K)	**Molecule**	$\mathbf{D}^G$ **(s^{-1})**	$\mathbf{D}^L_\perp$ **(s^{-1})**	$\mathbf{D}^L_\parallel$ **(s^{-1})**	$\mathbf{S}^L$
300	5DSA	3.8×10^7	1.26×10^8	1.68×10^8	0.36
300	SDS	6.9×10^7	3.24×10^8	9.55×10^9	0.55
310	5DSA	4.6×10^7	1.79×10^8	3.58×10^8	0.35
310	SDS	8.7×10^7	5.56×10^8	11.61×10^9	0.51
320	5DSA	6.7×10^7	2.14×10^8	5.45×10^8	0.34
320	SDS	10.6×10^7	7.37×10^8	19.25×10^9	0.46

T (K)	**Molecule**	$\mathbf{D}^G$ **(s^{-1})**	$\mathbf{D}^L_\perp$ **(s^{-1})**	$\mathbf{D}^L_\parallel$ **(s^{-1})**	$\mathbf{S}^L$
300	5DSA	5.7×10^7	1.39×10^8	3.71×10^8	0.47
300	DTAC	10.1×10^7	8.73×10^8	10.96×10^9	0.54
310	5DSA	7.4×10^7	2.11×10^8	4.52×10^8	0.44
310	DTAC	14.3×10^7	12.97×10^8	17.42×10^9	0.53
320	5DSA	9.1×10^7	2.75×10^8	5.67×10^8	0.40
320	DTAC	19.9×10^7	15.15×10^8	20.45×10^9	0.51

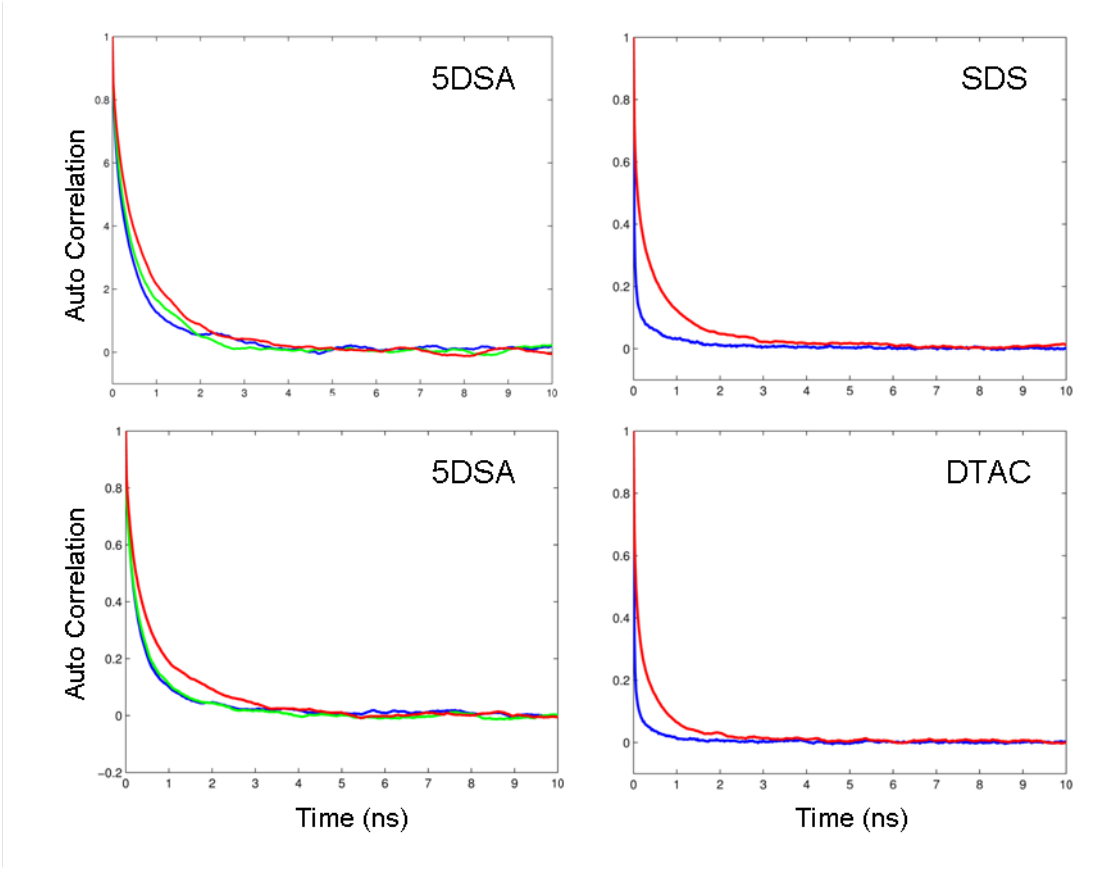

Figure 2.15: Autocorrelation functions of 5DSA magnetic axes (left) and SDS/DTAC geometric axes (right) in micelles at 320 K. X, Y and Z are indicated by blue, green and red respectively (in SDS/DTAC $X \approx Y$).

parameter($S^L = 0.47$) and global dynamics ($D^G = 5.7 \times 10^7$ s^{-1}) calculated for the probe in the DTAC micelle at 300K are both in good agreement with the ones reported by Lindblom and co-workers ($S^L = 0.5$ and $D^G = 3.88 \times 10^7$ s^{-1} at 298K) [8].

For the SDS micelle, the order parameter was found to be only slightly lower ($S^L = 0.36$ and $D^G = 3.8 \times 10^7$ s^{-1} at 300K) than that of Westlund and co-workers who fitted the EPR spectra with the two-dynamic model ($S^L = 0.43$ and DG $= 5.0 \times 10^7$ s^{-1} at 298K) [14]. Similar to microaggregates, the dynamics of the probe were found to be slower than that of the host in all micellar cases, as well as showing lower ordering.

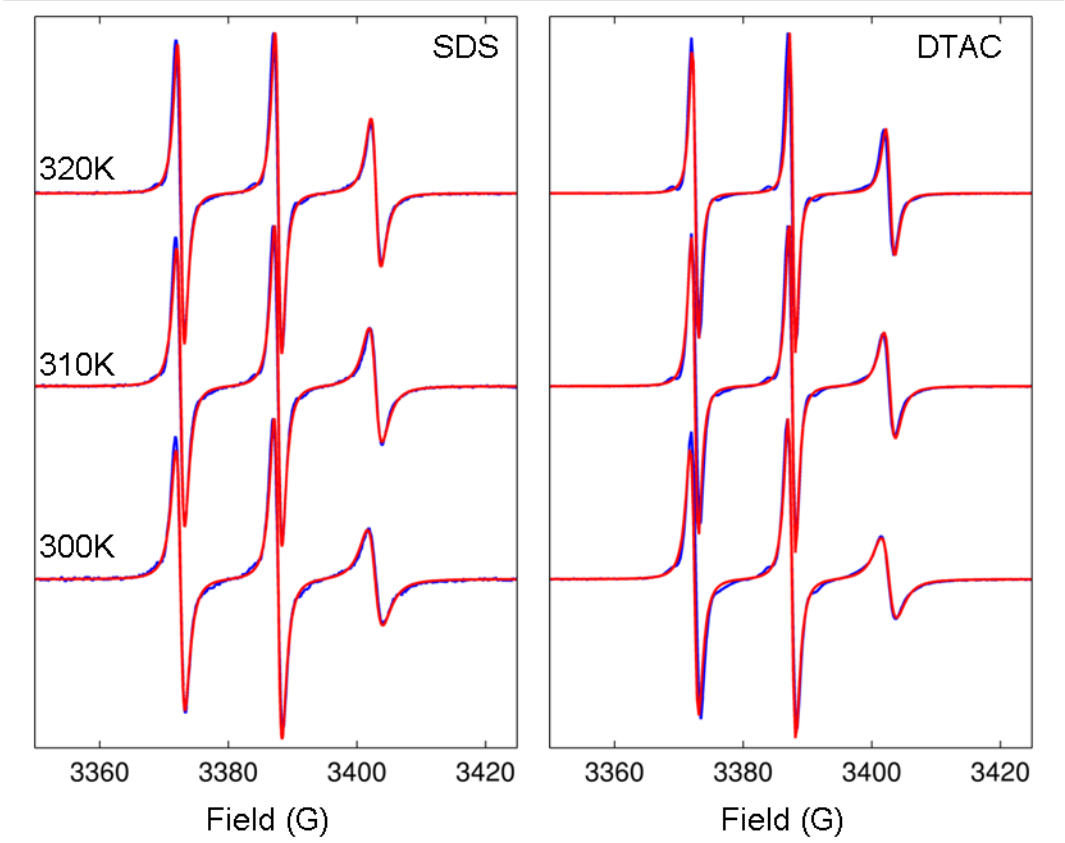

Figure 2.16: Comparison between experimental (blue) and predicted (red) EPR spectra of SDS (left panel) and DTAC (right panel) micelles doped with 5DSA at a range of temperatures.

However, although the calculated from MD values of the segmental order parameter of C-H bonds at different parts of the SDS tail show qualitative agreement with those obtained from NMR relaxation measurements, they are overestimated by approximately a factor of 2.5 as shown in Figure 2.17. Although there is some variation in the literature values for C-H order parameters, GAFF is known to produce overly ordered alkyl chains in lipid bilayers [96]. These discrepancies have mainly been attributed to an under representation of gauche conformers resulting in stiffened alkane chains [142][143]. It is interesting to note that recent modelling studies on non-ionic chromonic liquid crystals have also confirmed that GAFF also overestimates the interaction between the hydrophilic ethyleneoxy

chains of the molecules resulting in their aggregation into compact disorganized clusters instead of ordered stacks [144].

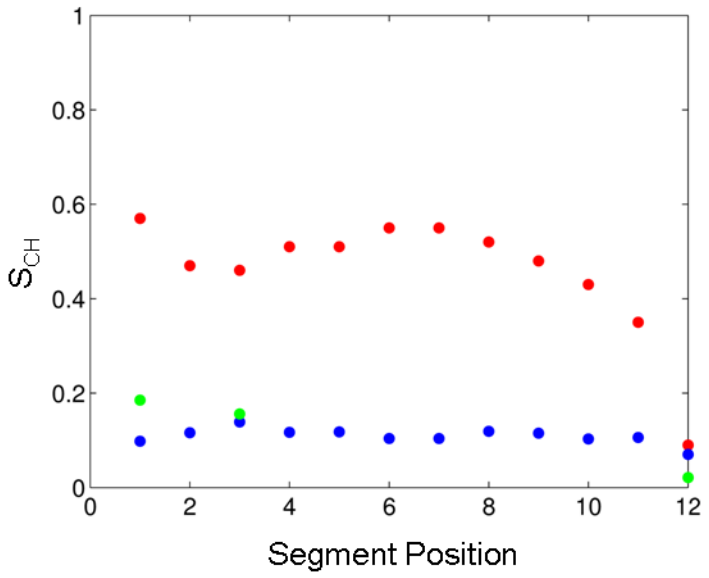

Figure 2.17: Comparison between experimentally determined (blue [6] and green [7]) and predicted from MD (red) S_{C-H} order parameters as a function of position along the carbonyl chain in micellar SDS at 310K. Full details are presented in appendix Table A.9.

This fact however does not affect the simulated EPR line shapes though, which demonstrate perfect agreement with experiment at different temperatures. This is because in micellar aggregates the nitroxide group of 5DSA remains fully water exposed throughout the MD runs and as such is relatively insensitive to the packing of internal alkyl chains of the host molecules overestimated by the GAFF model. Importantly, the agreement between the predicted and experimental EPR spectra conclude the validity of the MF approach for these micellar systems.

2.4.5 Hexagonal Phase

Figure 2.18 presents the snapshots of equilibrated structures of SDS (top) and DTAC (bottom) hexagonal phases doped with 5DSA spin probe (purple) at 320K demonstrating significant geometric differences between the two aggregates. The water content was 50% wt and 30% wt in the SDS and DTAC systems respectively. The lateral sizes of the simulation boxes were 3.9 nm and 4.7 nm for the SDS and DTAC phases respectively with the rods connected by periodic boundary conditions. SDS hexagonal phases form at a lower concentration but higher temperatures compared to DTAC [105][106]. The higher water content leads to the deviation of SDS from a circular to an elliptical cross section. This result is consistent with scattering and NMR studies [100] and other reports on the elliptical profile for rod-like micelles [145]. On the other hand, a close contact among the rods in DTAC forces the individual rods into having a hexagonal profile, in agreement with previous MD studies [111].

Preliminary MD simulations confirmed that at high concentrations of water DTAC rods become unstable. For instance, an MD simulation on a single rod with 50% wt resulted in its rapid decomposition into irregular micelles at times < 5 ns (Figure 2.19a). This is consistent with other MD studies of single DTAC [146] and CTAC [147] rods. Conversely the SDS hexagonal phase was more sensitive to temperature, with the molecules rapidly clustering at temperatures below 320K, followed by the growth of crystal patches, eventually leading to a lamellar-like ribbon structure [109] (Figure 2.19b) with dynamics that deviated significantly from those observed experimentally. Although the experimentally determined phase diagram [106] indicates that this temperature is near the phase boundary for a combined hexagonal and crystal region, the phase transition in MD appears to be particularly rapid, precluding measurement of comparable correlation functions. This might be related to the overly ordered alkyl chains suggested by the high C-H order parameters of the host molecules observed for the micellar phase. Similar crystal-like patches have previously been observed

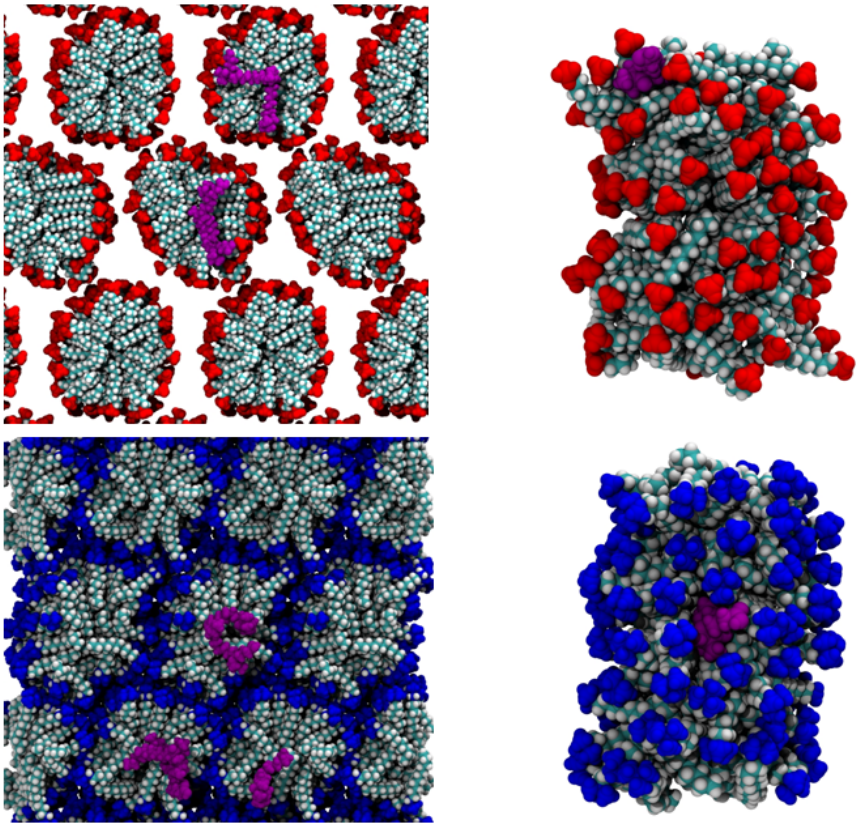

Figure 2.18: Snapshots of equilibrated structures of 5DSA (purple) doped SDS (top) and DTAC (bottom) hexagonal phase at 320 K.

by Tang et al using the GROMOS45A3 and OPLS-AA forcefields for rod-like micelles [109].

The autocorrelation plots for both the spin probe and the host molecule (Figure 2.20) again clearly indicate bi-modal dynamics which can be fitted using expression 2.6. In the case of DTAC both the probe and the host show higher local order compared to SDS, reflecting the more ordered packing in DTAC, but this time with slower global motions which is particularly evident for the host liquid crystal. SDS shows slightly higher order than in the micelle at the same temperature, evident from both the correlation plot and the more regular arrangement of the hydrophobic tails visible in the geometric snapshots. This

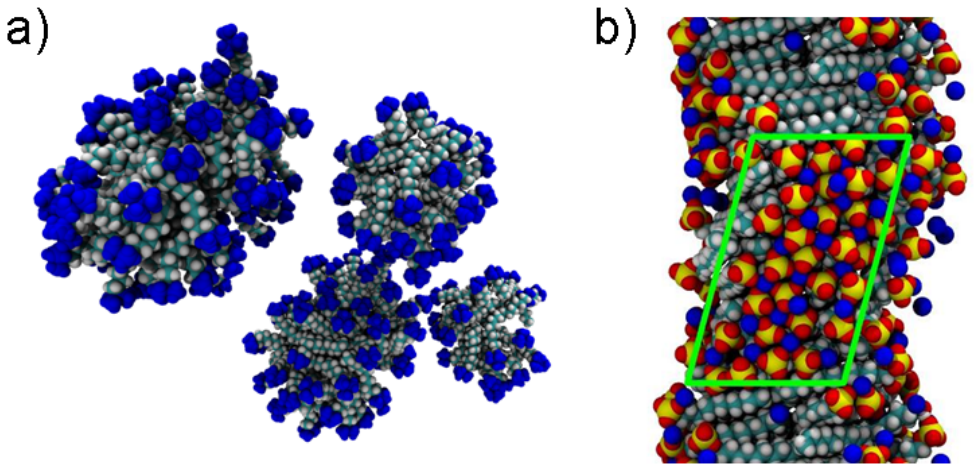

Figure 2.19: Snapshots of a) decomposition of single DTAC rod into irregularly sized micelles at 350K and b) single SDS rod at 300K highlighting crystal-like region.

difference in packing also potentially influences the observed global motion rate where the disordered SDS rods allow for a faster diffusion along the aggregate Z axis than in DTAC.

A slow transverse global motional tumbling ($D_{\perp}^{G}$) of the rods was required in both systems for adequate fits. As has been shown previously such motional contributions are too slow on the X-band EPR timescale and do not affect the EPR line shape [8]. The motional and order parameters obtained from the fitting of autocorrelation functions are summarised in Table 2.7. The adjusted order parameter for the alkyl chain of SDS has similar value to the ones corresponding to the micellar phase at 320K. The order parameter for DTAC hosts was found to be higher than in the corresponding micellar phase, due to the tighter packing of the rods, in agreement with the trend reported previously [8].

Table 2.7: Motional and order parameters of 5DSA, SDS (Top) and DTAC (Bottom) for hexagonal phases obtained from the fitting of the relevant autocorrelation functions at 320K. $D_{\perp}^{G}$, $D_{\parallel}^{G}$, $D_{\perp}^{L}$, $D_{\parallel}^{L}$ and S^{L} represent the two components of global diffusion, the two components of local diffusion and the local order parameter, respectively. 95% confidence bounds for the adjusted parameters are provided in Table A.7 of the appendices.

Molecule	$\mathbf{D}_{\perp}^{G}$ $(\mathbf{s}^{-1})$	$\mathbf{D}_{\parallel}^{G}$ $(\mathbf{s}^{-1})$	$\mathbf{D}_{\perp}^{L}$ $(\mathbf{s}^{-1})$	$\mathbf{D}_{\parallel}^{L}$ $(\mathbf{s}^{-1})$	$\mathbf{S}^{L}$
5DSA	1×10^{6}	5.91×10^{7}	1.15×10^{8}	2.08×10^{8}	0.43
SDS	1×10^{6}	6.27×10^{7}	3.75×10^{8}	11.19×10^{9}	0.50
Molecule	$\mathbf{D}_{\perp}^{G}$ $(\mathbf{s}^{-1})$	$\mathbf{D}_{\parallel}^{G}$ $(\mathbf{s}^{-1})$	$\mathbf{D}_{\perp}^{L}$ $(\mathbf{s}^{-1})$	$\mathbf{D}_{\parallel}^{L}$ $(\mathbf{s}^{-1})$	$\mathbf{S}^{L}$
5DSA	1×10^{6}	2.7×10^{7}	0.99×10^{8}	1.11×10^{8}	0.58
DTAC	1×10^{6}	3.6×10^{7}	2.73×10^{8}	10.16×10^{9}	0.61

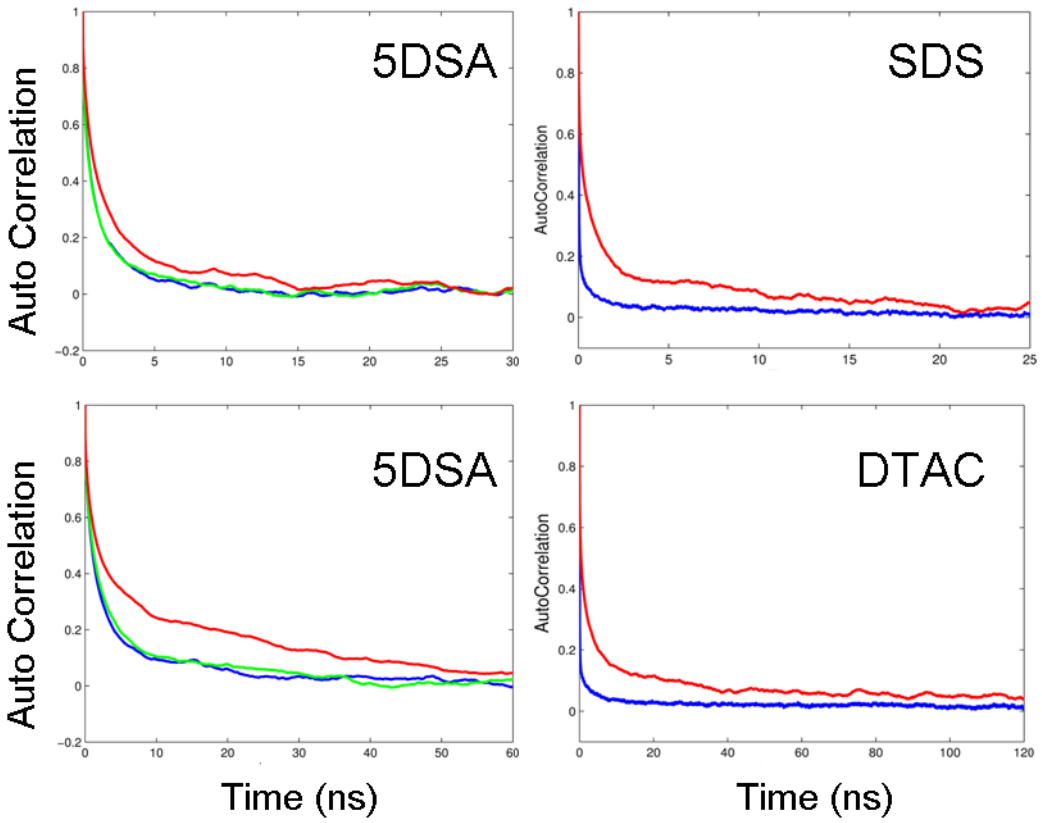

Figure 2.20: Left - Rotational autocorrelation functions of the magnetic axes X, Y and Z shown in blue, green and red, respectively, of 5DSA spin probe in SDS (top) and DTAC (bottom) hexagonal phases at 320K. Right - Rotational autocorrelation functions of SDS (top) and DTAC (bottom) surfactants XY (blue) and Z axis (red) molecular axes in micelles.

Comparison between the predicted EPR spectra of SDS and DTAC hexagonal phases at 320K (red lines) and experimental ones (blue lines) are shown in Figure 2.21, demonstrating reasonably good agreement between them. In particular, because of the overall slower and more restrained dynamics of the probe in DTAC, the simulated EPR spectra of DTAC are broader compared to SDS, in agreement with experiment. Similar to micelles, in both systems the nitroxide head group of 5DSA remains located at the aggregate surface throughout the MD simulations. As a result, the dynamics of the nitroxide group of the probe in both SDS and DTAC is predetermined by the interaction with the water molecules with relatively minor effect from the overly ordered dynamics of the alkyl chains. Some discrepancies observed between simulated and experimental EPR line shapes can

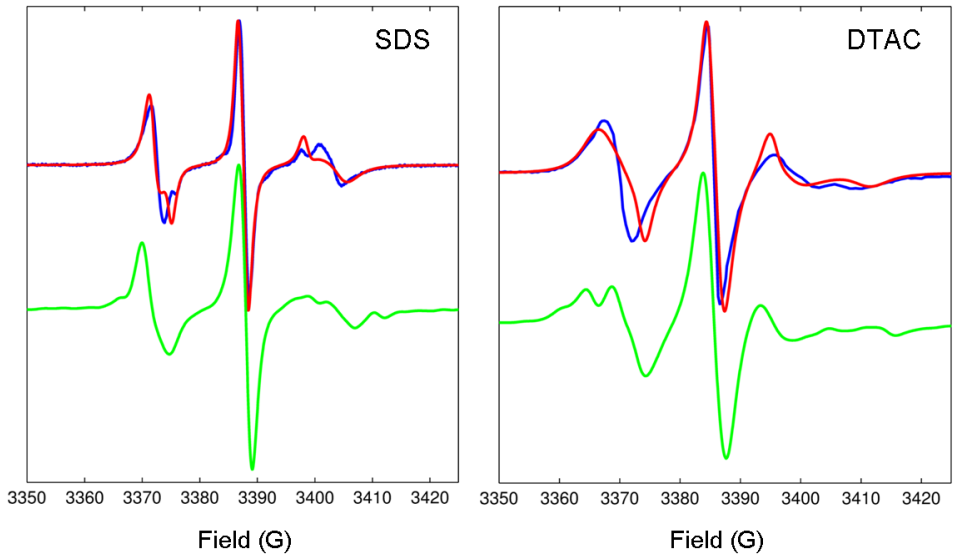

Figure 2.21: Comparison between experimental (blue) and predicted from MD (red) EPR spectra of SDS (left panel) and DTAC (right panel) hexagonal phases doped with 5DSA spin probe at 320 K. DTAC EPR experimental spectrum is reproduced with permission from Wikander et al. [8] (Copyright 1990, American Chemical Society). In each panel green lines represent the EPR line shapes predicted directly and completely from MD trajectories using the propagation approach.

be attributed to the simplicity of the simulation model employed. Previous studies have noted a number of defects [100] that could exist in rod-like aggregates but not be properly replicated in MD. The periodic boundaries used in MD runs imply rods of effectively infinite length. In fact, they are finite in length and their spherocylinder ends will provide a different contribution to the EPR spectra. The periodic nature of the rods also prevents "worm-like" distortions which could be significant in the SDS aggregates where the higher water content may allow their bending [14]. Temporary bulges were also observed in the SDS rods which could cause additional rotational contributions.

In order to check the validity of the MF approach in the simulation of EPR spectra, spectra were also predicted directly and completely from MD trajectories using the MD-EPR propagation method described in section 4.1.1. Significantly longer MD trajectories were required for an adequate simulation by the direct propagation method (see Table 2.1). Analysis clearly demonstrated the sensitivity of the simulated line shapes to their lengths. The resulting EPR spectra are shown in Figure 2.21 as green lines for both SDS and DTAC, demonstrating reasonably good agreement with both the experimental spectra and the ones predicted using the MF approach, confirming the validity of the latter.

2.4.6 Lamellar Phase

Equilibrated structures of lamellar phases of SDS (top) and DTAC (bottom) at 350K doped with 5DSA spin probes are shown in Figure 2.22. In both cases, because of the very low water content (30% wt in SDS and 10% wt in DTAC), two lamellae were used in all MD simulations in order to prevent direct interaction of the bilayer with its image in the simulation box. Considerable structural differences were observed between the lamellar phases of the two surfactants, with SDS showing a more prominent curvature of the surface resulting from the higher water content. Due to close molecular packing, repulsion between head groups of SDS causes a vertical translational motion. As a result the molecules remain well

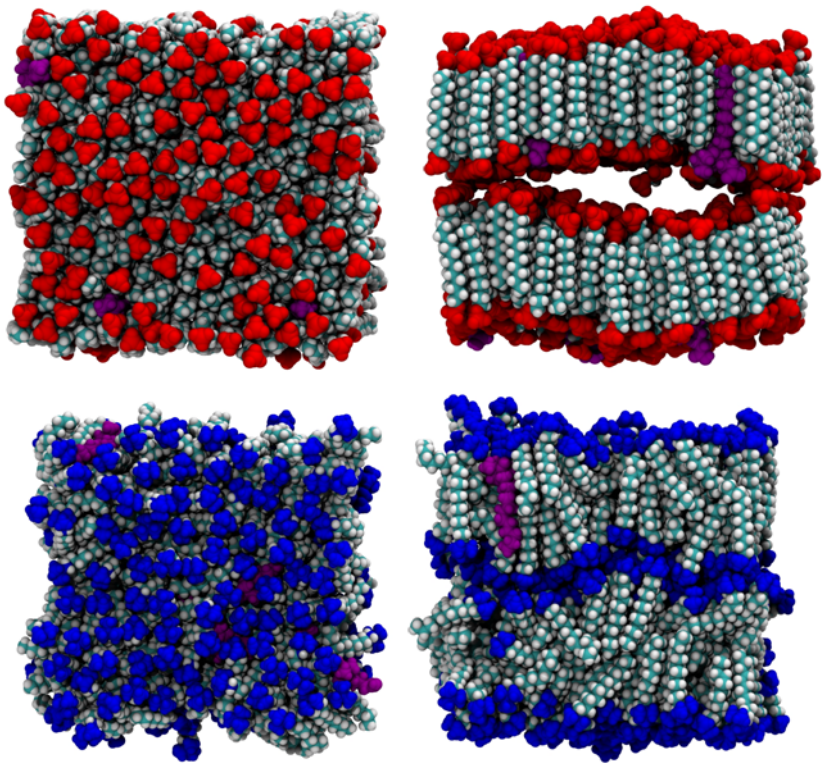

Figure 2.22: Equilibrated structures of SDS (top) and DTAC (bottom) in lamellar phases at 350K doped with 5DSA spin probe (purple).

aligned over these ripples. Because of the efficient packing of the molecules, the lamellae thickness of 1.9 nm, calculated as the distance from sulphur to sulphur, exceeds only slightly the all-trans molecular length of ≈ 1.68 nm, calculated as the distance between terminal carbon to sulphur. When the thickness of the water layer is included, the approximate value of the unit cell length calculated from MD (3.3 nm) is in perfect agreement with the one measured experimentally using neutron scattering (≈3.3 nm) [106]. The calculated area per head group in SDS (0.40 nm^2 (Figure 2.23a)) also shows perfect agreement with the experimentally determined one using X-ray scattering (0.40 nm^2) [148] and indicates that the structure is stable over the entire MD production run. The backbones of the probes remain located in the interior of the SDS lamellae, with the head groups exposed to water at the surface.

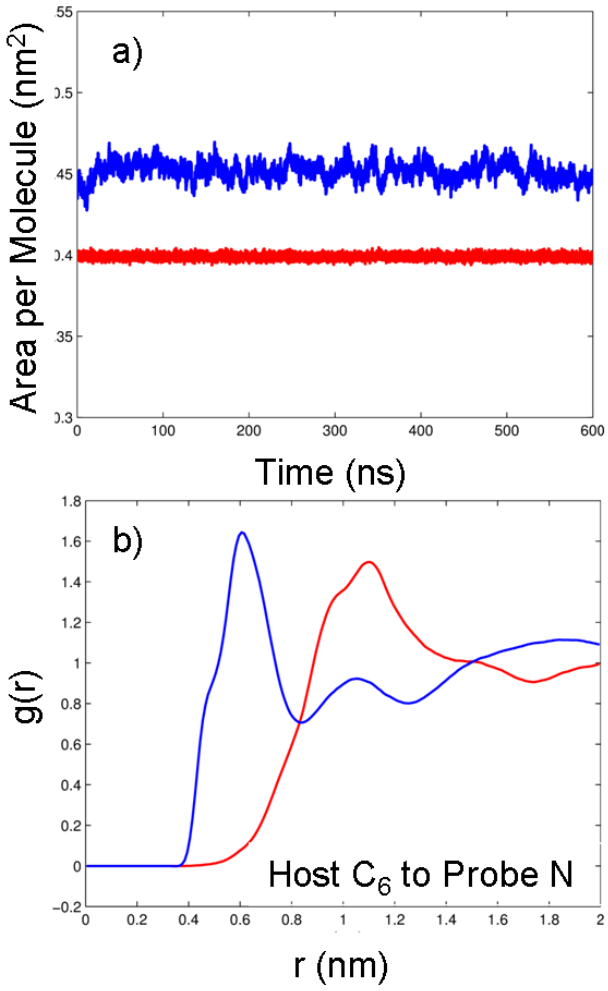

Figure 2.23: a) Time evolution of the area per molecule and b) radial distribution functions calculated as the distance between the mid carbon of surfactant (position C6) and the nitrogen of 5DSA spin probe for SDS (red) and DTAC (blue) lamellae at 350K.

In contrast, in the DTAC lamellar phase, although there is less surface curvature, the interior appears to be more disordered compared to the SDS case, as seen in Figure 2.22. The area per molecule (0.45 nm^2), shown as the blue line in Figure 2.23a, is characterised by significantly wider fluctuations compared to the SDS lamellae, again being consistent with a more disordered structure, although experimental data for this is not available for comparison. It is interesting to note that during the simulation a narrow pore structure formed in one of the DTAC lamellae (shown in Figure 2.24a) with a small degree of water penetration, both attributed to the high level of disorder in the alkyl chains. The packing arrangement was similar to that commonly observed for lipid bilayers with upper and lower leaflets, resulting in a thickness of $\sim$ 2.2 nm calculated as the distance between the head nitrogens. This is significantly greater than that of the all-trans molecular length of 1.54 nm calculated between the terminal carbon and nitrogen. Because of the thinner water layer in DTAC the two lamellae are in close contact with each other allowing the probe to drift between them as shown in Figure 2.24b. As a result 5DSA in DTAC experiences a significantly different environment to that of SDS lamellae and other phases with the nitroxide

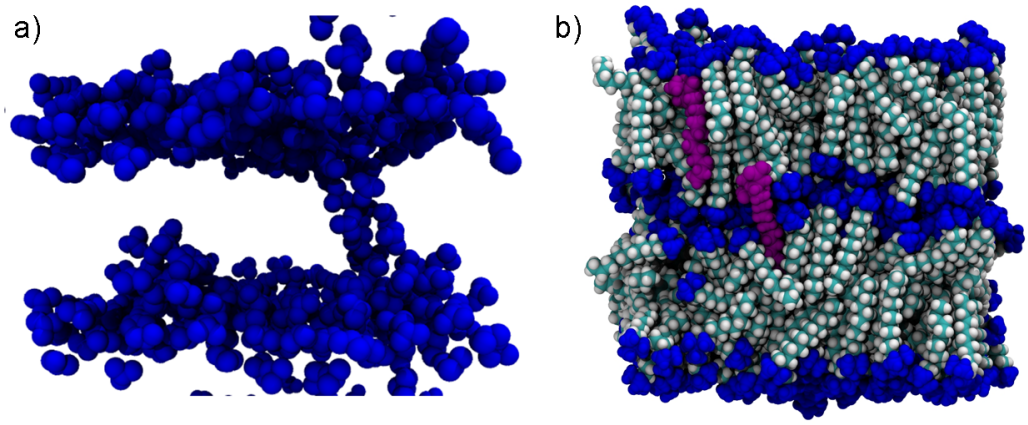

Figure 2.24: DTAC lamellar phase highlighting the structure of the pore (a) and the 5DSA probe drifting between layers (b).

group penetrating deep into the hydrophobic interior. This is confirmed by the calculated radial distribution functions shown in Figure 2.23b where the average distance between the mid-chain alkyl carbon on the host molecule and the nitroxide head group of the probe is found to be approximately twice as low as in the DTAC lamellae (0.6 nm) compared with the SDS lamellae (1.1 nm).

In order to check the size consistency of the simulated models, additional MD simulations were also performed for extended systems (3 lamellae in a larger simulation box) for both SDS and DTAC. The values of the calculated geometric parameters, namely the area per head group and thickness, were totally consistent with the ones obtained with 2 lamellae in the box, although sufficiently longer simulation times were required.

Because of slow global motions of the probe in these phases, long trajectories were required to resolve the dynamics and extract the motional and order parameters from the autocorrelation plots, even with multiple probes employed. The autocorrelation functions for the probes and host molecules in lamellar phases are shown in Figure 2.25. Dynamical and order parameters obtained from the fitting of the autocorrelation functions using the equation 2.7 are summarized in Table 2.8. In particular, for the SDS lamellae the global motional component is highly restrained for both 5DSA and SDS molecules. Also, there is a significant difference in the ordering between the probe and the host molecules in the SDS system, resulting in a much higher effective order parameter ($S^{Eff} = S^G S^L$) observed for the host compared to the probe. This is attributed to a more flexible position of the nitroxide head group at the surface. In contrast, in the DTAC lamellar phase both 5DSA and DTAC molecules are able to tilt during the motions resulting in significantly reduced effective order parameters for both.

The apparent ratio between the order parameters for the X/Y and Z axes of the liquid crystal hosts in both SDS and DTAC lamellae are consistent with the one predicted from the associated MF expression 2.7 i.e. $(S_X^{Eff} Y / S_Z^{Eff})^2 = 1/4$. The same ratio is observed for 5DSA, although the effect from the limited number

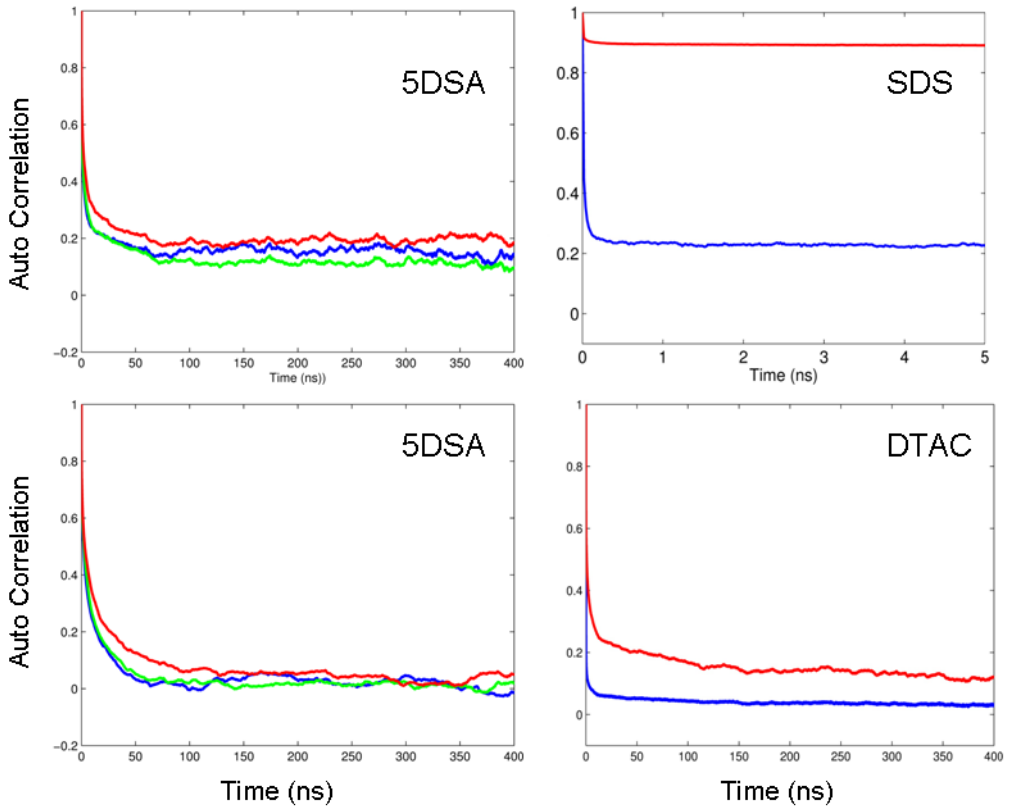

Figure 2.25: Left - Rotational autocorrelation functions of the magnetic axes X, Y and Z shown in blue, green and red respectively for 5DSA spin probe in SDS (top) and DTAC (bottom) in the lamellar phase at 350 K. Right - Rotational autocorrelation functions of SDS (top) and DTAC (bottom) surfactants XY (blue) and Z axis (red) molecular axes in the lamellar phase.

of 5DSA spin probes employed resulted in wider statistical fluctuations in the correlation functions at longer times, making this ratio less apparent, particularly in the case of DTAC lamellae.

Comparison between spectra predicted from MD using the MF approach and experimental EPR spectra for SDS and DTAC lamellar phases is shown in Figure 2.26. A reasonably good agreement is observed between the simulated and experimental spectra in the case of the SDS lamellae shown in Figure 2.26 (left) as red and blue lines respectively. The value of homogeneous line broadening was

Table 2.8: Motional and order parameters of 5DSA, SDS (Top) and DTAC (Bottom) for lamellar phases obtained from the fitting of the relevant autocorrelation functions at 350K. [a] $D_{\perp}^{G}$, S^{G} and $D_{\perp}^{L}$, S^{L} represent relevant rotation diffusion components and order parameters of global and local motions respectively. 95% confidence bounds for the adjusted parameters are provided in Table A.8 of the appendices. [b] $D_{\parallel}^{Eff}$ is the effective axial diffusion rate defined as: $D_{\parallel}^{Eff} = D_{\parallel}^{G} + D_{\parallel}^{L}$ (see equation 2.7).

Molecule	$\mathbf{D}_{\perp}^{G}$ ($\mathbf{s}^{-1}$)	$\mathbf{S}^{G}$ ($\mathbf{s}^{-1}$)	$\mathbf{D}_{\perp}^{L}$ ($\mathbf{s}^{-1}$)	$\mathbf{S}^{L}$ ($\mathbf{s}^{-1}$)[a]	$\mathbf{S}^{Eff}$	$\mathbf{D}_{\parallel}^{Eff}$[b]
5DSA	3.57×10^{6}	0.74	1.19×10^{8}	0.59	0.44	1.7×10^{6}
SDS	1.17×10^{7}	0.99	2.82×10^{8}	0.95	0.95	10.5×10^{9}

Molecule	$\mathbf{D}_{\perp}^{G}$ ($\mathbf{s}^{-1}$)	$\mathbf{S}^{G}$ ($\mathbf{s}^{-1}$)	$\mathbf{D}_{\perp}^{L}$ ($\mathbf{s}^{-1}$)	$\mathbf{S}^{L}$ ($\mathbf{s}^{-1}$)	$\mathbf{S}^{Eff}$	$\mathbf{D}_{\parallel}^{Eff}$
5DSA	4.69×10^{6}	0.38	9.34×10^{7}	0.68	0.24	1.3×10^{6}
DTAC	1.01×10^{6}	0.69	9.29×10^{7}	0.51	0.36	12.5×10^{9}

taken from [14] without further adjustment. The situation is principally different for DTAC lamellae where there is a clear disagreement between the predicted and experimental spectra. The simulated EPR line shape represented in Figure 2.26 (right) by the red line is significantly broader compared to the experimental one (blue line). In order to check the validity of the MF based simulation approach, EPR spectra were also simulated directly from MD trajectories using the propagation approach and are presented for comparison in Figure 2.26 as green lines for both SDS and DTAC lamellae. As in the case of hexagonal phases, significantly longer MD trajectories were required ($<\approx$ 900 ns) for this method. In both cases, for SDS and DTAC, the line shapes predicted directly from MD trajectories are broadly in agreement with the ones predicted by the simulation parameters extracted from MD data using the MF approach. Therefore, the MF approach remains valid in the case of the lamellar phase. The disagreement of the simulated EPR line shapes with the experimental ones for DTAC is attributed to the fact

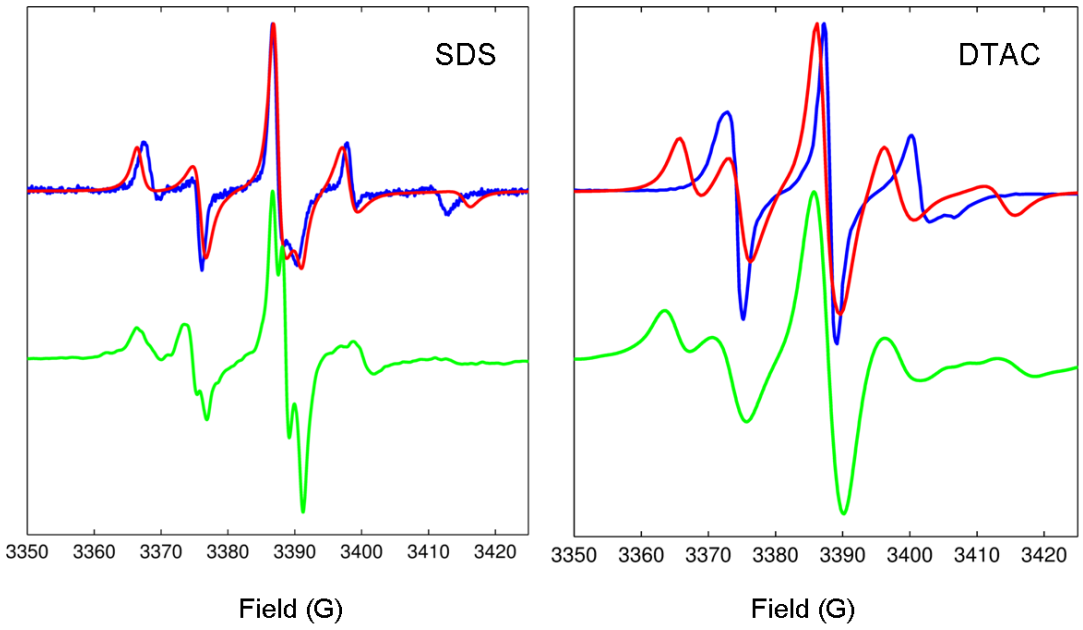

Figure 2.26: Comparison between experimental (blue) and predicted from MD (red) EPR spectra of SDS (left panel) and DTAC (right panel) lamellar phases doped with 5DSA at 350K. DTAC EPR experimental spectrum is reproduced with permission from Wikander et al. [8] (Copyright 1990, American Chemical Society). In each panel the green lines represent the EPR line shapes predicted directly and completely from MD trajectories using the propagation approach.

that the nitroxide head group of the probe in the DTAC lamellar phase, contrary to other DTAC phases and also SDS lamellae, spends a significant amount of time within the environment of the alkyl carbon chains. As a result, the packing of the carbon chains, which is overestimated by the GAFF model, also increases the order of the probe, resulting in the broadening of the respective EPR spectra. This effect is less pronounced in the case of SDS lamellae where the nitroxide head group remains positioned predominantly at the surface-water interface.

2.5 Conclusion

In this chapter the first simulation of CW EPR spectra of lyotropic liquid crystals at different aggregate states from the results of MD modelling has been performed. The simulations have been achieved by solving the SLE in the Fokker-Planck form that employs the rotational diffusional operator describing the stochastic motion of the probe. The parameters describing such motion in different lyotropic aggregates are extracted from MD trajectories using the MF approach. The purpose of this work was two-fold. Firstly, simulation of EPR line shapes from the results of MD modelling and comparing them to experiment provided an ultimate test bed for the forcefields currently employed to model such systems. Secondly, and of equal importance, such a combined MD-EPR methodology tests the validity of the application of the MF approach that is widely used to interpret spectroscopic data for surfactant/water systems. These results demonstrated perfect agreement between predicted and experimental EPR spectra for both microaggregate and micellar phases of SDS and DTAC liquid crystals. A good agreement has been achieved for hexagonal phases of SDS and DTAC and also for the lamellar phase of SDS. In hexagonal and lamellar phases of both SDS and DTAC, EPR simulations using the MF approach were broadly in agreement with the simulations of the EPR spectra from MD trajectories using the direct propagation approach, thus confirming the validity of the MF approach for the reported systems. For hexagonal phases some discrepancies observed in the EPR spectra simulated by both SLE-FP and propagation methods were attributed to additional effects, e.g. "worm-like" distortions and finite rod shapes, not accounted for in the MD simulation model. The disagreement between the simulated and experimental EPR spectra for the DTAC lamellar phase is attributed to the overestimation by GAFF of the packing and order of the carbon alkyl chains of the host lyotropics. In DTAC lamellae the nitroxide head group of the probe penetrates deep inside the environment of the carbon chains, resulting in its increased motional restraint

and consequent broadening of the EPR spectrum.

Finally, it is important to note that simulation parameters estimated by the fitting of autocorrelation curves generated from MD trajectories using the MF approach usually require much shorter trajectory lengths compared to the ones used in the direct propagation methods. Thus, in many cases EPR simulations from MD autocorrelation functions combined with the MF approach would be advantageous compared to direct propagation techniques.

Chapter 3

Prediction of Spin Labelled DNA Slow Motion EPR Spectra

The contents of this chapter and further developments (see Chapter 6) are currently in preparation for publication in collaboration with L. Danilane and V. S. Oganesyan.

3.1 Introduction

The internal dynamics and conformational flexibility of DNA are both known to be crucial to its biological functions including interaction with proteins and expression of genetic code [149][150]. Due to the semi-flexible nature of DNA this dynamic regime includes multiple contributions from breathing, bending and twisting modes, as well as groove fluctuations of the helix, making analysis a non-trivial matter and as such has been the subject of extensive studies. Experimental techniques including nuclear magnetic resonance (NMR)[67], fluorescence [151], dynamic light scattering [67] and Fourier transform infrared difference spectroscopy [152] amongst many others, have been utilised to probe these different motional components experimentally. EPR has also proven particularly convenient due to the intrinsic timescale of the technique overlapping with these

motions, coupled with a high sensitivity [9][10][17][26][25][153]. Furthermore, due to recent advances in click chemistry, an increasingly wide range of spin labels are being developed, allowing greater sequence selectivity [154]. However, the need to introduce a synthetic spin label with its own dynamics, combined with the potential to influence the local DNA structure could result in artefacts which may not be apparent from spectra alone. Additionally for short-chain DNA, global tumbling motions are also significant at the EPR timescale, thus requiring sophisticated spectral modelling to interpret results [26][153]. In the case of nitroxide labels attached via flexible tethers this typically requires multi-frequency measurements and fitting using the SRLS model [17] with global tumbling rates based on hydrodynamic theory [66][155].

An alternative approach to this is to use rigid spin labels such as the quinolonyl

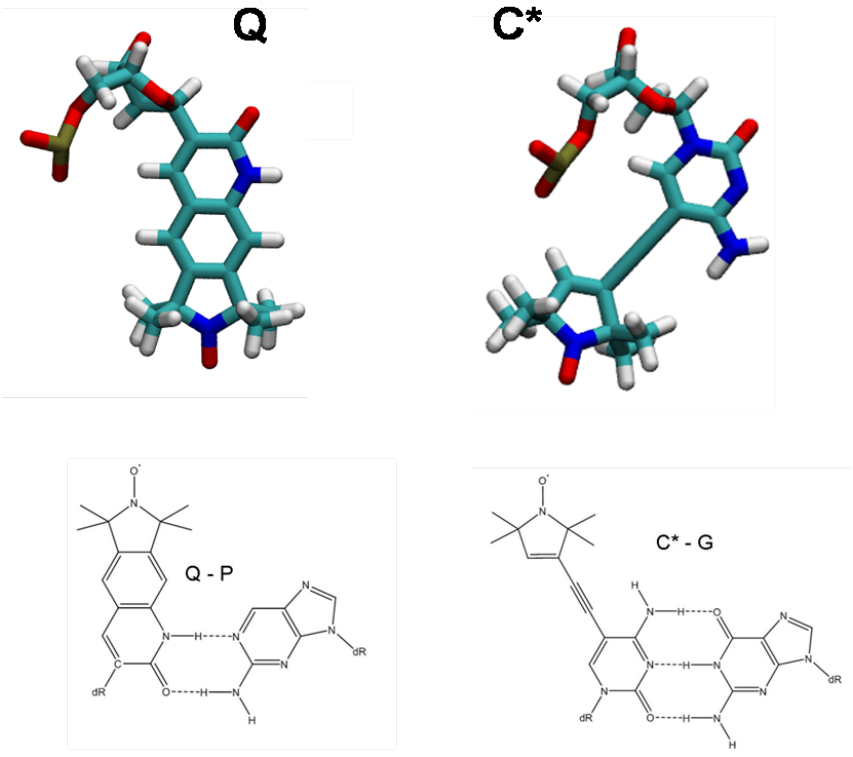

Figure 3.1: Structures of spin labels Q and C (top) and their associated base pairs in duplex DNA (bottom)*

derived Q [9] and alkyne tethered cystosine derived spin label C* [10] (Figure 3.1) developed by Robinson and co-workers to minimise the local motions of the label. This allows the labels to report more directly on the motions of the host DNA, with spectra typically interpreted through either assuming diffusion of a rigid cylinder [9] or weakly bending rods [153]. The Q label in particular is thought to exhibit negligible independent motion as well as being highly thermally stable. However it requires a synthetic 2-aminopurinyl complementary base pair (P), with the effect on the local dynamics and structure unclear from EPR alone [9].

C* is typical of alkyne-linked spin labels using modified conventional base pairs and thus is known to be less structurally perturbing [9][26][11]. Although such labels have been demonstrated to be highly sensitive to duplex length, they also exhibit rotation about the alkyne linkage leading to potentially compromised structural and dynamic information [26]. Spectra of the related thymine derived spin label T* have therefore been fitted with a simplified model which assumes that fast axial local motion ($\tau^L < 1$ns [26]) partially averages the magnetic parameters [156]. However Robinson and co-workers found that T* and double alkyne bridged T** had different internal mobilities, indicating that the location of the nitroxide group in the major groove hinders local motions for single alkyne bridged labels in duplex DNA [26]. In both cases, the local motional rate remained inaccessible.

Fully atomistic MD simulations have already provided significant insights into the sequence-dependent flexibility of DNA [157][158]. Furthermore it is becoming increasingly apparent that sequences can adopt a wide variety of conformations, depending on the chemical environment, and that therefore the structure of DNA should be considered in terms of conformational ensembles [69][159]. In this respect however, studies have been hindered by trajectory length with many helix properties requiring hundreds of nanoseconds of equilibration to fully converge [69]. Advances in computing power and refined forcefields, such as the recently parametrised parmbsc1 [95], have meant that reliable conformational behaviour

in trajectories of up to 10 μs are now obtainable for short-chain DNA [159][160]. Additionally it has recently been shown by Cheatham and co-workers that for undamaged Watson-Crick base paired DNA, motions in the 100 ns to 1 ms timescale are absent [69]. As such, the motional behaviour probed by X-band EPR should now be accessible using fully atomistic MD, allowing direct prediction of spectra to not only provide a thorough test of the forcefields, but also greater insight into the contributing factors to the EPR spectra.

3.2 Computational Methods

3.2.1 Calculation of Magnetic Parameters

Magnetic parameters for Q and C* spin labels were calculated using the method outlined in section 2.2.2 for 5DSA in solvent.

3.2.2 Details of Molecular Dynamics Modelling

Initial 14-mer DNA configurations were constructed using the w3DNA web server [161]. Conventional base pairs were described using the new parmbsc1 forcefield [95] with spin labels supplemented by additional parameters derived by DFT and from v1.5 of the General AMBER forcefield (GAFF) [93]. Rotation about the triple bond in the C* spin label was regulated using dummy atoms to introduce additional dihedral terms. Partial charges for spin labels were calculated using a multi-conformational Restrained Electrostatic Potential (RESP) [162] fit at the HF/6-31G* level of theory. The SPC/E water model [129] was used with Smith-Dang ion parameters for sodium counterions [163] with systems compositions given in Table 3.1. All MD calculations were performed using the AMBER 14 [164] software package. An NPT ensemble was maintained at a pressure of 1 atm using the Berendsen [165] algorithm with a coupling constant of 5 ps. The SHAKE algorithm [128] was used to maintain hydrogen bond lengths. Centre of

Table 3.1: DNA sequences and system size used in the MD simulations reported in this work.

Sequence	**Number of water molecules**
[5-d(GCC-TAC-ATG-**Q**GA-CG)-5-d(CGT-C**P**C-ATG-TAG-GC)]	6780
[5-d(GCC-TAC-ATG-**C***GA-CG)-5-d(CG-TCG-CAT-GTA-GGC)]	7000
[5-d(GCT-TAA-GCT-**Q**CG-CG]	6370
[5-d(GCC-TAC-ATG-**C***GA-CG]	6450

mass motion was removed every 20 ps to limit build-up of translational kinetic energy, allowing for a time step of 2 fs to be used. Long range electrostatic interactions were accounted for using the Particle Mesh Ewald method [97] with a cut-off of 10 Å. Systems were equilibrated for 700 ns prior to production runs of 700 ns. DNA conformational analysis was performed using w3DNA [161].

3.2.3 Parameterisation of Acetylene Tethered Spin Labels

DFT scans of the acetylene bond torsional energy at the B3LYP/6-311g(d,p) level of theory, shown by the green line in Figure 3.2a, confirmed that rotation about the acetylene group in C* is partially restrained [26]. In order to replicate this in MD, dummy atoms without non-bonded interactions were introduced to the acetylene bond as indicated in Figure 3.2b by atom type "du". Angle force constants for the inner C≡C-Du angle were taken from a C-C-H bend from GAFF, with the outer C-C-H angle being given a force constant of zero to avoid any stiffening of the C-C≡C bending [93]. Stiff torsional terms were used to maintain the position of the dummy atoms relative to the cytosine base ring shown by yellow lines in Figure 3.2b. The remaining torsional terms linking the dummy

atoms to the nitroxide-bearing ring (Figure 3.2b orange lines) were then fitted to reproduce the energy profile calculated by DFT (Figure 3.2a, blue line). Two short trajectories of the C* probe in SPC/E water confirmed the effect of the dummy atom potential, with the dummy atom scheme favouring the expected planar conformations compared with the random distribution observed without the potential (Figure 3.2c).

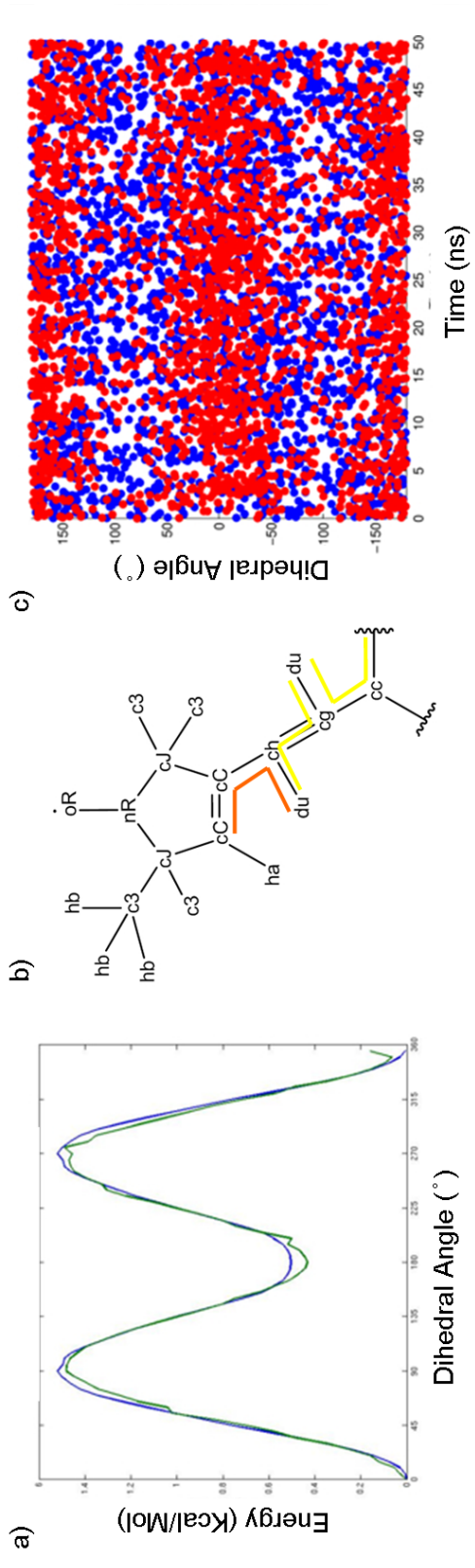

Figure 3.2: a) Comparison between torsional energy profiles calculated by DFT at the B3LYP/6-311g(d,p) level of theory (green) and MD (blue) for dihedral angle shown in orange in b). b) Atom types used in parametrisation of C spin label. Yellow lines indicate torsional terms that were fixed. c) Inter-plane torsional angle with (red) and without (blue) dummy atom torsional restraints over 50 ns for probe in water MD trajectory.*

3.2.4 Autocorrelation Functions

The local motional component was isolated using a mass-weighted RMS structural fit with the Ptraj module of AmberTools [166] to remove global tumbling (Figure 3.3). The global motion was approximated by the dynamics of the principal axes of the moment of inertia. As the x/y principal components are poorly defined, due to the effectively cylindrical shape of DNA, this was estimated by projecting the vector between the C1' atoms of two complementary base pairs onto the plane perpendicular to the principle z axis to prevent inversion and jumps. The autocorrelation function for the local diffusion was fitted with a weighted three component exponential function (Equation 3.1):

$$C^L(t) = w_1 e^{-\frac{t}{\tau_1}} + w_2 e^{-\frac{t}{\tau_2}} + w_3 e^{-\frac{t}{\tau_3}} + S_L^2 \tag{3.1}$$

where w_i are the weighting factors for motional components with correlation times of τ_i. The effective local correlation time, τ^{Eff}, is then calculated using normalised weights via (3.2):

$$\tau^{Eff} = w_1\tau_1 + w_2\tau_2 + w_3\tau_3 \tag{3.2}$$

The global diffusion was fitted with the expression for simple rod-like diffusion (Equation 2.4) used in Chapter 2.

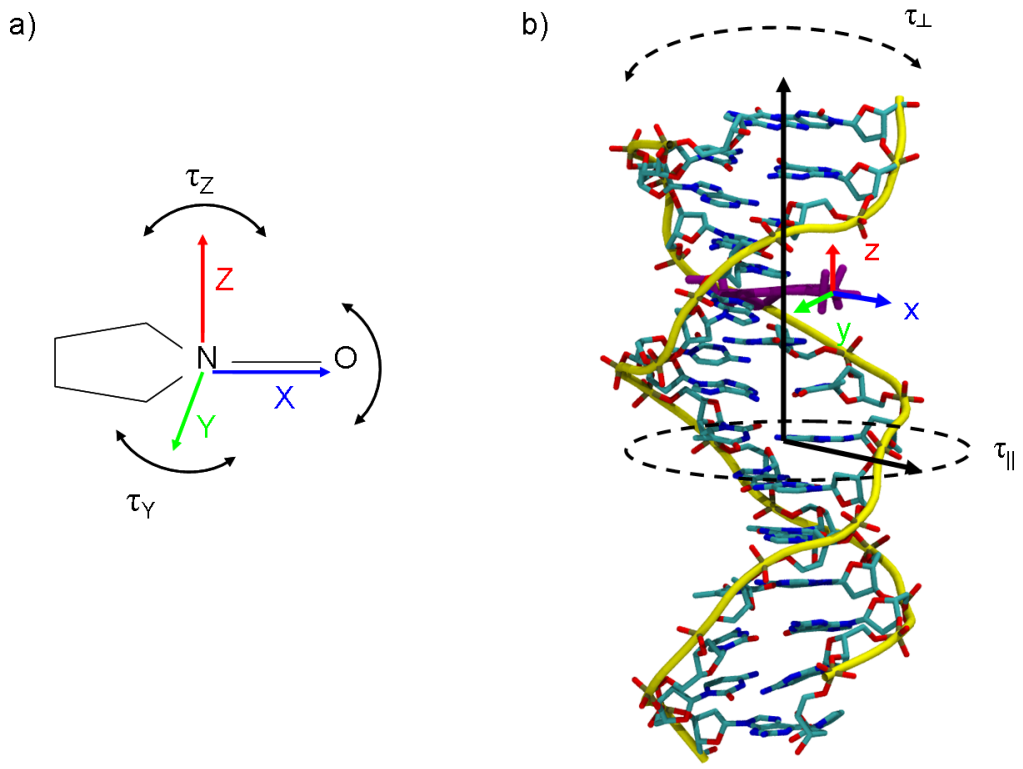

Figure 3.3: a) Magnetic axes X (blue), Y (green) and Z (red) of nitroxide label and relation to local motions τ_x, τ_y and τ_z, b) Principal global axes of DNA and relation to global motions $\tau_\perp$ and $\tau_\parallel$.

3.2.5 EPR Modelling

Spectra were predicted directly from MD using the propagation method outlined in Section 1.1.2.

3.3 Results and Discussion

3.3.1 DFT

Calculation of Magnetic Parameters

Previous experimental studies of alkyne tethered labels have determined g and A tensors from spectral fitting of diethylaminoethyl-Sephadex bound spin labelled

DNA, however the effects of the binding agent on the local motions of DNA and the contribution of partial averaging due to rotation about the alkyne tether has lead to discrepancies in these values compared with Q [10][11][26]. DFT calculated values (Table 3.2) indicate that the magnetic parameters of C* are in fact very close to those of Q, which are in good agreement with previous studies [9] as well as those calculated for 5DSA in Section 2.4.1.

Table 3.2: Magnetic parameters calculated using B3LYP/N07D with water solvent. Hyperfine coupling constants are reported in Gauss.

Label	$\mathbf{g}_{xx}$	$\mathbf{g}_{yy}$	$\mathbf{g}_{zz}$	$\mathbf{A}_{xx}$	$\mathbf{A}_{yy}$	$\mathbf{A}_{zz}$
Q	2.0087	2.0061	2.0021	6.18	6.29	33.60
C*	2.0078	2.0069	2.0021	6.16	6.27	33.77

3.3.2 Molecular Dynamics

Effect of Spin Label on Duplex DNA Structure

Both spin labels Q and C* were found to remain base-stacked between the natural bases within duplex DNA for the entire trajectories. The calculated RMSD of the DNA backbone with terminal base pairs removed (C* 1.72 Å, Q 2.16 Å) show values in agreement with those typically reported for B-DNA (1.6-2.2 Å) [159]. The small fluctuations ($< \pm$ 1.5 Å) without any long lasting deviations observed for this parameter, shown in Figure 3.4, confirms the structural stability of both labelled duplexes over the course of the production trajectory [69].

As the C* label is a modified cytosine base, helical base pair step geometric parameters, as defined in Figure B.1 of the appendices, were calculated using the W3DNA web server [161] in order to compare with the corresponding unlabelled sequence (Table 3.3). Good agreement between the twist, roll, slide and rise is observed between the average structures for labelled and unlabelled sequences, denoted by red and blue lines respectively in Figure 3.5. The shift and tilt of the

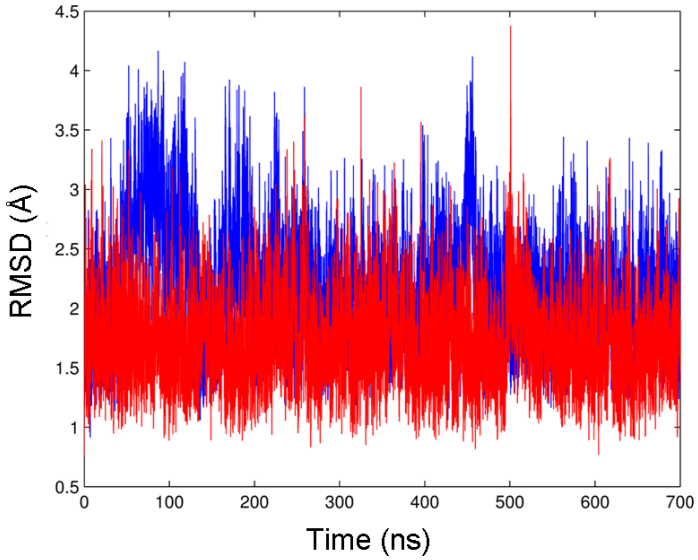

Figure 3.4: RMSD with terminal base pairs removed for Q (blue) and C (red) labelled duplex DNA at 293K.*

average structures display less good agreement, however in each case the geometry of selected random frames, denoted by square markers, shows this to be within the expected deviation of the structure due to dynamic effects. Sugar pucker angles (phase) [167], which are closely related to the backbone conformation, are within 1° difference between unlabelled and labelled sequences. Additionally, the average amplitude (Amp) values are within the range of 25°- 45°, as observed for standard B-DNA structures [167]. The combination of these parameters and the backbone RMSD unambiguously confirms that the C* label has negligible perturbing effects on the geometry and flexibility of the host sequence, as previously suggested by experimental studies [26]. As the Q probe and complementary base pair P have no natural equivalent, these parameters are not presented for this system.

Table 3.3: Sequence average conformational parameters (Figure B.1) obtained from full trajectories for the unlabelled C and C labelled base/pair in duplex DNA at 293K. Angles are reported in degrees and distances are reported in Angstroms.*

Parameter	**Unlabelled**	**C* Labelled**
Shear	-0.11	0.46
Stretch	-0.15	-0.56
Stagger	0.06	-0.33
Buckle	2.56	6.94
Propeller	-5.88	-1.33
Opening	-0.29	0.10
Shift	0.60	1.25
Slide	0.00	0.42
Rise	3.17	3.27
Tilt	3.59	6.54
Roll	3.29	9.36
Twist	31.74	31.68
Phase	143.7	144.3
Amp	41.0	43.2
α	-70.1	-72.9
β	168.2	169.4
γ	55.4	53.5
δ	133.7	137.1
ϵ	-140.2	-127.8
ζ	-143.8	-173.4
χ	-104.0	-97.0

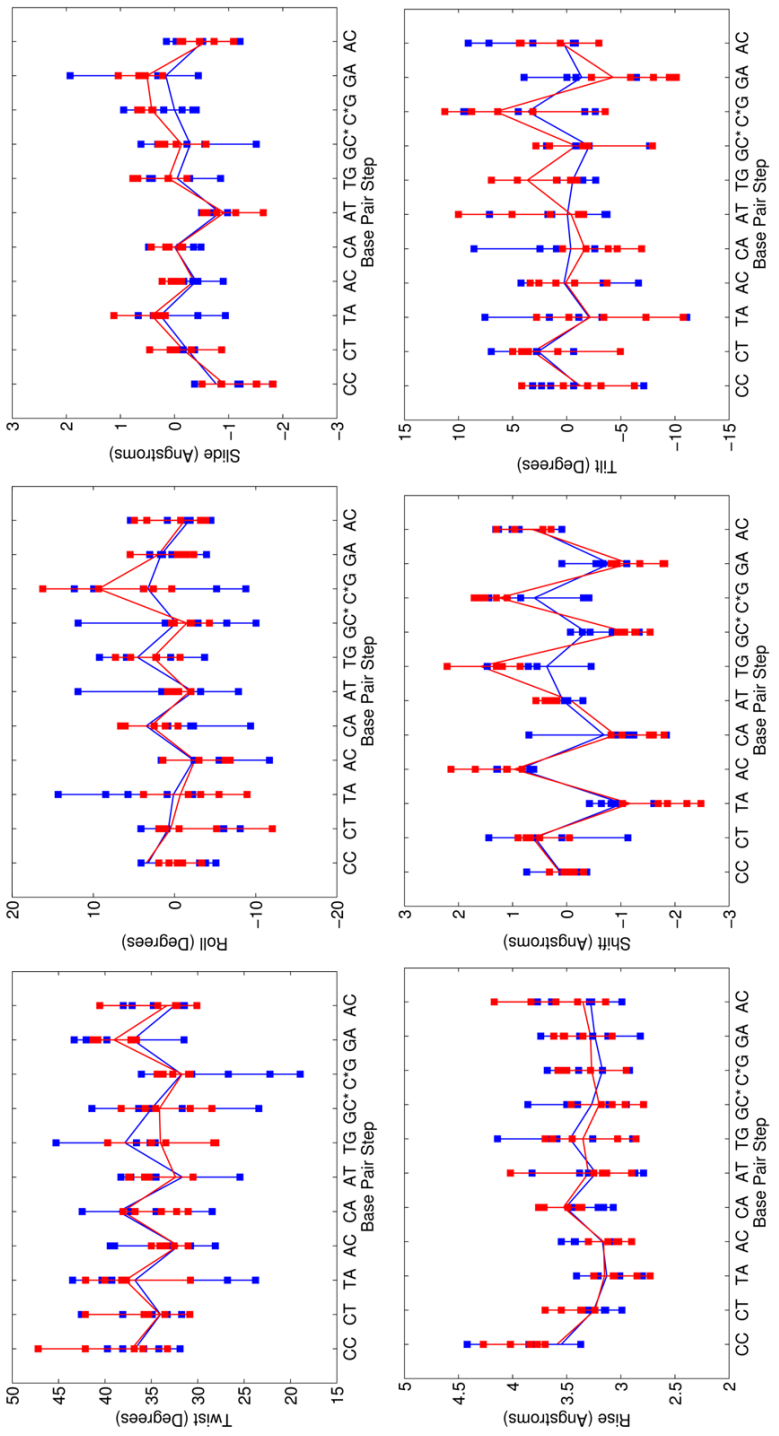

Figure 3.5: Average base pair step helical parameters as defined in Figure B.1 for standard (blue) and spin labelled (red) [5-d(GCC-TAC-ATG-C(/C)GA-CG)-5-d(CG-TCG-CAT-GTA-GGC)] duplex DNA at 293K. Error bars determined from the structure of five randomly selected frames. Terminal base pairs were excluded from the analysis.*

Dynamics of Spin Labelled Duplex DNA

The autocorrelation functions calculated from the MD trajectory of the Q label magnetic axes demonstrate a complex multi-component form (Figure 3.6a) which can be deconvoluted through structural fitting. By excluding the global tumbling of DNA through an RMS fit the local motion can be isolated to show an anisotropic form (Figure 3.6b). Due to the rigidity of Q, the local motion of the magnetic axes all demonstrate a high degree of order in duplex DNA. The y axis is found to exhibit the greatest local order as the majority of local motion arises from tilting about this axis, resulting in wider rotations of the x and z axes. A less pronounced twisting motion about x causes rotation of y and z. The z axis exhibits the lowest order, being affected by rotation of both x and y. Fitting of the local component requires a minimum of three exponential functions (Equation 3.1), with components on the $\approx$ 10 ps, $\approx$ 100 ps and $\approx$ 1 ns timescales (Table B.4 of the appendices), with the effective correlation times given in Table 3.4. This complexity prevents the use of the model-free analysis of the autocorrelation functions utilised in Chapter 2 for surfactant/water systems which assume that the local motion can be approximated using simple diffusion models of a particular symmetry.

As the local motions are highly restrained ($S^L > 0.9$), the autocorrelation functions for the principal axes of the entire duplex (Figure 3.6c) closely resemble that of the magnetic axes with full motional contributions (Figure 3.6a), confirming that the dynamics of Q in duplex DNA can be well approximated considering only global motion [9]. Fitting of the principal axes with an axial expression (Equation 2.4) yields the correlation times for global diffusion $\tau_\perp$ and $\tau_\parallel$ given in Table 3.4. Notably, as would be expected for a 14-mer, where the long cylinder axis is roughly twice the length of the short axis [26], $\tau_\perp \approx 2\tau_\parallel$. Both components of the global motion are approximately 1.5 times faster than those reported by Okonogi et al ($\tau_\perp = 9.89$ ns $\tau_\parallel = 4.43$ ns) [25] using the hydrodynamic theory of Tirado and de la Torre for duplex DNA of this size [66][155].

Table 3.4: Fitted motional parameters of spin labelled duplex DNA. $\tau_\perp$ and $\tau_\parallel$ represent the correlation times of the axial components of global diffusion. τ_x , τ_y ,τ_z ,S_x , S_y and S_z represent the effective correlation times and order parameters for the local motion calculated using Equation 3.2. All correlation times are reported in nanoseconds. 95% confidence bounds for all parameters are provided in Tables B.4 and B.5 of the appendices.

Label	**Temp (K)**	$\tau_\perp$	$\tau_\parallel$	τ_x	τ_y	τ_z	S_x	S_y	S_z
Q	293	6.21	2.99	0.22	0.27	0.19	0.91	0.96	0.90
C*	273	13.10	5.23	0.30	0.23	0.12	0.80	0.68	0.65
	293	7.02	2.88	0.25	0.21	0.13	0.78	0.66	0.64

The principal difference is that the hydrodynamic theory treats DNA as a rigid rod [66], whereas in this analysis a degree of DNA flexibility is afforded by the all-atom MD in the global motional rates. The value of $\tau_\perp$ (6.21 ns) is close to that reported by Miller et al using an isotropic fitting model (τ_{Iso} = 7.6 ns) [9].

The predicted EPR spectrum (Figure 3.7) is found to be in good agreement with the experimental spectrum reported by Miller et al [9] confirming the accuracy of the MD model over this timescale. Additionally, the line shape predicted by the propagation method (red line Figure 3.7) is found to show excellent agreement with that simulated using the SLE and the parameters extracted for global motion (green line Figure 3.7) in Table 3.4, further confirming that Q accurately reports on the tumbling of duplex DNA. This suggests that the flexibility of DNA included in the fully atomistic MD model, as opposed to treatment as a rigid body, is necessary in order to accurately reflect the global motions of duplex DNA. Previous simulations of protein rotational diffusion have shown that trajectories of up to 100 times the global tumbling rate are required for accurate determination of this parameter from MD [98], however some slight dependence

of the line shape on trajectory length is also observed, suggesting that even with 700 ns of simulation, as reported in this study, a single label may not experience all possible conformations.

The C* spin label also demonstrates complex multi-component dynamics evident from the autocorrelation functions (Figure 3.8). Extraction of the local motion (Figure 3.8b) confirms that rotation and bending of the alkyne tether leads to C* experiencing considerably lower local order than Q. Measurement of the interplanar dihedral angle between the plane of the C base and the nitroxide labelled ring of the C* label (Figure 3.9) indicates that, as has been inferred in the study of the related T* label, rotation about the alkyne linkage is not free, confirming that due to the short tether length, the nitroxide group is instead trapped in the major groove [26] (Figure 3.8). This partial rotation does however lead to the y and z magnetic axes experiencing a similar degree of local order, with x less affected. As with Q, fitting of the autocorrelation of local motion of the magnetic axes for the C* label required a minimum of three motional components on the ≈10 ps, ≈100 ps and ≈1-10 ns timescales. The value of the S_x local order parameter for C* (0.80 at 273 K) was found to be very close to that reported by Fischhaber ($S = 0.77$ at 273K) [10] and decreases slightly with increasing temperature (Table 3.4).

The global dynamics of the C*-labelled duplex are found to be in close agreement with those determined for the Q-labelled duplex at 293K (Table 3.4). Due to the additional partial rotation of the alkyne tether the EPR spectra of C*-labelled (Figure 3.10) duplex DNA demonstrates a sharper line shape than that of Q. Reasonable agreement between predicted and experimental line shapes is observed for both temperatures, validating the parmbsc1 forcefield for the dynamics of duplex DNA over long trajectories.

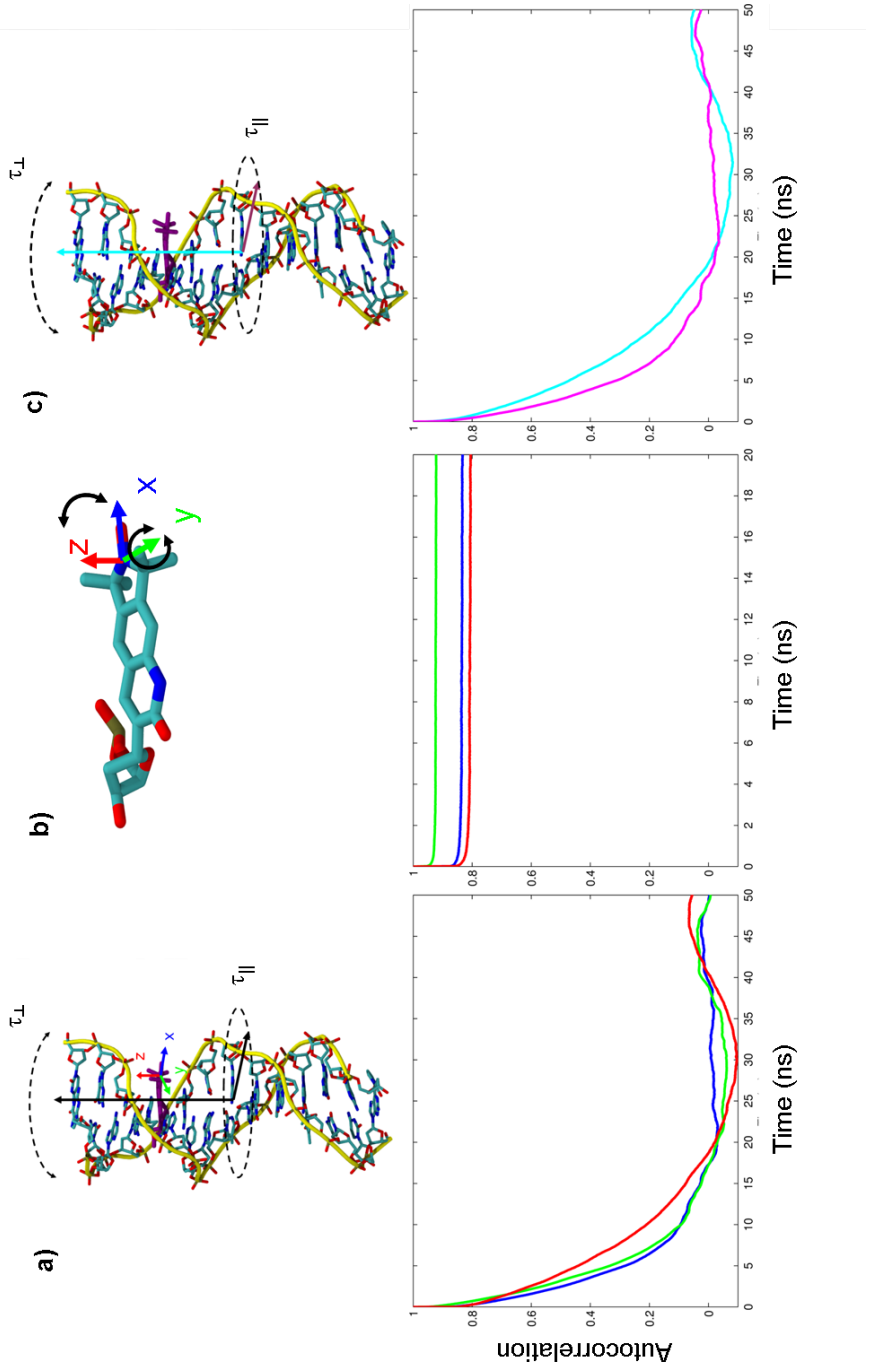

Figure 3.6: Structure and autocorrelation of magnetic axes X (blue), Y (green) and Z (red) of duplex Q with a) full motions, b) local motion only and c) DNA principal axes Z (cyan) and XY (magenta) representing global tumbling at 293K.

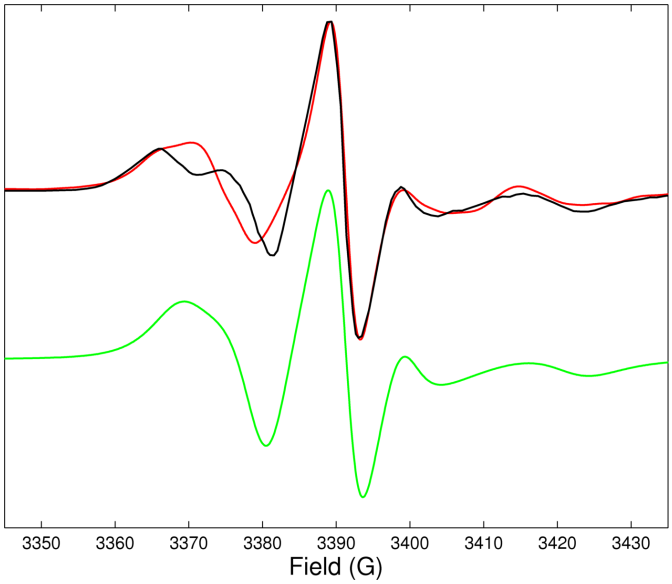

Figure 3.7: Comparison between experimental (black) and predicted from MD (red) EPR spectra of Q spin label in duplex DNA at 293K. The green line represents the spectra predicted using the SLE with $\tau_\perp$ and $\tau_\parallel$ from Table 3.4. The experimental EPR spectrum is reproduced from [9] with permission from the American Chemical Society.

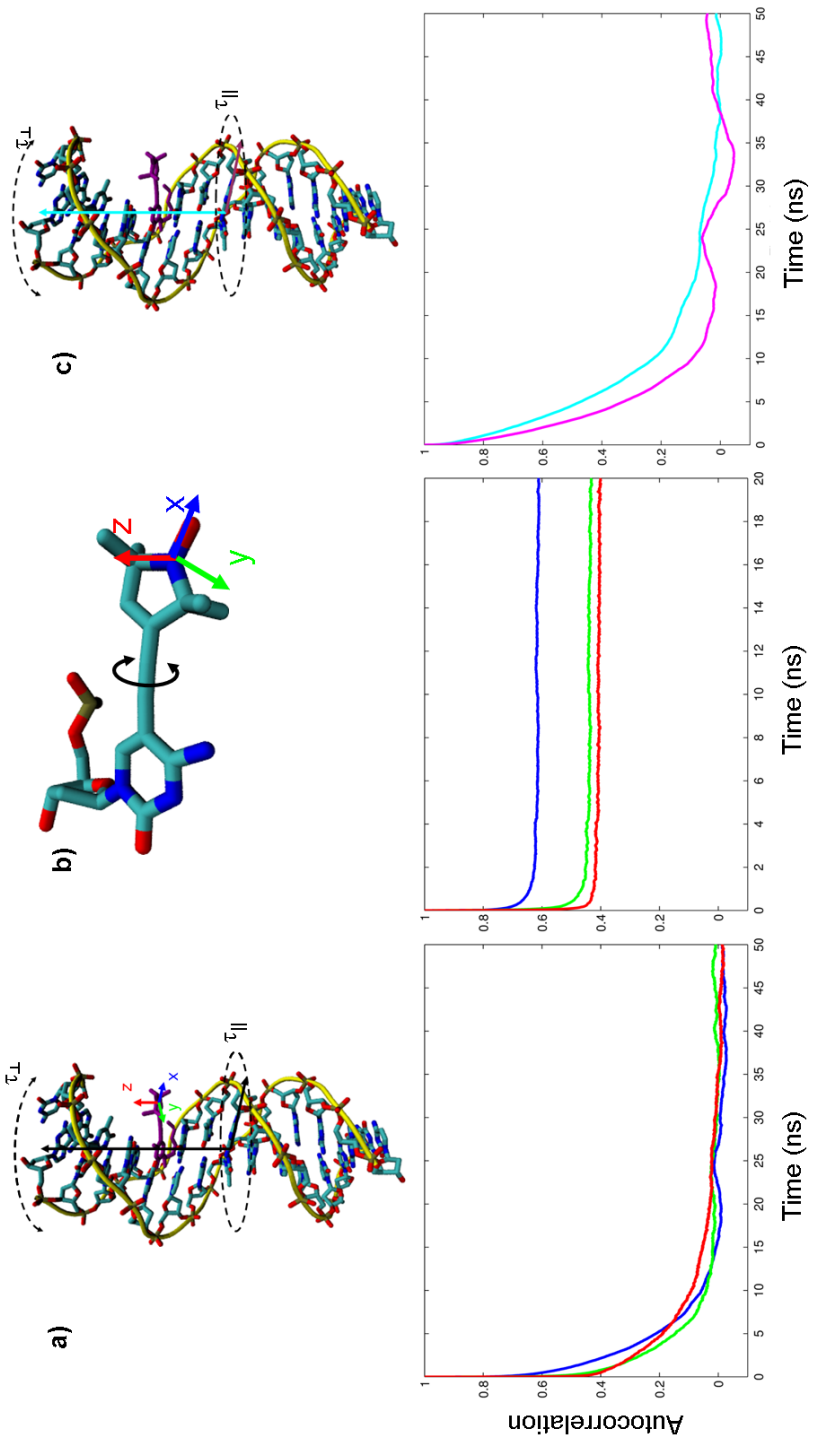

Figure 3.8: Structure and autocorrelation of magnetic axes X (blue), Y (green) and Z (red) of duplex C with a) full motions, b) local motion only and c) DNA principal axes Z (cyan) and XY (magenta) representing global tumbling at 293K*

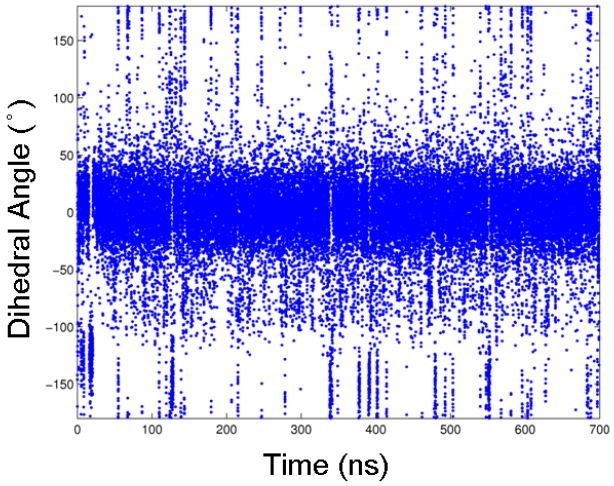

Figure 3.9: Interplanar angle between C base and nitroxide bearing ring in C probe in duplex DNA at 293K*

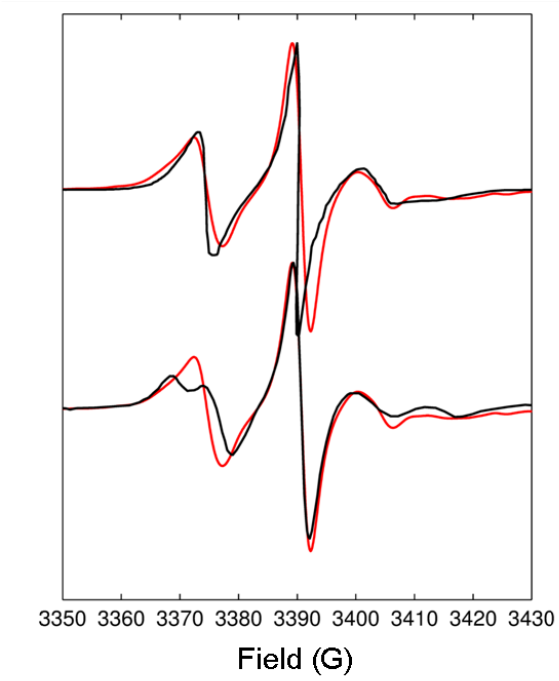

Figure 3.10: Comparison between experimental (black) and predicted from MD (red) EPR spectra of C spin label in duplex DNA at 273K (bottom) and 293K (top). Experimental EPR spectra are reproduced from [10] (bottom) with permission from Taylor and Francis and [11] (top).*

Dynamics of Spin Labelled Single-Strand DNA

Due to the location of the probes in the single-strand sequences, folding of terminal base pairs and temporary disruption of stacking of individual bases enables a greater degree of local flexibility for the label (Figure 3.11) than in duplex DNA. This is also demonstrated by the autocorrelation functions for local motion (Figure 3.12b) where the local order of the magnetic axes is found to be less than in the duplex. As in the case of duplex DNA the autocorrelation function of the local motion could be fitted with a minimum of three motional components (Table 3.5). Counter-intuitively the effective correlation times for local motions were slower than those observed in the duplex due to the presence of slow, large amplitude motions of the label when not fully stacked.

As with the duplex DNA, the autocorrelation function for the global motion of the single-strand DNA fragment (Figure 3.12c left) is similar to that of the magnetic axes of the Q probe with all motional components (Figure 3.12a left). Conversely, as the nitroxide group of C* is no longer trapped within the major groove as with duplex DNA, rotation of the alkyne tether for the label is relatively unrestricted in the single-strand. This results in the autocorrelation functions for the magnetic axes with all motional components (Figure 3.12a right) demonstrating significantly faster diffusion than those for the principal axes of inertia (Figure 3.12c right). This suggests that the EPR spectra for the C* label are significantly compromised by the effects of local motion. For both C* and Q-labelled single strand fragments global diffusion is highly axial with $\tau_\perp > 3.8\tau_\parallel$.

The EPR spectra predicted for both labels demonstrate notable narrowing of the line shapes as a result of the local motion with excellent agreement between experiment and MD (Figure 3.13) confirming the accuracy of the parmbsc1 forcefield for the dynamics of single DNA over long timescales.

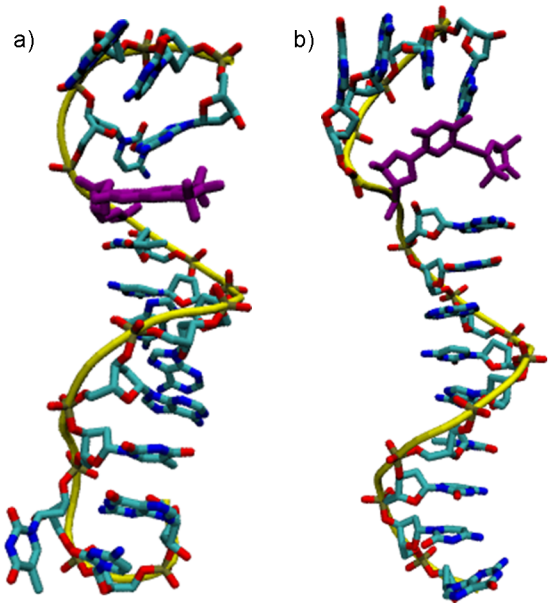

Figure 3.11: Structures of single-strand DNA highlighting a) Q and b) C spin labels (purple).*

Table 3.5: Fitted motional parameters of spin labelled single-strand DNA. $\tau_\perp$ and $\tau_\parallel$ represent the correlation times of the axial components of global diffusion. τ_x , τ_y ,τ_z ,S_x , S_y and S_z represent the effective correlation times and order parameters of the local motion. All correlation times are reported in nanoseconds. 95% confidence bounds for all parameters are provided in Tables B.6 and B.7 of the appendices.

Label	**Temp (K)**	$\tau_\perp$	$\tau_\parallel$	τ_x	τ_y	τ_z	S_x	S_y	S_z
Q	293	4.76	1.23	0.72	1.06	0.88	0.77	0.82	0.84
C*	273	9.65	1.91	1.66	1.41	1.08	0.60	0.51	0.60

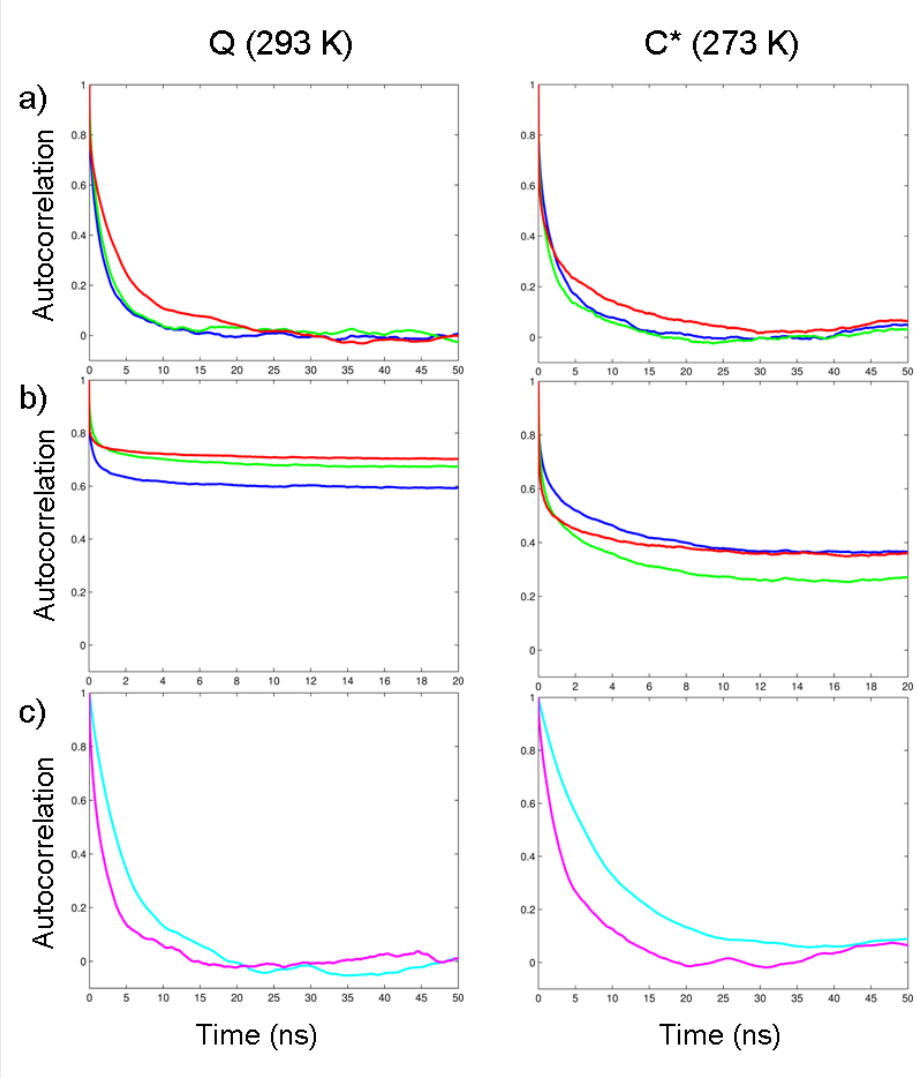

Figure 3.12: Autocorrelation of magnetic axes X (blue), Y (green) and Z (red) of single-strand DNA with a) full motions, b) local motion only and c) DNA principal axes Z (cyan) and XY (magenta) representing global tumbling.

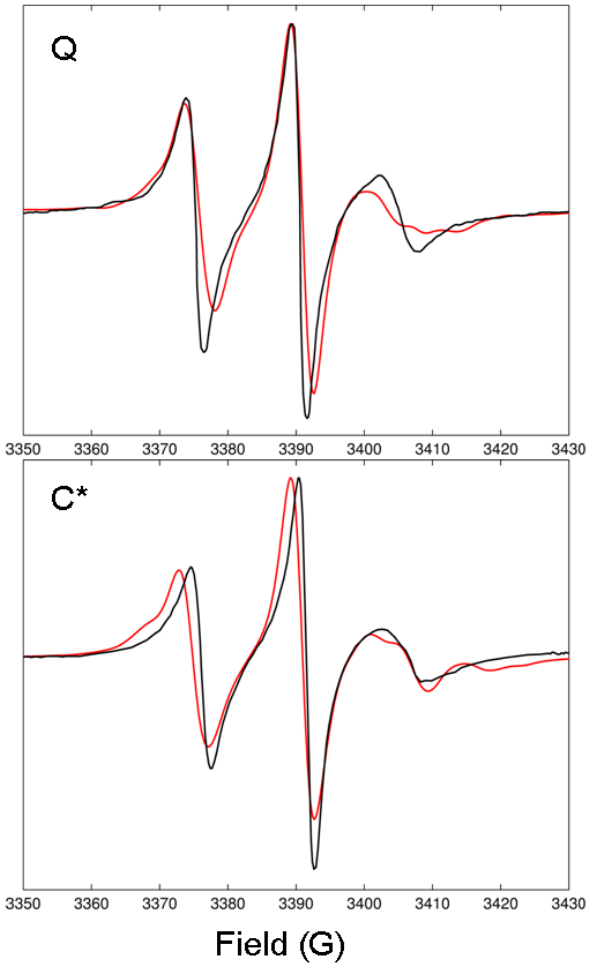

Figure 3.13: Comparison between experimental (black) and predicted from MD (red) EPR spectra of Q (293K - top) and C (273K - bottom) spin labels in single-strand DNA. The experimental EPR spectra of the Q-labelled single-strand is reproduced from [11] and C*-labelled single-strand from [10] with permission from Taylor and Francis.*

3.4 Conclusion

In this chapter the MD-EPR techniques outlined in Chapters 1 and 2 have been applied to spin labelled DNA with several significant outcomes. Firstly, the presence of the modified cytosine C* spin label in duplex DNA is confirmed to be structurally non-perturbing with the nitroxide group of this label concluded to be partially restrained within the major groove of duplex DNA. Secondly, the quinolonyl derived Q label is shown to accurately report on global dynamics of duplex DNA, with negligible contribution from local motion. Through analysis of autocorrelation functions the motional components contributing to X-band CW EPR spectra have been isolated for both single-stranded and duplex spin labelled DNA. The local motions of the labels are complex showing multi-modal dynamics, in agreement with previous studies. The global dynamics are shown to be axial but found to be systematically faster than those predicted by hydrodynamic theory for a rigid cylinder. Finally, through prediction of EPR spectra the recently optimised and developed parmbsc1 forcefield has been shown to accurately reproduce the dynamic behaviour observed by experiment on the 1 ps to 100 ns timescale for long trajectories.

Chapter 4

DFT Analysis of EPR spectra of Molybdenum Complexes

The contents of this chapter have been published in *Dalton Transactions*, 2016, **45**; Christopher Prior, Lee R. Webster, Saad K. Ibrahim, Joseph A. Wright, Ali F. Alghamdi, Vasily S. Oganesyan and Christopher J. Pickett; [2].

4.1 Introduction

1,2-bis(tertiary diphospho)alkane molybdenum complexes are known to support a wide range of chemistry [168][169][170] as well as having potential use as hydrogen evolution catalysts [171][172][173]. However, the proposed catalytic pathway by which they operate (Figure 4.1) has only been supported indirectly through experimental techniques [12][173] due to the instability of the Mo(II) intermediate. As the intermediate $[MoH_2(\eta^1\text{-MeCOO})(Ph_2PCH_2CH_2PPh_2)_2]$ (Figure 4.2, complex ***A***) is a paramagnetic 17 electron complex, EPR can be used to detect and provide information on the magnetic environment of the radical through standard fitting procedures to extract magnetic parameters. By combining EPR with DFT, the coordination of the carboxylate group can be investigated in order to characterise the structure of this experimentally transient species, and thus

confirm the rearrangement of this group in the proposed mechanism.

As the prediction of magnetic parameters for large transition metal complexes using DFT is non-trivial, a related chemically stable molybdenum complex, $[MoCl(NMe)(Ph_2PCH_2CH_2PPh_2)_2]^{2+}$ (Figure 4.2, complex ***B***), which has previously been thoroughly characterised experimentally [35] is first used as a test system for DFT calculations before expanding the method to the unstable intermediate.

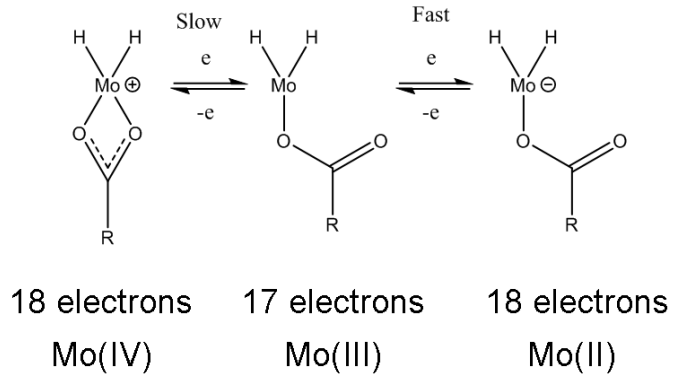

Figure 4.1: Proposed electron-transfer chemistry of Mo in the $[MoH_2(MeCOO)(Ph_2PCH_2CH_2PPh_2)_2]$ complex [12].

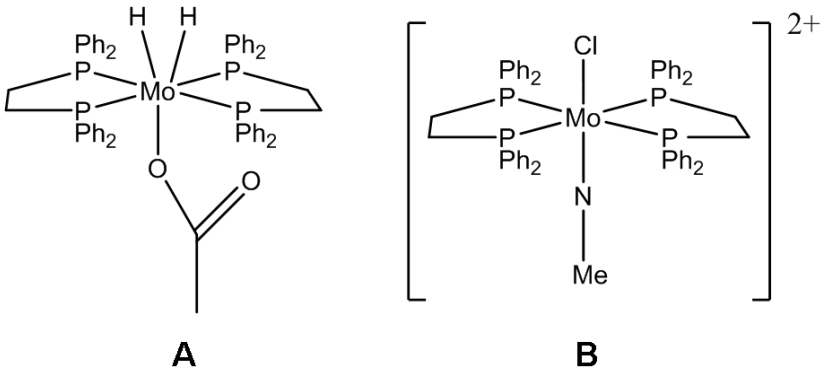

*Figure 4.2: Chemical structures of $MoH_2(MeCOO)(Ph_2PCH_2CH_2PPh_2)_2]$ (Complex **A**) and $[MoCl(NMe)(Ph_2PCH_2CH_2PPh_2)_2]^{2+}$ (Complex **B**).*

4.1.1 Prediction of Magnetic Parameters

As mentioned in section 1.1.1 the g value of the free electron, g_e, can be modulated by a number of different contributions which must accounted for in order to accurately predict experimentally observed values. This means g can be written generally as (4.1) [174]:

$$g = g_e\delta_3 + \Delta g^{RMC} + \Delta g^{DC} + \Delta g^{OZ+SOC} \tag{4.1}$$

where δ_3 indicates the three unit matrix used to define g. Δg^{RMC} is the relativistic mass correction and Δg^{DC} is the diamagnetic correction, also known as the gauge correction, which describes the effective spin-orbit coupling of the electron at the nucleus. However, as these terms are usually small and of opposite sign they tend to cancel out [174]. The most significant contribution comes from the third correction term, Δg^{OZ+SOC}, which describes the orbital Zeeman interaction and spin-orbit coupling.

Hyperfine coupling, A_{Tot}, has two main components; the Fermi contact and the electron-nuclear dipole interaction (ENDI) described by equations 4.2 and 4.3 respectively, for nucleus N[174][175]:

$$A_{Iso} = \frac{8\pi}{3} g\beta g_N\beta_N \sum^{u,v} \mathbf{P}_{uv}^{\alpha-\beta} \langle\phi_u|\delta(r_N)|\phi_v\rangle \tag{4.2}$$

$$A_{ENDI} = -g\beta g_N\beta_N \sum^{u,v} \mathbf{P}_{uv}^{\alpha-\beta} \langle\phi_u|(r^2\delta_{pq} - 3pq)r^{-5}|\phi_v\rangle \tag{4.3}$$

where ϕ_u is the linear combination of atomic orbitals used to define the molecular orbitals, $\mathbf{P}_{uv}^{\alpha-\beta}$ represents an element of the one-electron spin density matrix and pq are the spatial coordinates relative to N. The Fermi contact describes the magnetic interaction resulting from the presence of unpaired electron density at the nucleus. As only the spherical s type orbitals have non-zero electron density in this region this component is isotropic. The electron-nuclear dipole interaction term describes the anisotropic contributions from coupling between d functions and spin orbit coupling. As calculation of both components rely on the g value, inaccuracies in this parameter will also affect the calculation of A_{Tot}. Although

g and A can generally be calculated quite accurately for organic and first row radicals [176] [125], transition metals can show magnitudinal discrepancies and occasionally incorrect signs with significant dependence on choice of functional and basis set [177]. This variation is often attributed to an as yet unpredictable cancellation of errors in the computation of these parameters, meaning currently the only successful approach has been trial and error [174]. In particular, previous DFT studies of metal systems have found the Fermi contact especially sensitive to the degree of Hartree-Fock exchange in the functional, but a wider range of functionals can be successfully used if reliable X-ray geometries are available [178]. Additionally, as the core electrons are crucial to the magnetic resonance phenomena, ECPs used to improve the accuracy and speed of calculations involving transition metals cannot be used for the calculation of magnetic parameters. These calculations are also known to demonstrate a considerable conformation dependence and thus can be affected significantly by polar or hydrogen bond forming solvents [50].

4.2 Methods

4.2.1 Experimental Methods

EPR

X-band (9.562 GHz) EPR spectra of $\boldsymbol{A}$ were measured at room temperature using a Bruker EMX spectrometer fitted with an ER4102ST resonator. A microwave power of 2 mW was used with a modulation frequency of 100 kHz and amplitude of 1.0 G. Calibration of the magnetic field was performed using ionic Mn(II) doped in magnesium oxide powder. The reduction of the Mo(IV) dihydride to the paramagnetic Mo(III) form was performed in the cavity of the spectrometer by controlled-potential electrolysis with a platinum wire working electrode. Tetrahydrofuran solvent was used with 0.2M [NBu4][BF4] as the supporting electrolyte

under an argon atmosphere.

4.2.2 Computational Methods

DFT

All DFT calculation were performed using the Gaussian 09 (revision C01) suite of programs [122]. Structures were geometry optimised in the gas phase using the Tao-Perdew-Staroverov-Scuseria (TPSS) pure density functional [179]. The LACV3P basis set was implemented which describes molybdenum, phosphorous and chlorine atoms using the Hay and Wadt LAN2LDZ basis set and effective core potentials [82] [83], and oxygen, nitrogen, carbon and hydrogen were described with the 6-31+G** Pople type basis set. Magnetic parameters were calculated using the O3LYP hybrid functional [180] and the DZVP basis set for the heavy atoms, and 6-311+G** basis set for oxygen, nitrogen, carbon and hydrogen based on the work of Hadt and co-workers [178]. The process was repeated for the deuterated forms of both complexes. Full atomic coordinates of both structures are included in the appendices (Tables C.1 and C.2).

EPR Modelling

Simulation and fitting of EPR spectra were performed using the Garlic function of Easyspin [4] for the fast motion/isotropic regime which solves the Breit-Rabi formula [181] iteratively through the general approach of Stoll et al [4] via (4.4):

$$B_{k+1}(m_I) = \frac{hA_{Iso}}{\gamma(1-\zeta_k^2)}\left\{-m_I \pm \sqrt{m_I^2 + (1-\zeta_k^2)\left[(2\zeta_k^2)^{-2} - \left(I+\frac{1}{2}\right)\right]}\right\} \quad (4.4)$$

where m_I is the nuclear spin quantum number, h is the Planck constant and ζ and γ are given by (4.5):

$$\begin{aligned} \zeta_k &= \frac{A_{Iso}/2}{v_{mw} + \beta_n g_n B_k/h} \\ \gamma &= \beta_e g_{Iso} + \beta_n g_n \end{aligned} \quad (4.5)$$

where β_e is the Bohr magneton, h is the Planck constant and v_{mw} is the frequency.

4.3 Results and Discussion

4.3.1 $[MoCl(NMe)(Ph_2PCH_2CH_2PPh_2)_2]^{2+}$

Due to the large number of atoms, geometry optimisation of complex ***B*** was performed in two separate stages; firstly with phenyl groups replaced by methyl groups and then the resulting structure was subsequently used as a starting point for the full molecule to give the structure shown in Figure 4.3.

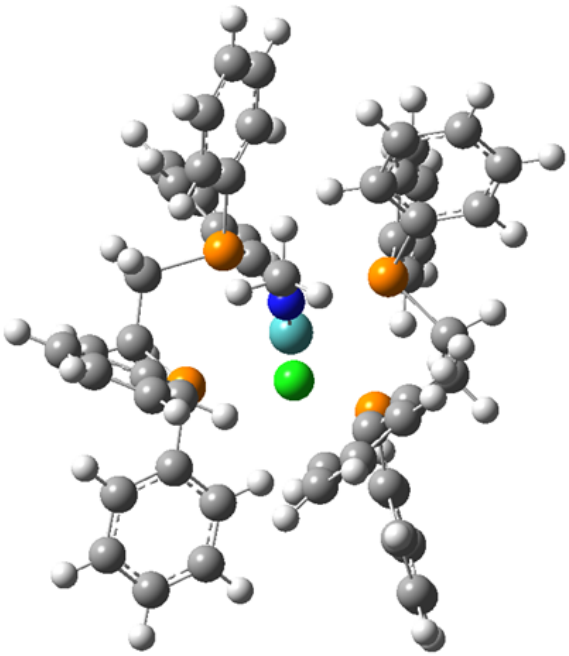

*Figure 4.3: Full DFT optimised structure of complex **B** at the TPSS/LACV3P level of theory. Molybdenum is shown in cyan, phosphorous in orange, chlorine in green, nitrogen in blue, carbon in grey and hydrogen in white. Full Cartesian coordinates are provided in Table C.2 of the appendices.*

The geometry optimised using the TPSS pure functional and a split basis set, as used in recent study of iron hydrides [182], was found to give excellent agreement (Table 4.1) with the structure determined experimentally by X-ray crystallography [35]. Deviations in phosphorous bond lengths were less than 4% and reproduced the pattern with two identical mid-length Mo-P bonds. Deviation

between experiment and DFT was even smaller for the other bonds.

The EPR spectrum of ***B*** mainly results from splitting by the four equivalent phosphorous atoms with intensities of 1:4:6:4:1 and a further splitting from the three hydrogens on the methyl group in a 1:3:3:1 pattern. Splitting by the single nitrogen with relative intensity 1:1:1 is only partially resolved using conventional X-band EPR, but has been confirmed by ENDOR measurements [35]. As the magnetic moment of ^{2}H is much less than that of ^{1}H the hydrogen splitting is no longer observable upon deuteration as the separation becomes smaller than the linewidth.

The O3LYP functional [180] with the DZVP basis set for heavy atoms, as used in previous studies [178], and 6-311+G** for first row atoms were found to provide the best description of the magnetic parameters with generally excellent agreement with the experimentally determined values (Table 4.2). The average A_{Iso} values for nitrogen and hydrogen were found to be in particularly good agreement, however values for phosphorous were systematically underestimated, as has been observed for previous DFT studies of Mo-P complexes [175], and so were scaled by a factor of 1.44. The small size of A_{Iso} for ^{2}H and ^{35}Cl is also consistent with the lack of splitting observed in the experimental spectra. Apart from chlorine, all A_{Iso} values were found to have a negative sign although, due to the symmetric nature of the spectra, this cannot be verified by experiment. g_{Iso} also shows relatively good agreement with the experimentally determined value.

The values of A_{Iso} are consistent with the observed core geometry and spin densities shown in Figure 4.4. Spin density is confirmed to be primarily located on the molybdenum centre, in agreement with previous DFT studies [175], with delocalisation predominantly to the phosphorous, nitrogen and hydrogen atoms on the methyl group. Contributions to the spin density are also observed on the chlorine and carbons on the methyl group and diphospho-alkane ligand. The pattern of A_{Iso} for phosphorous reflects the geometry with two atoms with a similar Mo-P bond length, however this is effectively averaged out by motion.

*Table 4.1: Comparison of selected geometric parameters from X-ray crystallography and DFT for complex **B**.*

Parameter	**Experiment** [35]	**DFT** (C_1)
Mo-P	2.56 Å	2.64 Å
	2.55 Å	2.63 Å
	2.55 Å	2.63 Å
	2.53 Å	2.62 Å
Mo-Cl	2.49 Å	2.53 Å
Mo-N	1.73 Å	1.75 Å
N-C	1.43 Å	1.44 Å
N-Mo-Cl	178.9 °	177.1 °

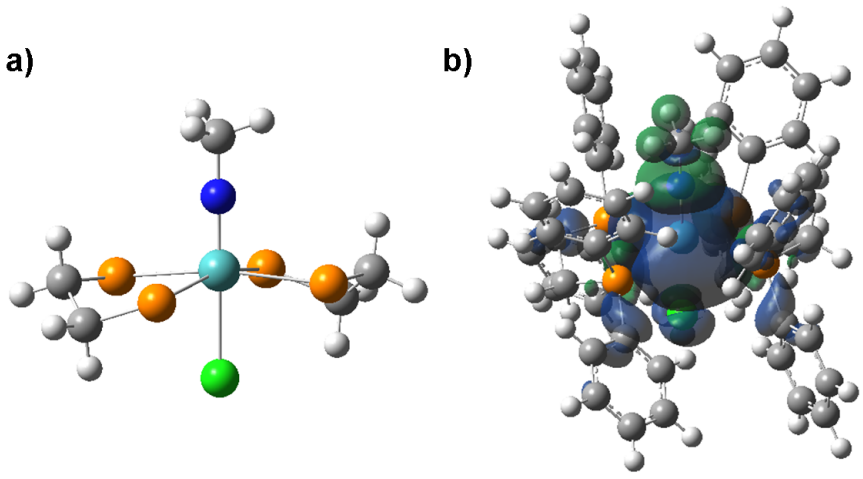

*Figure 4.4: DFT optimised structure of complex **B** highlighting a) the core of the complex. b) Isosurface of the spin density distribution with the two phases denoted with green and blue.*

*Table 4.2: Comparison of magnetic parameters from experimental EPR and DFT for complex **B**. A_{Iso} values are given in MHz.*

Parameter	**Experiment** [35]	**DFT** (C_1)
g_{Iso}	2.004	2.018
A_{Iso} (^{31}P) Average	56.1	-54.0
A_{Iso} (^{31}P) Individual	N/A	-62.6
		-59.3
		-47.2
		-46.9
A_{Iso} (^{14}N)	9.5	-12.3
A_{Iso} (^{1}H) Average	10.1	-16.1
A_{Iso} (^{1}H) Individual	N/A	-16.4
		-16.0
		-16.0
A_{Iso} (^{2}H) Average	N/A	-2.4
A_{Iso} (^{2}H) Individual	N/A	-2.5
		-2.4
		-2.4
A_{Iso} (^{35}Cl)	~ 1	2.1

4.3.2 $[MoH_2(\eta^1\text{-}MeCOO)(Ph_2PCH_2CH_2PPh_2)_2]^0$

Geometry optimisation for complex ***A*** was performed using the same two-stage approach used for ***B***, with the methylated structure being optimised first. Only C_1 symmetry was found to be valid for this fragment due to the arrangement of the hydrides and the phosphorous atoms being distorted slightly out of the molecular plane. Upon optimisation of the full complex with phenyl groups, phosphorous atoms were found to be in a two-up two-down arrangement as shown in Figure 4.5. Compared with ***B***, Mo-P bond lengths were found to be shorter in ***A*** (Table 4.3), indicating a stronger interaction between the metal and ligand. Crucially, reduction from the diamagnetic 18-electron Mo(IV) state to the 17-electron ***A*** causes the orientation of $COOCH_3$ to change from a symmetric η^2 bonding to a singly-bound form with an Mo-O-C angle of $\sim$125°, in agreement with the scheme proposed in Figure 4.1. The Mo-H and H-H bonds are found to be of similar lengths, suggesting a strong interaction between the metal and the hydrides.

The EPR spectra (Figure 4.6) is again indicative of unpaired electron density being primarily located on the molybdenum centre, confirmed by the spin density isosurface determined by DFT (Figure 4.7). Spin density calculations confirm this finding with 62% of the total unpaired spin density being located at the metal centre. Hyperfine coupling from the four phosphorous nuclei results in splitting with a 1:4:6:4:1 pattern and further splitting from the two hydrides with relative intensities of 1:2:1. As the isotropic coupling constants of the phosphorous atoms are approximately double that of the hydrides, eleven lines are discernible rather than fifteen as the hydride splittings are partially overlaid. Deuteration causes the hydrogen splitting to be reduced by the magnetogyric ratio of γ_D/γ_H ($A_{Iso}(^1H)$ = -39.1 MHz/$A_{Iso}(^2H)$ = -7.3 MHz). As with complex ***B***, this results in a splitting smaller than the linewidth and thus is not resolved, leaving only the splitting from the phosphorous nuclei, consistent with the green lines shown in Figure 4.6. Also apparent in the deuterated spectra are contributions to the hyperfine splitting pattern from the Mo^{95} (I = 5/2, 15.92%) and Mo^{97} (I = 5/2, 9.55%) isotopes

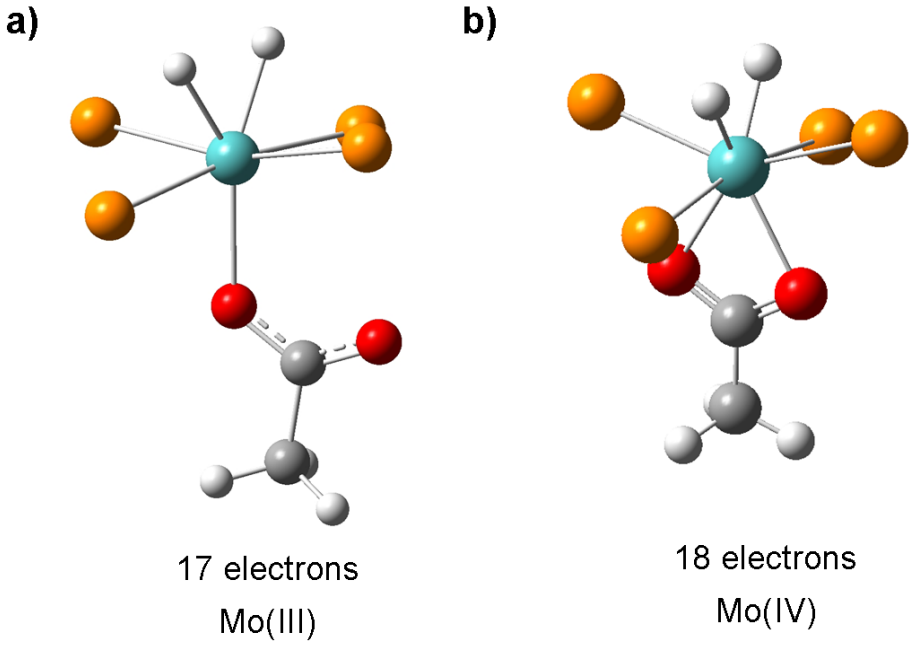

Figure 4.5: DFT optimised structures highlighting the core of a) Mo(III) ***A*** *complex showing the* η^1 *arrangement of the acetate group and b)* η^2 *arrangement of the optimised Mo(IV) form. Molybdenum is shown in cyan, phosphorous in orange, oxygen in red, carbon in grey and hydrogen in white.*

resulting in the low intensity features visible either side of the five lines arising from phosphorous splitting (Figure4.8). The acetate group has no significant interaction with the spin system and the dynamics are at the isotropic limit.

Once the hyperfine coupling constants for phosphorous were scaled as before, the fitted parameters and those predicted by DFT are in good agreement (Table 4.4), particularly for coupling to the hydrides. The negative signs of the major hyperfine components predicted by DFT were confirmed by an increase in the quality of fit as well as an increase in linewidth across the spectra, with the low magnetic field m_I = -I line being slightly narrower than that of the high field m_I = +I line. This is consistent with the DFT results for complex ***B*** as well as a recent DFT study of a paramagnetic di-iron complex with a bridging hydride [182]. The quality of fit was also improved by treating each phosphorous atom individually

Table 4.3: Selected geometric parameters of the DFT optimised structure of ***A****. Full Cartesian coordinates are provided in Table C.1 of the appendices.*

Parameter	DFT	Parameter	DFT
Mo-P	2.50 Å	Mo-H	1.74 Å
	2.49 Å		1.73 Å
	2.49 Å	H-H	1.71 Å
	2.47 Å	H-Mo-H	59.0 °
Mo-O	2.19 Å	Mo-O-C	125.0 °

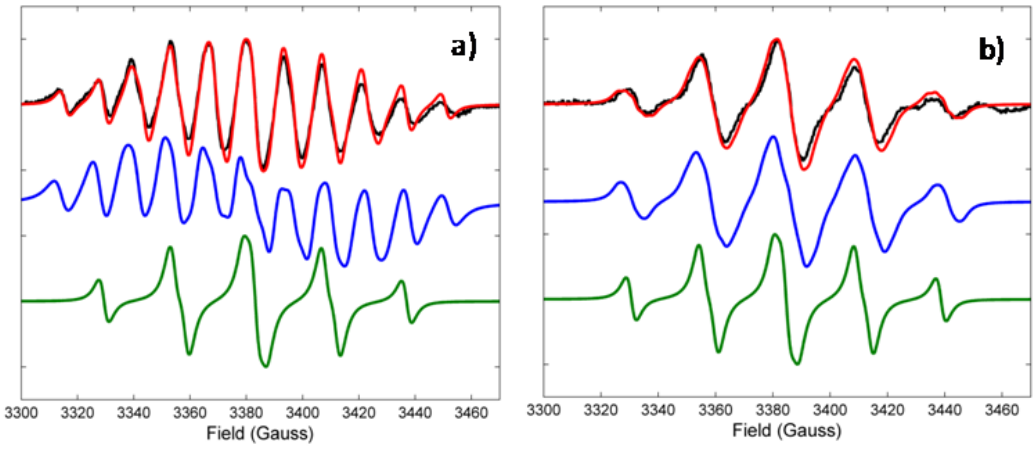

Figure 4.6: EPR spectra of a) ^{1}H *and b)*^{2}H *forms of complex* ***A****. Experimental spectra are shown in black with the fitted spectra shown in red. Spectra predicted from the DFT parameters are shown in blue. Spectra resulting from phosphorous splitting only are shown in green.*

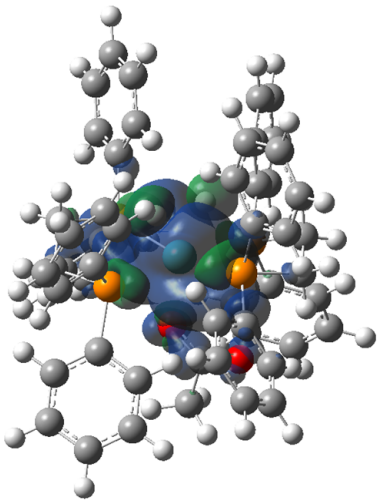

Figure 4.7: Isosurface of the spin density distribution with the two phases denoted with green and blue for ***A****.*

Table 4.4: Comparison of magnetic parameters fitted from experiment and predicted by DFT for ***A****. A_{Iso} values are given in MHz. Values for ^{31}P have been scaled by a factor of 1.44.*

Parameter	**Experiment**	**DFT**
g_{Iso}	2.016	2.039
A_{Iso} (^{31}P)	-82.2	-88.8
	-78.9	-78.1
	-73.0	-76.1
	-69.2	-66.2
A_{Iso} (^{1}H)	-37.8	-38.4
	-40.4	-38.5
A_{Iso} (^{2}H)	-7.4	-6.0
	-7.3	-6.0

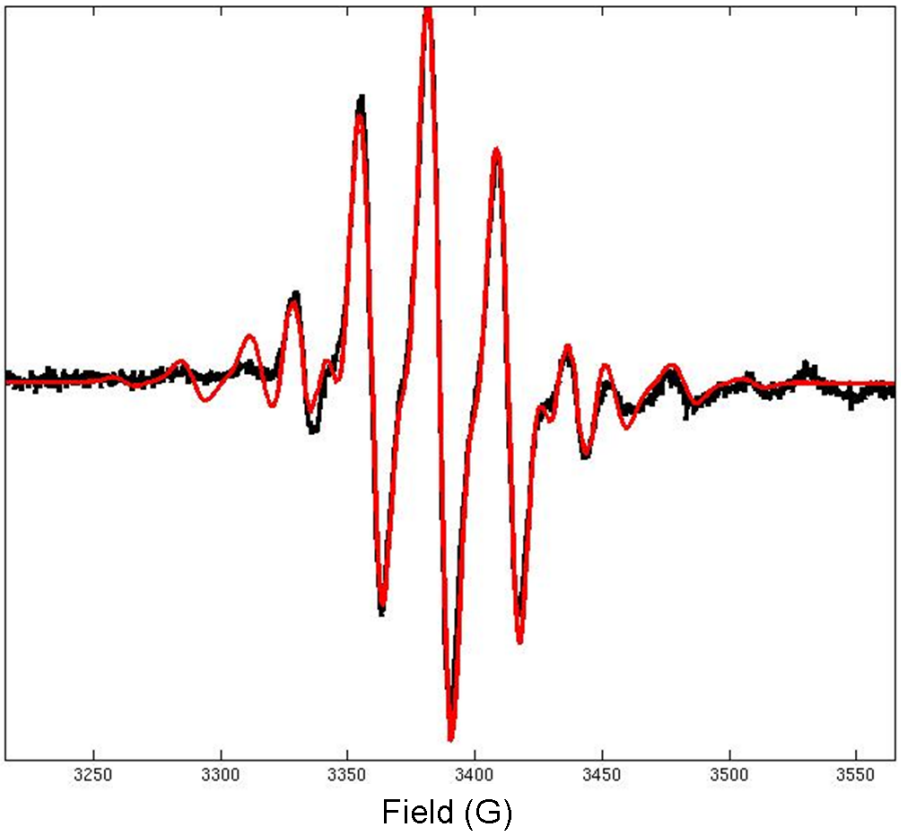

Figure 4.8: EPR spectrum of the deuterated form of ***A*** *with contributions from* Mo^{95} *(I=5/2, 15.92%) and* Mo^{97} *(I=5/2,9.55%) isotopes hyperfine coupling included. Black and red lines correspond to experimental and fitted spectra, respectively.*

suggesting that, unlike in ***B*** where motions appear to average out the hyperfine, the short lived ***A*** is more rigid, and is in agreement with the distribution of spin density predicted by MD. Calculating the *s*-orbital spin density by the method outlined by Morton and Preston [37] from the fitted values confirms that the phosphorous atoms bear a considerable amount of the spin density (totalling $\sim 12\%$). Each hydride also demonstrates a significant *s*-orbital spin density with $\sim 3\%$ per hydride, confirming the direct interaction. In contrast, only $\sim 1\%$ is located on the oxygen from the acetate group that interacts with the molybdenum centre.

4.4 Conclusion

By comparison with experimental X-ray and EPR data, DFT has been shown to be able to accurately predict spectroscopic data for phosphorous ligated molybdenum complexes. By extension of the technique it has provided access to data not otherwise accessible in the form of the geometry of a transient species, allowing a key process in the catalytic cycle for hydrogen evolution to be confirmed. The phosphate geometry of complex ***A*** is found to be similar to stable species ***B*** previously characterised, but stronger interactions between phosphorous and molybdenum result in stronger hyperfine coupling. The nature of the eleven line EPR spectra is confirmed as resulting from the splitting of phosphorous being double that of the hydrides. The strong hydride coupling observed in EPR combined with DFT indicates that the hydrides are directly ligated to the Mo(III) metal centre where the majority of the spin density is located. The concerted $\eta^2\eta^1$ rearrangement of the acetate group has been confirmed via DFT as the coupling is too weak to be detected experimentally, further demonstrating the value of hybrid theoretical/spectroscopic methods.

Chapter 5

DFT Analysis of Nuclear Inelastic Scattering Spectra of Iron-Sulphur Clusters

The contents of this chapter have been published in *Angewandte Chemie International Edition*, 2016, **55**;Pauline N. Serrano, Hongxin Wang, Jason C. Crack, Christopher Prior, Matthew I. Hutchings, Andrew J. Thomson, Saeed Kamali, Yoshitaka Yoda, Jiyong Zhao, Michael Y. Hu, Ercan E. Alp, Vasily S. Oganesyan, Nick E. LeBrun, Stephen P. Cramer ; [3]

5.1 Introduction

Metalloproteins are crucial to a wide variety of biological functions including electron transfer, substrate binding, regulation of gene expression and enzyme activity, sulphide reduction, storage and chemical sensing [183]. One particularly important class of these proteins are those containing iron-sulphur clusters which, amongst a range of functions, are believed to be important chemical sensors of O_2 and NO [184]. However many are susceptible to damage under oxidative and nitrosative stress leading to impairment [185][186]. Reaction of NO with [Fe-S]

clusters typically leads to conversion into a range of nitrosyl iron complexes [187].

The major known iron-nitrosyl species are the [Fe-2S] dinitrosyl iron complex (DNIC), the [2Fe-2S] Roussin's red ester (RRE) and the [4Fe-3S] Roussin's black salt (RBS) (Figure 5.1). An equilibrium between DNIC and RRE clusters has been observed that is dependent on the availability of thiolate ligands [188]. Additionally, as the related sulphide-bridged Roussin's red salt (RRS) is known to be able to reversibly convert to RBS clusters [189][190] as well as exchanging sulphide for cysteine thiolate ligands [191], this suggests that RRE may be able to convert to a hypothetical thiolate-bridged "Roussin's black ester" structure. As nitrosylation can result in some sulphides being reduced [192][193] it has also been suggested coordination may occur through formation of cysteine persulphide ligands [194][195].

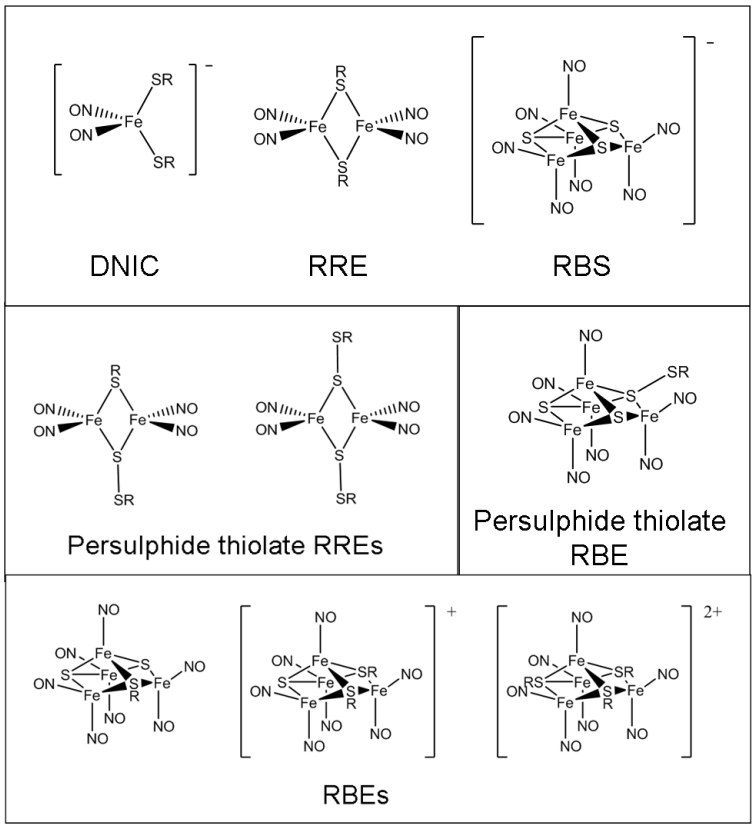

Figure 5.1: Structures of major iron-nitrosyl species and possible ligated variants

However due to the complex nature and size of the host proteins, analysis and identification of these clusters is complicated as conventional techniques such as infrared spectroscopy and NMR are often overwhelmed. Although EPR is selective many oxidation states are diamagnetic, and so only fragments of the rich redox chemistry can be investigated with this technique [196][197]. Similarly, Resonance Raman spectroscopy can be subject to destructive interference, leaving certain oxidation states inaccessible [198] as well as limits on the observable vibrational modes from the selection rules further constraining its diagnostic ability. Mössbauer spectroscopy is selective to specific isotopes, including ^{57}Fe, and probes the magnetic environment through splitting patterns and chemical shifts and the rigidity of an atomic lattice through the Lamb-Mössbauer factor (the fraction of γ-ray absorptions that are recoil free). Although this is highly sensitive to the spin state of iron, it only has limited ability to discriminate between different clusters. Nuclear inelastic scattering (NIS), also called nuclear resonance vibrational spectroscopy (NRVS), offers a potential solution to this problem as it can report selectively on all the vibrational modes of Mössbauer active nuclei regardless of the electronic state of the cluster or symmetry of the vibration. It has already been used successfully in conjunction with DFT to analyse a range of iron complexes and clusters with good agreement for model systems [15][18][199][200][201][202]. Furthermore, it has been shown the effects of anharmonicity on the calculated spectra are small compared with the error resulting from the choice of functional and basis set in the DFT calculations [203] and the effect of conformation [18].

Although NIS can discriminate well between DNIC, RRE and RBS model compounds (Figure 5.2), as a relatively new technique [204] it's ability to distinguish between the different potential ligation schemes shown in Figure 5.1 has not been explored. As the nitrosylation products of the reaction of NO with [4Fe-4S] containing proteins such as NsrR and WhiD (from the *Streptomyces coelicolor* bacterium) are unclear, with features suggestive of both RRE and RBS

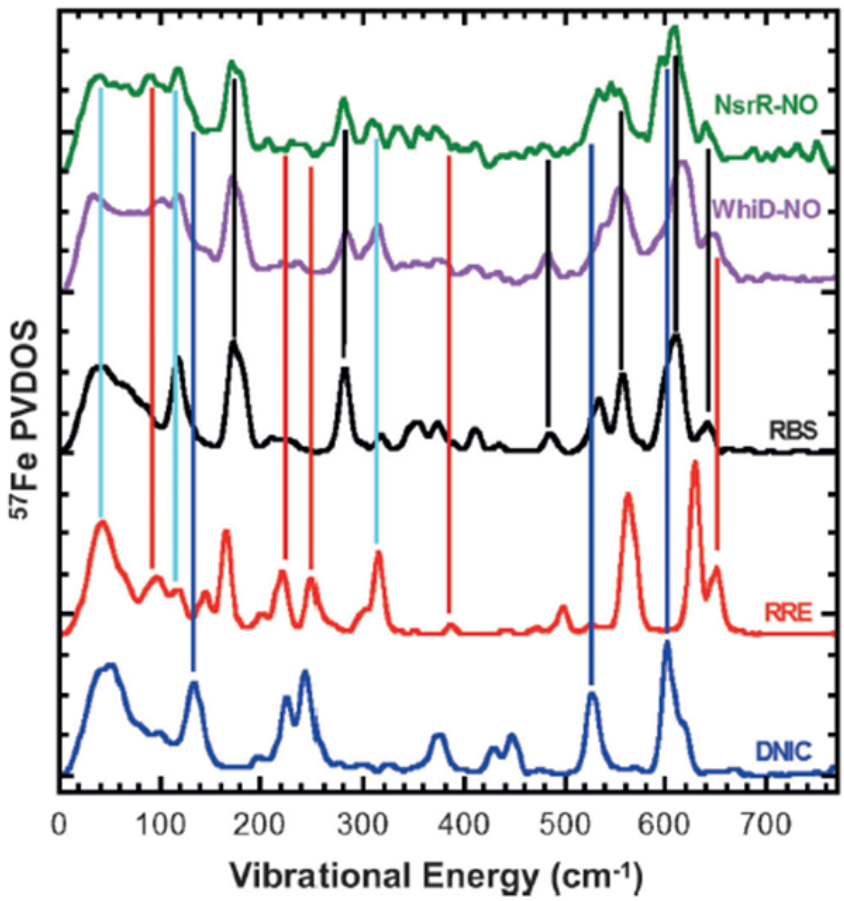

Figure 5.2: Comparison of experimental NIS spectra of nitrosylated WhiD (purple) and NsrR (green) metalloproteins with those of model DNIC (blue), RRE (red) and RBS (black) compounds. Pale blue lines highlight features present in WhiD, NsrR, RRE and RBS spectra. [3]

type clusters (Figure 5.2), this is of pressing concern. It is also unknown how an RBS type cluster would interact with a protein.

In this chapter therefore, DFT is used to predict NIS spectra and assign vibrations in order to investigate the ability of the experimental technique to distinguish between a series of closely related hypothetical nitrosyl iron-sulphur complexes after initial benchmarking against the known RRE and RBS structures. The results are then compared with experimental data to determine whether any of the hypothetical structures are consistent with the experimental spectra for

nitrosylated WhiD and NsrR.

5.1.1 Nuclear Inelastic Scattering Theory

In order to be considered Mössbauer active nuclei need to fulfil two main criteria relating to the excited states formed upon absorption of a photon. Firstly, the excited state formed should have a lifetime of between $\sim 10^{-6}$ and $\sim 10^{-11}$ seconds to provide a suitable resolution. Secondly, the isotope requires very low-lying excited states with transition energies between ~ 5 and ~ 180 keV. Energies larger than this result in significant recoil effects which prevent resonance, whereas smaller energies are mostly absorbed, resulting in few recoil-free events and a weak signal. The high resolution provided by the Mössbauer effect means the mechanical movement of the source or sample is able to provide a detectable Doppler shift which is harnessed with NIS to measure partial vibrational density of states (PVDOS) through the use of tunable synchrotron radiation to match the resonant frequency of the Doppler shifts.

Figure 5.3 shows the basic experimental setup for the NIS procedure [13]. Firstly, X-rays are generated from a synchrotron beam using an undulator before being passed through two sets of monochromators to reduce the bandwidth to ~ 1 meV, giving the technique a resolution of ~ 7 cm^{-1}. The sample is then irradiated by photons around the energy of the target isotope's Mössbauer resonance (14.413

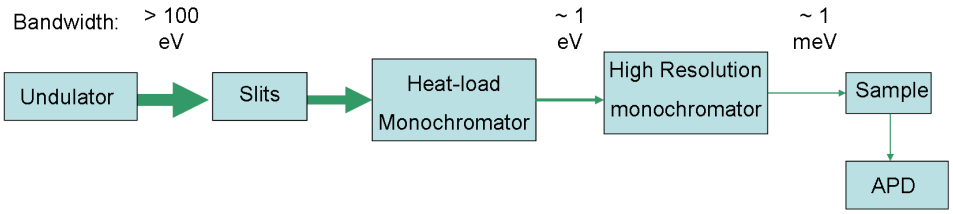

Figure 5.3: Schematic diagram indicating experimental setup for [13]. APD indicates the avalanche photodiode detector.

keV for ^{57}Fe), raising the nucleus to an excited state prior to relaxation by internal conversion. The avalanche photodiode detector is then enabled to record the delayed fluorescent X-rays that result from this process [13].

The PVDOS, which describes the vibrational frequencies of the Mössbauer active nuclei, can be calculated from DFT results via:

$$D_{Fe}(v) = \frac{1}{3}\sum_{\alpha} e^2_{Fe,\alpha} \cdot f(v - v_\alpha) \tag{5.1}$$

where $f(v - v_\alpha)$ is the line shape function used to account for instrumental and lifetime broadening and the composition factor, $e^2_{Fe,\alpha}$, for normal mode α is given by (5.2):

$$e^2_{Fe,\alpha} = \frac{(\Delta r_{Fe.\alpha})^2 m_{Fe}}{\sum_{k=1}^{N}(\Delta r_{k,\alpha})^2 m_k} \tag{5.2}$$

where $(\Delta r_{Fe.\alpha})$ is the mean square displacement of atom k, with mass m_k as described previously [199][200][205][206][207][208][209][210][211]. Due to the dependence on mass, isotopic substitution is frequently used in order to resolve overlapping lines and assign vibrational character to spectral features. Bridging sulphur atoms can be labelled with ^{34}S or ^{15}N in the nitrosyl groups to produce an isotopic frequency shift to active vibrations involving these atoms which can be used to clearly correlate features in experimental and DFT predicted spectra.

5.2 Methods

5.2.1 Computational Methods

All DFT calculation were performed using the Gaussian 09 (revision C01) suite of programs [122]. Structures were geometry optimised in the gas phase using the PW91 pure density functional [212]. Iron atoms were described using the Hay and Wadt LAN2LDZ basis set and effective core potentials [82] [83], with all other atoms being described using the 6-311G** Pople type basis set as used by Mitra et al [18]. All structures were confirmed as minima during the frequency analysis.

NIS spectra were predicted from the DFT outputs as described in section 5.1.1 using an in-house MATLAB computer program developed by Oganesyan [200]. Lines were assigned a Lorentzian line shape of width 6 cm^{-1}.

5.2.2 Experimental Methods

NIS spectra of $\sim$ 1 mM ^{57}Fe-enriched nitrosylated WhiD and NsrR, including $^{32/34}$S and $^{14/15}$N isotopically labelled variants were recorded in accordance with published procedures [205][213] at 03-ID at the Advanced Photon Source and at BLO9XU at Spring-8 [214][215][216][217]. Samples were loaded in $3 \times 10 \times 1$ mm^3 Lucite sample cells encased with Kapton tape and frozen in liquid nitrogen. The bandwidth was 0.8 meV at 14.4125 keV in a 0.6 mm $\times$ 1 mm spot and flux was of the order of 1.4×10^9 photons/s. Scans took approximately 45 minutes and the PVDOS were calculated from the raw NIS spectra using the PHOENIX software package [218]. The temperature of the sample was maintained at 50-80K during measurement using a liquid helium cryostat.

5.3 Results and Discussion

Tables detailing the full assignment of vibrational modes and optimised geometries are presented in appendices (D). Results are presented without scaling.

5.3.1 Roussin's Red Esters

Roussin's Red Ester

Roussin's red ester was successfully optimised with C_{2h} symmetry constraints. The DFT optimised geometry (Figure 5.4a) shows excellent agreement with that previously reported using X-ray crystallography for the phenylated analogue [$Fe_2(\mu$-$SPh)_2(NO)_4$] (Table 5.1) [15]. The predicted NIS PVDOS spectra also shows generally good agreement, particularly for features below 500 cm^{-1}, with

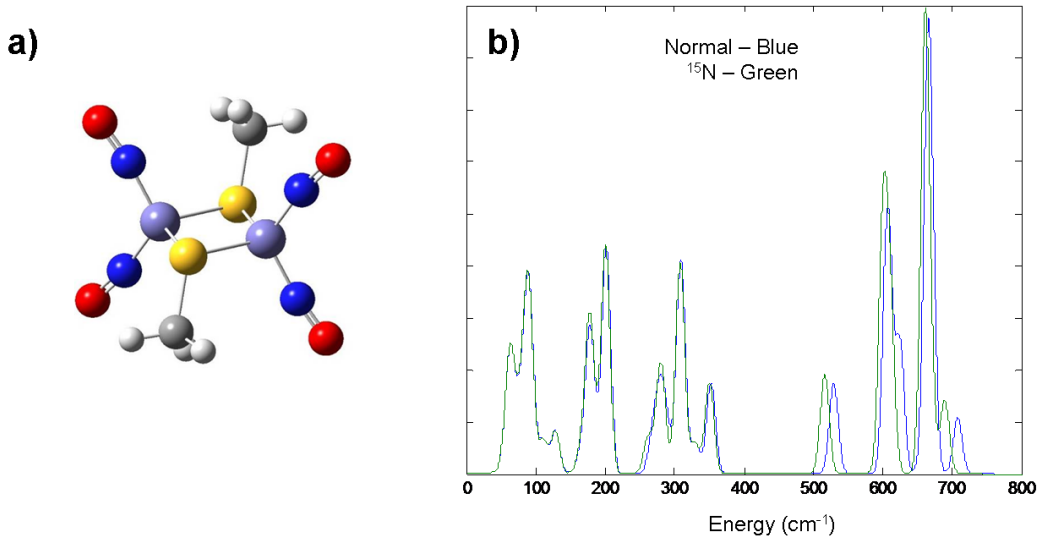

Figure 5.4: a) Optimised geometry of Roussin's red ester $[Fe_2(\mu\text{-}SCH_3)_2(NO)_4]$ with C_{2h} point group symmetry. b) DFT predicted NIS spectra of RRE with isotopic substitution of ^{15}N as indicated. Iron atoms are in pale purple, sulphur in yellow, nitrogen in dark blue, oxygen in red, carbon in grey and hydrogen in white.

features above this still generally well reproduced with regards to intensity but shifted to higher wavenumbers. Although vibrations cannot be fully described as resulting from one vibrational mode due to the symmetrical ring-like molecular structures, regions of the spectra can typically be categorised as resulting predominantly from particular combinations.

The broad feature below ∼100 cm^{-1} in the predicted spectra (Figure 5.4) results primarily from combinations of S-Fe-S twisting modes with slight N-Fe-N motion, although not enough to result in significant shifts in the ^{15}N spectrum. The sharp line at ∼175 cm^{-1} is primarily from S-Fe-S twisting/scissoring with some S-Me motion, overlapped with a line at ∼200 cm^{-1} arising from a S-Fe-S scissor/stretching mode. S-Fe-S asymmetric stretches lead to lines at ∼280 cm^{-1} and ∼310 cm^{-1}. Features at the high wavenumber region (>∼ 450 cm^{-1}) result from N-Fe-N motion with lines at ∼530 cm^{-1} (N-Fe-N wagging), ∼605 cm^{-1}

Table 5.1: Comparison of selected geometric parameters between reported X-ray crystallographic structure [15] and DFT optimised values for Roussin's red ester.

Parameter	**Experiment [15]**	**DFT**
Fe-S	2.26 Å	2.24 Å
Fe-N	1.68 Å	1.65 Å
N-O	1.17 Å	1.17 Å
S-C	1.79 Å	1.84 Å
S-Fe-S	106.9 °	107.8 °
Fe-S-Fe	73.1 °	72.2 °
N-Fe-N	117.4 °	118.7 °

(symmetric stretch) and ∼665 cm^{-1} (asymmetric stretch) resulting in the only significant ^{15}N shifts.

Single Persulphide Roussin's Red Ester

As a result of the differing ligations, the single persulphide Roussin's red ester was found to be of C_s point group symmetry due to the loss of the inversion centre and mirror plane, giving the geometry shown in Figure 5.5a. The geometry of the $[Fe_2S_2(NO)_4]$ subunit was found to be virtually identical to that of the standard RRE (see appendix D), with the persulphide S-S bond of length 2.12 Å. The pattern of lines in the NIS spectra in 5.5b for this species is very similar to that of the standard thiolate RRE despite the change in symmetry. This persulphide form does however allow for the introduction of an ^{34}S label on the cystine group, confirming the assignment of S-Fe-S stretching motions in the middle region (∼250-450 cm^{-1}) as having significant sulphur motion. The main difference is that the feature at ∼175 cm^{-1} (S-Fe-S twist/scissor) is of lower intensity compared to the analogous line in the RRE spectra relative to the neighbouring S-Fe-S scissoring feature at ∼200 cm^{-1}.

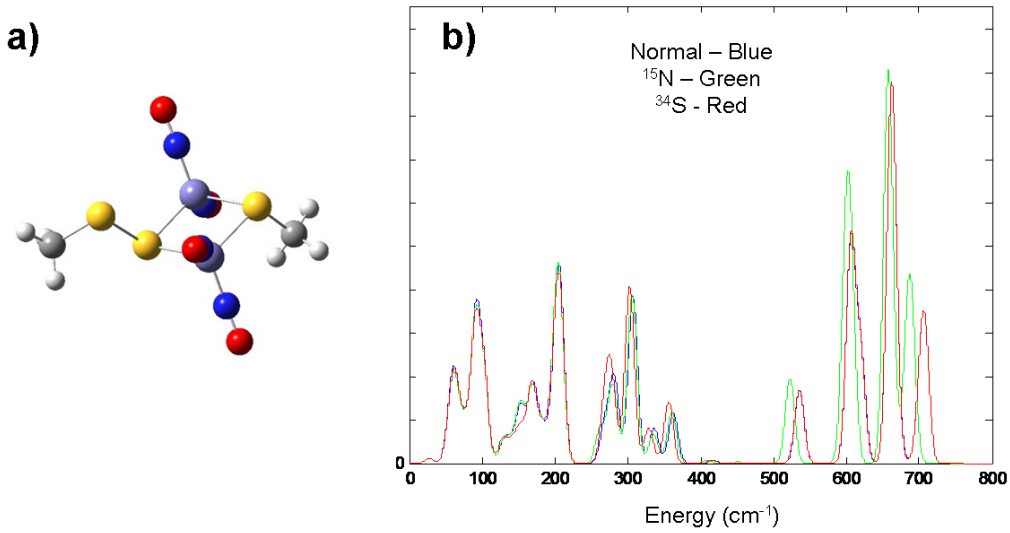

Figure 5.5: a) Optimised geometry of Roussin's red ester with single persulphide bridge [Fe_2(μ-SCH3)(μ-SSCH3)$(NO)_4$] with C_s point group symmetry. b) DFT predicted NIS spectra of single persulphide RRE with isotopic substitution of ^{15}N and ^{34}S as indicated.

Double Persulphide Roussin's Red Ester

The double persulphide Roussin's red ester was successfully optimised using C_{2h} point group symmetry constraints to give the structure shown in Figure 5.6a and was also found to have a similar core geometry to that of the other RRE species considered here. The predicted NIS spectra shown in Figure 5.6b demonstrate significant differences in the 100-400 cm^{-1} region compared with the RRE and single persulphide form. The lines at ~200 (S-Fe-S scissoring/stretching), ~140 (S-Fe-S wagging) and ~160 (Fe-S-Fe scissoring) cm^{-1} all increase significantly in intensity as well as becoming slightly more separated resulting in a distinctive fingerprint. Between 230 and 400 cm^{-1} the spectra is similar to the other RRE species, but with the medium intensity features at the upper end (S-Fe-S Scissor/Stretch) being slightly less separated from the stretching/rocking lines at ~360 cm^{-1}.

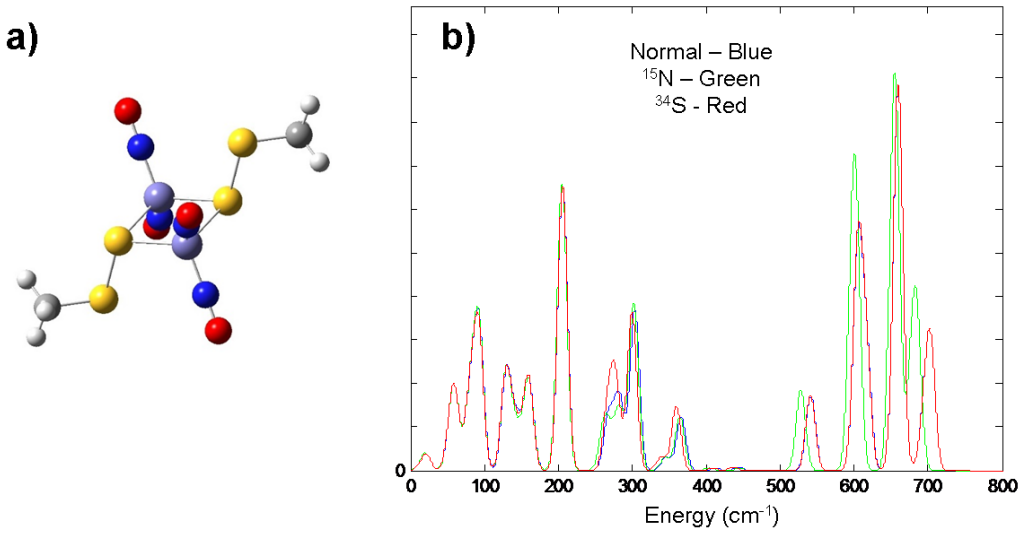

Figure 5.6: a) Optimised geometry of Roussin's red ester with double persulphide bridge [$Fe_2(\mu$-$SSCH3)_2(NO)_4$] with C_{2h} point group symmetry. b) DFT predicted NIS spectra of double persulphide RRE with isotopic substitution of ^{15}N and ^{34}S as indicated.

Roussin's Red Ester/Salt

The Roussin's red ester/salt hybrid (Figure 5.7a) was found to have C_s symmetry with a distorted molecular plane, unlike the other RRE structures, and the resulting NIS spectra (Figure 5.7b) were also found to be particularly distinctive. The features below 100 cm^{-1} are similar to the normal RRE, albeit with a slightly different intensity distribution, arising from combinations of S-Fe-S twisting and slight N-Fe-N recoiling motions with negligible isotopic shifts. The double peaked feature centred at ~190 cm^{-1} (resulting from S-Fe-S rocking and scissor/stretching respectively) displays greater separation in the ester salt compared to the RRE. Features between 220 and 450 cm^{-1} are similarly spread out with lower intensity. The N-Fe-N wag/Fe-S-Fe rock feature at ~500 cm^{-1} is also shifted considerably lower than in the RRE. The region above ~550 cm^{-1} is also particularly characteristic with overlapping features and no small peak at the upper end. The pattern of isotopic shifts, with ^{34}S shifts mainly in the mid

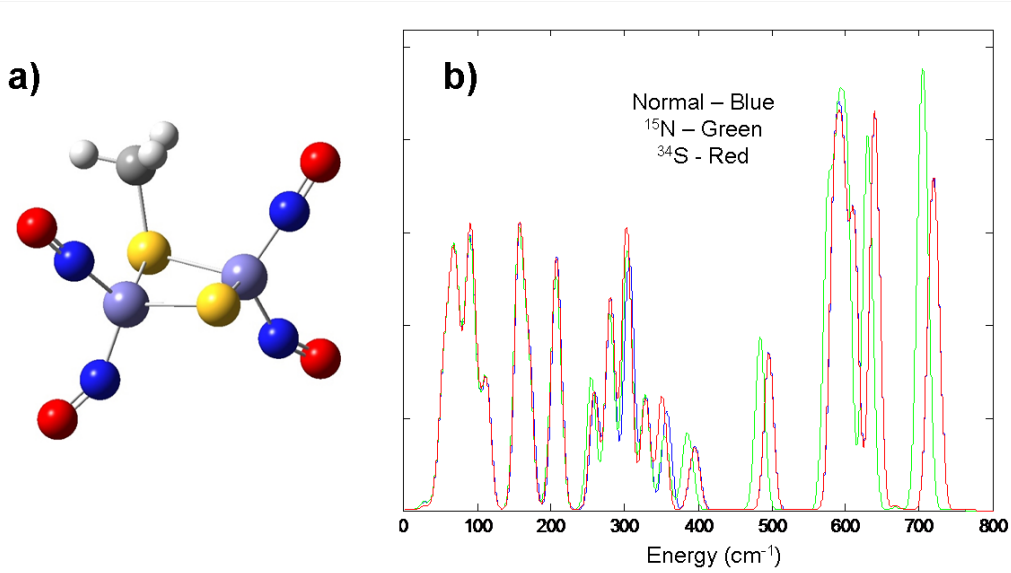

Figure 5.7: a) Optimised geometry of Roussin's red ester/salt $[Fe_2(\mu\text{-}S)(\mu\text{-}SCH3)(NO)_4]^{-1}$ with C_s point group symmetry. b) DFT predicted NIS spectra of Roussin's red ester/salt with isotopic substitution of ^{15}N and ^{34}S as indicated.

region and substantial ^{15}N shifts at the upper end, is still consistent with the pattern observed in the other clusters.

5.3.2 Roussin's Black Salts

Roussin's Black Salt

The optimised geometry (Figure 5.8a) again shows excellent agreement (Table 5.2) with both previous experimental [16] and computational [219] studies of Roussin's black salt. The NO pairs are distorted away from the [2Fe-2S] subunit, however the bond lengths are still generally similar for analogous structural motifs for the RRE shown in Table 5.1.

Predicted spectra again show good agreement with previously reported spectra of RBS [15] with regards to the pattern of lines and intensities but with a systematic shift of up to 60 cm^{-1} discernible at higher wavenumbers. The broad features up to 100 cm^{-1} are a combination of Fe-N=O bending modes with some slight

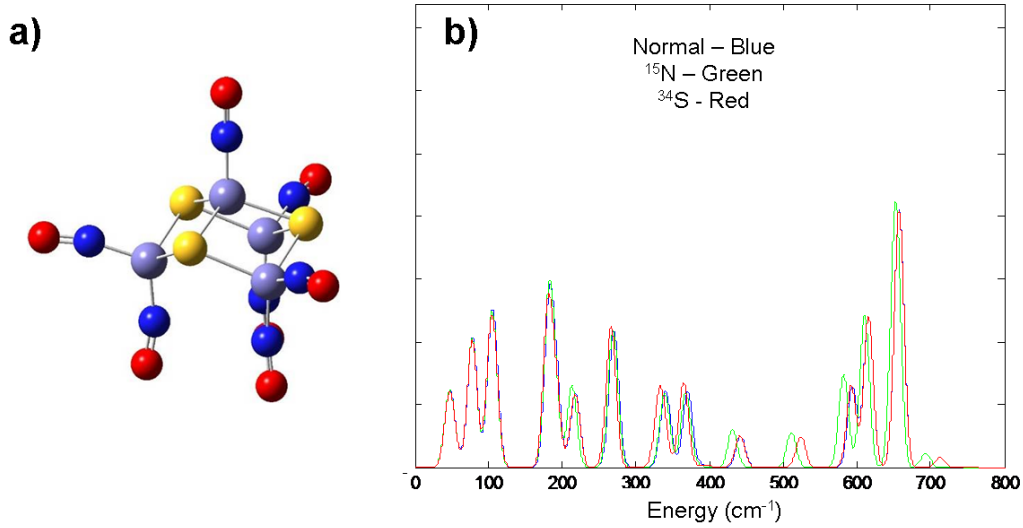

Figure 5.8: a) Optimised geometry of Roussin's black salt $[Fe_4(\mu\text{-}S)_3(NO)_7]^-$ with C_{3v} point group symmetry. b) DFT predicted NIS spectra of RBS with isotopic substitution of ^{15}N and ^{34}S as indicated.

S-Fe-S twisting. A sharp feature at ∼110 cm^{-1} results from a Fe-S-Fe scissoring motion. The slightly asymmetric line at ∼180 cm^{-1} results from two overlapping vibrations of predominantly S-Fe-S scissoring/rocking character which produce a slight shift upon ^{34}S substitution. The band at ∼280 cm^{-1} is a combination of S-Fe-S stretches with some N-Fe-N twisting and those at ∼350 cm^{-1} and ∼360 cm^{-1}, arising from S-Fe-S stretching and rocking, are more prominent than the equivalent bands in the majority of the RRE spectra. As with the RRE species, spectral features over 400 cm^{-1} result from N-Fe-N modes, confirmed by the clear ^{15}N shifts observed in the majority of lines in this region. The major first line in this region at ∼595 cm^{-1} arises from N-Fe-N wagging with slight S-Fe recoil. The prominent lines at ∼620 cm^{-1} and ∼600 cm^{-1} result from symmetric and asymmetric N-Fe-N stretches respectively with some S-Fe-S recoil.

Table 5.2: Comparison of selected geometric parameters between reported X-ray crystallographic structure [16] and DFT optimised values for Roussin's black salt. Fe_c is used to denote the unique central iron atom.

Parameter	**Experiment [16]**	**DFT**
Fe_c-Fe	2.70 Å	2.67 Å
Fe-Fe	3.57 Å	3.55 Å
Fe_c-S	2.21 Å	2.18 Å
Fe/Fe_c-N	1.66 Å	1.64 Å
N-O	1.16 Å	1.18 Å
S-Fe-S	104.1 °	103.5 °
S-Fe_c-S	107.2 °	108.2 °
Fe-S-Fe	104.8 °	104.5°
Fe-S-Fe_c	74.3 °	74.1 °

Roussin's Black Ester (Single Thiolate)

Introduction of a single thiolate group to the RBS cluster lowers the symmetry from the C_{3v} point group to C_s with a slight distortion of the single NO away from the methyl group along the mirror plane(Figure 5.9a). As with the other clusters, features up to ∼100 cm^{-1} arising from N-Fe-N and Fe-S-Fe scissoring motions result in a broad feature in the predicted NIS spectra shown in Figure 5.9b. In the region above this though the lowering of symmetry has a significant effect as the degeneracy of several features is lifted, leading to broader lines and more discernible features. In particular in the middle region (∼250 - 500 cm^{-1}) of the spectra a S-Fe-S wagging vibration occurs at ∼140 cm^{-1} that is not discernible in the RBS spectra as well as an additional peak at ∼240 cm^{-1} arising from S-Fe-S twisting/stretching. The feature at ∼380 cm^{-1} resulting from multiple S-Fe-S stretching modes is broader and of lower intensity than in the RBS. The pattern of bands in the N-Fe-N region of the spectrum is also slightly modified by a

splitting of the line at ∼590 cm^{-1} from N-Fe-N wagging modes.

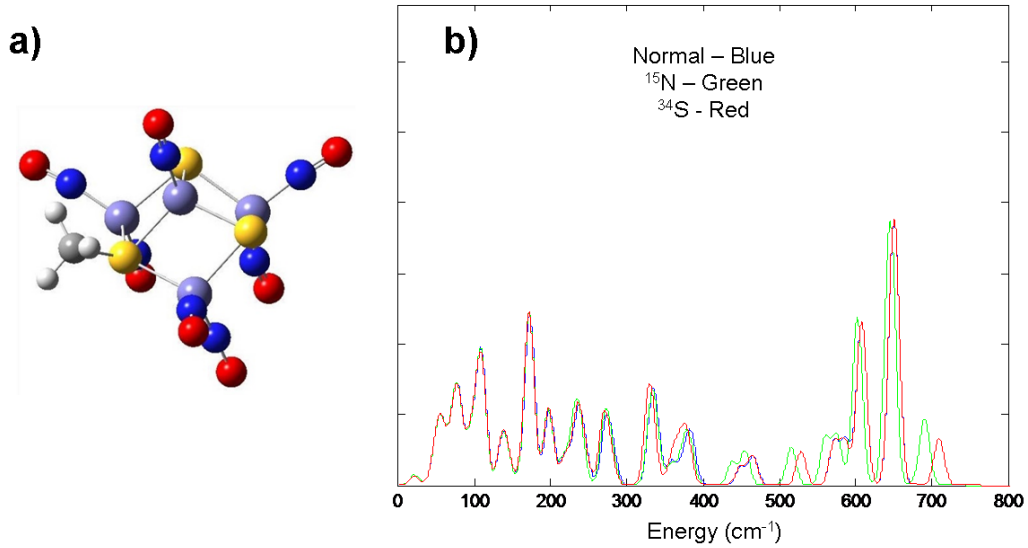

Figure 5.9: a) Optimised geometry of Roussin's black ester with single thiolate bridge [$Fe_4(\mu\text{-}S)_2(\mu\text{-}SCH_3)(NO)_7$] with C_s point group symmetry. b) DFT predicted NIS spectra of RBE with single thiolate bridge and isotopic substitution of ^{15}N and ^{34}S as indicated.

Roussin's Black Ester (Double Thiolate)

Addition of a second thiolate to the Roussin's black ester cluster again results in a structure with C_s symmetry (Figure 5.10a). As with the single thiolate RBE, the lower symmetry results in a lifting of degeneracy compared with the RBS spectra leading to an increase in the number of discernible features for the double thiolate species (Figure 5.10b), however there are several notable differences. In particular the low and low-middle regions of the spectra form a single broad feature as a result of overlap, whereas the 200 to 400 cm^{-1} region of the spectra is well separated compared with the single thiolate group. The pattern of the N-Fe-N region is also modified when compared with the single thiolate species with the N-Fe-N wagging mode shifting by ∼20 cm^{-1}, resulting in six well separated lines above 400 cm^{-1}.

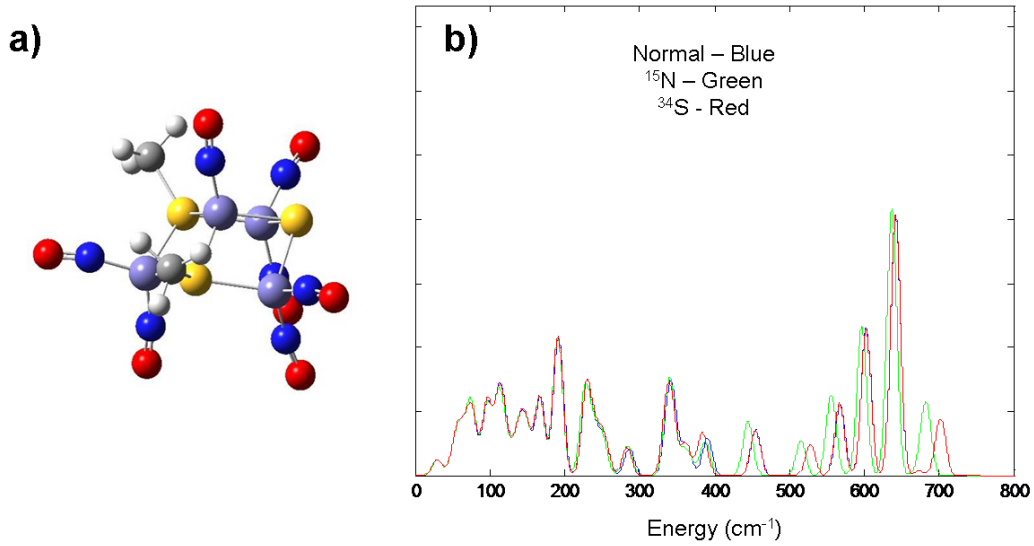

Figure 5.10: a) Optimised geometry of Roussin's black ester with two thiolate bridges $[Fe_4(\mu\text{-}S)(\mu\text{-}SCH_3)_2(NO)_7]^+$ *with* C_s *point group symmetry. b) DFT predicted NIS spectra of RBE with two thiolate bridges and isotopic substitution of* ^{15}N *and* ^{34}S *as indicated.*

Roussin's Black Ester (Triple Thiolate)

By replacing all the bridging sulphur atoms with thiolates, the geometry was successfully optimised (Figure 5.11a) with the same C_{3v} point group symmetry as the standard RBS. The resulting NIS spectra (Figure 5.11b) is significantly different to those of RBS and the other RBE species. The vibrational modes up to ∼150 cm^{-1} primarily result from combinations of methyl motions unlike the other clusters. The intense peaks at ∼235 and 350 cm^{-1} arise from overlapping combinations of Fe-S-Fe stretching modes and are particularly characteristic of this structure. The N-Fe-N region of the spectra bears close resemblance to that of the double thiolate structure with six well separated lines above 400 cm^{-1}. As all sulphur atoms have been replaced with thiolate ligands, no ^{34}S substitutions occur, therefore only ^{15}N isotopic spectra were calculated.

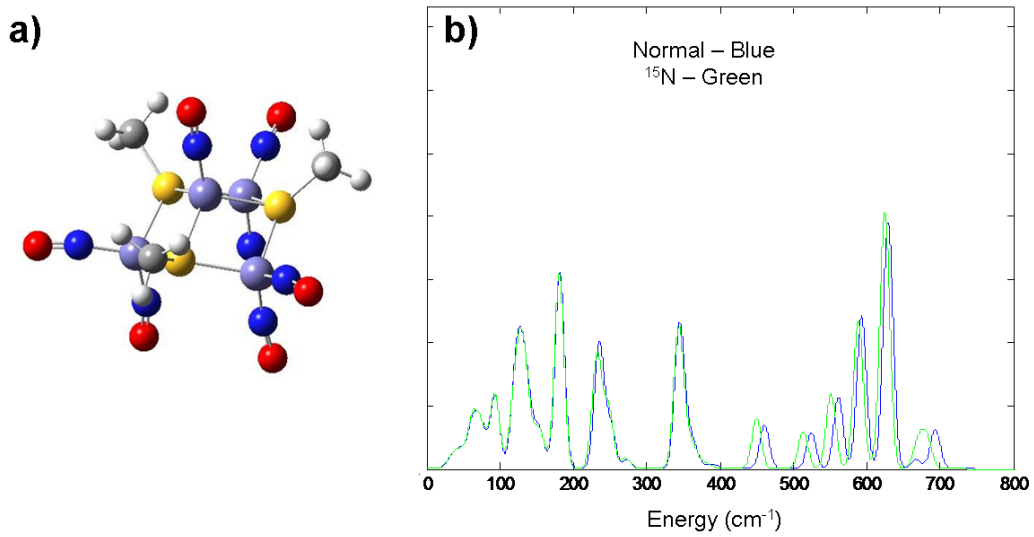

Figure 5.11: a) Optimised geometry of Roussin's black ester with three thiolate bridges $[Fe_4(\mu\text{-}SCH_3)_3(NO)_7]^{2+}$ *and* C_{3v} *point group symmetry. b) DFT predicted NIS spectra of RBE with three thiolate bridges and isotopic substitution of* ^{15}N *as indicated.*

Roussin's Black Ester (Single Persulphide)

The singly substituted persulphide thiolate version of the RBS used to model cystine coordination of this complex was successfully optimised with C_s symmetry (Figure 5.12a). As with the single thiolate RBE structure, the persulphide RBE demonstrated a similar NIS spectra (5.12b) to that of RBS in the region below 120 cm^{-1}, although slightly less clearly defined. The features between 120 and 260 cm^{-1} are broader with less defined line shapes than both the RBS and single thiolate RBE. The region between 400 and 500 cm^{-1} is similar to the single thiolate RBE, albeit with greater peak separation but above this region the remaining N-Fe-N modes are identical.

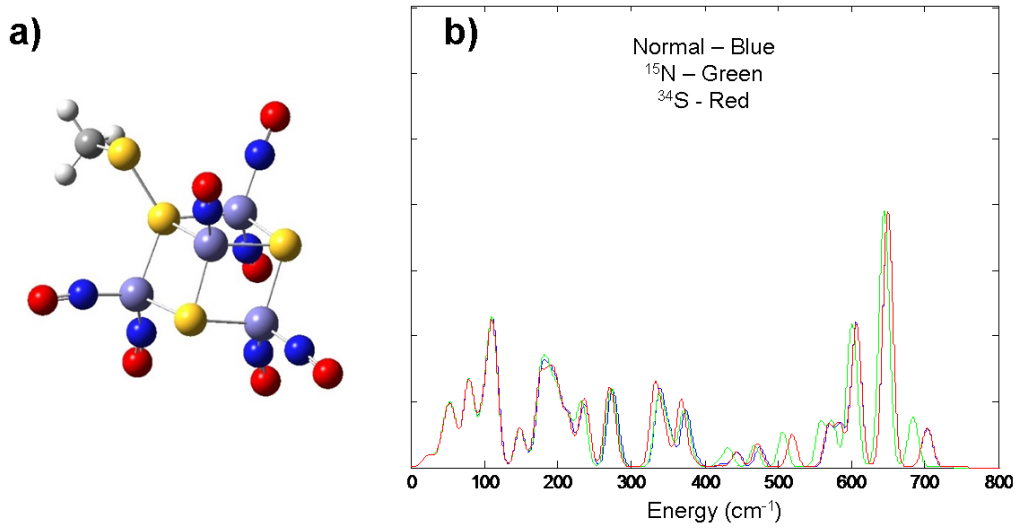

Figure 5.12: a) Optimised geometry of Roussin's black ester with single persulphide bridge $[Fe_4(\mu\text{-}S)_2(\mu\text{-}SSCH_3)(NO)_7]$ with C_s point group symmetry. b) DFT predicted NIS spectra of RBE with single persulphide bridge and isotopic substitution of ^{15}N and ^{34}S as indicated.

5.3.3 Comparison with Experimental Data

Figure 5.13 shows the experimental spectra of nitrosylated WhiD and NsrR proteins and confirms the general trend observed in the DFT calculations that ^{34}S shifts occur mainly in the middle region of the spectra and ^{15}N occur at the high wavenumber region. The predicted spectra for the Roussin's red salt/ester structure and double persulphide Roussin's red ester with their distinctive S-Fe-S and N-Fe-N regions indicate that these structures should be clearly identifiable, and thus can be excluded. However, the spectra predicted for the single persulphide RRE demonstrated closer agreement with that of the unsubstituted RRE, and thus may not be clearly distinguished by this technique. Furthermore, although the triple thiolate RBE may be distinguished from the RBS spectra, the single and double thiolate and single persulphide thiolate forms may not be so readily distinguished, especially when the effect of the protein environment is considered,

and therefore these structures may be consistent with the experimental data.

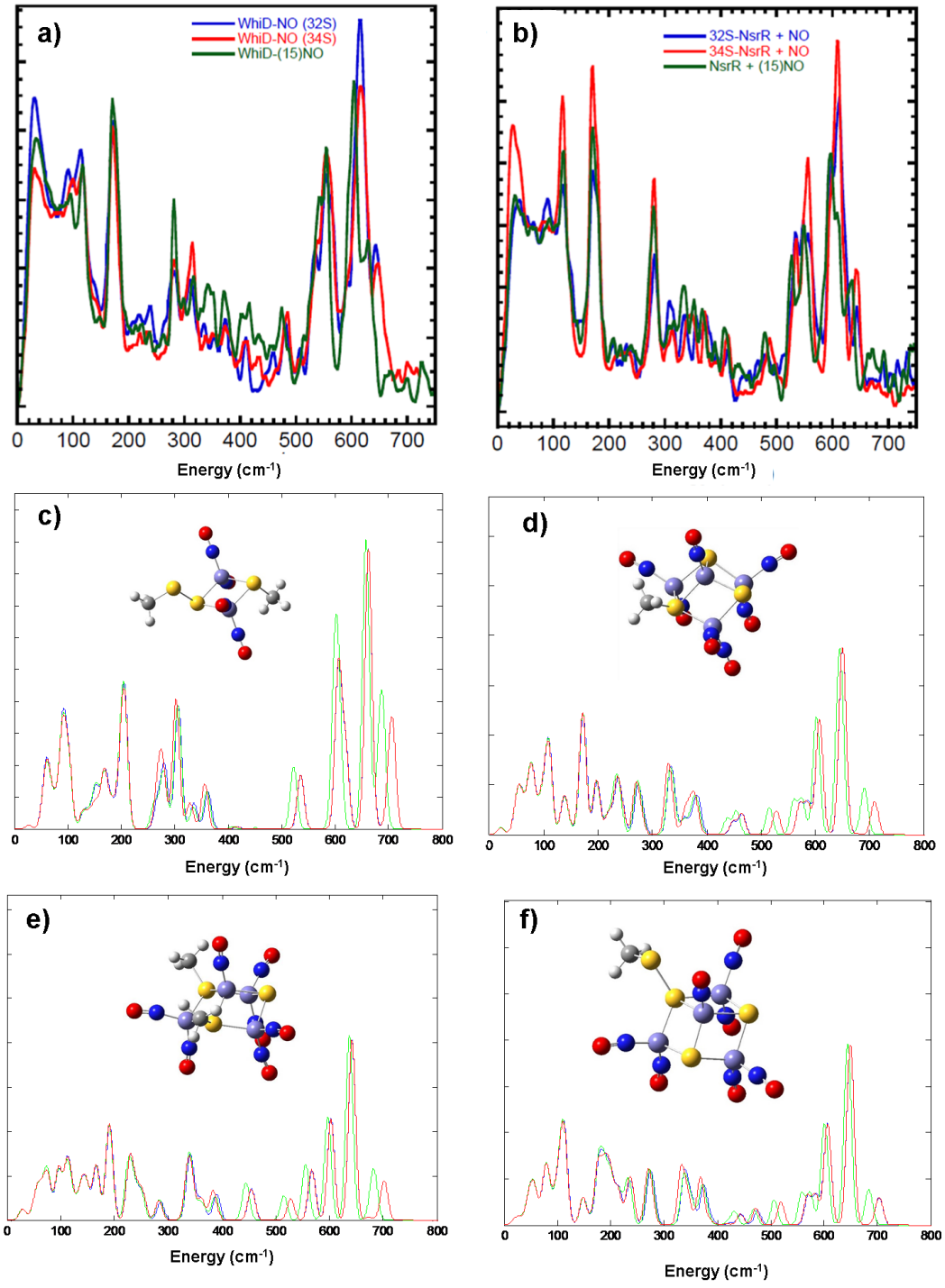

Figure 5.13: Comparison of experimental NIS spectra for nitrosylated a) WhiD and b) NsrR proteins with spectra predicted for c) single persulphide RRE, d) single thiolate RBS, e) double thiolate RBS and f) single single persulphide RBS. ^{15}N *and* ^{34}S *isotopic substitutions as indicated.*

5.4 Conclusion

In this chapter, DFT calculations have been shown to be able to reliably reproduce the features, including isotopic shifts, observed in the nuclear inelastic scattering, Raman and IR spectra of the Roussin's red ester and Roussin's black salt model compounds in the < 700 cm^{-1} region, without detailed knowledge of the protein environment. The results of these simulations have then been used to aid the analysis of experimental spectra through relating spectral features of the lower frequency region to the underlying vibrational modes.

This procedure was then expanded to hypothetical ligated variants, allowing the ability of NIS to discriminate between closely related iron sulphur clusters to be evaluated, with several important outcomes. Firstly, it has been shown that although the C_{2h} point group RRE and double persulphide version can be readily distinguished by NIS, the C_s point group single persulphide version cannot. Secondly, in the case of putative RBE structures, only the triple thiolate substituted form could be readily discerned from the RBS using NIS. This therefore means that the experimental NIS spectrum is consistent with the presence of a cluster with an RRE and RBE-like form and shows that, where possible, this technique should be supplemented through the use of additional vibrational spectroscopies.

This combined approach could also be further extended through the use of MD to determine likely ligation geometries, as has been recently applied to an [Fe4-S4] ferredoxin [18]. This could not only provide more accurate predicted spectra, but also act as a useful test bed to determine the degree to which this effects the experimental data.

Chapter 6

Final Remarks and Future Works

In Chapters 2 and 3 the EPR spectra of two topical soft matter systems, namely lyotropic liquid crystals and DNA, have been investigated, with several important outcomes. Firstly, the model-free framework has been shown to provide good results for the prediction of EPR from MD trajectories. In the case of the lyotropic liquid crystals in Chapter 2 good agreement between prediction and experiment was observed for the majority of aggregates simulated using the GAFF forcefield. Excellent agreement between MD and EPR is demonstrated for the micellar spectra in particular, including reproducing the observed temperature dependence. Some small differences between the predicted and experimental spectra of the rod-like systems were attributed to simplifications arising from how periodicity is treated in MD. Future studies could improve on this through the use of longer rods to enable greater flexibility and reduce the impact of boundary effects. This chapter also highlighted how a combined MD-EPR approach can be used both as a thorough test of forcefields and theoretical models for the interpretation of data. In particular calculation of the C-H order parameters for the host molecules showed that GAFF produces overly ordered alkyl chains in surfactant/water systems, which was not clearly evident from geometric parameters alone. This resulted in disagreement between predicted and experimental spectra for the DTAC lamellar phase where the low water content caused the head group

of the nitroxide probe to remain in the alkyl region of the lamellae. Conversely, the spectra of the SDS lamellar phase demonstrated far better agreement with experiment as a result of the head groups of the spin probes remaining exposed to the solvent throughout.

In Chapter 3 structural fitting and principal component analysis allowed the global and local motions of DNA to be explicitly separated. This enabled a detailed analysis of the complex internal dynamics of the spin labels, as well as comparison of the global motions with those predicted by rigid body hydrodynamic theory. The local component of the spin label motion was shown to have multiple modes, reflecting the many degrees of freedom associated with the complex structure of DNA. The global motion was confirmed to be axial with $\tau_{\parallel} \sim 2\tau_{\perp}$ for duplex DNA of this length. Analysis of the NRMSD and helical geometric parameters showed that the modified cytosine spin label, C*, was non-perturbing to the geometry of duplex DNA. The quinolonyl derived Q spin label was shown to accurately report the global dynamics of DNA by comparison between directly and model-free predicted spectra. Agreement between predicted and experimental spectra was found to be good for all systems, confirming the accuracy of the parmbsc1 forcefield.

Extension of the techniques developed in these chapters to the four-stranded Holliday junction, which is of significance in the study of how the body responds to DNA damage (cancer), with the thymine-derived T* spin label is currently in progress. As the Holliday junction is known to exhibit several conformational modes, which may exhibit substantially different global diffusional behaviour, spin label CW-EPR could prove to be a useful diagnostic tool. Another way these techniques could be utilised would be the simulation of DNA units of significantly greater lengths, possibly through the use of coarse grain techniques, in order to further test the validity of hydrodynamic theory. As longer DNA may be more flexible, treatment as a rigid cylinder could be less valid than for the short sequences used here which would be of consequence as this theory currently underpins

the majority of motional NMR and EPR fitting for these systems. Additionally, a hybrid technique has since been developed and applied to the DNA simulations of Chapter 3 which uses the separated motions to explicitly determine the averaging effect of the local component on the magnetic parameters and thereby provide a further link between MD and EPR modelling. This is currently in preparation for publication.

In Chapter 4 the EPR spectra of two molybdenum complexes were investigated. Firstly complex ***B*** which had previously been characterised experimentally by X-ray crystallography and EPR was used as a test of method for DFT with good results. This was then extended to investigate the geometry of unstable intermediate species ***A***, allowing the proposed electron transfer scheme to be confirmed by the agreement of predicted and experimental EPR spectra.

In Chapter 5 DFT was used to provide a complete assignment of the lower frequency vibrational modes of RRE and RBS model complexes and found to generally be in good agreement with reported experimental NIS data. In particular DFT was found to reliably predict isotope shifts as well as major bands resulting from groups of vibrations. This approach was then expanded to a series of hypothetical ligated RRE and RBS species in order to investigate the ability of NIS to distinguish between these structures. It was found that several ligation schemes could not be readily identified from the model compounds. Specifically, although the double persulphide and ester salt RRE-like structures could be distinguished from the RRE, the single persulphide version could not. Similarly, in the case of the RBE-like species, only the triple thiolate substituted species could be unambiguously identified through NIS alone. As a result, this demonstrated that the NIS data for the nitrosylated WhiD and NsrR proteins was consistent with previous experimental data if an RBE-like species is considered. This chapter also highlighted how NIS could be used in combination other vibrational techniques, such as Raman and IR spectroscopy, and DFT in order to identify iron-sulphur clusters in a more selective manner.

6.1 Other publications not reported in this work

- R. A. Arthurs, M. Ismail, C. C. Prior, V. S. Oganesyan, P. N. Horton, S. J. Colesand, C. J. Richards; Enantiopure Ferrocene-Based Planar-Chiral Iridacycles: Stereospecific Control of Iridium-Centred Chirality; *Chemistry - A European Journal*, 2016; [220]

Bibliography

[1] V. S. Oganesyan and C. Prior. Prediction of EPR Spectra of Lyotropic Liquid Crystals using a Combination of Molecular Dynamics Simulations and the Model-Free Approach. *Chem. Eur. J.*, 23:13192–13204, 2017.

[2] C. Prior, L. R. Webster, S. K. Ibrahim, J. A. Wright, A. F. Alghamdi, V. S. Oganesyan, and C. J. Pickett. EPR detection and characterisation of a paramagnetic Mo(III) dihydride intermediate involved in electrocatalytic hydrogen evolution. *Dalton Trans.*, 45:2399–2403, 2016.

[3] P. N. Serrano, H. Wang, J. C. Crack, C. Prior, M. I. Hutchings, A. J. Thomson, S. Kamali, Y. Yoda, J. Zhao, M. Y. Hu, E. E. Alp, V. S. Oganesyan, N. E. LeBrun, and S. P. Cramer. Nitrosylation of Nitric-Oxide-Sensing Regulatory Proteins Containing [4Fe-4S] Clusters Gives Rise to Multiple Iron-Nitrosyl Complexes. *Angew. Chem. Int. Ed.*, 55:14575–14579, 2016.

[4] S. Stoll and A. Schweiger. EasySpin, a comprehensive software package for spectral simulation and analysis in EPR. *J. Magn. Reson.*, 178:42 – 55, 2006.

[5] W. K. Subczynski, M. Pasenkiewicz-Gierula, R. N. McElhaney, J. S. Hyde, and A. Kusumi. Molecular Dynamics of 1-Palmitoyl-2-oleoylphosphatidylcholine Membranes Containing Transmembrane α-Helical Peptides with Alternating Leucine and Alanine Residues. *Biochemistry*, 42:3939–3948, 2003.

[6] J. F. Ellena, R. N. Dominey, and D. S. Cafiso. Molecular dynamics in sodium dodecyl sulfate micelles elucidated using carbon-13 and proton spin-lattice relaxation, carbon-13 spin-spin relaxation, and proton nuclear Overhauser effect spectroscopy. *J. Phys. Chem.*, 91:131–137, 1987.

[7] O. Soderman, G. Carlstrom, U. Olsson, and T. C. Wong. Nuclear magnetic resonance relaxation in micelles. Deuterium relaxation at three field strengths of three positions on the alkyl chain of sodium dodecyl sulphate. *J. Chem. Soc., Faraday Trans.*, 84:4475–4486, 1988.

[8] G. Wikander, P. O. Eriksson, E. E. Burnell, and G. Lindblom. ESR line shapes in lyotropic systems: the micellar and liquid-crystalline phases of the dodecyltrimethylammonium chloride/water system. *J. Phys. Chem.*, 94:5964–5972, 1990.

[9] T. R. Miller, S. C. Alley, A. W. Reese, M. S. Solomon, W. V. McCallister, C. Mailer, B. H. Robinson, and P. B. Hopkins. A Probe for Sequence-Dependent Nucleic Acid Dynamics. *J. Am. Chem. Soc.*, 117:9377–9378, 1995.

[10] P. L. Fischhaber, A. W. Reese, T. Nguyen, J. J. Kirchner, E. J. Hustedt, B. H. Robinson, and P. B. Hopkins. Synthesis of Duplex DNA Containing a Spin Labeled Analog of 2 Deoxycytidine. *Nucleosides Nucleotides*, 16:365–377, 1997.

[11] A. W. Reese. *Analysis of CW-EPR Spectra and the Internal Dynamics of DNA*. PhD thesis, School of Chemistry, University of Washington, 1996.

[12] S. A. Fairhurst, R. A. Henderson, D. L. Hughes, S. K. Ibrahim, and C. J. Pickett. An intramolecular W-H$\cdots$O=C hydrogen bond? Electrosynthesis and X-ray crystallographic structure of [WH3(η1-OCOMe)(Ph2PCH2CH2PPh2)2]. *J. Chem. Soc., Chem. Commun.*, pages 1569–1570, 1995.

[13] W. R. Scheidt, S. M. Durbin, and J. T. Sage. Nuclear resonance vibrational spectroscopy NRVS. *J. Inorg. Biochem.*, 99:60 – 71, 2005.

[14] Z. Liang, G. Wikander, and P. O. Westlund. Slow motion electron spin resonance line shapes of lyotropic liquid crystals in hexagonal phase. *J. Chem. Phys.*, 102:1471–1480, 1995.

[15] Z. J. Tonzetich, H. Wang, De. Mitra, C. E. Tinberg, L. H. Do, F. E. Jenney, M. W. W. Adams, S. P. Cramer, and S. J. Lippard. Identification of Protein-Bound Dinitrosyl Iron Complexes by Nuclear Resonance Vibrational Spectroscopy. *J. Am. Chem. Soc.*, 132:6914–6916, 2010.

[16] S. D'Addario, F. Demartin, L. Grossi, M. C. Iapalucci, F. Laschi, G. Longoni, and P. Zanello. Redox behavior of the black roussinate heptanitrosyltrisulfotetraferrate(1-) monoanion. Synthesis and spectroscopic characterization of the [Fe4S3(NO)7]n- (n = 2, 3) anions and crystal structures of the mono- and dianions in their [NEt4]+ salts. *Inorg. Chem.*, 32:1153–1160, 1993.

[17] Z. Liang, J. H. Freed, R. S. Keyes, and A. M. Bobst. An Electron Spin Resonance Study of DNA Dynamics Using the Slowly Relaxing Local Structure Model. *J. Phys. Chem. B*, 104:5372–5381, 2000.

[18] D. Mitra, V. Pelmenschikov, Y. Guo, D. A. Case, H. Wang, W. Dong, M. Tan, T. Ichiye, F. E. Jenney, M. W. W. Adams, Y. Yoda, J. Zhao, and S. P. Cramer. Dynamics of the [4Fe-4S] Cluster in Pyrococcus furiosus D14C Ferredoxin via Nuclear Resonance Vibrational and Resonance Raman Spectroscopies, Force Field Simulations, and Density Functional Theory Calculations. *Biochemistry*, 50:5220–5235, 2011.

[19] M. J. N. Junk. *Electron Paramagnetic Resonance Theory*, pages 7–52. Springer Berlin Heidelberg, Berlin, Heidelberg, 2012.

[20] P. C. Jost, O. H. Griffith, R. A. Capaldi, and G. Vanderkooi. Evidence for Boundary Lipid in Membranes. *Proc. Nat.l Acad. Sci. USA*, 70:480–484, 1973.

[21] W. K. Subczynski, J. Widomska, and J. B. Feix. Physical properties of lipid bilayers from epr spin labeling and their influence on chemical reactions in a membrane environment. *Free Radic. Biol. Med.*, 46:707–718, 2009.

[22] J. Widomska, M. Raguz, J. Dillon, E. R. Gaillard, and W. K. Subczynski. Physical properties of the lipid bilayer membrane made of calf lens lipids: Epr spin labeling studies. *Biochim. Biophys. Acta.*, 1768:1454–1465, 2007.

[23] M. D. Matteucci and M. H. Caruthers. Synthesis of deoxyoligonucleotides on a polymer support. *J. Am. Chem. Soc.*, 103:3185–3191, 1981.

[24] E. J. Hustedt, A. Spaltenstein, J. J. Kirchner, P. B. Hopkins, and B. H. Robinson. Motions of short DNA duplexes: An analysis of DNA dynamics using an EPR-active probe. *Biochemistry*, 32:1774–1787, 1993.

[25] T.M. Okonogi, A.W. Reese, S.C. Alley, P.B. Hopkins, and B.H. Robinson. Flexibility of Duplex DNA on the Submicrosecond Timescale. *Biophys. J.*, 77:3256 – 3276, 1999.

[26] E. J. Hustedt, J. J. Kirchner, A. Spaltenstein, P. B. Hopkins, and B. H. Robinson. Monitoring DNA Dynamics Using Spin-Labels with Different Independent Mobilities. *Biochemistry*, 34:4369–4375, 1995.

[27] G. Palmer. The electron paramagnetic resonance of metalloproteins. *Biochemical Society Transactions*, 13:548–560, 1985.

[28] J. M. Ribeiro, J. M. Hazzard, R. H. Nussenzveig, D. E. Champagne, and F. A. Walker. Reversible binding of nitric oxide by a salivary heme protein from a bloodsucking insect. *Science*, 260:539–541, 1993.

[29] F. A. Walker. Magnetic spectroscopic (epr, eseem, mssbauer, mcd and nmr) studies of low-spin ferriheme centers and their corresponding heme proteins. *Coord. Chem. Rev.*, 185:471–534, 1999.

[30] Y. E. Nesmelov and David D. T. Protein structural dynamics revealed by site-directed spin labeling and multifrequency epr. *Biophys. Rev.*, 2:91–99, 2010.

[31] O. H. Griffith and H. M. McConnell. A Nitroxide-Maletimide Spin Label. *Proc. Natl. Acad. Sci. USA*, 55:8–11, 1966.

[32] G.F. White, L. Ottignon, T. Georgiou, C. Kleanthous, G.R. Moore, A.J. Thomson, and V.S. Oganesyan. Analysis of nitroxide spin label motion in a proteinprotein complex using multiple frequency epr spectroscopy. *J. Magn. Reson.*, 185:191–203, 2007.

[33] C. F. Polnaszek and J. H. Freed. Electron spin resonance studies of anisotropic ordering, spin relaxation, and slow tumbling in liquid crystalline solvents. *J. Phys. Chem.*, 79:2283–2306, 1975.

[34] F. Chami, M. R. Wilson, and V. S. Oganesyan. Molecular dynamics and EPR spectroscopic studies of 8CB liquid crystal. *Soft Matter*, 8:6823–6833, 2012.

[35] D. L. Hughes, D. J. Lowe, M. Y. Mohammed, C. J. Pickett, and N. M. Pinhal. Determination of structural features of electrogenerated trans-[MoCl(NMe)(Ph2PCH2CH2PPh2)2]2+ by multinuclear electron paramagnetic resonance and electron nuclear double resonance spectroscopy and comparison of interatomic distances with those measured by X-ray analysis of the parent monocation. *Dalton Trans.*, pages 2021–2027, 1990.

[36] J. H. Freed. Anisotropic Rotational Diffusion and Electron Spin Resonance Linewidths. *J. Chem. Phys.*, 41:2077–2083, 1964.

[37] J. R. Morton and K. F. Preston. Atomic parameters for paramagnetic resonance data. *J. Magn. Reson.*, 30:577 – 582, 1978.

[38] H. M. Swartz, S. Boyer, P. Gast, J. F. Glockner, H. Hu, K. J. Liu, M. Moussavi, S. W. Norby, N. Vahidi, T. Walczak, M. Wu, and R. B. Clarkson. Measurements of pertinent concentrations of oxygen in vivo. *Magn. Reson. Med.*, 20:333–339, 1991.

[39] B. Guigliarelli, M. Asso, C. More, V. Augier, F. Blasco, J. Pommier, G. Giodano, and P. Bertrand. Epr and redox characterization of iron-sulfur centers in nitrate reductases a and z from escherichia coli. *Eur. J. Biochem.*, 207:61–68, 1992.

[40] M. J. Schmidt, A. Fedoseev, D. Bcker, J. Borbas, C. Peter, M. Drescher, and D. Summerer. EPR Distance Measurements in Native Proteins with Genetically Encoded Spin Labels. *ACS Chem. Biol.*, 10:2764–2771, 2015.

[41] J. Fuchs, N. Groth, T. Herrling, R. Milbradt, G. Zimmer, and L. Packer. Electron Paramagnetic Resonance (EPR) Imaging in Skin: Biophysical and Biochemcial Microscopy. *J. Invest. Dermatol.*, 98:713 – 719, 1992.

[42] M. A. Bahri, M. Hoebeke, A. Grammenos, L. Delanaye, N. Vandewalle, and A. Seret. Investigation of SDS, DTAB and CTAB micelle microviscosities by electron spin resonance. *Colloids Surf. A*, 290:206 – 212, 2006.

[43] G. Breit and I. I. Rabi. Measurement of Nuclear Spin. *Phys. Rev.*, 38:2082–2083, 1931.

[44] A. G. Redfield. On the Theory of Relaxation Processes. *IBM J. Res. Dev.*, 1:19–31, 1957.

[45] A.G. Redfield. The Theory of Relaxation Processes. *Adv. Magn. Opt. Reson.*, 1:1 – 32, 1965.

[46] E. Meirovitch, A. Nayeem, and J. H. Freed. Analysis of protein-lipid interactions based on model simulations of electron spin resonance spectra. *J. Phys. Chem.*, 88:3454–3465, 1984.

[47] V.S. Oganesyan. A novel approach to the simulation of nitroxide spin label EPR spectra from a single truncated dynamical trajectory. *J. Magn. Reson.*, 188:196 – 205, 2007.

[48] V. S. Oganesyan. A general approach for prediction of motional EPR spectra from Molecular Dynamics (MD) simulations: application to spin labelled protein. *Phys. Chem. Chem. Phys.*, 13:4724–4737, 2011.

[49] V. S. Oganesyan. Chapter 2 Computational approaches for simulating motional EPR spectra. In *Electron Paramagnetic Resonance*, volume 24, pages 32–61. The Royal Society of Chemistry, 2015.

[50] A. Polimeno, V. Barone, and J. H. Freed. *Stochastic Methods for Magnetic Resonance Spectroscopies*, pages 549–582. John Wiley & Sons, Inc., 2011.

[51] M. Zerbetto, A. Polimeno, P. Cimino, and V. Barone. On the interpretation of continuous wave electron spin resonance spectra of tempo-palmitate in 5-cyanobiphenyl. *J. Chem. Phys.*, 128:024501, 2008.

[52] D. J. Schneider and J. H. Freed. *Calculating Slow Motional Magnetic Resonance Spectra*, pages 1–76. Springer US, Boston, MA, 1989.

[53] J. H. Freed, G. V. Bruno, and C. F. Polnaszek. Electron spin resonance line shapes and saturation in the slow motional region. *J. Phys. Chem.*, 75:3385–3399, 1971.

[54] I. Kuprov. Fokker-Planck formalism in magnetic resonance simulations. *J. Magn. Reson.*, 270:124 – 135, 2016.

[55] G. Moro and J. H. Freed. Calculation of ESR spectra and related FokkerPlanck forms by the use of the Lanczos algorithm. *J. Chem. Phys.*, 74:3757–3773, 1981.

[56] J. H. Freed and G. K. Fraenkel. Theory of Linewidths in Electron Spin Resonance Spectra. *J. Chem. Phys.*, 39:326–348, 1963.

[57] C. F. Polnaszek, G. V. Bruno, and J. H. Freed. ESR line shapes in the slowmotional region: Anisotropic liquids. *J. Chem. Phys.*, 58:3185–3199, 1973.

[58] David E. Budil, Sanghyuk Lee, Sunil Saxena, and Jack H. Freed. Nonlinear-Least-Squares Analysis of Slow-Motion EPR Spectra in One and Two Dimensions Using a Modified LevenbergMarquardt Algorithm. *J. Magn. Reson. Ser. A*, 120:155 – 189, 1996.

[59] M. Zerbetto, A. Polimeno, and V. Barone. Simulation of electron spin resonance spectroscopy in diverse environments: An integrated approach. *Comput. Phys. Comm.*, 180:2680 – 2697, 2009.

[60] A. Polimeno and J. H. Freed. Slow Motional ESR in Complex Fluids: The Slowly Relaxing Local Structure Model of Solvent Cage Effects. *J. Phys. Chem.*, 99:10995–11006, 1995.

[61] Z. Liang, P. O. Westlund, and G. Wikander. A quantitative electronspin resonance line shape study of the local motion in the micellar and liquid crystalline lamellar phases of the oleoyllysolecithin water system. *J. Chem. Phys.*, 99:7098–7107, 1993.

[62] B. J. Gaffney and H. M. McConnell. The paramagnetic resonance spectra of spin labels in phospholipid membranes. *J. Magn. Reson.*, 16:1 – 28, 1974.

[63] D. D. Lasic and H. Hauser. The potential of electron spin resonance spin-labeling in determining micelle shapes. *J. Phys. Chem.*, 89:2648–2651, 1985.

[64] Z. Liang and J. H. Freed. An Assessment of the Applicability of Multifrequency ESR to Study the Complex Dynamics of Biomolecules. *J. Phys. Chem. B*, 103:6384–6396, 1999.

[65] V. Barone, M. Zerbetto, and A. Polimeno. Hydrodynamic modeling of diffusion tensor properties of flexible molecules. *J. Comput. Chem.*, 30:2–13, 2009.

[66] M. M. Tirado and J. G. de la Torre. Rotational dynamics of rigid, symmetric top macromolecules. Application to circular cylinders. *J. Chem. Phys.*, 73:1986–1993, 1980.

[67] W. Eimer, J. R. Williamson, S. G. Boxer, and R. Pecora. Characterization of the overall and internal dynamics of short oligonucleotides by depolarized dynamic light scattering and NMR relaxation measurements. *Biochemistry*, 29:799–811, 1990.

[68] E. Meirovitch, A. Polimeno, and J. H. Freed. Comment on The physical basis of model-free analysis of NMR relaxation data from proteins and complex fluids. *J. Chem. Phys.*, 132:207101, 2010.

[69] R. Galindo-Murillo, D. R. Roe, and T. E. Cheatham III. On the absence of intrahelical DNA dynamics on the μs to ms timescale. *Nat. Commun.*, 5:5152, 2014.

[70] C. Beier and H. J. Steinhoff. A Structure-Based Simulation Approach for Electron Paramagnetic Resonance Spectra Using Molecular and Stochastic Dynamics Simulations. *Biophys. J.*, 91:2647 – 2664, 2006.

[71] P. Hakansson, P. O. Westlund, E. Lindahl, and O. Edholm. A direct simulation of EPR slow-motion spectra of spin labelled phospholipids in liquid crystalline bilayers based on a molecular dynamics simulation of the lipid dynamics. *Phys. Chem. Chem. Phys.*, 3:5311–5319, 2001.

[72] S. C. DeSensi, D. P. Rangel, A. H. Beth, T. P. Lybrand, and E. J. Hustedt. Simulation of Nitroxide Electron Paramagnetic Resonance Spectra from Brownian Trajectories and Molecular Dynamics Simulations. *Biophys. J.*, 94:3798 – 3809, 2008.

[73] V. S. Oganesyan, F. Chami, G. F. White, and A. J. Thomson. A combined EPR and MD simulation study of a nitroxyl spin label with restricted internal mobility sensitive to protein dynamics. *J. Magn. Reson.*, 274:24 – 35, 2017.

[74] G. F. White, S. Field, S. Marritt, V. S. Oganesyan, R. B. Gennis, L. L. Yap, A. Katsonouri, and A. J. Thomson. An EPR Spin Label Study of the Quinol Oxidase, E. coli Cytochrome bo3: A Search for Redox Induced Conformational Changes. *Biochemistry*, 46:2355–2363, 2007.

[75] V. Fock. Naherungsmethode zur Losung des quantenmechanischen Mehrkorperproblems. *Z. Phys.*, 61:126–148, 1930.

[76] B. J. Alder and T. E. Wainwright. Phase Transition for a Hard Sphere System. *J. Chem. Phys.*, 27:1208–1209, 1957.

[77] W. Pauli. Uber den Zusammenhang des Abschlusses der Elektronengruppen im Atom mit der Komplexstruktur der Spektren. *Z. Phys.*, 31:765–783, 1925.

[78] N. M. Hugenholtz. Variational Principle in Quantum Mechanics. *Phys. Rev.*, 96:1158–1159, 1954.

[79] J. C. Slater. Atomic Shielding Constants. *Phys. Rev.*, 36:57–64, 1930.

[80] S. F. Boys. Electronic wave functions - I. A general method of calculation for the stationary states of any molecular system. *Proc. R. Soc.*, 200:542–554, 1950.

[81] R. Ditchfield, W. J. Hehre, and J. A. Pople. Self-Consistent Molecular-Orbital Methods. IX. An Extended Gaussian-Type Basis for Molecular-Orbital Studies of Organic Molecules. *J. Chem. Phys.*, 54:724–728, 1971.

[82] P. J. Hay and W. R. Wadt. Ab initio effective core potentials for molecular calculations. Potentials for the transition metal atoms Sc to Hg. *J. Chem. Phys.*, 82:270–283, 1985.

[83] P. J. Hay and W. R. Wadt. Ab initio effective core potentials for molecular calculations. Potentials for K to Au including the outermost core orbitals. *J. Chem. Phys.*, 82:299–310, 1985.

[84] J. Almlof and P. R. Taylor. Atomic Natural Orbital (ANO) Basis Sets for Quantum Chemical Calculations. volume 22 of *Advances in Quantum Chemistry*, pages 301 – 373. Academic Press, 1991.

[85] T. H. Dunning Jr. Gaussian basis sets for use in correlated molecular calculations. I. The atoms boron through neon and hydrogen. *J. Chem. Phys.*, 90:1007–1023, 1989.

[86] P. O. Lowdin. Quantum Theory of Many-Particle Systems. III. Extension of the Hartree-Fock Scheme to Include Degenerate Systems and Correlation Effects. *Phys. Rev.*, 97:1509–1520, 1955.

[87] P. Hohenberg and W. Kohn. Inhomogeneous Electron Gas. *Phys. Rev.*, 136:864–871, 1964.

[88] W. Kohn and L. J. Sham. Self-Consistent Equations Including Exchange and Correlation Effects. *Phys. Rev.*, 140:1133–1138, 1965.

[89] V. Barone, A. Bencini, M. Cossi, A. Matteo, M. Mattesini, and F. Totti. Assessment of a Combined QM/MM Approach for the Study of Large Nitroxide Systems in Vacuo and in Condensed Phases. *J. Am. Chem. Soc.*, 120:7069–7078, 1998.

[90] S. Miertuus, E. Scrocco, and J. Tomasi. Electrostatic interaction of a solute with a continuum. A direct utilizaion of AB initio molecular potentials for the prevision of solvent effects. *Chem. Phys.*, 55:117–129, 1981.

[91] C. J. Cramer and D. G. Truhlar. Implicit Solvation Models: Equilibria, Structure, Spectra, and Dynamics. *Chem. Rev.*, 99:2161–2200, 1999.

[92] B. J. Leimkuhler, S. Reich, and R. D. Skeel. *Integration Methods for Molecular Dynamics*, pages 161–185. Springer New York, New York, NY, 1996.

[93] J. Wang, R. M. Wolf, J. W. Caldwell, P. A. Kollman, and D. A. Case. Development and testing of a general amber force field. *J. Comput. Chem.*, 25:1157–1174, 2004.

[94] S. J. Weiner, P. A. Kollman, D. A. Case, U. C. Singh, C. Ghio, G. Alagona, S. Profeta, and P. Weiner. A new force field for molecular mechanical simulation of nucleic acids and proteins. *J. Am. Chem. Soc.*, 106:765–784, 1984.

[95] I. Ivani, P. D. Dans, A. Noy, A. Perez, I. Faustino, A. Hospital, J. Walther, P. Andrio, R. Goni, A. Balaceanu, G. Portella, F. Battistini, J. L. Gelpi, C. Gonzalez, M. Vendruscolo, C. A. Laughton, S. A. Harris, D. A. Case, and M. Orozco. Parmbsc1: a refined force field for DNA simulations. *Nat. Meth.*, 13:55–58, 2016.

[96] C. J. Dickson, L. Rosso, R. M. Betz, R. C. Walker, and I. R. Gould. GAFF-lipid: a General Amber Force Field for the accurate molecular dynamics simulation of phospholipid. *Soft Matter*, 8:9617–9627, 2012.

[97] T. Darden, D. York, and L. Pedersen. Particle mesh Ewald: An Nlog(N) method for Ewald sums in large systems. *J. Chem. Phys.*, 98:10089–10092, 1993.

[98] V. Wong and D. A. Case. Evaluating Rotational Diffusion from Protein MD Simulations. *J. Phys. Chem. B*, 112:6013–6024, 2008.

[99] P. Mark and L. Nilsson. Structure and Dynamics of the TIP3P, SPC, and SPC/E Water Models at 298 K. *J. Phys. Chem. A*, 105:9954–9960, 2001.

[100] P. O. Quist, B. Halle, and I. Fur. Nuclear spin relaxation in a hexagonal lyotropic liquid crystal. *J. Chem. Phys.*, 95:6945–6961, 1991.

[101] O. Soederman, H. Walderhaug, U. Henriksson, and P. Stilbs. NMR relaxation in isotropic surfactant systems. A deuterium, carbon-13, and nitrogen-14 NMR study of the micellar (L1) and cubic (I1) phases in the dodecyltrimethylammonium chloride water system. *J. Phys. Chem.*, 89:3693–3701, 1985.

[102] M. F. Ottaviani, R. Daddi, M. Brustolon, N. J. Turro, and D. A. Tomalia. Interaction between Starburst Dendrimers and SDS micelles studied by continuous-wave and pulsed electron spin resonances. *Appl. Magn. Reson.*, 13:347–363, 1997.

[103] L. B. A. Johansson and O. Soederman. The cubic phase (i1) in the dodecyltrimethylammonium chloride/water system: a fluorescence quenching study. *J. Phys. Chem.*, 91:5275–5278, 1987.

[104] F. Reiss-Husson and V. Luzzati. The Structure of the Micellar Solutions of Some Amphiphilic Compounds in Pure Water as Determined by Absolute Small-Angle X-Ray Scattering Techniques. *J. Phys. Chem.*, 68:3504–3511, 1964.

[105] R. R. Balmbra, J. S. Clunie, and J. F. Goodman. Cubic Mesomorphic Phases. *Nature*, 222:1159–1160, 1969.

[106] P. Kekicheff and B. Cabane. Crystallography of systems with long periods: a neutron-scattering study of sodium dodecyl sulfate/water mesophases. *Acta Crystallogr. Sect. A*, 44:395–406, 1988.

[107] N. A. Mazer, G. B. Benedek, and M. C. Carey. An investigation of the micellar phase of sodium dodecyl sulfate in aqueous sodium chloride solutions using quasielastic light scattering spectroscopy. *J. Phys. Chem.*, 80:1075–1085, 1976.

[108] B. J. Chun, J. I. Choi, and S. S. Jang. Molecular dynamics simulation study of sodium dodecyl sulfate micelle: Water penetration and sodium dodecyl sulfate dissociation. *Colloids Surf. A*, 474:36 – 43, 2015.

[109] X. Tang, P. H. Koenig, and R. G. Larson. Molecular Dynamics Simulations of Sodium Dodecyl Sulfate Micelles in WaterThe Effect of the Force Field. *J. Phys. Chem. B*, 118:3864–3880, 2014.

[110] C. D. Bruce, M. L. Berkowitz, L. Perera, and M. D. E. Forbes. Molecular Dynamics Simulation of Sodium Dodecyl Sulfate Micelle in Water: Micellar Structural Characteristics and Counterion Distribution. *J. Phys. Chem. B*, 106:3788–3793, 2002.

[111] V. Kocherbitov. Molecular dynamics simulations of liquid crystalline phases of dodecyltrimethylammonium chloride . *J. Mol. Liq.*, 210:74 – 81, 2015.

[112] F. Palazzesi, M. Calvaresi, and F. Zerbetto. A molecular dynamics investigation of structure and dynamics of SDS and SDBS micelles. *Soft Matter*, 7:9148–9156, 2011.

[113] G. Lipari and A. Szabo. Model-free approach to the interpretation of nuclear magnetic resonance relaxation in macromolecules. 1. Theory and range of validity. *J. Am. Chem. Soc.*, 104:4546–4559, 1982.

[114] B. Liang and L. K. Tamm. NMR as a tool to investigate the structure, dynamics and function of membrane proteins. *Nat. Struct. Mol. Biol.*, 23:468–474, 2016.

[115] A. Wozniak-Braszak, K. Jurga, and M. Baranowski. The Lipari-Szabo Model-Free Analysis as a Method for Study of Molecular Motion in Solid State Heteronuclear Systems Using NMR Off-Resonance. *Appl. Magn. Reson.*, 47:567–574, 2016.

[116] L. Banci, I. Bertini, F. Cramaro, R. Del Conte, A. Rosato, and M. S. Viezzoli. Backbone Dynamics of Human Cu,Zn Superoxide Dismutase and of Its Monomeric F50E/G51E/E133Q Mutant: The Influence of Dimerization on Mobility and Function. *Biochemistry*, 39:9108–9118, 2000.

[117] V. A. Daragan and K. H. Mayo. A Novel Model-Free Analysis of13C NMR Relaxation of Alanine-Methyl Side-Chain Motions in Peptides. *J. Magn. Reson., Series B*, 110:164 – 175, 1996.

[118] R. Cole and J. P. Loria. FAST-Modelfree: A program for rapid automated analysis of solution NMR spin-relaxation data. *J. Biomol. NMR*, 26:203–213, 2003.

[119] J. M. Bui, J. Gsponer, M. Vendruscolo, and C. M. Dobson. Analysis of Sub-τ_c and Supra-τ_c Motions in Protein $G\beta 1$ Using Molecular Dynamics Simulations. *Biophys. J.*, 97:2513–2520, 2009.

[120] T. M. Ferreira, O. H. Samuli Ollila, R. Pigliapochi, A. P. Dabkowska, and D. Topgaard. Model-free estimation of the effective correlation time for CH bond reorientation in amphiphilic bilayers: 1H13C solid-state NMR and MD simulations. *J. Chem. Phys.*, 142:044905, 2015.

[121] E. Meirovitch, Y. E. Shapiro, A. Polimeno, and J. H. Freed. Structural Dynamics of Bio-Macromolecules by NMR: The Slowly Relaxing Local Structure Approach. *Prog. Nucl. Magn. Reson. Spectrosc.*, 56:360–405, 2010.

[122] M. J. Frisch, G. W. Trucks, H. B. Schlegel, G. E. Scuseria, M. A. Robb, J. R. Cheeseman, G. Scalmani, V. Barone, B. Mennucci, G. A. Petersson, H. Nakatsuji, M. Caricato, X. Li, H. P. Hratchian, A. F. Izmaylov, J. Bloino, G. Zheng, J. L. Sonnenberg, M. Hada, M. Ehara, K. Toyota, R. Fukuda, J. Hasegawa, M. Ishida, T. Nakajima, Y. Honda, O. Kitao, H. Nakai, T. Vreven, J. A. Montgomery, Jr., J. E. Peralta, F. Ogliaro, M. Bearpark, J. J. Heyd, E. Brothers, K. N. Kudin, V. N. Staroverov, R. Kobayashi, J. Normand, K. Raghavachari, A. Rendell, J. C. Burant, S. S. Iyengar, J. Tomasi, M. Cossi, N. Rega, J. M. Millam, M. Klene, J. E. Knox, J. B. Cross, V. Bakken, C. Adamo, J. Jaramillo, R. Gomperts, R. E. Stratmann, O. Yazyev, A. J. Austin, R. Cammi, C. Pomelli, J. W. Ochterski, R. L. Martin, K. Morokuma, V. G. Zakrzewski, G. A. Voth, P. Salvador, J. J. Dannenberg, S. Dapprich, A. D. Daniels, . Farkas, J. B. Foresman, J. V. Ortiz, J. Cioslowski, and D. J. Fox. Gaussian 09 Revision A.1. Gaussian Inc. Wallingford CT 2009.

[123] C. M. Breneman and K. B. Wiberg. Determining atom-centered monopoles from molecular electrostatic potentials. The need for high sampling density in formamide conformational analysis. *J. Comp. Chem.*, 11:361–373, 1990.

[124] W. D. Cornell, P. Cieplak, C. I. Bayly, I. R. Gould, K. M. Merz, D. M. Ferguson, D. C. Spellmeyer, T. Fox, J. W. Caldwell, and P. A. Kollman. A Second Generation Force Field for the Simulation of Proteins, Nucleic Acids, and Organic Molecules. *J. Am. Chem. Soc.*, 117:5179–5197, 1995.

[125] V. Barone, P. Cimino, and E. Stendardo. Development and Validation of the B3LYP/N07D Computational Model for Structural Parameter and Magnetic Tensors of Large Free Radicals. *J. Chem. Theory Comput.*, 4:751–764, 2008.

[126] P. Cimino, A. Pedone, E. Stendardo, and V. Barone. Interplay of stereo-electronic, environmental, and dynamical effects in determining the EPR

parameters of aromatic spin-probes: INDCO as a test case. *Phys. Chem. Chem. Phys.*, 12:3741–3746, 2010.

[127] L. Martnez, R. Andrade, E. G. Birgin, and J. M. Martnez. PACKMOL: A package for building initial configurations for molecular dynamics simulations. *J. Comput. Chem.*, 30:2157–2164, 2009.

[128] J. P. Ryckaert, G. Ciccotti, and H. J. C. Berendsen. Numerical integration of the cartesian equations of motion of a system with constraints: molecular dynamics of n-alkanes. *J. Comput. Phys.*, 23:327 – 341, 1977.

[129] H. J. C. Berendsen, J. R. Grigera, and T. P. Straatsma. The missing term in effective pair potentials. *J. Phys. Chem.*, 91:6269–6271, 1987.

[130] I. S. Joung and T. E. Cheatham. Determination of Alkali and Halide Monovalent Ion Parameters for Use in Explicitly Solvated Biomolecular Simulations. *J. Phys. Chem. B*, 112:9020–9041, 2008.

[131] D. A. Case, T. A. Darden, T. E. Cheatham, C. L. Simmerling, J. Wang, R. E. Duke, R. Luo, R. C. Walker, W. Zhang, K. M. Merz, B. Roberts, S. Hayik, A. Roitberg, G. Seabra, J. Swails, A. W. Goetz, I. Kolossváry, K. F. Wong, F. Paesani, J. Vanicek, R. M. Wolf, J. Liu, X. Wu, S. R. Brozell, T. Steinbrecher, H. Gohlke, Q. Cai, X. Ye, J. Wang, M. J. Hsieh, G. Cui, D. R. Roe, D. H. Mathews, M. G. Seetin, R. Salomon-Ferrer, C. Sagui, V. Babin, T. Luchko, S. Gusarov, A. Kovalenko, and P. A. Kollman. Amber 12, 2012. University of California, San Francisco.

[132] B. J. Gaffney and H. M. McConnell. The paramagnetic resonance spectra of spin labels in phospholipid membranes. *J. Magn. Reson.*, 16:1 – 28, 1974.

[133] N. Usova, L. Persson, and P. O. Westlund. Theory of slow-motion EPR lineshapes for studies of membrane curvature. *Phys. Chem. Chem. Phys.*, 2:2785–2793, 2000.

[134] M. Pavone, M. Biczysko, N. Rega, and V. Barone. Magnetic Properties of Nitroxide Spin Probes: Reliable Account of Molecular Motions and Non-specific Solvent Effects by Time-Dependent and Time-Independent Approaches. *J. Phys. Chem. B*, 114:11509–11514, 2010.

[135] V. Barone and P. Cimino. Accurate and feasible computations of structural and magnetic properties of large free radicals: The PBE0/N07D model. *Chem. Phys. Lett.*, 454:139 – 143, 2008.

[136] M. M. Haugland, E. A. Anderson, and J. E. Lovett. Tuning the properties of nitroxide spin labels for use in electron paramagnetic resonance spectroscopy through chemical modification of the nitroxide framework. In *Electron Paramagnetic Resonance: Volume 25*, volume 25, pages 1–34. The Royal Society of Chemistry, 2017.

[137] M. Witwicki, J. Jezierska, and A. Ozarowski. Solvent effect on EPR, molecular and electronic properties of semiquinone radical derived from 3,4-dihydroxybenzoic acid as model for humic acid transient radicals: High-field EPR and DFT studies. *Chem. Phys. Lett.*, 473:160 – 166, 2009.

[138] R. Owenius, M. Engstrom, M. Lindgren, and M. Huber. Influence of Solvent Polarity and Hydrogen Bonding on the EPR Parameters of a Nitroxide Spin Label Studied by 9-GHz and 95-GHz EPR Spectroscopy and DFT Calculations. *J. Phys. Chem. A*, 105:10967–10977, 2001.

[139] B. L. Bales, L. Messina, A. Vidal, M. Peric, and O. R. Nascimento. Precision Relative Aggregation Number Determinations of SDS Micelles Using a Spin Probe. A Model of Micelle Surface Hydration. *J. Phys. Chem. B*, 102:10347–10358, 1998.

[140] S. Salaniwal, S. T. Cui, H. D. Cochran, and P. T. Cummings. Molecular Simulation of a Dichain Surfactant/Water/Carbon Dioxide System. 1. Structural Properties of Aggregates. *Langmuir*, 17:1773–1783, 2001.

[141] S. Vass, J. S. Pedersen, J. Plestil, P. Laggner, E. Retfalvi, I. Varga, and T. Gilanyi. Ambiguity in Determining the Shape of Alkali Alkyl Sulfate Micelles from Small-Angle Scattering Data. *Langmuir*, 24:408–417, 2008.

[142] N. J. Boyd and M. R. Wilson. Optimization of the GAFF force field to describe liquid crystal molecules: the path to a dramatic improvement in transition temperature predictions. *Phys. Chem. Chem. Phys.*, 17:24851–24865, 2015.

[143] A. P. Lyubartsev and A. L. Rabinovich. Recent development in computer simulations of lipid bilayers. *Soft Matter*, 7:25–39, 2011.

[144] A. Akinshina, M. Walker, M. R. Wilson, G. J. T. Tiddy, A. J. Masters, and P. Carbone. Thermodynamics of the self-assembly of non-ionic chromonic molecules using atomistic simulations. The case of TP6EO2M in aqueous solution. *Soft Matter*, 11:680–691, 2015.

[145] M. Bergstrom and J. S. Pedersen. Structure of pure SDS and DTAB micelles in brine determined by small-angle neutron scattering (SANS). *Phys. Chem. Chem. Phys.*, 1:4437–4446, 1999.

[146] J. Gujt, M. Bester-Rogac, and E. Spohr. Structure and Stability of Long Rod-like Dodecyltrimethylammonium Chloride Micelles in Solutions of Hydroxybenzoates: A Molecular Dynamics Simulation Study. *Langmuir*, 32:8275–8286, 2016.

[147] Z. Wang and R. G. Larson. Molecular Dynamics Simulations of Threadlike Cetyltrimethylammonium Chloride Micelles: Effects of Sodium Chloride and Sodium Salicylate Salts. *J. Phys. Chem. B*, 113:13697–13710, 2009.

[148] M. K. Minasyanc, V. A. Zakaryan, and A. A. Shahinyan. X-ray analysis of Na-dodecylsulfatewater system. *Kristallografiya*, 43, 1979.

[149] S. C. Schultz, G. C. Shields, and T. A. Steitz. Crystal structure of a CAP-DNA complex: the DNA is bent by 90 degrees. *Science*, 253:1001–1007, 1991.

[150] Z. A. E. Waller, B. J. Pinchbeck, B. S. Buguth, T. G. Meadows, D. J. Richardson, and A. J. Gates. Control of bacterial nitrate assimilation by stabilization of G-quadruplex DNA. *Chem. Commun.*, 52:13511–13514, 2016.

[151] S. Georghiou, T. D. Bradrick, A. Philippetis, and J. M. Beechem. Large-amplitude picosecond anisotropy decay of the intrinsic fluorescence of double-stranded DNA. *Biophys. J.*, 70:1909–1922, 1996.

[152] S. Rudisser, A. Hallbrucker, and E. Mayer. B-DNA's Conformational Substates Revealed by Fourier Transform Infrared Difference Spectroscopy. *J. Am. Chem. Soc.*, 119:12251–12256, 1997.

[153] T.M. Okonogi, S.C. Alley, A.W. Reese, P.B. Hopkins, and B.H. Robinson. Sequence-Dependent Dynamics of Duplex DNA: The Applicability of a Dinucleotide Model. *Biophys. J.*, 83:3446 – 3459, 2002.

[154] S. A. Shelke and S. Th. Sigurdsson. Site-Directed Spin Labelling of Nucleic Acids. *Eur. J. Org. Chem.*, 2012:2291–2301, 2012.

[155] J. G. de la Torre, M. C. Lopez Martinez, and J. J. Garcia Molina. Approximate methods for calculating rotational diffusion constants of rigid macromolecules. *Macromolecules*, 20:661–666, 1987.

[156] S. P. Van, G. B. Birrell, and O. H. Griffith. Rapid anisotropic motion of spin labels. models for motion averaging of the ESR parameters. *J. Magn. Reson.*, 15:444 – 459, 1974.

[157] F. Lankas, J. Sponer, P. Hobza, and J. Langowski. Sequence-dependent elastic properties of DNA. *J. Mol. Biol.*, 299:695 – 709, 2000.

[158] M. Pasi, J. H. Maddocks, D. Beveridge, T. C. Bishop, D. A. Case, T. Cheatham, III, P. D. Dans, B. Jayaram, F. Lankas, C. Laughton, J. Mitchell, R. Osman, M. Orozco, A. Perez, D. Petkeviciute, N. Spackova, J. Sponer, K. Zakrzewska, and R. Lavery. μABC: a systematic microsecond molecular dynamics study of tetranucleotide sequence effects in B-DNA. *Nucleic Acids Res.*, 42:12272–12283, 2014.

[159] P. D. Dans, L. Danilane, I. Ivani, T. Drsata, F. Lankas, A. Hospital, J. Walther, R. I. Pujagut, F. Battistini, J. L. Gelpi, R. Lavery, and M. Orozco. Long-timescale dynamics of the DrewDickerson dodecamer. *Nucleic Acids Res.*, 44:4052–4066, 2016.

[160] P. D. Dans, I. Ivani, A. Hospital, G. Portella, C. Gonzalez, and M. Orozco. How accurate are accurate force-fields for b-dna? *Nucleic Acids Res.*, 45:4217–4230, 2017.

[161] G. Zheng, X. Lu, and W. K. Olson. Web 3DNA-a web server for the analysis, reconstruction, and visualization of three-dimensional nucleic-acid structures. *Nucleic Acids Res.*, 37:240, 2009.

[162] P. Cieplak, W. D. Cornell, C. Bayly, and P. A. Kollman. Application of the multimolecule and multiconformational RESP methodology to biopolymers: Charge derivation for DNA, RNA, and proteins. *J. Comput. Chem.*, 16:1357–1377, 1995.

[163] D. E. Smith and L. X. Dang. Computer simulations of NaCl association in polarizable water. *J. Chem. Phys.*, 100:3757–3766, 1994.

[164] D. A. Case, V. Babin, J. T. Berryman, R. M. Betz, Q. Cai, D. S. Cerutti, T. E. Cheatham, T. A. Darden, R. E. Duke, H. Gohlke, A. W. Goetz, S. Gusarov, N. Homeyer, P. Janowski, J. Kaus, I. Kolossváry, A. Kovalenko, T. S. Lee, S. LeGrand, T. Luchko, R. Luo, B. Madej, K. M. Merz, F. Paesani,

D. R. Roe, A. Roitberg, C. Sagui, R. Salomon-Ferrer, G. Seabra, C. L. Simmerling, W. Smith, J. Swails, Walker, J. Wang, R. M. Wolf, X. Wu, and P. A. Kollman. *Amber 14*. University of California, San Francisco, 2014.

[165] H. J. C. Berendsen, J. P. M. Postma, W. F. van Gunsteren, A. DiNola, and J. R. Haak. Molecular dynamics with coupling to an external bath. *J. Chem. Phys.*, 81:3684–3690, 1984.

[166] D. R. Roe and T. E. Cheatham. PTRAJ and CPPTRAJ: Software for Processing and Analysis of Molecular Dynamics Trajectory Data. *J. Chem. Theory Comput.*, 9:3084–3095, 2013.

[167] R. E. Dickerson. Definitions and nomenclature of nucleic acid structure components. *Nucleic Acids Res.*, 17:1797–1803, 1989.

[168] J. Chatt, J. R. Dilworth, and R. L. Richards. Recent advances in the chemistry of nitrogen fixation. *Chem. Rev.*, 78:589–625, 1978.

[169] H. Seino, Y. Mizobe, and M. Hidai. Transformation of organic molecules on the low-valent [M(Ph2PCH2CH2PPh2)2] moiety derived from trans-[M(N2)2(Ph2PCH2CH2PPh2)2] or related complexes (M = MO, W). *Chem. Rec.*, 1:349–361, 2001.

[170] A. Hills, D. L. Hughes, C. J. Macdonald, M. Y. Mohammed, and C. J. Pickett. Transformation of a methyleneamide ligand at molybdenum: electrochemical oxidation to a cyanide, reactions with elemental oxygen, sulphur or selenium and X-ray crystal structures of trans-[Mo(CN)Cl(dppe)2]·MeOH and trans-[Mo(NCS)Cl(dppe)2]; electroreduction of the cyanide to an aminocarbyne, trans-[Mo(CNH2)Cl(dppe)2](dppe = Ph2PCH2CH2PPh2). *Dalton Trans.*, pages 121–129, 1991.

[171] Ito T., Takahashi A., and Tamura S. Preparation, Characterization, and Some Reactions of Cationic Hydrido Carboxylato Complexes of Molybde-

num(IV), [MoH2(O2CR)(dppe)2]+. *Bulletin of the Chemical Society of Japan*, 59:3489–3494, 1986.

[172] D. L. Hughes, S. K. Ibrahim, C. J. Macdonald, H. M. Ali, and C. J. Pickett. Electrosynthesis of amino acids from a molybdenum nitride via nitrogen-carbon and carbon-carbon bond formation reactions involving imides and nitrogen ylides: X-ray structure of trans-[MoCl(NCHCO2Me)(Ph2PCH2CH2PPh2)2]·CH2Cl2. *J. Chem. Soc., Chem. Commun.*, pages 1762–1763, 1992.

[173] D. L. Hughes, S. K. Ibrahim, C. J. Pickett, G. Querne, A. Laouenan, J. Talarmin, A. Queiros, and A. Fonseca. On carboxylate as a leaving group at the active site of Mo nitrogenase: electrochemical reactions of some MO and W carboxylates, formation of mono-, di- and tri-hydrides and the detection of an MoH2(N2) intermediate. *Polyhedron*, 13:3341 – 3348, 1994.

[174] Alessandro B. Some considerations on the proper use of computational tools in transition metal chemistry. *Inorg. Chim. Acta*, 361:3820 – 3831, 2008.

[175] B. Ndiaye, S. Bhat, A. Jouaiti, T. Berclaz, G. Bernardinelli, and M. Geoffroy. EPR and DFT Studies of the Structure of Phosphinyl Radicals Complexed by a Pentacarbonyl Transition Metal. *J. Phys. Chem. A*, 110:9736–9742, 2006.

[176] M. Kaupp, C. Remenyi, J. Vaara, O. L. Malkina, and V. G. Malkin. Density Functional Calculations of Electronic g-Tensors for Semiquinone Radical Anions. The Role of Hydrogen Bonding and Substituent Effects. *J. Am. Chem. Soc.*, 124:2709–2722, 2002.

[177] M. Kaupp, R. Reviakine, O. L. Malkina, A. Arbuznikov, B. Schimmelpfennig, and V. G. Malkin. Calculation of electronic g-tensors for transition

metal complexes using hybrid density functionals and atomic meanfield spin-orbit operators. *J. Comp. Chem.*, 23:794–803, 2002.

[178] R. G. Hadt, V. N. Nemykin, J. G. Olsen, and P. Basu. Comparative calculation of EPR spectral parameters in [MoVOX4]-, [MoVOX5]2-, and [MoVOX4(H2O)]- complexes. *Phys. Chem. Chem. Phys.*, 11:10377–10384, 2009.

[179] J. Tao, J. P. Perdew, V. N. Staroverov, and G. E. Scuseria. Climbing the Density Functional Ladder: Nonempirical Meta˘Generalized Gradient Approximation Designed for Molecules and Solids. *Phys. Rev. Lett.*, 91:146401, 2003.

[180] W. Hoe, A. J. Cohen, and N. C. Handy. Assessment of a new local exchange functional OPTX. *Chem. Phys. Lett.*, 341:319 – 328, 2001.

[181] J. A. Weil. The analysis of large hyperfine splitting in paramagnetic resonance spectroscopy. *J. Magn. Reson.*, 4:394 – 399, 1971.

[182] A. Jablonskyt, J. A. Wright, S. A. Fairhurst, J. N. T. Peck, S. K. Ibrahim, V. S. Oganesyan, and C. J. Pickett. Paramagnetic Bridging Hydrides of Relevance to Catalytic Hydrogen Evolution at Metallosulfur Centers. *J. Am. Chem. Soc.*, 133:18606–18609, 2011.

[183] D. C. Johnson, D. R. Dean, A. D. Smith, and M. K. Johnson. Structure, Function, and Formation of Biological Iron-Sulfur Clusters. *Annu. Rev. Biochem.*, 74:247–281, 2005.

[184] N. P. Tucker, N. E. Le Brun, . Dixon, and M. I. Hutchings. There's {NO} stopping NsrR, a global regulator of the bacterial {NO} stress response. *Trends Microbiol.*, 18:149 – 156, 2010.

[185] J. C. Crack, J. Green, A. J. Thomson, and N. E. Le Brun. Iron-Sulfur Clusters as Biological Sensors: The Chemistry of Reactions with Molecular Oxygen and Nitric Oxide. *Acc. Chem. Res.*, 47:3196–3205, 2014.

[186] J. Drapier. Interplay between NO and [Fe-S] Clusters: Relevance to Biological Systems. *Methods*, 11:319 – 329, 1997.

[187] M. W. Foster and J. A. Cowan. Chemistry of Nitric Oxide with Protein-Bound Iron Sulfur Centers. Insights on Physiological Reactivity. *J. Am. Chem. Soc.*, 121:4093–4100, 1999.

[188] J. Fitzpatrick, H. Kalyvas, J. Shearer, and E. Kim. Dioxygen mediated conversion of Fe(NO)29 dinitrosyl iron complexes to Roussin's red esters. *Chem. Commun.*, 49:5550–5552, 2013.

[189] S. Yeh, C. Tsou, and W. Liaw. The dinitrosyliron complex [Fe4((μ3-S)2(μ2-NO)2(NO)6]2- containing bridging nitroxyls: 15N (NO) NMR analysis of the bridging and terminal NO-coordinate ligands. *Dalton Trans.*, 43:9022–9025, 2014.

[190] A. R. Butler, C. Glidewell, and M. Li. Nitrosyl Complexes of Iron-Sulfur Clusters. *Adv. Inorg. Chem.*, 32:335 – 393, 1988.

[191] T. Chen, F. Lo, M. Tsai, K. Shih, M. Chiang, G. Lee, and W. Liaw. Dinitrosyl iron complexes [Fe(NO)2] (E = S, Se): A precursor of Roussins black salt [Fe4E3(NO)7]. *Inorg. Chim. Acta*, 359:2525 – 2533, 2006.

[192] J. C. Crack, L. J. Smith, M. R. Stapleton, J. Peck, N. J. Watmough, M. J. Buttner, R. S. Buxton, J. Green, V. S. Oganesyan, A. J. Thomson, and N. E. Le Brun. Mechanistic Insight into the Nitrosylation of the [4Fe4S] Cluster of WhiB-like Proteins. *J. Am. Chem. Soc.*, 133:1112–1121, 2011.

[193] T. C. Harrop, Z. J. Tonzetich, E. Reisner, and S. J. Lippard. Reactions of Synthetic [2Fe-2S] and [4Fe-4S] Clusters with Nitric Oxide and Nitrosothiols. *J. Am. Chem. Soc.*, 130:15602–15610, 2008.

[194] J. C. Crack, M. R. Stapleton, J. Green, A. J. Thomson, and N. E. Le Brun. Mechanism of [4Fe-4S](Cys)4 Cluster Nitrosylation Is Conserved among NO-responsive Regulators. *J. Biol. Chem.*, 288:11492–11502, 2013.

[195] B. Zhang, J. C. Crack, S. Subramanian, J. Green, A. J. Thomson, N. E. Le Brun, and M. K. Johnson. Reversible cycling between cysteine persulfide-ligated [2Fe-2S] and cysteine-ligated [4Fe-4S] clusters in the FNR regulatory protein. *Proc. Nat. Acad. Sci.*, 109:15734–15739, 2012.

[196] M. . Kennedy, W. E. Antholine, and H. Beinert. An EPR Investigation of the Products of the Reaction of Cytosolic and Mitochondrial Aconitases with Nitric Oxide. *J. Biol. Chem.*, 272:20340–20347, 1997.

[197] H. Cruz-Ramos, J. Crack, G. Wu, M. N. Hughes, C. Scott, A. J. Thomson, J. Green, and R. K. Poole. NO sensing by FNR: regulation of the Escherichia coli NO-detoxifying flavohaemoglobin, Hmp. *EMBO J.*, 21:3235–3244, 2002.

[198] T. G. Spiro and R. S. Czernuszewicz. Resonance Raman spectroscopy of metalloproteins. *Methods Enzymol.*, 246:416 – 460, 1995.

[199] V. S. Oganesyan, J. E. Barclay, S. M. Hardy, D. J. Evans, C. J. Pickett, and U. A. Jayasooriya. Nuclear inelastic scattering spectroscopy of iron-sulfur cubane compounds. *Chem. Commun.*, pages 214–215, 2003.

[200] U. A. Jayasooriya, J. N. T. Peck, J. E. Barclay, S. M. Hardy, A. I. Chumakov, D. J. Evans, C. J. Pickett, and V. S. Oganesyan. Nuclear inelastic scattering spectroscopy of tris(acetylacetonate)iron(III); A vibrational probe via the iron atom. *Chem. Phys. Lett.*, 518:119 – 123, 2011.

[201] J.W. Pavlik, A. Barabanschikov, A.G. Oliver, E.E. Alp, W. Sturhahn, Jiyong Zhao, J.T. Sage, and W.R. Scheidt. Probing Vibrational Anisotropy with Nuclear Resonance Vibrational Spectroscopy. *Angew. Chem. Int. Ed.*, 49:4400–4404, 2010.

[202] Y. Xiao, M. Koutmos, D. A. Case, D. Coucouvanis, H. Wang, and S. P. Cramer. Dynamics of an [Fe4S4(SPh)4]2- cluster explored via IR, Raman, and nuclear resonance vibrational spectroscopy (NRVS)-analysis using 36S substitution, DFT calculations, and empirical force fields. *Dalton Trans.*, pages 2192–2201, 2006.

[203] T. Petrenko, S. DeBeer George, Nria A. A., E. Bill, B. Mienert, Y. Xiao, Y. Guo, W. Sturhahn, S. P. Cramer, K. Wieghardt, and F. Neese. Characterization of a Genuine Iron(V)Nitrido Species by Nuclear Resonant Vibrational Spectroscopy Coupled to Density Functional Calculations. *J. Am. Chem. Soc.*, 129:11053–11060, 2007.

[204] U. Bergmann, J. B. Hastings, and D. P. Siddons. Time evolution of incoherent nuclear scattering from ^{57}Fe excited with synchrotron radiation. *Phys. Rev. B*, 49:1513–1516, 1994.

[205] M. C. Smith, Y. Xiao, H. Wang, S. J. George, D. Coucouvanis, M. Koutmos, W. Sturhahn, E. E. Alp, J. Zhao, and S. P. Cramer. Normal-Mode Analysis of FeCl4- and Fe2S2Cl42- via Vibrational Mssbauer, Resonance Raman, and FT-IR Spectroscopies. *Inorg. Chem.*, 44:5562–5570, 2005.

[206] B. M. Leu, M. Z. Zgierski, G. R. A. Wyllie, W. R. Scheidt, W. Sturhahn, E. E. Alp, S. M. Durbin, and J. T. Sage. Quantitative Vibrational Dynamics of Iron in Nitrosyl Porphyrins. *J. Am. Chem. Soc.*, 126:4211–4227, 2004.

[207] W. Sturhahn, T. S. Toellner, E. E. Alp, X. Zhang, M. Ando, Y. Yoda, S. Kikuta, M. Seto, C. W. Kimball, and B. Dabrowski. Phonon Density

of States Measured by Inelastic Nuclear Resonant Scattering. *Phys. Rev. Lett.*, 74:3832–3835, 1995.

[208] R. Ruffer and A. I. Chumakov. Nuclear Resonance Beamline at ESRF. *Hyperfine Interact.*, 97:589–604, 1996.

[209] A. Q. R. Baron, A. I. Chumakov, R. Rffer, H. Grnsteudel, H. F. Grnsteudel, and O. Leupold. Single-nucleus quantum beats excited by synchrotron radiation. *EPL (Europhysics Letters)*, 34:331, 1996.

[210] M. Seto, Y. Yoda, S. Kikuta, X. W. Zhang, and M. Ando. Observation of Nuclear Resonant Scattering Accompanied by Phonon Excitation Using Synchrotron Radiation. *Phys. Rev. Lett.*, 74:3828–3831, 1995.

[211] A. I. Chumakov, R. Rffer, H. Grnsteudel, H. F. Grnsteudel, G. Grbel, J. Metge, O. Leupold, and H. A. Goodwin. Energy Dependence of Nuclear Recoil Measured with Incoherent Nuclear Scattering of Synchrotron Radiation. *EPL*, 30:427, 1995.

[212] J. P. Perdew, J. A. Chevary, S. H. Vosko, K. A. Jackson, M. R. Pederson, D. J. Singh, and C. Fiolhais. Atoms, molecules, solids, and surfaces: Applications of the generalized gradient approximation for exchange and correlation. *Phys. Rev. B*, 46:6671–6687, 1992.

[213] Y. Xiao, K. Fisher, M. C. Smith, W. E. Newton, D. A. Case, S. J. George, H. Wang, W. Sturhahn, E. E. Alp, J. Zhao, Y. Yoda, and S. P. Cramer. How Nitrogenase Shakes Initial Information about PCluster and FeMo-cofactor Normal Modes from Nuclear Resonance Vibrational Spectroscopy (NRVS). *J. Am. Chem. Soc.*, 128:7608–7612, 2006.

[214] S. Kamali, H. Wang, D. Mitra, H. Ogata, W. Lubitz, B. C. Manor, T. B. Rauchfuss, D. Byrne, V. Bonnefoy, F. E. Jenney, M. W. W. Adams, Y. Yoda, E. Alp, J. Zhao, and S. P. Cramer. Observation of the Fe-CN

and Fe-CO Vibrations in the Active Site of [NiFe] Hydrogenase by Nuclear Resonance Vibrational Spectroscopy. *Angew. Chem. Int. Ed.*, 52:724–728, 2013.

[215] L. Lauterbach, H. Wang, M. Horch, L. B. Gee, Y. Yoda, Y. Tanaka, I. Zebger, O. Lenz, and S. P. Cramer. Nuclear resonance vibrational spectroscopy reveals the FeS cluster composition and active site vibrational properties of an O2-tolerant NAD(+)-reducing [NiFe] hydrogenase. *Chem Sci*, 6:1055–1060, 2015.

[216] S. P. Cramer, Y. Xiao, H. Wang, Y. Guo, and M. C. Smith. Nuclear Resonance Vibrational Spectroscopy (NRVS) of Fe-S model compounds, Fe-S proteins, and nitrogenase. *Hyperfine Interact.*, 170:47–54, 2006.

[217] H. Ogata, T. Kramer, H. Wang, D. Schilter, V. Pelmenschikov, M. van Gastel, F. Neese, T. B. Rauchfuss, L. B. Gee, A. D. Scott, Y. Yoda, Y. Tanaka, W. Lubitz, and S. P. Cramer. Hydride bridge in [NiFe]-hydrogenase observed by nuclear resonance vibrational spectroscopy. *Nat. Commun.*, 6:7890, 2015.

[218] W. Sturhahn. CONUSS and PHOENIX: Evaluation of nuclear resonant scattering data. *Hyperfine Interact.*, 125:149–172, 2000.

[219] M. Jaworska and Z. Stasicka. Structure and UVvis spectroscopy of roussin black salt [Fe4S3(NO)7]-. *J. Mol. Struct.*, 785:68 – 75, 2006.

[220] R. A. Arthurs, C. C. Ismail, M.and Prior, V. S. Oganesyan, P. N. Horton, S. J. Coles, and C. J. Richards. Enantiopure Ferrocene-Based Planar-Chiral Iridacycles: Stereospecific Control of Iridium-Centred Chirality. *Chem. Eur. J.*, 22:3065–3072, 2016.

[221] X. Lu and W. K. Olson. 3DNA: a software package for the analysis, rebuilding and visualization of three-dimensional nucleic acid structures. *Nucleic. Acids. Res.*, 31:5108–5121, 2003.

Appendix A

Prediction of Lyotropic Liquid Crystal Slow Motion EPR Spectra

A.1 DFT Optimised Coordinates

A.1.1 SDS

Table A.1: DFT optimised Cartesian coordinates of dodecyl-sulphate anion.

Atom Type	X	Y	Z
C	3.537	1.423	0.000
H	3.601	0.778	-0.882
H	3.601	0.778	0.883
H	4.415	2.074	0.000
C	2.237	2.231	0.000
H	2.216	2.890	-0.876
H	2.216	2.891	0.876
C	0.977	1.357	0.000
H	0.998	0.696	-0.876

Table A.1: Continued from previous page

H	0.998	0.696	0.877
C	-0.330	2.157	0.000
H	-0.348	2.818	-0.877
H	-0.349	2.818	0.877
C	-1.589	1.283	0.000
H	-1.570	0.622	-0.877
H	-1.570	0.622	0.877
C	-2.896	2.085	0.000
H	-2.914	2.745	-0.877
H	-2.914	2.745	0.876
C	-4.156	1.212	0.000
H	-4.138	0.551	-0.877
H	-4.138	0.551	0.877
C	-5.462	2.014	0.000
H	-5.479	2.675	-0.877
H	-5.479	2.675	0.876
C	-6.723	1.143	0.000
H	-6.707	0.482	-0.877
H	-6.707	0.481	0.876
C	-8.028	1.947	0.000
H	-8.045	2.607	0.876
H	-8.045	2.608	-0.877
C	-9.289	1.075	0.000
H	-9.292	0.420	0.879
H	-9.292	0.420	-0.879
C	-10.575	1.892	0.000
H	-10.621	2.538	-0.888

Table A.1: Continued from previous page

H	-10.621	2.536	0.888
O	-11.667	0.988	0.000
S	-13.210	1.734	0.000
O	-13.218	2.536	-1.239
O	-14.079	0.553	-0.001
O	-13.218	2.535	1.240

A.1.2 DTAC

Table A.2: DFT optimised Cartesian coordinates of dodecyltrimethylammonium cation.

Atom Type	X	Y	Z
C	3.537	1.423	0.000
H	3.692	0.803	-0.882
H	2.526	1.828	-0.004
H	4.258	2.234	0.018
N	3.710	0.571	1.230
C	3.537	1.422	2.460
H	2.526	1.828	2.464
H	3.692	0.803	3.341
H	4.259	2.234	2.443
C	2.649	-0.501	1.230
H	2.766	-1.114	2.121
H	1.667	-0.028	1.230
H	2.766	-1.114	0.338
C	5.082	-0.121	1.230
H	5.080	-0.763	2.113
H	5.080	-0.763	0.347
C	6.303	0.790	1.230
H	6.306	1.437	0.348
H	6.306	1.437	2.112
C	7.593	-0.051	1.230
H	7.600	-0.707	0.351
H	7.600	-0.707	2.108
C	8.861	0.814	1.230
H	8.850	1.471	2.108

Table A.2: Continued from previous page

H	8.850	1.471	0.352
C	10.152	-0.012	1.230
H	10.161	-0.670	2.107
H	10.161	-0.670	0.352
C	11.420	0.849	1.230
H	11.410	1.509	2.107
H	11.410	1.509	0.353
C	12.715	0.028	1.230
H	12.725	-0.632	2.107
H	12.725	-0.632	0.353
C	13.983	0.890	1.230
H	13.972	1.550	2.107
H	13.972	1.550	0.353
C	15.279	0.071	1.230
H	15.289	-0.589	2.107
H	15.290	-0.589	0.353
C	16.546	0.933	1.230
H	16.536	1.593	2.107
H	16.536	1.593	0.353
C	17.844	0.116	1.230
H	17.855	-0.543	2.107
H	17.855	-0.543	0.354
C	19.104	0.987	1.230
H	19.139	1.632	2.113
H	19.140	1.632	0.347
H	20.010	0.375	1.230

A.1.3 5DSA

Table A.3: DFT optimised Cartesian coordinates of 5-DOXYL stearic acid spin probe.

Atom Type	X	Y	Z
C	-4.593063	-2.130602	-1.477736
C	-4.173821	-3.004399	-0.280156
C	-3.839262	-0.571554	0.071243
H	-4.285378	-2.545400	-2.437789
H	-5.679120	-1.976486	-1.490252
N	-3.815718	-1.928136	0.685940
O	-3.650258	-2.121882	1.929227
O	-3.910063	-0.880715	-1.316506
C	-5.105832	0.165801	0.560516
C	-6.423247	-0.568494	0.290368
H	-5.107663	1.155865	0.093037
H	-4.998702	0.335765	1.637884
C	-7.602009	0.127994	0.971517
H	-6.621071	-0.626164	-0.782057
H	-6.352319	-1.599413	0.647399
H	-7.471216	0.168414	2.058518
H	-7.685577	1.172965	0.649903
C	-2.551512	0.203341	0.364957
C	-1.249372	-0.510097	-0.008177
H	-2.553693	0.436804	1.434799
H	-2.611418	1.154702	-0.171110
C	-0.009626	0.342592	0.287805
H	-1.177896	-1.450958	0.546825
H	-1.269409	-0.765288	-1.072686

Table A.3: Continued from previous page

H	-0.076295	1.289060	-0.264208
H	0.001811	0.610346	1.352245
C	-8.933678	-0.529931	0.696599
O	-9.130989	-1.469825	-0.031330
O	-9.935762	0.079471	1.382924
H	-10.757901	-0.381193	1.156987
C	1.305481	-0.359238	-0.069556
H	1.367875	-1.307620	0.479593
H	1.294831	-0.625101	-1.134679
C	2.553502	0.479065	0.228970
H	2.493989	1.427175	-0.321088
H	2.563474	0.746047	1.293716
C	3.865437	-0.230047	-0.125896
H	3.856306	-0.494582	-1.191375
H	3.920779	-1.180061	0.421425
C	5.118007	0.599852	0.177285
H	5.066688	1.548219	-0.373193
H	5.125446	0.867396	1.241962
C	6.427171	-0.117225	-0.171831
H	6.475244	-1.066753	0.377015
H	6.420516	-0.383294	-1.236934
C	7.683065	0.706374	0.134832
H	7.639061	1.653865	-0.417770
H	7.687495	0.976173	1.198966
C	8.990192	-0.017877	-0.207237
H	9.031694	-0.966333	0.344004
H	8.986710	-0.286295	-1.271779

Table A.3: Continued from previous page

C	10.248293	0.800779	0.102566
H	10.210488	1.748157	-0.451054
H	10.251344	1.071957	1.166533
C	11.554897	0.073140	-0.234416
H	11.592765	-0.873291	0.318690
H	11.553131	-0.196832	-1.297600
C	12.806730	0.897569	0.079728
H	13.719840	0.351626	-0.173760
H	12.813956	1.836024	-0.483856
H	12.856485	1.151763	1.143343
C	-5.312564	-3.859146	0.280238
H	-5.599232	-4.627552	-0.442897
H	-4.991794	-4.350498	1.200382
H	-6.191057	-3.250661	0.507474
C	-2.935063	-3.862209	-0.578929
H	-2.148779	-3.266694	-1.046252
H	-2.544096	-4.288253	0.347749
H	-3.197333	-4.682762	-1.252758

A.2 Fitted Correlation Plots

A.2.1 Microaggregates

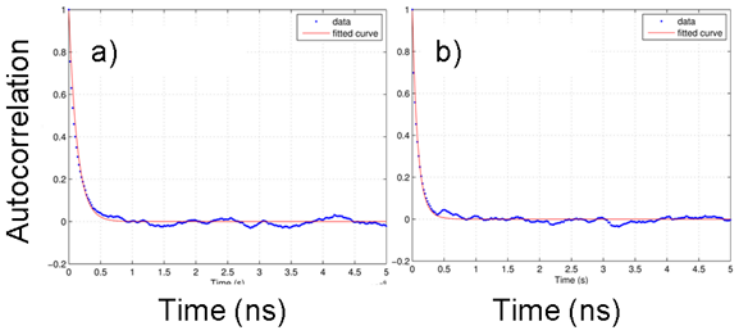

Figure A.1: Fitted autocorrelation function of 5DSA Z (a) and X/Y (b) magnetic axes in n = 2 SDS micro-aggregate at 300K.

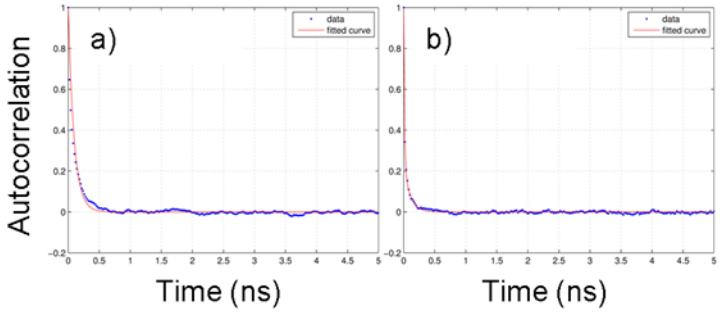

Figure A.2: Fitted autocorrelation function of SDS Z (a) and X/Y (b) molecular axes in n = 2 SDS micro-aggregate at 300K.

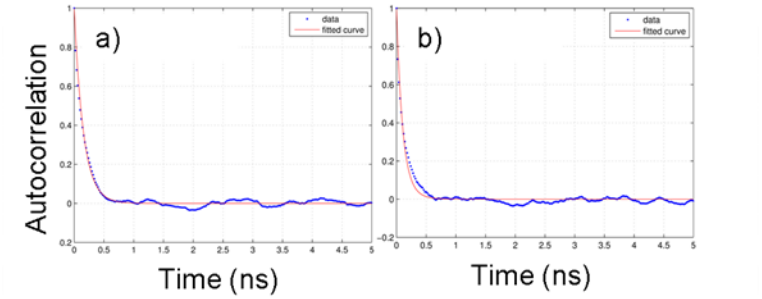

Figure A.3: Fitted autocorrelation function of 5DSA Z (a) and X/Y (b) magnetic axes in n = 3 SDS micro-aggregate at 300K.

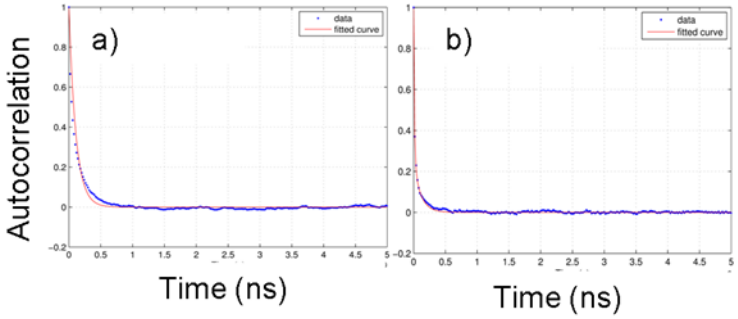

Figure A.4: Fitted autocorrelation function of SDS Z (a) and X/Y (b) molecular axes in n = 3 SDS micro-aggregate at 300K.

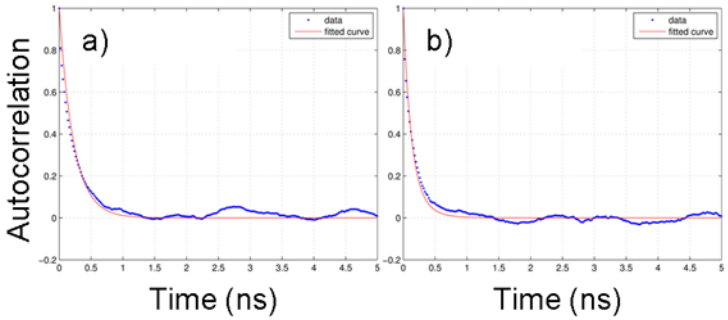

Figure A.5: Fitted autocorrelation function of 5DSA Z (a) and X/Y (b) magnetic axes in n = 4 SDS micro-aggregate at 300K.

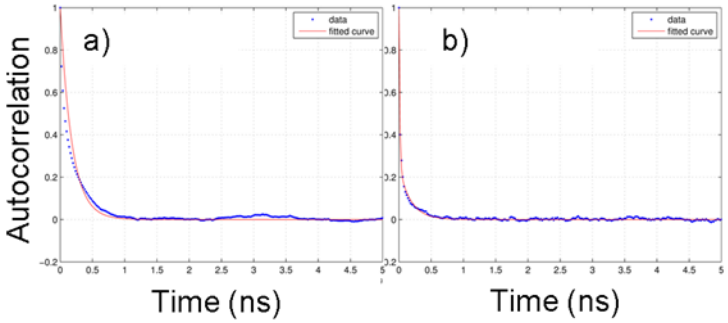

Figure A.6: Fitted autocorrelation function of SDS Z (a) and X/Y (b) molecular axes in n = 4 SDS micro-aggregate at 300K.

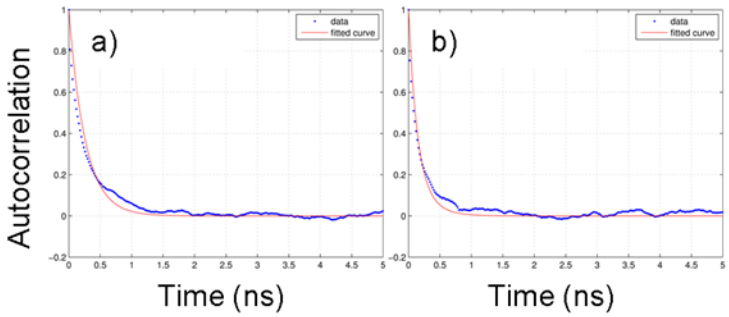

Figure A.7: Fitted autocorrelation function of 5DSA Z (a) and X/Y (b) magnetic axes in n = 5 SDS micro-aggregate at 300K.

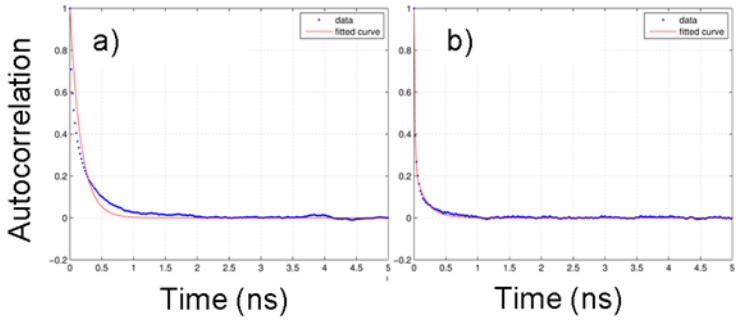

Figure A.8: Fitted autocorrelation function of SDS Z (a) and X/Y (b) molecular axes in n = 5 SDS micro-aggregate at 300K.

Table A.4: 95% confidence bounds for motional parameters of 5DSA and SDS in different micro-aggregate states at 300K obtained from the fitting of the relevant autocorrelation functions.

	$D_{\perp}$ (s^{-1})		$D_{\parallel}$ (s^{-1})	
	Fit	**Min/Max**	**Fit**	**Min/Max**
	2 SDS Molecules			
5DSA	12.67×10^8	$12.57/12.78 \times 10^8$	2.73×10^9	$2.72/2.75 \times 10^9$
SDS	17.60×10^8	$17.58/17.65 \times 10^8$	2.01×10^{10}	$1.93/2.11 \times 10^{10}$
	3 SDS Molecules			
5DSA	10.75×10^8	$10.69/10.81 \times 10^8$	2.11×10^9	$2.09/2.12 \times 10^9$
SDS	15.26×10^8	$15.23/15.30 \times 10^8$	1.84×10^{10}	$1.77/1.91 \times 10^{10}$
	4 SDS Molecules			
5DSA	7.45×10^8	$7.21/7.69 \times 10^8$	1.79×10^9	$1.78/1.80 \times 10^9$
SDS	9.73×10^8	$9.72/9.74 \times 10^8$	1.80×10^{10}	$1.80/1.81 \times 10^{10}$
	5 SDS Molecules			
5DSA	6.39×10^8	$6.18/6.61 \times 10^8$	1.57×10^9	$1.55/1.58 \times 10^9$
SDS	9.27×10^8	$9.26/9.29 \times 10^8$	1.75×10^{10}	$1.75/1.76 \times 10^{10}$

A.2.2 Micelles

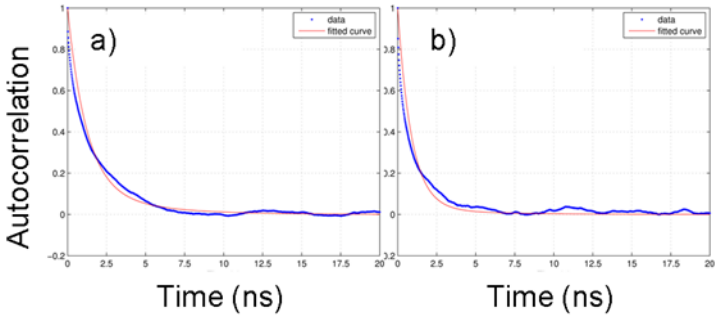

Figure A.9: Fitted autocorrelation function of 5DSA Z (a) and X/Y (b) magnetic axes in SDS micelle at 300K.

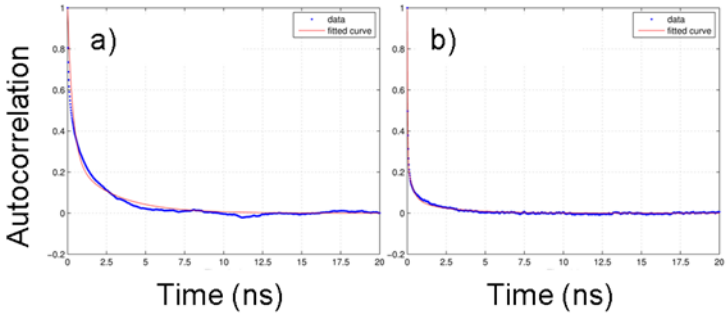

Figure A.10: Fitted autocorrelation function of SDS Z (a) and X/Y (b) molecular axes in SDS micelle at 300K.

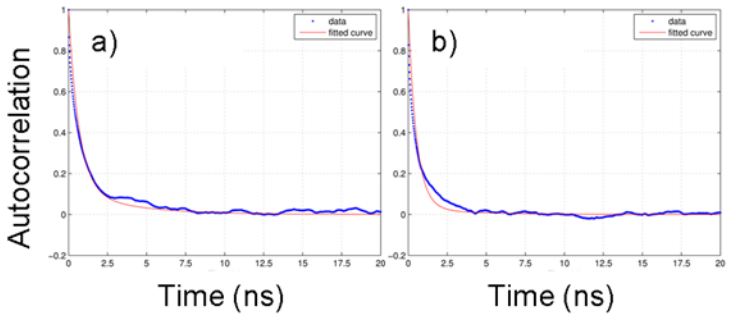

Figure A.11: Fitted autocorrelation function of 5DSA Z (a) and X/Y (b) magnetic axes in SDS micelle at 310K.

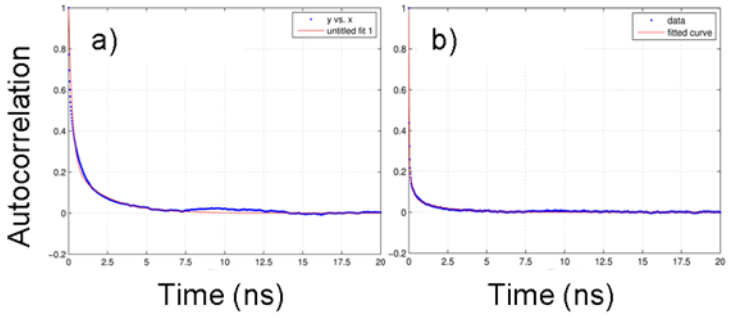

Figure A.12: Fitted autocorrelation function of SDS Z (a) and X/Y (b) molecular axes in SDS micelle at 310K.

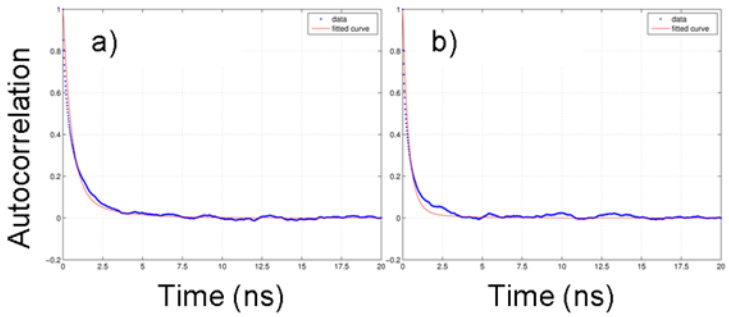

Figure A.13: Fitted autocorrelation function of 5DSA Z (a) and X/Y (b) magnetic axes in SDS micelle at 320K.

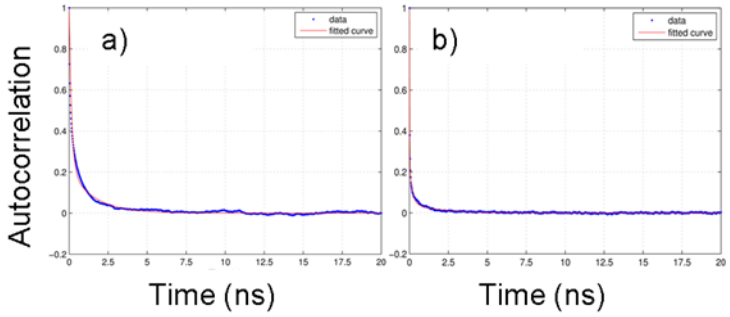

Figure A.14: Fitted autocorrelation function of SDS Z (a) and X/Y (b) molecular axes in SDS micelle at 320K.

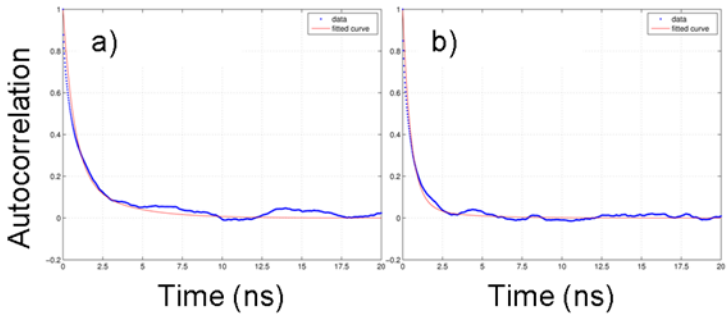

Figure A.15: Fitted autocorrelation function of 5DSA Z (a) and X/Y (b) magnetic axes in DTAC micelle at 300K.

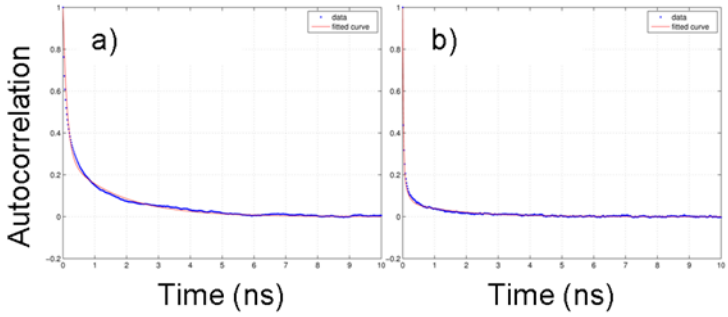

Figure A.16: Fitted autocorrelation function of DTAC Z (a) and X/Y (b) molecular axes in DTAC micelle at 300K.

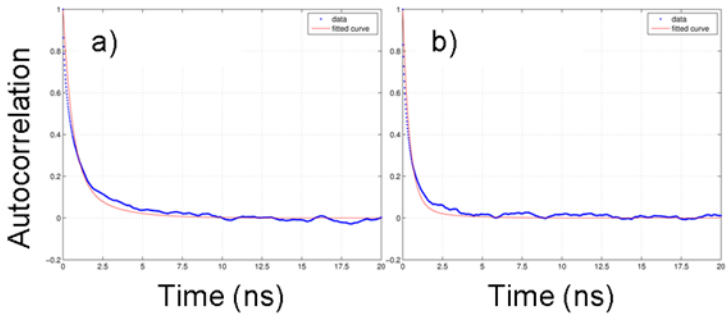

Figure A.17: Fitted autocorrelation function of 5DSA Z (a) and X/Y (b) magnetic axes in DTAC micelle at 310K.

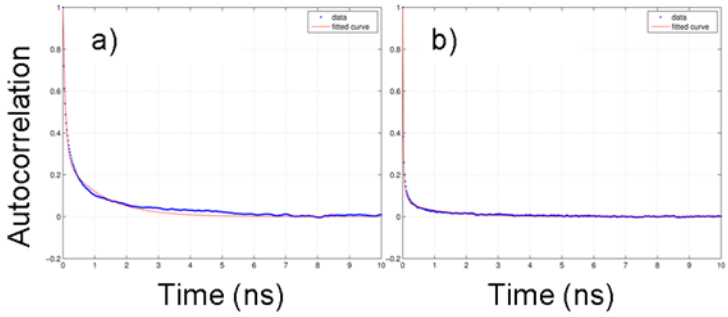

Figure A.18: Fitted autocorrelation function of DTAC Z (a) and X/Y (b) molecular axes in DTAC micelle at 310K.

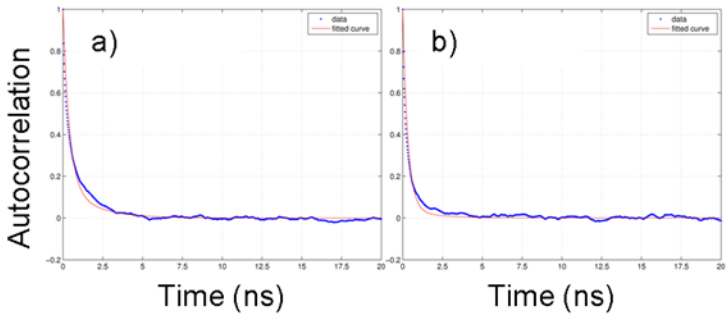

Figure A.19: Fitted autocorrelation function of 5DSA Z (a) and X/Y (b) magnetic axes in DTAC micelle at 320K.

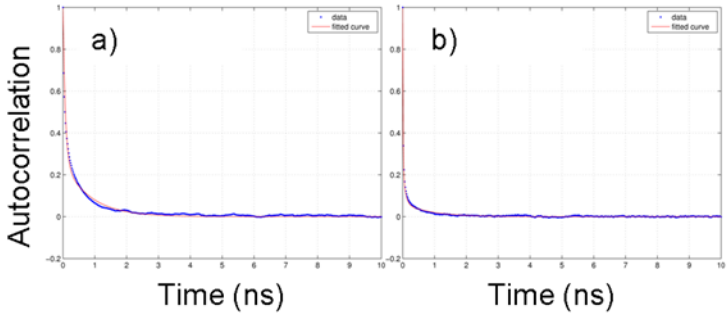

Figure A.20: Fitted autocorrelation function of DTAC Z (a) and X/Y (b) molecular axes in DTAC micelle at 320K.

Table A.5: 95% confidence bounds for motional and order parameters of 5DSA and SDS in N60 SDS micelles fitted from autocorrelation functions.

T (K)		D^G ($\times 10^7\ s^{-1}$)		$D_\perp^L$ ($\times 10^8\ s^{-1}$)		$D_\parallel^L$ ($\times 10^9\ s^{-1}$)		S^L	
		Fit	**Min/Max**	**Fit**	**Min/Max**	**Fit**	**Min/Max**	**Fit**	**Min/Max**
		SDS N60 Micelle							
300	5DSA	3.8	3.5/4.1	1.26	1.24/1.29	0.168	0.167/0.169	0.36	0.33/0.42
300	SDS	6.9	6.6/7.3	3.24	3.19/3.29	9.55	9.54/9.56	0.55	0.50/0.61
310	5DSA	4.6	4.1/5.0	1.79	1.73/1.88	0.358	0.356/0.362	0.35	0.32/0.38
310	SDS	8.7	8.3/9.2	5.56	5.55/5.61	1.16	1.16/1.18	0.51	0.45/0.56
320	5DSA	6.7	6.4/7.1	2.14	2.10/2.18	0.545	0.544/0.547	0.34	0.32/0.39
320	SDS	10.6	10.4/10.8	7.37	7.36.7.39	1.93	1.92/1.93	0.46	0.40/0.52

Table A.6: 95% confidence bounds for motional and order parameters of 5DSA and DTAC in N40 DTAC micelles fitted from autocorrelation functions.

T (K)		D^G ($\times 10^7\ s^{-1}$)		$D_\perp^L$ ($\times 10^8\ s^{-1}$)		$D_\parallel^L$ ($\times 10^9\ s^{-1}$)		S^L	
		Fit	**Min/Max**	**Fit**	**Min/Max**	**Fit**	**Min/Max**	**Fit**	**Min/Max**
		DTAC N40 Micelle							
300	5DSA	5.7	5.6/5.8	1.39	1.35/1.46	0.371	0.371/0.373	0.47	0.43/0.53
300	DTAC	10.1	10.0/10.2	8.73	8.70/8.76	1.1	1.1/1.1	0.54	0.49/0.60
310	5DSA	7.4	6.9/7.9	2.11	2.00/2.25	0.452	0.452/0.454	0.44	0.40/0.49
310	DTAC	14.3	13.9/14.8	12.97	12.89/13.10	1.74	1.74/1.76	0.53	0.49/0.57
320	5DSA	9.1	8.9/9.4	2.75	2.71/2.80	0.567	0.567/0.579	0.40	0.35/0.46
320	DTAC	19.9	19.3/20.8	15.15	14.98/15.32	2.05	2.04/2.06	0.51	0.49/0.55

A.2.3 Rods

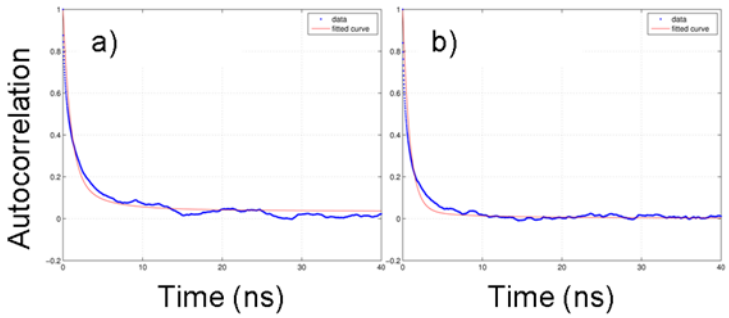

Figure A.21: Fitted autocorrelation function of 5DSA Z (a) and X/Y (b) magnetic axes in SDS hexagonal phase at 320K.

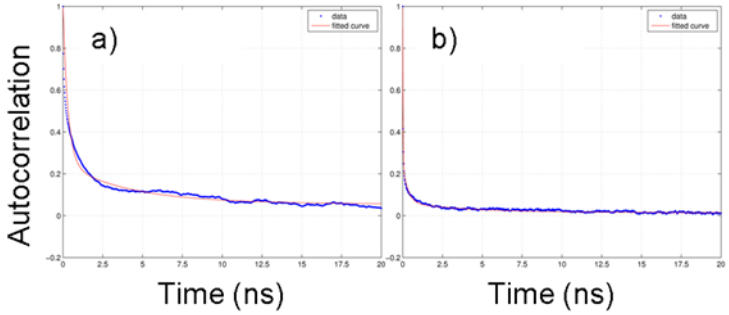

Figure A.22: Fitted autocorrelation function of SDS Z (a) and X/Y (b) molecular axes in SDS hexagonal phase at 320K.

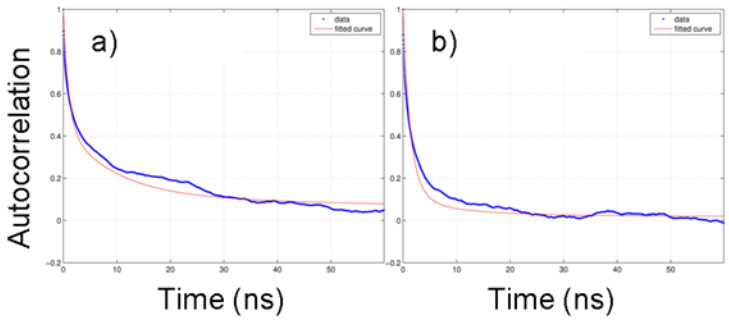

Figure A.23: Fitted autocorrelation function of 5DSA Z (a) and X/Y (b) magnetic axes in DTAC hexagonal phase at 320K.

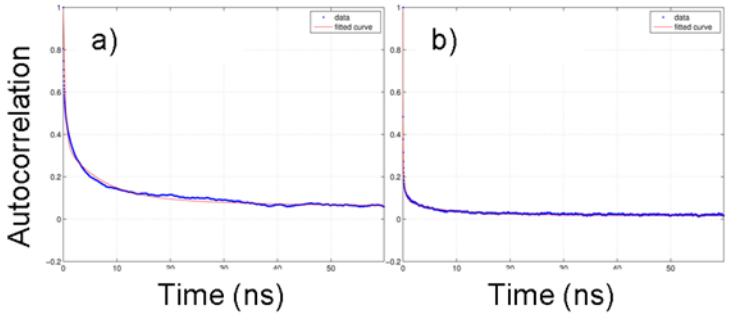

Figure A.24: Fitted autocorrelation function of DTAC Z (a) and X/Y (b) molecular axes in DTAC hexagonal phase at 320K.

Table A.7: 95% confidence bounds for motional and order parameters of 5DSA , SDS and DTAC in hexagonal phases at 320K fitted from autocorrelation functions.

	$D_{\parallel}^{G}$ ($\times 10^{7}\,s^{-1}$)		$D_{\perp}^{L}$ ($\times 10^{8}\,s^{-1}$)		$D_{\parallel}^{L}$ ($\times 10^{9}\,s^{-1}$)		S^{L}	
	Fit	**Min/Max**	**Fit**	**Min/Max**	**Fit**	**Min/Max**	**Fit**	**Min/Max**
	SDS Hexagonal Phase							
5DSA	5.91	5.10/6.76	1.15	1.01/1.29	0.208	0.208/0.210	0.43	0.36/0.47
SDS	6.27	6.03/6.41	3.75	3.59/3.93	11.19	11.16/11.23	0.50	0.45/0.55
	DTAC Hexagonal Phase							
5DSA	2.70	1.88/3.69	0.99	0.86/1.08	0.111	0.109/0.114	0.58	0.51/0.65
DTAC	3.60	3.14/4.05	2.73	2.66/2.7	10.16	10.15/10.20	0.61	0.56/0.67

A.2.4 Lamellae

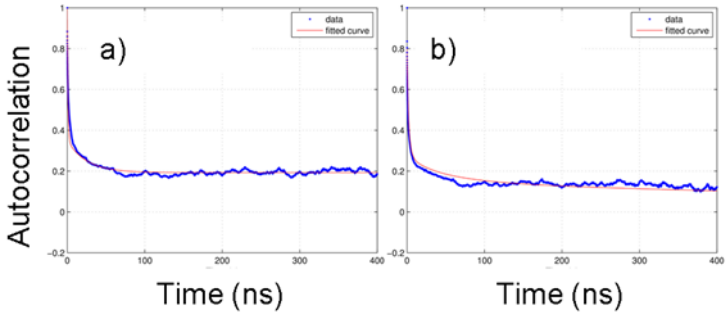

Figure A.25: Fitted autocorrelation function of 5DSA Z (a) and X/Y (b) magnetic axes in SDS lamellar phase at 350K.

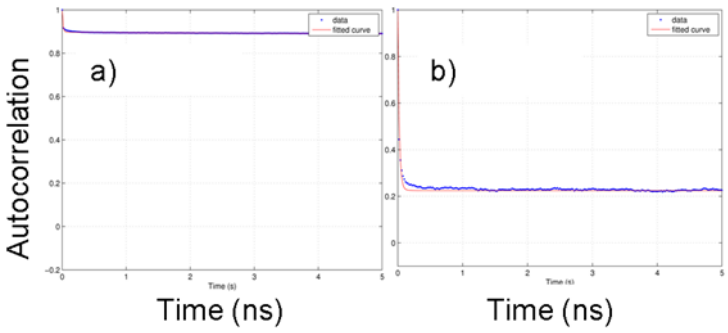

Figure A.26: Fitted autocorrelation function of SDS Z (a) and X/Y (b) molecular axes in SDS lamellar phase at 350K.

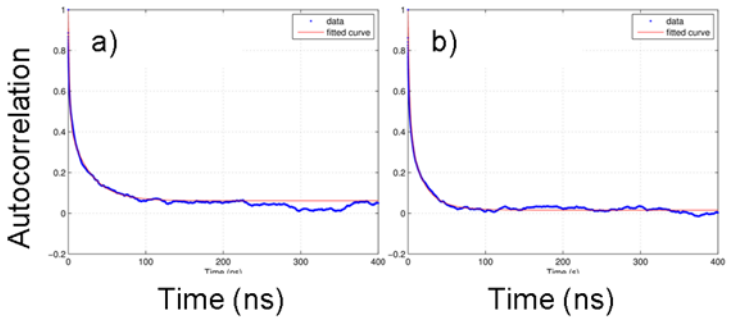

Figure A.27: Fitted autocorrelation function of 5DSA Z (a) and X/Y (b) magnetic axes in DTAC lamellar phase at 350K.

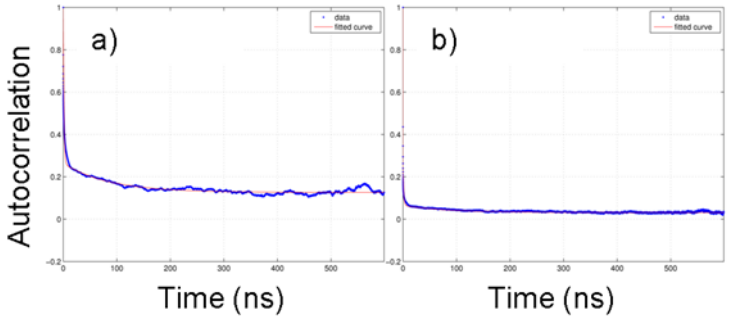

Figure A.28: Fitted autocorrelation function of DTAC Z (a) and X/Y (b) molecular axes in DTAC lamellar phase at 350K.

Table A.8: 95% confidence bounds for motional and order parameters of 5DSA, SDS and DTAC in lamellar phases at 350K fitted from autocorrelation functions.

	$D_{\perp}^{G}$ ($\times 10^{6}$ s^{-1})		S^{G}		$D_{\perp}^{L}$ ($\times 10^{8}$ s^{-1})		S^{L}	
	Fit	**Min/Max**	**Fit**	**Min/Max**	**Fit**	**Min/Max**	**Fit**	**Min/Max**
	SDS Lamellar Phase							
5DSA	3.57	3.52/3.62	0.74	0.70/0.76	1.19	1.12/1.25	0.59	0.55/0.64
SDS	11.7	10.8/12.3	0.99	0.99/0.99	2.82	2.78/2.89	0.95	0.93/0.97
	DTAC Lamellar Phase							
5DSA	4.69	4.62/4.77	0.38	0.35/0.40	0.93	0.90/0.95	0.68	0.64/0.72
DTAC	1.01	0.99/1.02	0.69	0.66/0.71	0.93	0.91/0.95	0.51	0.50/0.52

A.3 C-H Order Parameters

Table A.9: Fitted data for determination of $S_C - H$ order parameters as a function of position along the carbonyl chain in micellar SDS at 310K.

Carbon Atom	$\mathbf{D}^G_{Iso}$ ($\mathbf{s}^{-1}$)	$\mathbf{D}^L_{\perp}$ ($\mathbf{s}^{-1}$)	$\mathbf{D}^L_{\parallel}$ ($\mathbf{s}^{-1}$)	S^L
CH1	8.87E7	28.13E8	19.81E9 (8.4 ps)	0.57
CH2	8.87E7	12.71E8	11.56E9 (14.4 ps)	0.47
CH3	8.87E7	10.2E8	12.10E9 (13.8 ps)	0.46
CH4	8.87E7	6.52E8	11.62E9 (14.3 ps)	0.51
CH5	8.87E7	5.56E8	11.61E9 (14.4 ps)	0.51
CH6	8.87E7	5.32E8	11.79E9 (14.1 ps)	0.55
CH7	8.87E7	5.62E8	12.31E9 (13.5 ps)	0.55
CH8	8.87E7	6.44E8	17.72E9 (9.4 ps)	0.52
CH9	8.87E7	8.21E8	19.84E9 (8.4 ps)	0.48
CH10	8.87E7	13.27E8	22.75E9 (7.3 ps)	0.43
CH11	8.87E7	27.85E8	25.04E9 (6.7 ps)	0.35
CH12	8.87E7	16.04E8	22.37E9 (7.4 ps)	0.09

A.4 NRMSD of Micellar EPR Spectra

RMSD for normalised spectra was calculated via (A.1):

$$RMSD = \sqrt{\frac{\sum(M(B_i) - S(B_i))^2}{N}} \tag{A.1}$$

where $M(B_i)$ and $S(B_i)$ are the EPR spectral values at magnetic field B_i and N is the number of data points. In each case parameters were varied by ±20% from those obtained from MD and the RMSD calculated in order to quantify the sensitivity.

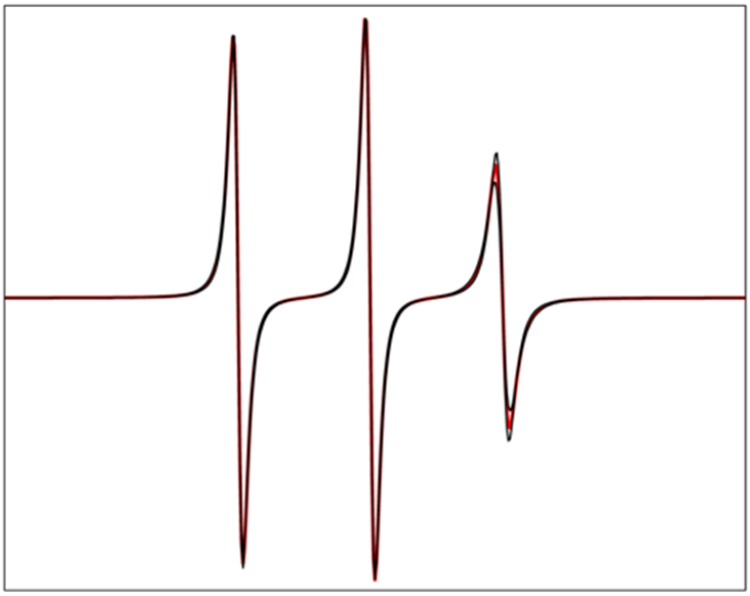

D_{Iso} (s^{-1})	RMSD relative to MD spectra
8.08E7 (MD + 20%)	0.0113
6.7E7 (MD)	N/A
5.36E7 (MD - 20%)	0.0150

Figure A.29: Effect of D^G_{Iso} on EPR spectra of 5DSA doped in SDS micelle (red) with D^G_{Iso} ±20% (black) at 320K.

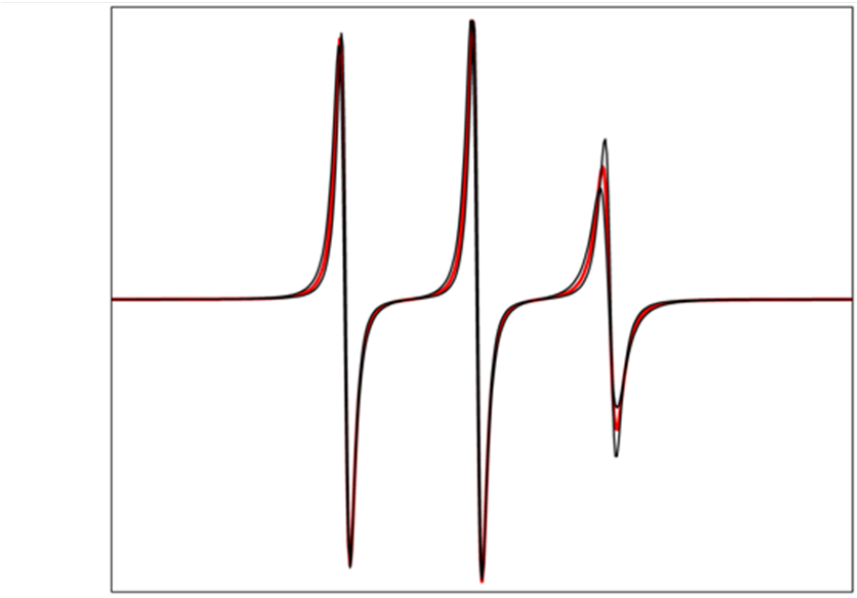

S^L	RMSD relative to MD spectra
0.41 (MD + 20%)	0.0455
0.34 (MD)	N/A
0.27 (MD - 20%)	0.0469

Figure A.30: Effect of S^L on EPR spectra of 5DSA doped in SDS micelle (red) with S^L ±20% (black) at 320K.

Appendix B

Prediction of Spin Labelled DNA Slow Motion EPR Spectra

B.1 Optimised Geometries

B.1.1 Q Spin Label

Table B.1: Cartesian coordinates of Q label.

Atom Type	X	Y	Z
P	2.322	1.778	-0.482
O1P	1.943	3.074	-1.087
O2P	3.166	0.872	-1.295
O5’	3.000	2.143	0.920
C5’	2.160	2.553	2.015
H5’1	1.456	1.756	2.252
H5’2	1.610	3.452	1.735
C4’	3.010	2.849	3.240
H4’	2.448	3.478	3.930
O4’	3.228	1.606	3.975
C1’	4.559	1.151	3.778

Table B.1: Continued from previous page

H1'	5.070	1.095	4.738
C3'	4.419	3.378	2.961
H3'	4.417	3.941	2.028
C2'	5.232	2.096	2.780
H2'1	5.672	2.080	1.783
H2'2	6.026	2.060	3.528
O3'	5.031	4.129	3.999
C	4.499	-0.316	3.312
C	4.657	-1.384	4.300
C	4.301	-0.583	1.998
N	4.584	-2.672	3.757
O	4.839	-1.223	5.502
H	4.186	0.232	1.287
C	4.234	-1.932	1.497
C	4.383	-2.992	2.428
H	4.693	-3.416	4.437
C	4.029	-2.240	0.138
C	4.328	-4.330	2.001
H	3.916	-1.423	-0.572
C	3.975	-3.558	-0.279
C	4.126	-4.599	0.658
H	4.444	-5.133	2.725
C	3.766	-4.090	-1.681
C	4.035	-5.959	0.000
N	3.815	-5.557	-1.418
C	2.393	-3.729	-2.278
C	4.895	-3.712	-2.657

Table B.1: Continued from previous page

C	5.337	-6.775	0.101
C	2.835	-6.795	0.483
O	3.680	-6.416	-2.349
H	2.345	-2.660	-2.514
H	2.235	-4.301	-3.196
H	1.587	-3.964	-1.575
H	4.780	-4.283	-3.584
H	4.856	-2.643	-2.895
H	5.876	-3.935	-2.227
H	6.201	-6.177	-0.204
H	5.499	-7.120	1.128
H	5.267	-7.647	-0.557
H	2.719	-7.667	-0.167
H	2.991	-7.138	1.511
H	1.911	-6.209	0.450

B.1.2 P Base

Table B.2: Cartesian coordinates of P base.

Atom Type	**X**	**Y**	**Z**
P	2.314	1.777	-0.478
O1P	1.933	3.073	-1.082
O2P	3.157	0.872	-1.292
O5’	2.994	2.142	0.923
C5’	2.156	2.552	2.020
H5’1	1.453	1.754	2.258
H5’2	1.605	3.450	1.741

Table B.2: Continued from previous page

C4'	3.008	2.848	3.243
H4'	2.447	3.477	3.934
O4'	3.228	1.605	3.977
C1'	4.559	1.151	3.778
H1'	5.072	1.095	4.737
C3'	4.416	3.378	2.961
H3'	4.412	3.941	2.028
C2'	5.230	2.096	2.779
H2'1	5.668	2.081	1.781
H2'2	6.025	2.061	3.525
O3'	5.030	4.129	3.998
N	4.502	-0.249	3.333
C	4.785	-1.363	4.085
C6	4.151	-0.706	2.070
C7	4.585	-2.449	3.211
N1	5.168	-1.434	5.352
H	3.879	-0.018	1.282
N2	4.189	-2.003	1.956
C8	4.827	-3.706	3.758
C9	5.356	-2.700	5.762
H6	4.716	-4.618	3.179
N3	5.210	-3.828	5.026
N4	5.706	-2.882	7.072
H7	6.055	-3.791	7.330
H8	6.035	-2.080	7.583

B.1.3 C* Spin Label

Table B.3: Cartesian coordinates of C label.*

Atom Type	X	Y	Z
P	2.338	1.780	-0.490
O1P	1.963	3.076	-1.097
O2P	3.184	0.872	-1.301
O5’	3.012	2.145	0.914
C5’	2.168	2.555	2.005
H5’1	1.462	1.760	2.240
H5’2	1.620	3.456	1.723
C4’	3.014	2.851	3.234
H4’	2.450	3.480	3.922
O4’	3.228	1.608	3.971
C1’	4.559	1.151	3.778
H1’	5.066	1.095	4.740
C3’	4.425	3.378	2.961
H3’	4.427	3.941	2.028
C2’	5.236	2.096	2.782
H2’1	5.680	2.078	1.787
H2’2	6.028	2.058	3.534
O3’	5.033	4.129	4.001
N	4.502	-0.249	3.333
C	4.662	-1.222	4.375
C6	4.313	-0.564	2.036
N1	4.611	-2.533	3.985
O	4.825	-0.816	5.513
C7	4.264	-1.878	1.643
H	4.203	0.254	1.332

Table B.3: Continued from previous page

C8	4.430	-2.854	2.721
C9	4.067	-2.268	0.298
N2	4.399	-4.167	2.402
C10	3.898	-2.631	-0.855
Du	4.115	-3.300	0.578
Du	4.479	-4.843	3.146
H8	4.217	-4.469	1.457
C11	3.705	-3.071	-2.184
H9	3.769	-1.614	-1.164
C12	3.693	-4.558	-2.537
C13	3.518	-2.299	-3.274
C14	2.535	-5.325	-1.876
C15	5.037	-5.251	-2.265
N3	3.460	-4.473	-4.002
C16	3.346	-3.092	-4.542
H10	3.490	-1.215	-3.265
H11	2.695	-5.413	-0.796
H12	1.582	-4.814	-2.041
H13	2.474	-6.328	-2.307
H14	5.020	-6.258	-2.695
H15	5.863	-4.694	-2.717
H16	5.223	-5.329	-1.189
O6	3.379	-5.510	-4.739
C17	1.963	-2.905	-5.196
C18	4.464	-2.844	-5.573
H17	1.871	-1.901	-5.624
H18	1.840	-3.641	-5.996

Table B.3: Continued from previous page

H19	1.161	-3.047	-4.465
H20	4.381	-3.578	-6.380
H21	4.378	-1.838	-6.000
H22	5.452	-2.943	-5.112

B.2 Definitions of Rigid Body Parameters of DNA

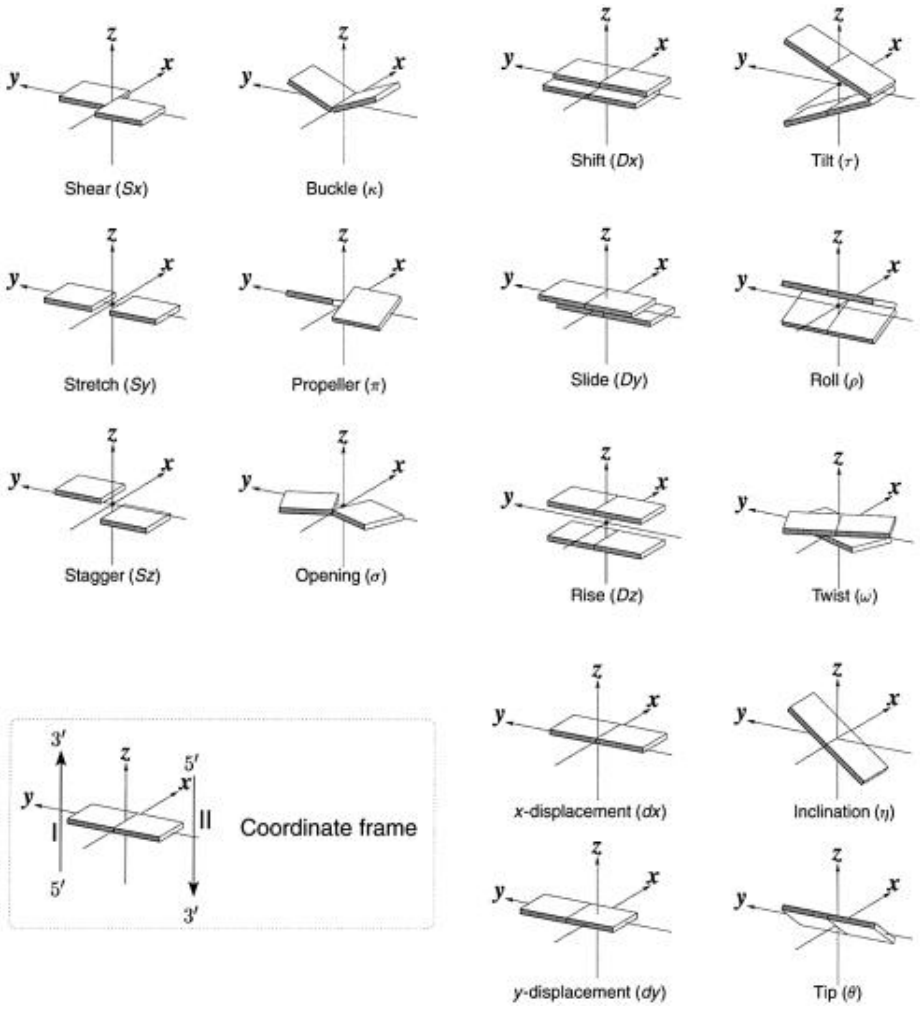

Figure B.1: Definitions of rigid body parameters used to describe the geometry of complementary and non-complementary base pairs and sequential base pair steps as defined by [167]. Figure reproduced from [221] with permission from Oxford University Press.

B.3 Fitted Rotational Autocorrelation Functions

B.3.1 dQ ([5-d(GCC-TAC-ATG-QGA-CG)-5-d(CGT-CPC-ATG-TAG-GC)])

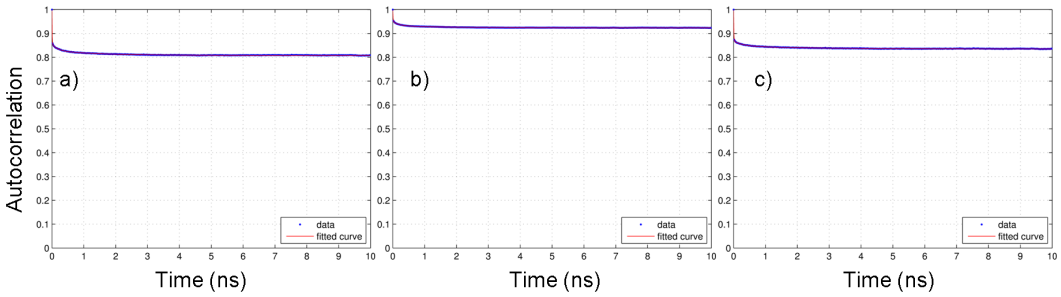

Figure B.2: Fitted autocorrelation functions of local motion of Q-labelled duplex DNA magnetic Z (a), Y (b) and X (c) axes at 293K using tri-exponential expression with global motion excluded.

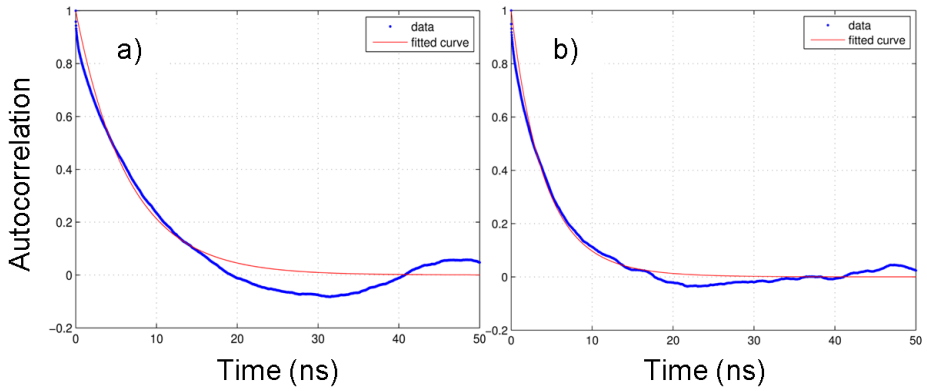

Figure B.3: Fitted autocorrelation functions of Q-labelled duplex DNA Z (a) and X/Y (b) principal axes at 293K.

Table B.4: Parameters obtained from fitting autocorrelation functions of a) local motion of magnetic axes and b) principal axes for Q-labelled duplex DNA magnetic axes with 95% confidence bounds. Weights are presented prior to normalisation.

a)

T (K)	Axis	w_1		τ_1 (ns)		w_2		τ_2 (ns)		w_3		τ_3 (ns)		S_L^2
		Fit	Min/ Max	Fit	Min/ Max	Fit	Min/ Max	Fit	Min/ Max	Fit	Min/ Max	Fit	Min/ Max	
293	X	0.132	0.131/ 0.132	0.007	0.007/ 0.007	0.020	0.020/ 0.021	0.275	0.268/ 0.284	0.013	0.013/ 0.013	2.22	2.19/ 2.25	0.835
	Y	0.050	0.049/ 0.051	0.009	0.008/ 0.010	0.018	0.017/ 0.019	0.201	0.188/ 0.216	0.009	0.008/ 0.009	1.94	1.87/ 2.02	0.923
	Z	0.145	0.144/ 0.147	0.007	0.006/ 0.007	0.027	0.026/ 0.028	0.197	0.182/ 0.215	0.020	0.019/ 0.020	1.49	1.44/ 1.55	0.808

b)

T (K)	$\tau_\perp$ (ns)		$\tau_\parallel$ (ns)	
	Fit	Min/Max	Fit	Min/Max
293	6.21	6.12/6.30	2.99	2.93/3.06

B.3.2 dC ([5-d(GCC-TAC-ATG-C*GA-CG)-5-d(CG-TCG-CAT-GTA-GGC)])

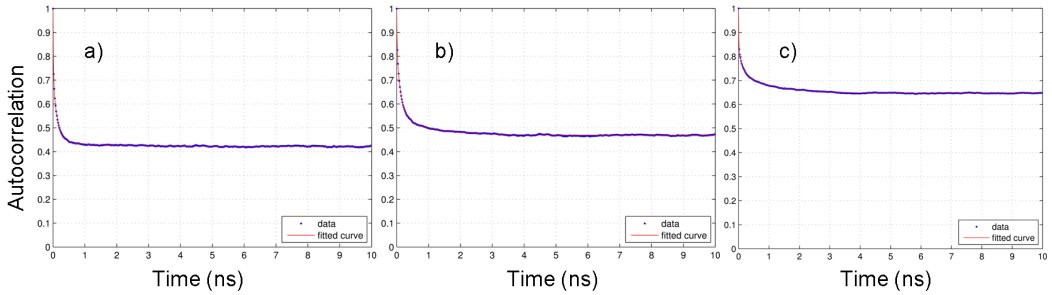

Figure B.4: Fitted autocorrelation functions of local motion of C-labelled duplex DNA magnetic Z (a), Y (b) and X (c) axes at 273K using tri-exponential expression with global motion excluded.*

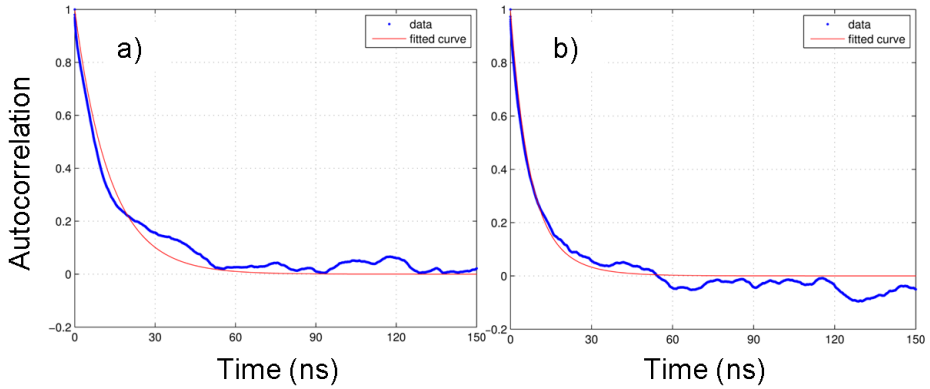

Figure B.5: Fitted autocorrelation functions of C-labelled duplex DNA Z (a) and X/Y (b) principal axes at 273K.*

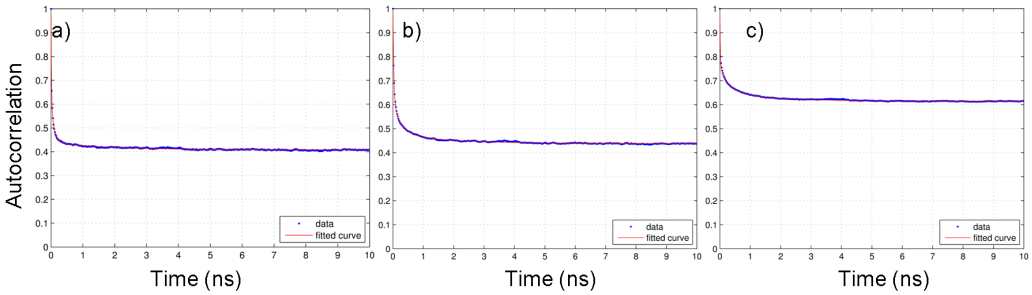

Figure B.6: Fitted autocorrelation functions of local motion of C-labelled duplex DNA magnetic Z (a), Y (b) and X (c) axes at 293K using tri-exponential expression with global motion excluded.*

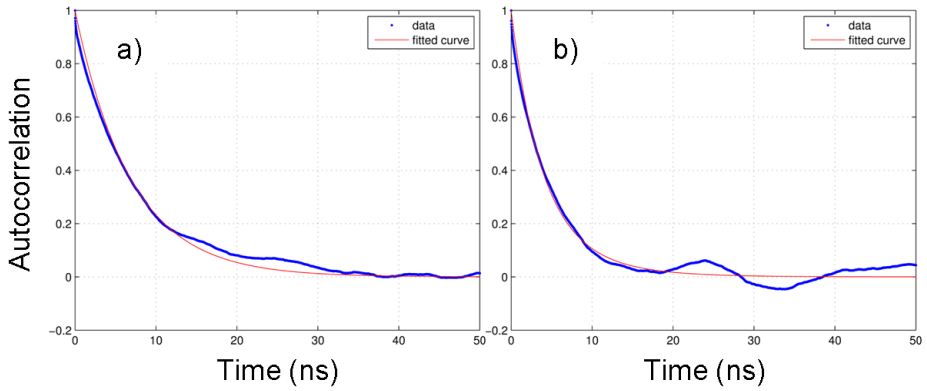

Figure B.7: Fitted autocorrelation functions of C-labelled duplex DNA Z (a) and X/Y (b) principal axes at 293K.*

Table B.5: Parameters obtained from fitting autocorrelation functions of a) local motion of magnetic axes and b) principal axes for C-labelled duplex DNA magnetic axes with 95% confidence bounds. Weights are presented prior to normalisation.*

a)

T (K)	Axis	w_1		τ_1 (ns)		w_2		τ_2 (ns)		w_3		τ_3 (ns)		S_L^2
		Fit	Min/ Max	Fit	Min/ Max	Fit	Min/ Max	Fit	Min/ Max	Fit	Min/ Max	Fit	Min/ Max	
273	X	0.166	0.162/ 0.170	0.008	0.007/ 0.009	0.105	0.102/ 0.108	0.138	0.131/ 0.146	0.082	0.080/ 0.084	1.08	1.06/ 1.11	0.647
	Y	0.171	0.162/ 0.179	0.013	0.012/ 0.015	0.281	0.275/ 0.288	0.132	0.127/ 0.137	0.079	0.076/ 0.082	1.06	1.02/ 1.10	0.469
	Z	0.285	0.283/ 0.287	0.011	0.011/ 0.011	0.275	0.273/ 0.276	0.136	0.135/ 0.137	0.018	0.018/ 0.019	1.47	1.43/ 1.51	0.422
293	X	0.240	0.239/ 0.242	0.013	0.012/ 0.013	0.097	0.096/ 0.099	0.266	0.260/ 0.273	0.048	0.046/ 0.049	1.44	1.42/ 1.47	0.615
	Y	0.382	0.380/ 0.385	0.028	0.028/ 0.029	0.137	0.135/ 0.139	0.255	0.249/ 0.260	0.043	0.042/ 0.044	1.75	1.72/ 1.78	0.438
	Z	0.355	0.351/ 0.360	0.011	0.011/ 0.011	0.205	0.200/ 0.209	0.083	0.081/ 0.085	0.032	0.032/ 0.036	1.78	1.75/ 1.81	0.408

b)

T (K)	$\tau_\perp$ (ns)		$\tau_\parallel$ (ns)	
	Fit	Min/Max	Fit	Min/Max
273	13.10	12.99/13.20	5.23	5.14/5.30
293	7.02	6.95/7.09	2.88	2.83/2.93

B.3.3 sQ ([5-d(GCT-TAA-GCT-QCG-CG])

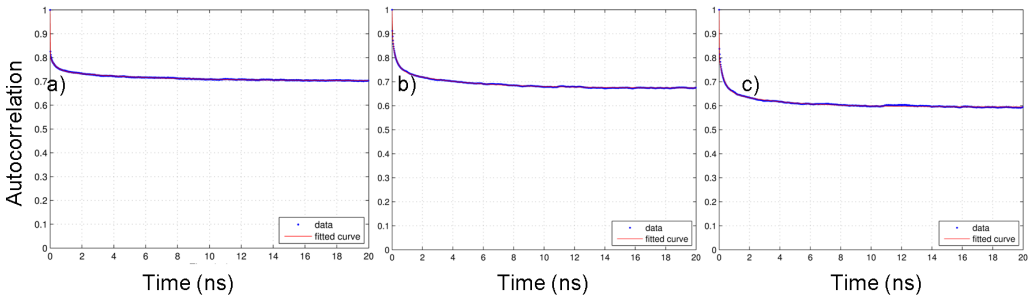

Figure B.8: Fitted autocorrelation functions of local motion of Q-labelled single strand DNA magnetic Z (a), Y (b) and X (c) axes at 293K using tri-exponential expression with global motion excluded.

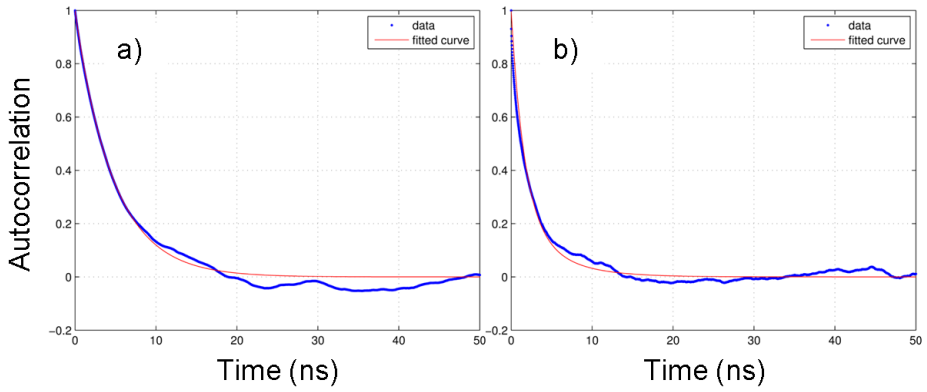

Figure B.9: Fitted autocorrelation functions of Q-labelled single strand DNA Z (a) and X/Y (b) principal axes at 293K.

Table B.6: Parameters obtained from fitting autocorrelation functions of a) local motion of magnetic axes and b) principal axes for Q-labelled single strand DNA magnetic axes with 95% confidence bounds. Weights are presented prior to normalisation.

a)

T (K)	Axis	w_1		τ_1 (ns)		w_2		τ_2 (ns)		w_3		τ_3 (ns)		S_L^2
		Fit	Min/ Max	Fit	Min/ Max	Fit	Min/ Max	Fit	Min/ Max	Fit	Min/ Max	Fit	Min/ Max	
293	X	0.201	0.199/ 0.204	0.014	0.013/ 0.014	0.138	0.136/ 0.139	0.345	0.339/ 0.351	0.067	0.066/ 0.067	3.61	3.58/ 3.65	0.595
	Y	0.132	0.131/ 0.133	0.036	0.036/ 0.037	0.120	0.118/ 0.120	0.325	0.323/ 0.328	0.074	0.074/ 0.075	4.05	4.04/ 4.06	0.674
	Z	0.199	0.198/ 0.199	0.010	0.010/ 0.010	0.057	0.057/ 0.058	0.393	0.389/ 0.397	0.042	0.042/ 0.043	5.59	5.57/ 5.61	0.702

b)

T (K)	$\tau_\perp$ (ns)		$\tau_\parallel$ (ns)	
	Fit	Min/Max	Fit	Min/Max
293	4.76	4.73/4.80	1.23	1.21/1.25

B.3.4 sC ([5-d(GCC-TAC-ATG-C*GA-CG])

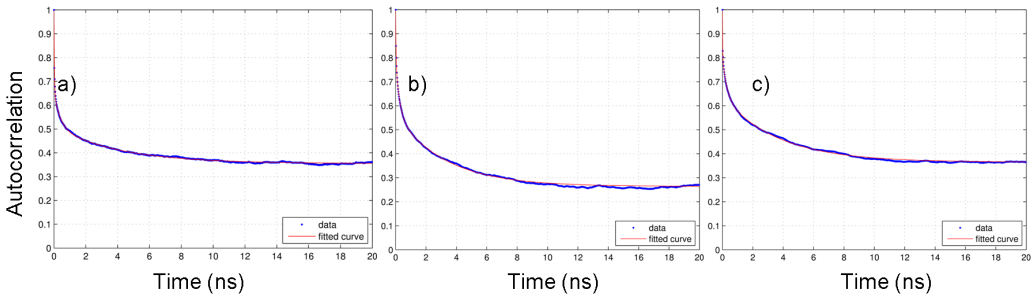

Figure B.10: Fitted autocorrelation functions of local motion of C-labelled single strand DNA magnetic Z (a), Y (b) and X (c) axes at 273K using tri-exponential expression with global motion excluded.*

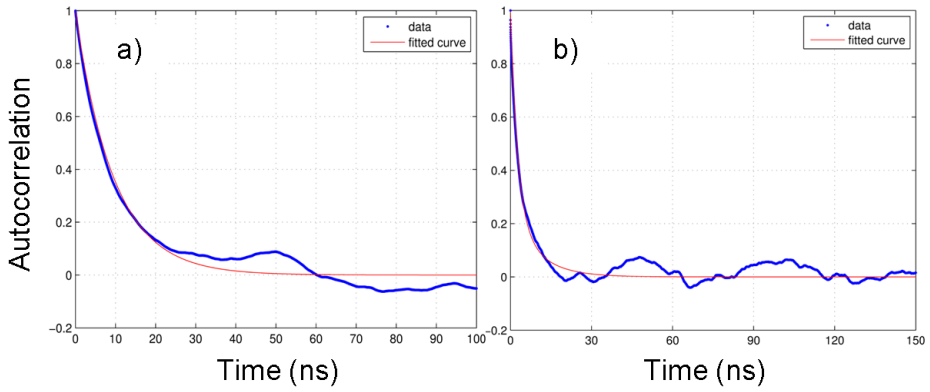

Figure B.11: Fitted autocorrelation functions of C-labelled single strand DNA Z (a) and X/Y (b) principal axes at 273K.*

Table B.7: Parameters obtained from fitting autocorrelation functions of a) local motion of magnetic axes and b) principal axes for C-labelled single strand DNA magnetic axes with 95% confidence bounds. Weights are presented prior to normalisation.*

a)

T (K)	Axis	w_1		τ_1 (ns)		w_2		τ_2 (ns)		w_3		τ_3 (ns)		S_L^2
		Fit	Min/ Max	Fit	Min/ Max	Fit	Min/ Max	Fit	Min/ Max	Fit	Min/ Max	Fit	Min/ Max	
273	X	0.194	0.184/ 0.205	0.012	0.010/ 0.014	0.168	0.161/ 0.174	0.289	0.273/ 0.308	0.273	0.271/ 0.276	3.67	3.64/ 3.70	0.365
	Y	0.211	0.193/ 0.230	0.027	0.023/ 0.032	0.226	0.212/ 0.241	0.262	0.241/ 0.286	0.298	0.295/ 0.302	3.27	3.23/ 3.31	0.264
	Z	0.339	0.337/ 0.341	0.024	0.024/ 0.025	0.148	0.147/ 0.150	0.361	0.357/ 0.365	0.158	0.157/ 0.158	4.01	4.00/ 4.02	0.355

b)

T (K)	$\tau_\perp$ (ns)		$\tau_\parallel$ (ns)	
	Fit	Min/Max	Fit	Min/Max
273	9.65	9.57/9.74	1.91	1.88/1.93

Appendix C

Prediction of Magnetic Parameters of Molybdenum Complexes

C.1 Optimised Geometries

C.1.1 $[MoH_2(\eta^1\text{-}MeCOO)(Ph_2PCH_2CH_2PPh_2)_2]^0$

*Table C.1: DFT optimised Cartesian coordinates of Molybdenum complex **A**.*

Atom Type	X	Y	Z
C	-0.407457	2.484234	-1.709813
C	-0.691758	-1.400486	-3.195558
C	0.782758	-1.777914	-2.974532
C	-0.638397	1.476794	3.278807
C	0.602857	0.611375	3.549915
H	-0.768589	-0.448737	-3.736498
H	-1.221461	-2.177456	-3.766823
H	1.339709	-1.794346	-3.923021
H	-0.338578	2.512941	3.063307

Table C.1: Continued from previous page

H	0.862785	-2.776416	-2.520213
H	-1.310868	1.502133	4.149164
H	0.601678	-1.689260	0.009801
H	-0.472902	-1.225633	1.254582
H	1.244511	1.059439	4.323190
H	0.305757	-0.388766	3.897179
O	-0.906028	1.768490	-2.608873
O	0.036145	2.050192	-0.561906
P	-1.560543	-1.104652	-1.537668
P	-1.586019	0.867352	1.735543
P	1.614696	-0.576392	-1.762977
P	1.588776	0.345045	1.945687
Mo	0.028297	-0.051978	0.079205
C	-0.248746	3.991313	-1.926419
H	0.772753	4.194791	-2.277470
H	-0.950934	4.340490	-2.689619
H	-0.393216	4.543465	-0.990686
C	-2.029423	-2.918398	-1.212114
C	-1.371927	-3.691656	-0.238121
C	-2.987929	-3.555283	-2.031566
C	-1.665552	-5.056163	-0.077376
H	-0.622826	-3.216247	0.392262
C	-3.283521	-4.916168	-1.872821
H	-3.514445	-2.984624	-2.795586
C	-2.623613	-5.673390	-0.891925
H	-1.143477	-5.632166	0.686419
H	-4.029755	-5.382867	-2.514877

Table C.1: Continued from previous page

H	-2.854098	-6.730596	-0.767324
C	-3.250645	-0.465564	-2.035514
C	-4.340552	-0.727495	-1.176852
C	-3.472167	0.293499	-3.200775
C	-5.623965	-0.258675	-1.484949
H	-4.187203	-1.302868	-0.265155
C	-4.761222	0.757553	-3.509804
H	-2.642566	0.553511	-3.851580
C	-5.839940	0.482285	-2.657386
H	-6.451145	-0.471715	-0.809106
H	-4.915343	1.340897	-4.416929
H	-6.837607	0.845893	-2.900055
C	-2.912485	-0.196823	2.548956
C	-2.891899	-1.596398	2.411980
C	-3.940549	0.388042	3.318782
C	-3.864974	-2.395959	3.032192
H	-2.113791	-2.057902	1.807729
C	-4.911913	-0.408830	3.940519
H	-3.998483	1.470472	3.420813
C	-4.877476	-1.805087	3.800224
H	-3.830817	-3.477214	2.904710
H	-5.699717	0.063119	4.526585
H	-5.635958	-2.422861	4.279095
C	-2.572879	2.409334	1.327496
C	-2.797449	3.462355	2.238654
C	-3.126493	2.505961	0.037395
C	-3.567366	4.576355	1.869563

Table C.1: Continued from previous page

H	-2.379198	3.428652	3.243327
C	-3.899971	3.615625	-0.330697
H	-2.932605	1.717420	-0.685838
C	-4.124237	4.654181	0.584737
H	-3.729713	5.379954	2.587191
H	-4.314700	3.667660	-1.336054
H	-4.720629	5.519538	0.298602
C	2.283022	0.784942	-2.867483
C	2.729576	1.966700	-2.242773
C	2.427727	0.669902	-4.264271
C	3.324985	2.994518	-2.989368
H	2.595707	2.087081	-1.170302
C	3.006235	1.704246	-5.014428
H	2.096872	-0.225418	-4.785795
C	3.463998	2.867817	-4.378936
H	3.670019	3.895234	-2.482742
H	3.102162	1.596052	-6.094111
H	3.918545	3.667957	-4.961486
C	2.777200	1.787097	1.912161
C	3.917143	1.692954	1.084595
C	2.569457	2.976779	2.636692
C	4.831219	2.751592	0.999522
H	4.098165	0.780853	0.516346
C	3.477130	4.043079	2.539538
H	1.703111	3.085002	3.285490
C	4.611655	3.933893	1.723701
H	5.710610	2.652181	0.364527

Table C.1: Continued from previous page

H	3.295804	4.955718	3.105789
H	5.317786	4.759868	1.653163
C	2.684387	-1.038371	2.602707
C	2.178894	-2.353145	2.566571
C	3.918945	-0.805489	3.239307
C	2.885743	-3.408653	3.158942
H	1.228609	-2.539480	2.068511
C	4.634321	-1.866024	3.817275
H	4.327553	0.201872	3.289040
C	4.119514	-3.169540	3.782651
H	2.475886	-4.417782	3.126152
H	5.590916	-1.668125	4.299553
H	4.673466	-3.990124	4.236632
C	3.198498	-1.543669	-1.444971
C	4.469486	-1.074100	-1.833000
C	3.112769	-2.800342	-0.811061
C	5.620792	-1.841248	-1.593195
H	4.566802	-0.112200	-2.331964
C	4.260205	-3.571242	-0.583773
H	2.142554	-3.173418	-0.484694
C	5.520960	-3.093670	-0.972452
H	6.593152	-1.458543	-1.901685
H	4.169129	-4.539650	-0.093683
H	6.413680	-3.690339	-0.790703

C.1.2 $[MoCl(NMe)(Ph_2PCH_2CH_2PPh_2)_2]^{2+}$

*Table C.2: DFT optimised Cartesian coordinates of Molybdenum complex **B**.*

Atom Type	X	Y	Z
C	3.651691	-0.379104	-0.012580
C	3.322008	0.917442	-0.770451
C	-3.479029	-0.568321	-0.696666
C	-3.526150	0.712564	0.155641
H	4.521637	-0.880019	-0.457686
H	3.893233	-0.173754	1.038775
H	3.116066	0.719094	-1.830654
H	-3.316707	-0.337086	-1.757144
H	4.158807	1.626808	-0.717365
H	-4.421145	-1.126953	-0.616443
H	-4.339619	1.372605	-0.174378
H	-3.701479	0.481457	1.215025
P	2.193142	-1.559271	-0.039411
P	-2.069668	-1.674688	-0.148805
P	1.790470	1.760851	-0.080386
P	-1.906677	1.666618	0.032886
Mo	0.004603	-0.133943	0.261910
Cl	-0.050278	-0.093752	-2.267222
N	-0.001152	-0.240683	2.010249
C	-0.013240	-0.360975	3.439955
H	-0.146890	0.628780	3.897010
H	-0.834521	-1.019385	3.753213
H	0.936675	-0.789275	3.787242
C	-1.994529	2.783674	1.523003
C	-1.668029	4.151191	1.416575

Table C.2: Continued from previous page

C	-2.369054	2.263089	2.780498
C	-1.733968	4.983311	2.543868
H	-1.384978	4.571370	0.454069
C	-2.440396	3.101159	3.903044
H	-2.626163	1.210279	2.892705
C	-2.124226	4.463603	3.786387
H	-1.493565	6.040149	2.445098
H	-2.758027	2.693104	4.860995
H	-2.191846	5.115389	4.655018
C	-2.303654	2.813255	-1.384393
C	-3.434211	3.648007	-1.203762
C	-1.619775	2.839577	-2.610670
C	-3.864303	4.487212	-2.237015
H	-3.974323	3.659200	-0.257901
C	-2.060783	3.682920	-3.643023
H	-0.759958	2.201844	-2.770465
C	-3.179826	4.503735	-3.463128
H	-4.732821	5.124301	-2.082414
H	-1.525146	3.688281	-4.590115
H	-3.519799	5.151982	-4.268133
C	1.633949	3.219427	-1.217536
C	1.797394	3.064316	-2.610995
C	1.444454	4.509204	-0.679980
C	1.787588	4.188557	-3.447203
H	1.927395	2.078050	-3.051085
C	1.425765	5.626923	-1.525942
H	1.343877	4.648572	0.394467

Table C.2: Continued from previous page

C	1.602268	5.470420	-2.908148
H	1.931989	4.060472	-4.518330
H	1.292918	6.619681	-1.100272
H	1.603618	6.341526	-3.560017
C	2.393165	2.503973	1.515915
C	1.498597	2.685247	2.587579
C	3.724359	2.956747	1.650995
C	1.925751	3.293822	3.777483
H	0.461775	2.373539	2.483170
C	4.150250	3.553553	2.845040
H	4.435648	2.867471	0.832817
C	3.253739	3.721276	3.911634
H	1.219397	3.438429	4.592590
H	5.179599	3.894321	2.935953
H	3.587545	4.189487	4.835263
C	2.388563	-2.692652	1.415197
C	1.620493	-3.879085	1.438874
C	3.244336	-2.408878	2.499009
C	1.727117	-4.772277	2.513542
H	0.967328	-4.125873	0.601816
C	3.342202	-3.304812	3.575397
H	3.855744	-1.509424	2.513956
C	2.587932	-4.486936	3.584725
H	1.148600	-5.694294	2.505103
H	4.020439	-3.082036	4.396650
H	2.678470	-5.185068	4.414275
C	2.608612	-2.619164	-1.523260

Table C.2: Continued from previous page

C	2.540369	-2.077346	-2.825623
C	3.168423	-3.903644	-1.343777
C	3.010503	-2.812973	-3.922652
H	2.109877	-1.095872	-2.995139
C	3.632805	-4.631506	-2.448401
H	3.269067	-4.337902	-0.353598
C	3.552872	-4.092977	-3.739791
H	2.950431	-2.379724	-4.919207
H	4.065440	-5.617358	-2.289977
H	3.916114	-4.661158	-4.593626
C	-2.699190	-2.363360	1.470106
C	-1.806151	-3.110814	2.265495
C	-4.035550	-2.226863	1.901319
C	-2.237645	-3.717609	3.452573
H	-0.769515	-3.227215	1.954522
C	-4.463791	-2.827952	3.095886
H	-4.765106	-1.671608	1.316075
C	-3.569363	-3.576879	3.872529
H	-1.535515	-4.301156	4.045517
H	-5.500241	-2.716890	3.408332
H	-3.907091	-4.049717	4.792276
C	-2.073489	-3.156583	-1.264989
C	-1.086104	-3.359713	-2.247761
C	-3.122043	-4.092427	-1.117731
C	-1.157606	-4.482146	-3.085740
H	-0.279754	-2.644600	-2.373710
C	-3.189033	-5.203313	-1.967438

Table C.2: Continued from previous page

H	-3.879238	-3.963380	-0.346461
C	-2.206817	-5.401328	-2.951045
H	-0.391742	-4.631483	-3.844064
H	-4.005616	-5.913842	-1.856263
H	-2.260338	-6.269249	-3.605025

Appendix D

Nuclear Inelastic Scattering of Iron Sulphur Clusters

D.1 Roussin's Red Esters

D.1.1 Roussin's Red Ester

Table D.1: DFT optimised Cartesian coordinates of Roussin's Red Ester.

Atom Type	X	Y	Z
Fe	0.000000	0.000000	1.316447
S	1.805994	-0.054880	0.000000
Fe	0.000000	0.000000	-1.316447
S	-1.805994	0.054880	0.000000
N	-0.017058	-1.421447	-2.159118
N	-0.017058	-1.421447	2.159118
O	-0.048322	-2.320287	2.909286
O	-0.048322	-2.320287	-2.909286
N	0.017058	1.421447	2.159118
N	0.017058	1.421447	-2.159118
O	0.048322	2.320287	2.909286

O	0.048322	2.320287	-2.909286
C	2.533320	1.634255	0.000000
H	3.161216	1.727617	0.894258
H	3.161216	1.727617	-0.894258
H	1.752169	2.399440	0.000000
C	-2.533320	-1.634255	0.000000
H	-3.161216	-1.727617	0.894258
H	-3.161216	-1.727617	-0.894258
H	-1.752169	-2.399440	0.000000

Table D.2: DFT calculated vibrational modes and frequencies for Roussin's Red Ester. ***R*** *indicates modes that are strong in NIS and Raman,* ***IR*** *- modes that are strong in NIS and IR.*

Mode	**DFT Frequency (cm^{-1})**
S-Fe-S Wagt	80.99
O-N-Fe-N-O Rock / Fe-S-Fe Twist	90.49
S-Fe-S Twist / Me-S-Fe Bend (**R**)	175.72
Fe-S-Fe Twist / Me-S-S-Me Twist	181.06
S-Fe-S Twist / Fe-S-Fe Scissor / S-S-Me Bend (**R**)	201.39
S-Fe-S Scissor/Stretch (**IR**)	279.30
N-Fe-N Rock / O-N-Fe Bend / S-Fe-S/Fe-S-Fe Asymmetric Stretch	309.00
N-Fe-N Rock / O-N-Fe Bend / S-Fe-S Asymmetric Stretch (**IR**)	352.68
N-Fe-N Wags	529.68
N-Fe-N Symmetric Stretches / Fe-S-Fe Rock	606.60
N-Fe-N Symmetric Stretches / Fe-S-Fe Scissor (**R**)	608.09
N-Fe-N Wag / Fe-S-Fe Symmetric Stretch (**IR**)	624.81
N-Fe-N Asymmetric Stretch / Fe-S-Fe Twist (**R**)	665.34
N-Fe-N Asymmetric Stretch / Fe-S-Fe Wag	666.99

D.1.2 Single Persulphide Roussin's Red Ester

Table D.3: DFT optimised Cartesian coordinates of Single Persulphide Roussin's Red Ester.

Atom Type	X	Y	Z
Fe	0.349289	-0.142790	1.314693
S	1.825219	-1.197404	0.000000
Fe	0.349289	-0.142790	-1.314693
S	-1.104741	0.908614	0.000000
N	-0.456431	-1.304305	-2.177821
N	-0.456431	-1.304305	2.177821
O	-0.988333	-2.008290	2.943442
O	-0.988333	-2.008290	-2.943442
N	1.152061	1.033519	2.151231
N	1.152061	1.033519	-2.151231
O	1.685634	1.766626	2.892971
O	1.685634	1.766626	-2.892971
C	3.359705	-0.183895	0.000000
H	3.93695	-0.448074	0.894260
H	3.93695	-0.448074	-0.894260
H	3.12194	0.883457	0.000000
S	-2.954048	-0.127098	0.000000
C	-4.093559	1.301332	0.000000
H	-3.962273	1.909882	-0.901644
H	-5.10277	0.868201	0.000000
H	-3.962273	1.909882	0.901644

Table D.4: DFT calculated vibrational modes and frequencies for of Single Persulphide Roussin's Red Ester. ***R*** *indicates modes that are strong in NIS and Raman,* ***IR*** *- modes that are strong in NIS and IR.*

Mode	**DFT Frequency (cm^{-1})**
O=N-Fe-N=O Scissor (**R**)	59.43
O=N-Fe-N=O Wag / Me-S-S Rock (**R**)	59.87
O=N-Fe-N=O Scissor	65.67
N-Fe-S Scissor (Slight)	77.29
Fe-S-Fe Twist (**R**)	91.17
S-S-S Wag / Fe-S-Fe Rock (Slight)	102.75
S-S-Me Wag / Fe-S-Fe Rock (Slight)	153.42
S-Fe-S Scissor (**R**)	169.50
S-S-Me Wag / Fe-S-Fe Rock (Slight)	183.31
Fe-S-Fe Wag (Slight) / S-S-Me Scissor	199.10
Fe-S-Fe Scissor / S-S-Me Scissor (**R**)	206.65
Fe-N=O Bend/ N-Fe-N Rock / Fe-S-Fe Twist	268.19
Fe-N=O Bend / N-Fe-N Rock / S-Fe-S Wag (**IR**)	280.91
S-Fe-S Scissor/Stretch (**IR**)	281.57
N-Fe-N Wag / Fe-S-Fe Asymmetric Stretch	306.76
S-Fe-S Scissor/Stretch / S-S-Me Scissor (**R**)	336.09
S-Fe-S Stretch/Rock / S-S-Me Scissor (**IR**)	362.64
Fe-N=O Bend / N-Fe-N Wag / Fe-S-Fe Rock (**R**)	535.97
N-Fe-N Asymmetric Stretch / Fe-S-Fe Rock	605.37
N-Fe-N Symmetric Stretch / Fe-S-Fe Scissor (**R**)	607.29

Table D.4: Continued from previous page

Fe-N=O Bend / N-Fe-N Wag / Fe-S-Fe Symmetric Stretch (**IR**)	620.60
N-Fe-N Asymmetric Stretch / Fe-S-Fe Twist (**R**)	661.80
N-Fe-N Asymmetric Stretch / Fe-S-Fe Wag	663.67
Fe-N=O Bend / N-Fe-N Scissor / Fe-S-Fe Rock (**IR**)	701.65
Fe-N=O Bend / N-Fe-N Scissor / Fe-S-Fe Scissor	708.00

D.1.3 Double Persulphide Roussin's Red Ester

Table D.5: DFT optimised Cartesian coordinates of Double Persulphide Roussin's Red Ester.

Atom Type	X	Y	Z
Fe	0.000000	0.000000	1.312152
S	1.556229	-0.906998	0.000000
Fe	0.000000	0.000000	-1.312152
S	-1.556229	0.906998	0.000000
N	-0.680488	-1.242935	-2.167658
N	-0.680488	-1.242935	2.167658
O	-1.142256	-2.004991	2.923442
O	-1.142256	-2.004991	-2.923442
N	0.680488	1.242935	2.167658
N	0.680488	1.242935	-2.167658
O	1.142256	2.004991	2.923442
O	1.142256	2.004991	-2.923442
S	-3.281139	-0.327425	0.000000
S	3.281139	0.327425	0.000000
C	-4.572374	0.964835	0.000000
H	-4.510241	1.584307	-0.901657
H	-5.526785	0.421438	0.000000
H	-4.510241	1.584307	0.901657
C	4.572374	-0.964835	0.000000
H	4.510241	-1.584307	-0.901657
H	5.526785	-0.421438	0.000000
H	4.510241	-1.584307	0.901657

Table D.6: DFT calculated vibrational modes and frequencies for Double Persulphide Roussin's Red Ester. ***R*** *indicates modes that are strong in NIS and Raman,* ***IR*** *- modes that are strong in NIS and IR.*

Mode	**DFT Frequency (cm^{-1})**
O=N-Fe-N=O Rock / S-S-Me Rock	53.56
O=N-Fe-N=O Wag / S-S-Me Rock	60.22
O=N-Fe-N=O Scissor / Fe-S-Fe Rock / S(Cys)-S-S Wag	81.09
Fe-S-Fe Twist (**R**)	92.78
S-Fe-S Rock (**R**)	129.99
Fe-N=O Bend / N-Fe-N Rock / S-Fe-S Wag / S-S-Me Rock	143.20
Fe-S-Fe Rock (Slight)	157.80
Fe-S-Fe Scissor	162.50
S-Fe-S Scissor/Stretch (Slight) / S-S-Me Scissor	204.07
S-Fe-S Scissor / S-S-Me Scissor (**R**)	206.95
Fe-N=O Bend / N-Fe-N Rock / S-Fe-S Asymmetric Stretch	267.82
Fe-N=O Bend / N-Fe-N Rock/ S-Fe-S Rock (**IR**)	277.38
N-Fe-N Twist / S-Fe-S Scissor/Stretch (**IR**)	283.75
Fe-N=O Bend / N-Fe-N Rock/Twist / S-Fe-S Asymmetric Stretch	303.60
N-Fe-N Wag / S-Fe-S Rock/Asymmetric Stretch (**IR**)	366.58
Fe-N=O Bend / N-Fe-N Wag / Fe-S-Fe Rock (**R**)	541.80
N-Fe-N Asymmetric Stretch (**IR**)	604.18
N-Fe-N Symmetric Stretch / Fe-S-Fe Scissor (**R**)	606.42

Table D.6: Continued from previous page

Fe-N=O Bend / N-Fe-N Wag / Fe-S-Fe Symmetric Stretch / S-Fe-S Rock (**IR**)	617.14
N-Fe-N Asymmetric Stretch / Fe-S-Fe Twist (**R**)	658.88
N-Fe-N Asymmetric Stretch / Fe-S-Fe Wag	660.75
Fe-N=O Bend / N-Fe-N Scissor / Fe-S-Fe Rock (**IR**)	695.06
Fe-N=O Bend / N-Fe-N Scissor / Fe-S-Fe Scissor (**R**)	703.70

D.1.4 Roussin's Red Ester/Salt

Table D.7: DFT optimised Cartesian coordinates of Roussin's Red Ester/Salt.

Atom Type	X	Y	Z
Fe	0.12007964	0.169586	1.320700
S	1.89479644	0.284369	0.000000
Fe	0.12007964	0.169586	-1.320700
S	-1.59768157	-0.452291	0.000000
N	0.4318857	-1.004501	-2.409157
N	0.4318857	-1.004501	2.409157
O	0.63776813	-1.890851	3.170222
O	0.63776813	-1.890851	-3.170222
N	-0.29833827	1.645344	1.996944
N	-0.29833827	1.645344	-1.996944
O	-0.59250652	2.304539	2.941475
O	-0.59250652	2.304539	-2.941475
C	-1.51272113	-2.294527	0.000000
H	-2.02392648	-2.666695	0.897087
H	-2.02392648	-2.666695	-0.897087
H	-0.46764976	-2.621915	0.000000

Table D.8: DFT calculated vibrational modes and frequencies for Roussin's Red Ester/Salt. ***R*** *indicates modes that are strong in NIS and Raman,* ***IR*** *- modes that are strong in NIS and IR,* ***All*** *- modes that are strong in NIS, IR and Raman.*

Mode	**DFT Frequency (cm^{-1})**
O=N-Fe-N=O Wag	55.12
O=N-Fe-N=O Scissor / S-Fe-S Rock	68.49
N-Fe-S(Cys) Scissor (**R**)	76.30
Fe-S-Fe Twist (**R**)	89.66
Fe-N=O Bend / S-Fe-S Wag (**R**)	99.44
S-Fe-S Rock	112.94
Fe-N=O Bend / N-Fe-N Rock / S-Fe-S Scissor/Twist (**R**)	156.91
S-Fe-S Rock (Slight) / S-Me Motion (**R**)	170.68
Fe-N=O Bend / N-Fe-N Rock / S-Fe-S Scissor/Stretch (**IR**)	204.93
S-Fe-S Scissor/Wag (**All**)	208.90
Fe-N=O Bend / N-Fe-N Rock / S-Fe-S Wag (**All**)	259.70
Fe-N=O Bend / N-Fe-N Rock / Fe-S(Salt)-Fe Rock / S-Fe-S Scissor/Stretch (**IR**)	281.38
Fe-N=O Bend / N-Fe-N Rock / S-Fe-S Asymmetric Stretches	306.30
Fe-S(Cys)-Fe Stretch (**All**)	328.96
Fe-N=O Bend N-Fe-N Twist/ Fe-S(Salt)-Fe Stretch (**All**)	357.52
Fe-N=O Bend / N-Fe-N Twist	392.50
Fe-N=O Bend / N-Fe-N Twist	398.13
Fe-N=O Bends / N-Fe-N Wag / Fe-S-Fe Rock (**All**)	496.21

Table D.8: Continued from previous page

Fe-N=O Bends / N-Fe-N Wag / Fe-S-Fe Scissor/Stretch (**All**)	584.85
Fe-N=O Bends / Fe-N Stretch / Fe-S-Fe Rock/Stretch (**R**)	596.43
Fe-N=O Bends / N-Fe-N Wag / Fe-S-Fe Scissor/Stretch (**All**)	611.96
Fe-N=O Bend / N-Fe-N Rock/Bend / Fe-S-Fe Twist (**All**)	638.51
Fe-N=O Bend / N-Fe Stretch / Fe-S-Fe Wag (**All**)	641.89
Fe-N=O Bends / N-Fe-N Rock / Fe-S-Fe Rock/Stretch (**R**)	716.68
Fe-N=O Bends / N-Fe-N Rock / Fe-S-Fe Scissor/Stretch (**IR**)	724.64

D.2 Roussin's Black Salts

D.2.1 Roussin's Black Salt

Table D.9: DFT optimised Cartesian coordinates of Roussin's Black Salt.

Atom Type	X	Y	Z
Fe	0.000000	2.049968	-0.290073
Fe	0.000000	0.000000	1.411969
Fe	1.775324	-1.024984	-0.290073
Fe	-1.775324	-1.024984	-0.290073
S	0.000000	-2.035114	0.641093
S	-1.762460	1.017557	0.641093
S	1.762460	1.017557	0.641093
N	0.000000	0.000000	3.045780
O	0.000000	0.000000	4.224895
N	0.000000	3.600887	0.267499
N	-3.118459	-1.800443	0.267499
N	3.118459	-1.800443	0.267499
O	0.000000	4.775668	0.388657
O	-4.135850	-2.387834	0.388657
O	4.135850	-2.387834	0.388657
N	1.669489	-0.963880	-1.935250
O	1.848665	-1.067327	-3.095108
N	0.000000	1.927759	-1.935250
O	0.000000	2.134655	-3.095108
N	-1.669489	-0.963880	-1.935250
O	-1.848665	-1.067327	-3.095108

Table D.10: DFT calculated vibrational modes and frequencies for Roussin's Black Salt. ***DD*** *indicates doubly degenerate modes of vibration,* ***R*** *- modes that are strong in NIS and Raman,* ***IR*** *- modes that are strong in NIS and IR.*

Mode	**DFT Frequency (cm^{-1})**
O-N-Fe-N-O Wag	77.04
O-N-Fe Bends/Twists/Rocks (**DD**)	79.13
N-Fe-N Wag / S-Fe-S Twists/Wag (**DD**)	103.65
Fe-S-Fe Scissor (**R**)	108.85
S-Fe-S Scissor/Rock (**DD**)	182.55
N-Fe-N Rock / O-N-Fe Bend / Fe-S-Fe/S-Fe-S Scissor (**R**)	192.05
N-Fe-N Rock / O-N-Fe Bend / Fe-Fe Stretch	216.47
N-Fe-N Rock / O-N-Fe Bend (**DD**)	219.40
N-Fe-N Twists / S-Fe-S Stretches (**DD,IR**)	269.75
N-Fe-N Twist / O-N-Fe Bend / S-Fe-S Rock/Asymmetric Stretch	343.52
N-Fe-N Wag / O-N-Fe Bend / S-Fe-S Rock/Asymmetric Stretch (**DD**)	371.00
N-Fe-N Wag / O-N-Fe Bend / Fe-S-Fe Asymmetric Stretch	524.15
N-Fe-N Wags / O-N-Fe (Single) Bend / Fe-S-Fe Scissor/Stretch (**DD,IR**)	594.02
N-Fe-N Symmetric Stretch / Fe-S-Fe Scissor/Wag	615.58
N-Fe-N Symmetric Stretch / Fe-S-Fe Scissor/Wag/Rock (**DD**)	616.30
N-Fe-N Asymmertric Stretches / N-Fe (Single) Stretch (**R**)	656.59
N-Fe-N Asymmertric Stretches (**DD,R**)	656.59
N-Fe-N Asymmertric Stretches / N-Fe (Single) Stretch (**R**)	659.56

D.2.2 Roussin's Black Ester (Single Thiolate)

Table D.11: DFT optimised Cartesian coordinates of Roussin's Black Ester with single thiolate group.

Atom Type	X	Y	Z
Fe	0.035271	2.205018	0.000000
Fe	-1.377449	-0.054083	0.000000
Fe	0.446339	-0.842334	1.775324
Fe	0.446339	-0.842334	-1.775324
S	-0.341433	-1.967878	0.000000
S	-0.749522	1.057393	-1.762460
S	-0.749522	1.057393	1.762460
N	-2.996595	-0.272495	0.000000
O	-4.165126	-0.430122	0.000000
N	-0.724627	3.667479	0.000000
N	-0.002563	-1.685370	-3.118459
N	-0.002563	-1.685370	3.118459
O	-1.001745	4.815518	0.000000
O	-0.044110	-2.283686	-4.135850
O	-0.044110	-2.283686	4.135850
N	2.068580	-0.561847	1.669489
O	3.231857	-0.509312	1.848665
N	1.682019	2.303837	0.000000
O	2.803808	2.663929	0.000000
N	2.068580	-0.561847	-1.669489
O	3.231857	-0.509312	-1.848665
C	-0.606167	-3.728081	0.000000
H	0.338373	-4.230817	0.000000
H	-1.158007	-4.005762	0.873651

Table D.11: Continued from previous page

H	-1.158007	-4.005762	-0.873651

Table D.12: DFT calculated vibrational modes and frequencies for Roussin's Black Ester with single thiolate group. ***R*** *indicates modes that are strong in NIS and Raman,* ***IR*** *- modes that are strong in NIS and IR,* ***All*** *- modes that are strong in NIS, IR and Raman.*

Mode	**DFT Frequency (cm^{-1})**
Fe-N=O Bend / Fe-S-Fe Twists/ Rocks	80.05
S-Fe-S Rock / Fe-S-Me Scissor	94.86
Fe-S-Fe Scissor (**R**)	110.46
S-Fe-S Wag / Fe-S-Me Bend (**R**)	136.39
Fe-N=O Bends / Fe-S-Fe Scissor/Rock (**R**)	172.74
N-Fe-N Rock / Fe-N=O Bend / Fe-S-Fe Scissor / Fe-S-Me Scissor (**R**)	198.35
N-Fe-N Rock / Fe-N=O Bend / Fe-S-Me Scissor (**R**)	219.64
Fe-N=O Bend / N-Fe-N Rock / S-Fe-S Twist/Stretch	237.30
N-Fe-N Twist/Rock / S-Fe-S Stretches / S-Fe-S Twist / Fe-N=O Bend (**IR**)	273.10
N-Fe-N Rock / S-Fe-S Wag/Stretch / Fe-N=O Bend (**IR**)	282.48
S(Cys)-Fe(Central) Stretch / S(Bridging)-Fe(Non-Central) Stretch / S-Fe-S Wag	332.56
S-Fe-S Rock / S-Fe-S Asymmetric Stretch	335.57
N-Fe-N Twist / S-Fe-S Asymmetric Stretch (**IR**)	359.42
S-Fe-S Scissor/Stretch / Fe-N=O Bend (Single) (**R**)	374.62
Fe-N=O Bend / N-Fe-N Twist / S-Fe-S Asymmetric Stretch/ Scissor (**R**)	383.74
N-Fe-N Wag / S-Fe-S Rock / Fe-N=O Bend (Single) (**R**)	449.48

Table D.12: Continued from previous page

N-Fe-N Wag / Fe-N=O (Single) Bend / S-Fe-S Scissor	465.91
N-Fe-N Wag / Fe-S-Fe Rock	528.72
Fe-N=O Bend (All) / N-Fe-N Wag / Fe-S-Fe Symmetric Stretch	572.48
Fe-N=O Bend (All) / N-Fe-N Wag / Fe-S-Fe Scissor	587.60
N-Fe-N Symmetric Stretch (Opposite S-Me) (**R**)	606.00
N-Fe-N Symmetric Stretches (Adjacent to S-Me) (**R**)	609.09
N-Fe-N Symmetric Stretches / Fe-S-Fe Rock (Adjacent to S-Me) (**All**)	609.88
N-Fe-N Asymmetric Stretch / Fe-S-Fe Scissor / Fe-N Stretch (Single) (**R**)	647.51
N-Fe-N Asymmetric Stretch / Fe-S-Fe Wag/Rock / Fe-N Stretch (Single) (**R**)	649.62
N-Fe-N Asymmetric Stretch / Fe-S-Fe Wag / Fe-N Stretch (Single) (**R**	652.28
N-Fe-N Asymmetric Stretch / Fe-S-Fe Twist (**R**)	652.76

D.2.3 Roussin's Black Ester (Double Thiolate)

Table D.13: DFT optimised Cartesian coordinates of Roussin's Black Ester with two thiolate groups.

Atom Type	X	Y	Z
Fe	1.19754713	-0.160620	1.775325
Fe	-0.10827148	1.336836	0.000000
Fe	-1.83038448	-0.696300	0.000000
Fe	1.19754713	-0.160620	-1.775325
S	-0.97597572	0.400482	-1.762461
S	2.03001555	0.932280	0.000000
S	-0.97597572	0.400482	1.762461
N	-0.39289367	2.945665	0.000000
O	-0.59830438	4.106750	0.000000
N	1.86401516	0.523517	3.118460
N	1.86401516	0.523517	-3.118460
N	-3.4547211	-0.417435	0.000000
O	2.42131672	0.745150	4.135851
O	2.42131672	0.745150	-4.135851
O	-4.63264606	-0.502786	0.000000
N	-1.42344314	-2.295031	0.000000
O	-1.42511797	-3.473196	0.000000
N	1.42397926	-1.791285	1.669489
O	1.72790135	-2.915386	1.848666
N	1.42397926	-1.791285	-1.669489
O	1.72790135	-2.915386	-1.848666
C	-1.90411284	0.741677	-3.242511
H	-2.06022315	-0.168288	-3.783337
H	-2.85005494	1.167404	-2.980118

Table D.13: Continued from previous page

H	-1.35998512	1.431016	-3.853768
C	-1.90411284	0.741677	3.242511
H	-2.06022315	-0.168288	3.783337
H	-1.35998512	1.431016	3.853768
H	-2.85005494	1.167404	2.980118

Table D.14: DFT calculated vibrational modes and frequencies for Roussin's Black Ester with two thiolate groups. ***R*** *indicates modes that are strong in NIS and Raman,* ***IR*** *- modes that are strong in NIS and IR,* ***All*** *- modes that are strong in NIS, IR and Raman.*

Mode	**DFT Frequency (cm^{-1})**
O=N-Fe-N=O Wag / S-Fe-S/Fe-S-Fe Rock	70.05
S-Fe-S Twist	76.65
Fe-S-Fe Rock	96.73
Fe-S-Fe Twist	111.16
Fe-Fe-S Rock	116.99
S-Fe-S Twist	138.78
Fe-Fe-S Scissor / Me Wagging	143.65
S-Fe-S/Fe-S-Fe Rock / Me Rocking	150.66
Fe-S-Fe Scissor /S-Fe-S Rock (**R**)	167.16
Fe-S-Fe Scissor /S-Fe-S Rock	189.32
S-Fe-S Scissor (**R**)	193.09
N-Fe-N Rock / S-Fe-S Wag (**R**)	227.08
O=N-Fe Bend / N-Fe-N Rock / S-Fe-S Asymmetric Stretch	230.29
O=N-Fe Bend / N-Fe-N Rock / Fe-S-Fe Scissor	241.34
O=N-Fe Bend / N-Fe-N Rock / S-Fe-S Twist	246.46
N-Fe-N Rock / S-Fe-S Wag / Fe-N=O Bend (**IR**)	286.19
S-Fe-S Symmetric Stretch (**R**)	336.30
S-Fe-S Asymmetric Stretches / Rock	340.67
S-Fe-S Asymmetric Stretch/Rock / Fe-N=O Bend (Single) (**IR**)	346.28
N-Fe-N Twist / S-Fe-S Stretches (**IR**)	360.16

Table D.14: Continued from previous page

Fe-N=O Bend (All) / N-Fe-N Wag / Fe-S(Bridging) Stretch	390.69
Fe-N=O Bend (Single) / Fe-S(Bridging) Stretch	453.03
Fe-N=O Bend (Single) (**All**)	457.03
Fe-N=O Bend / Ne-Fe-N Wag	528.30
Fe-N=O Bend / Ne-Fe-N Wag (**IR**)	566.23
Fe-N=O Bend / Ne-Fe-N Wag	569.43
N-Fe-N Symmetric Stretches / Fe-S-Fe Rock (**All**)	602.40
N-Fe-N Symmetric Stretch (**All**)	602.77
N-Fe-N Symmetric Stretches (**All**) / Fe-S-Fe Wag	603.14
N-Fe-N Asymmetric Stretches / Fe-S-Fe Rock (**R**)	640.82
N-Fe-N Asymmetric Stretches / Fe-S-Fe Scissor (**All**)	640.97
Fe-N Stretch (Single) / N-Fe-N Asymmetric Stretch (**R**)	642.58
N-Fe-N Asymmetric Stretch / Fe-S-Fe Rock (**R**)	644.08
Fe-N=O Bend / N-Fe-N Scissor	699.04
Fe-N=O Bend / N-Fe-N Scissor	699.47
Fe-N=O Bend / N-Fe-N Scissor	704.17

D.2.4 Roussin's Black Ester (Triple Thiolate)

Table D.15: DFT optimised Cartesian coordinates of Roussin's Black Ester with three thiolate groups.

Atom Type	X	Y	Z
Fe	0.000000	-2.049967	-0.401496
Fe	0.000000	0.000000	1.300546
Fe	1.775323	1.024983	-0.401496
Fe	-1.775323	1.024983	-0.401496
S	0.000000	2.035112	0.529671
S	-1.762459	-1.017556	0.529671
S	1.762459	-1.017556	0.529671
N	0.000000	0.000000	2.934357
O	0.000000	0.000000	4.113472
N	0.000000	-3.600885	0.156076
N	-3.118458	1.800442	0.156076
N	3.118458	1.800442	0.156076
O	0.000000	-4.775665	0.277234
O	-4.135847	2.387833	0.277234
O	4.135847	2.387833	0.277234
N	1.669488	0.963880	-2.046672
O	1.848665	1.067327	-3.206530
N	0.000000	-1.927759	-2.046672
O	0.000000	-2.134654	-3.206530
N	-1.669488	0.963880	-2.046672
O	-1.848665	1.067327	-3.206530
C	0.000000	3.744125	1.027338
H	0.000000	4.368617	0.158482
H	0.869135	3.946542	1.611346

Table D.15: Continued from previous page

H	-0.869135	3.946542	1.611346
C	3.242507	-1.872063	1.027338
H	3.783333	-2.184309	0.158482
H	2.983238	-2.725964	1.611346
H	3.852373	-1.220578	1.611346
C	-3.242507	-1.872063	1.027338
H	-3.783333	-2.184309	0.158482
H	-3.852373	-1.220578	1.611346
H	-2.983238	-2.725964	1.611346

Table D.16: DFT calculated vibrational modes and frequencies for Roussin's Black Ester with three thiolate groups. ***DD*** *indicates doubly degenerate modes of vibration,* ***R*** *- modes that are strong in NIS and Raman,* ***IR*** *- modes that are strong in NIS and IR,* ***R/IR*** *- modes that are strong in Raman and IR only,* ***All*** *- modes that are strong in NIS, IR and Raman.*

Mode	**DFT Frequency (cm^{-1})**
Me-S-Fe(Central) Scissor (Slight) / Me Motion	91.99
Fe-S-Fe Rock/Scissor (Slight) / Me Motion	93.57
Fe-S-Fe Rock/Scissor (Slight) / Me Motion	94.33
Fe-S-Fe Scissor (Slight) / Me Motion	120.41
Fe-S-Fe Scissor / S-Fe-S Wag (Slight) / Me Motion	121.47
S-Fe-S Twist (Slight) / Me Motion	127.15
S-Fe-S Rock/Scissor (Slight) / Me Motion	130.28
Fe-S-Fe Scissor (Slight) / Me Motion (**R**)	131.07
Fe-S-Fe Twist (Slight) / Me Motion	135.02
Fe-S-Fe Twist (Slight) / Me Motion	141.64
S-Fe-S Rock / Me Motion	154.99
Fe-S-Fe Scissor/Rock / Fe-N=O Bends (**R**)	180.71
S-Fe-S Rock / Fe-S-Fe Scissor	181.42
S-Fe-S Rock / Fe-S-Fe Scissor	181.93
N-Fe-N Rock / S-Fe-S Wag (**R**)	231.41
N-Fe-N Rock / Fe-N=O Bends / Fe-S-Fe Stretches	235.55
N-Fe-N Rock / Fe-N=O Bends / Fe-S-Fe Stretches	237.25
Fe-N=O Bend (Single) / S-Fe-S Scissors/Stretches/Rock (**DD**)	344.41
S-Fe-S Asymmetric Stretches / Rock	353.31
Fe-N=O Bend (Single)	459.81

Table D.16: Continued from previous page

Fe-N=O Bend (Single)	461.81
N-Fe-N Wag / Fe-S-Fe Asymmetric stretches	524.33
N-Fe-N Wags (**DD,IR**)	561.27
N-Fe-N Symmetric Stretches / Fe-S-Fe Twist (**DD,R/IR**)	592.53
N-Fe-N Symmetric Stretches / Fe-S-Fe Wag (**DD, R/IR**)	594.41
N-Fe-N Asymmetric Stretches / Fe-S-Fe Wag (**DD, R/IR**)	627.28
N-Fe-N Asymmetric Stretches / Fe-S-Fe Rock (**R**)	628.42
N-Fe-N Asymmetric Stretches / Fe-S-Fe Scissor (**R**)	629.02
Fe-N Stretch (Single) (**R/IR**)	633.11

D.2.5 Roussin's Black Ester (Single Persulphide Thiolate)

Table D.17: DFT optimised Cartesian coordinates of Roussin's Black Ester with single persulphide thiolate group.

Atom Type	X	Y	Z
Fe	0.254098	2.343206	-0.010000
Fe	1.258602	-0.087029	0.010000
Fe	-0.574032	-0.549652	-1.893234
Fe	-0.554032	-0.509652	1.933234
S	-0.250681	-1.649473	0.040000
S	0.940352	1.163600	1.749207
S	0.920352	1.123600	-1.749207
N	2.797577	-0.666889	0.000000
O	3.915580	-1.002717	-0.010000
N	1.204766	3.689152	-0.030000
N	-0.115477	-1.350840	3.290137
N	-0.115477	-1.390840	-3.250137
O	1.713380	4.741353	-0.040000
O	-0.031112	-1.897729	4.318086
O	-0.031111	-1.937729	-4.278086
N	-2.064766	0.143156	-1.933310
O	-3.123062	0.577098	-2.195832
N	-1.371787	2.690814	0.000000
O	-2.382091	3.284085	0.000000
N	-2.064766	0.183156	1.973310
O	-3.123062	0.597098	2.215832
S	0.646468	-3.594900	0.050000
C	-0.866730	-4.616224	-0.400000
H	-0.509603	-5.654801	-0.420000

Table D.17: Continued from previous page

H	-1.672589	-4.532214	0.383232
H	-1.252589	-4.352214	-1.423232

Table D.18: DFT calculated vibrational modes and frequencies for Roussin's Black Ester with single persulphide thiolate group. ***DD*** *indicates doubly degenerate modes of vibration,* ***R*** *- modes that are strong in NIS and Raman,* ***IR*** *- modes that are strong in NIS and IR,* ***All*** *- modes that are strong in NIS, IR and Raman.*

Mode	**DFT Frequency (cm^{-1})**
Fe-S-Fe Twist	76.78
N-Fe-N Rock / Fe-S-Fe Wag	82.66
Fe-S-S(Me) Wag /S-Fe-S Rock	97.77
S-Fe-S Twist / Fe-S-S(Me) Scissor (**R**)	106.73
Fe-S-Fe Scissor (**R**)	111.09
Fe-S-Fe Rock	116.37
S-Fe-S Twist/Wag / S-S-Me Scissor (**R**)	148.91
S-Fe-S Scissor/Rock	177.78
Fe-N=O Bend / N-Fe-N Rock / Fe-S-Fe Scissor /Wag / S-S-Me Scissor (**R**)	189.09
Fe-N=O Bend / N-Fe-N Rock / Fe-S-Fe Scissor / Fe-S-S(Me) Scissor (**R**)	200.54
Fe-N=O Bend / N-Fe-N Rock /S-Fe-S Scissor/Wag / S-S-Me Scissor (**R**)	215.04
Fe-N=O Bend / N-Fe-N Rock / Fe-S-Fe Twist	231.37
Fe-N=O Bend / N-Fe-N Rock / S-Fe-S Wag / S-S-Me Scissor (**R**) (**R**)	238.67
Fe-N=O Bend / N-Fe-N Twist / S-Fe-S Stretches/Scissors (**IR**) (**IR**)	273.20
Fe-N=O Bend / N-Fe-N Twists/Rock / S-Fe-S Symmetric Stretch/Scissors (**IR**)	281.36
S-Fe-S Stretches/Scissors/Rocks / S-S-Me Scissor (**IR**)	338.05

Table D.18: Continued from previous page

S-Fe-S Stretches/Scissors/Rocks / S-S-Me Scissor	339.58
S-Fe-S Symmetric Stretches/Scissors / S-S-Me Scissor (**All**)	349.67
N-Fe-N Twist / N-Fe-S(-S-Me) Twist (**All**)	354.51
Fe-N=O Bends / S-Fe-S Scissor/Stretches (**R**)	373.45
N-Fe-N Twist / S-Fe-S Scissor/Stretches/Rocks	375.62
Fe-N=O Bend (Single) / N-Fe-N Wag / S-Fe-S Rock (**All**)	444.45
Fe-N=O Bend (Single) / N-Fe-N Wag / Fe-S-S Asymmetric Stretch (**All**)	475.86
Fe-N=O Bends / N-Fe-N Wags / Fe-S-Fe Twist (**IR**)	519.77
Fe-N=O Bends (All) / N-Fe-N Wags / Fe-S-Fe Stretches/Scissors (**All**)	570.32
Fe-N=O Bends (All) / N-Fe-N Wags / Fe-S-Fe Stretches/Scissors (**IR**)	585.96
N-Fe-N Symmetric Stretches (**All**)	605.08
N-Fe-N Symmetric Stretches (**R**)	605.42
N-Fe-N Symmetric Stretch (**R**)	609.55
Fe-N Stretch (Single) / Fe-S-Fe Rock (**R**)	646.45
Fe-N Stretch (All) / Fe-S-Fe Twist (**R**)	649.18
N-Fe-N Asymmetric Stretch (**R**)	651.62
Fe-N Stretch (All) / Fe-S-Fe Scissor (**R**)	651.84
Fe-N=O Bends / N-Fe-N Scissors (**R**)	700.54
Fe-N=O Bends / N-Fe-N Scissors	703.60
Fe-N=O Bends / N-Fe-N Scissors (**All**)	707.65

Appendix E

Example EPR Model Scripts

Scripts in this section require the export_fig and Easyspin [4] Matlab modules.

E.1 Simple Rotation

```
clear, clf
%=========================================================
%% Magnetic parameters
%=========================================================
Nitroxide.g = [2.0087,2.0061,2.0021];
Nitroxide.Nucs = '14N';
Nitroxide.A = mt2mhz([6.18  6.27  33.60]/10); %Gauss

%=========================================================
%% Dynamic parameters
%=========================================================
Nitroxide.lw = [0  0.07]; %Linewidth (Lorentzian - mT)
Nitroxide.tcorr = [7e-9 2.5e-9]; %Correlation time (s)

% Experimental parameters
Experiment.mwFreq = 9.5; %Frequency (GHz)
```

```
%==========================================================
%% Load in Experimental data
%==========================================================
Flname1 = 'dQ20_Exp'; % Set filename
Ext = '.txt'; % Set extension

ExpShift = 3384; % For use if experimental spectra has been
    centred on 0

File1 = [Flname1 Ext];
EPR_Exp1 = importdata(File1);

EM1 = max(EPR_Exp1(:,2));   % Normalisation
NormExp1 = [EPR_Exp1(:,1)+ExpShift (EPR_Exp1(:,2)/EM1)];

%==========================================================
%% Simulation of Spectra
%==========================================================
[Sim1(:,1),Sim1(:,2)] = chili(Nitroxide,Experiment);
SM1 = max(Sim1(:,2));
NormSim1 = Sim1(:,2)/SM1;

%==========================================================
%% Plotting Data
%==========================================================
fig=figure;
plot(NormExp1(:,1),NormExp1(:,2),'k-','LineWidth',1.0)
hold on
plot(Sim1(:,1)*10,NormSim1(:,1),'g-','LineWidth',1.0)
axis([Sim1(1,1)*10,Sim1(1024,1)*10,-1.1,1.05]);
```

```
set(gca, 'YTick', []);
hold off
set(gcf, 'Color', 'white')
xlabel('Field (G)','fontsize',14)

%==========================================================
%% Save output
%==========================================================
Flout2 = ['DNA_dQ20_Iso_t6_2'];
export_fig(fig,Flout2,'-dpng','-m3.5','-painters') % Save
    image
Res = [Sim1(:,1)*10 NormSim1(:,1)];
dlmwrite('DNA_dQ20_Iso.txt',Res,'precision','%.4f','delimiter'
    ,' '); % Save data as txt file
```

E.2 Two-Component Motion

```
clear, clf
%==========================================================
%% Input files
%==========================================================

%Input filenames?
Flname1 = 'dQ20_Exp'; % Set filename
Ext = '.txt'; % Set extension

ExpShift = 3388;

%==========================================================
%% Initial Magnetic Parameters
%==========================================================
```

```
gxx = 2.0085;
gyy = 2.0060;
gzz = 2.0021;

Axx = 7.04;
Ayy = 7.18;
Azz = 34.07;

%=========================================================
%% Dynamic Parameters
%=========================================================

S1 = 0.91; %Order parameters

Diff1 = 3E7; %DPar
Diff2 = 1E7; %DPerp

%=========================================================
%% Other Parameters
%=========================================================

Freq1 = 9.5125; %GHz

Lw = 0.1; %Linewidth (Lorentzian)

%Desired range for EPR plot (Experimental range determined
    automatically)
FieldRange = [3345 3425]; %Gauss

%=========================================================
```

```
%% Effect of Order parameter
%=========================================================
% g
gmean = (gxx+gyy+gzz)/3;
gxy2 = (gxx+gyy)/2;
gzxy2 = (gzz-gxy2);

G_1 = [gmean-(1/3)*S1*gzxy2 gmean+(2/3)*S1*gzxy2];

Amean = (Axx+Ayy+Azz)/3;
Axy2 = (Axx+Ayy)/2;
Azxy = (Azz-Axy2);

AVal_1 = mt2mhz([(Amean-(1/3)*S1*Azxy) (Amean+(2/3)*S1*Azxy)
    ]/10);

%=========================================================
%% Simulation of Spectra
%=========================================================

File1 = [Flname1 Ext];
EPR_Exp1 = importdata(File1);
EM1 = max(EPR_Exp1(:,2));
NormExp1 = [EPR_Exp1(:,1)+ExpShift (EPR_Exp1(:,2)/EM1)];

Exp1 = struct('mwFreq',Freq1,'Range',[FieldRange/10],'1024',
    Points);
Sys1 = struct('g',G_1,'Nucs','14N','A',AVal_1,'lwpp',[0 Lw],'
    Diff',[Diff2 Diff1]);

Opt.LLKM = [30 10 10 10]; % Basis set
```

```
Opt.Allocation = [4e7 2e5]; % Memory usage

[Sim1(:,1),Sim1(:,2)] = chili(Sys1,Exp1,Opt);
SM1 = max(Sim1(:,2));
NormSim1 = Sim1(:,2)/SM1;

%=========================================================
%% Plot EPR Spectra
%=========================================================

fig = figure;
plot(NormExp1(:,1),NormExp1(:,2),'k-','LineWidth',1.0)
axis([FieldRange(1),FieldRange(2),-1.1,1.05]);
set(gca, 'YTick', []);
%set(gca,'XTick',[3370 3390 3410]);
daspect([50,2,1]);
hold on
plot(Sim1(:,1)*10,NormSim1(:,1),'r-','LineWidth',1.0)
%legend('Exp.','Easyspin/MD');
hold off
set(gcf, 'Color', 'white') %Sets plot background colour -
    stops it putting in a grey border
xlabel('Field (G)','fontsize',14) % x-axis label

%=========================================================
%% Save output
%=========================================================

Flout2 = ['DNA_dQ20_Iso'];
export_fig(fig,Flout2,'-dpng','-m3.5','-painters') % Save
    image
```

```
Res = [NormExp1(:,1) NormExp1(:,2) Sim1(:,1)*10 NormSim1];
dlmwrite('DNA_dQ20_Iso.txt',Res,'precision','%.4f','delimiter'
    ,' '); % Save data as txt file
```